University of Tennessee, Knoxville
Trace: Tennessee Research and Creative Exchange

Doctoral Dissertations | Graduate School

8-2006

Manifestations of Broken Symmetry: The Surfaces Phases of $Ca_{2-x}Sr_xRuO_4$

Robert G. Moore II
University of Tennessee - Knoxville

Recommended Citation

Moore, Robert G. II, "Manifestations of Broken Symmetry: The Surfaces Phases of $Ca_{2-x}Sr_xRuO_4$. " PhD diss., University of Tennessee, 2006.
https://trace.tennessee.edu/utk_graddiss/1834

This Dissertation is brought to you for free and open access by the Graduate School at Trace: Tennessee Research and Creative Exchange. It has been accepted for inclusion in Doctoral Dissertations by an authorized administrator of Trace: Tennessee Research and Creative Exchange. For more information, please contact trace@utk.edu.

To the Graduate Council:

I am submitting herewith a dissertation written by Robert G. Moore II entitled "Manifestations of Broken Symmetry: The Surfaces Phases of $Ca_{2-x}Sr_xRuO_4$." I have examined the final electronic copy of this dissertation for form and content and recommend that it be accepted in partial fulfillment of the requirements for the degree of Doctor of Philosophy, with a major in Physics.

E. Ward Plummer, Major Professor

We have read this dissertation and recommend its acceptance:

Takeshi Egami, Elbio Dagotto, Hanno Weitering

Accepted for the Council:
Dixie L. Thompson

Vice Provost and Dean of the Graduate School

(Original signatures are on file with official student records.)

To the Graduate Council:

I am submitting herewith a dissertation written by Robert G. Moore II entitled "Manifestations of Broken Symmetry: The Surfaces Phases of $Ca_{2-x}Sr_xRuO_4$". I have examined the final electronic copy of this dissertation for form and content and recommend that it be accepted in partial fulfillment of the requirements for the degree of Doctor of Philosophy, with a major in Physics.

E. Ward Plummer
Major Professor

We have read this dissertation
and recommend its acceptance:

Takeshi Egami

Elbio Dagotto

Hanno Weitering

Accepted for the Council:

Anne Mayhew
Vice Chancellor and Dean of
Graduate Studies

(Original signatures are on file with official student records.)

Manifestations of Broken Symmetry: The Surface Phases of $Ca_{2-x}Sr_xRuO_4$

A Dissertation
Presented for the
Doctor of Philosophy
Degree
The University of Tennessee, Knoxville

Robert G. Moore II
August 2006

Copyright © 2006 by Robert G. Moore II.
All rights reserved.

Dedication

To Tammy, for not only supporting my dreams, but adding to them.

∞

Acknowledgments

The undertaking of a difficult Physics problem is too much for one person. While we all have an infinite thirst to learn everything, the world is too immense and real progress can only be accomplished through the efforts of a collective group. One of the primary objectives of the collective is to teach as the advancement of science is accelerated through the conveyance of knowledge and experience. Learning centuries of scientific achievements within a lifetime is a daunting task. Only by helping each other and teaching each other can we truly move forward and discover what potential the future has to offer. My road through science and academia has been long and has had many turns. Luckily, I have been fortunate as there have been many to give me directions and show me the way. Without their help, I would never be able to do this work nor write these words.

First and foremost I would like to thank my wife, Tammy, and my family. I have had some crazy dreams and ideas and their confidence in me is what gives me the courage to pursue them. I would also like to thank my advisor Ward Plummer. Not only has his scientific insight guided me along the way, but his allowance of my persistence when things were not working as expected and support of my goals wherever they evolved has taught me the skills necessary to survive as a scientist. I am grateful for the doors he has opened and the passion he has instilled. I would also like to thank my masters advisor Larry Sorensen and collaborator Steve Kevan. Trying to enter Physics coming from an Engineering background after several years away from school is quite a challenge. They helped me get up to speed and allowed me to shine when few would. I would like to thank Rongying Jin and David Mandrus for the endless supply of samples. Without their support, I would have nothing to look at. I would like to thank Jiandi Zhang for teaching me the vast world of complex oxide surfaces and helping me interpret the confusion that came out of my surface and bulk measurements. In addition to the Physics I have learned, I have learned how to do Physics through numerous experimental and theoretical techniques. I have always been impressed by the willingness of scientists to spend years learning how to do something only to be excited about teaching it to you within days. I would like to thank Von Braun Nascimento for his guidance and assistance with LEED. I would also like to thank J. Rundgren for his assistance with LEED phase shifts and Zac Ward for helping me with the LEED data analysis software. I would like to thank Mark Lumsden and Matt Stone for teaching me neutron scattering. They went out of their way to not only teach me the technique but to ensure I did not screw up the analysis. I would like to thank Art Baddorf for teaching me HREELS and SPM. I would also like to thank Sergei Kalinin and Jiandong Guo for their help with SPM although our results are not presented in this dissertation. I would like to thank Rene Matzdorf, Juergen Hager, and Bernard Nansseu for helping me with STS. While I am an experimentalist, I like to dabble in computational

theory. I would like to thank Vincent Meunier for helping me remember how to write and run Fortran and for stimulating discussions about how to approach DFT calculations. I would also like to thank Von Braun Nascimento, Bill Shelton for helping me figure out how to run realistic calculations and Zong Fang for performing several theoretical calculations to support our experimental results. There were numerous students and post docs who assisted me perform experiments and helped me understand experiments through in depth discussions and pointing out the obvious. Te-Yu Chen, Hong Liu, Minghu Pan, Chenxi Lu, Lei Cai, Biao Hu, Michael Pierce and Bo Hu are but a few of the people whose contributions both large and small have made me the scientist I am. I would also like to thank John Wendelken, Gary Ownby for their technical expertise and Vickie Chiocca, Vicki Barnes, and Maria Fawver for their administrative expertise. Last but definitely not least, I would like to thank my financial patrons as it is their dollars that made sense. I would like to thank the Tennessee Advanced Materials Laboratory (TAML) and the Joint Institute for Neutron Sciences (JINS) for financial support.

Abstract

Manifestations of Broken Symmetry:
The Surface Phases of $Ca_{2-x}Sr_xRuO_4$

Robert G. Moore II
E. W. Plummer

The discovery of superconductivity in Sr_2RuO_4 has renewed vigor in the study of correlated electron systems. The evolution of a p-wave superconducting state from a paramagnetic 2-dimensional Fermi liquid shows the ruthenate superconductivity is anything but conventional. Sr_2RuO_4 is isostructural with La_2CuO_4, the parent compound for the high temperature superconducting family $La_{2-x}Sr_xRuO_4$. The substitution of Ca^{2+} for Sr^{2+} generates a different structure involving a static rotation and tilt of the RuO_6 octahedral, however, the antiferromagnetic insulating ground state of Ca_2RuO_4 is more akin to the cuprate parent. The generation of $Ca_{2-x}Sr_xRuO_4$ has offered a new family of compounds where the evolution from an antiferromagnetic insulator to a superconductor can be studied. Bulk studies have demonstrated how the intricate couplings between structural, orbital, electronic, and magnetic degrees of freedom are responsible for the exotic phases of the system. The layered perovskite structure which plays a key role in the properties observed also makes the crystals amenable to cleaving. Breaking symmetry by the creation of a surface on a quasi 2-dimensional system offers an opportunity to gain insight into the role of structure and symmetry on the properties of the system and offers a new avenue to discover new physics. Inelastic neutron scattering has been utilized to reveal the structural instability against the RuO_6 tilt. While the Σ_4 phonon mode involving the octahedral tilt shows classic soft phonon mode behavior across a tetragonal to orthorhombic phase transition, a new anomalous mode is discovered and its origin is explored. Surface phonon dynamics have been investigated across a Mott metal-to-insulator transition utilizing High Resolution Electron Energy Loss Spectroscopy where it is revealed the surface electronic transition temperature is significantly lower than the bulk. Low Energy Electron Diffraction has been employed to investigate the surface structure and structural transitions on the surface. Results show surface relaxations inhibit the RuO_6 tilt dramatically altering the ensuing orthorhombic phase transition near a quantum critical point at $x_c = 0.5$. It is also revealed that structural distortions accompanying the bulk metal-to-insulator transition are simply nonexistent on the surface. Physical manifestations from breaking symmetry in a correlated electron system are revealed.

Contents

List of Tables

List of Figures

Chapter 1

Introduction

The past several years have seen extensive experimental and theoretical activity in correlated electron systems. Transition metal oxides (TMOs) play a pivotal role in the search for understanding due to the exotic properties they exhibit. With properties as superconductivity, colossalmagnetoresistance, ferroelectricity, and enhancing catalytic reactions such systems hold immense potential from both academic and technological points of view. The advances in recent years of laser-MBE techniques has allowed the growth of high quality thin films with the hopes of engineering TMO based materials with the properties we desire. However, understanding the fundamental physics behind the exotic phases of correlated electron systems is currently one of the deepest intellectual challenges in the physical sciences [1, 2, 3, 4]. The unusual behavior in TMOs stems from the creation of many nearly degenerate ground states arising from strong interactions between various degrees of freedom. Structural, orbital, electronic, and magnetic properties couple to form intricately balanced phases where small perturbations often create large responses in material behavior. Before we can harness the potential we must first tame the complexity.

Many different materials have been fabricated by mixing different elements of systems forming similar structures. Entire crystalline families have been created by systematically doping parent compounds. While parent compounds may have complex structure and exhibit exotic phases themselves, we have learned to substitutionally dope these compounds tuning both structure and properties. While immense information has been learned about TMO systems, the fundamental physics governing the exotic behavior has been elusive. To further our understanding new research avenues are sought to gain new access to the coupling degrees of freedom. Controlling material properties through environmental changes as temperature, pressure, and magnetic fields has revealed different aspects of the intricate balance of phases including the importance of symmetry. Several TMO compounds form layered structures resulting in many quasi 2-dimensional properties. Not only can the evolution from 3-dimensional to 2-dimensional behavior be explored by the alteration of structure and environment, but questions arise as to the implications of breaking symmetry in such complex systems. The layered systems offer a unique opportunity to study not only bulk properties, but surface properties of the same crystal. The layered nature of the material makes the crystals amenable to *in situ* cleaving under ultra-high vacuum yielding pristine surfaces never complicated by exposure to atmosphere. The breaking of symmetry by the creation of a surface allows for not only an enhanced understanding of bulk properties and phases but an avenue to search for new phases.

The breaking of symmetry induces relaxations and even reconstructions on the surfaces of materials. Structural altercations on surfaces involving strong coupling and competing ground states allow opportunity for the discovery of new emergent phenomena. The study of TMO surfaces can further our understanding of exotic bulk properties as well as further our understanding of fundamental physics of condensed matter. Even with the discovery of fundamental bulk processes, the challenge to create practical applications on the nanoscale, where surface/interface physics and chemistry dominate, will still remain. Understanding differences between bulk and surface properties of TMO systems is paramount for realizing the full potential through tailored material design.

The complexity of the TMO surface raises several experimental and theoretical issues. While well over one thousand surface structures have been solved utilizing surface sensitive techniques, only a few are oxide materials [5]. Complex structures involving many atoms of different species within a unit cell, charge transfer, and extended electronic orbitals involving hybridization are but a few of the reasons why structural refinements of oxide surfaces have produced unreliable results [6, 7]. The motivations of this dissertation are not only explore the surface phases of a prototype TMO system, but to explore steps necessary to achieve reliable surface structural results on complex oxide systems.

The surface phases of $Ca_{2-x}Sr_xRuO_4$ have been explored using Low Energy Electron Diffraction (LEED-IV) and High Resolution Electron Energy Loss Spectroscopy (HREELS). While the ruthenates are not high temperature superconducting materials, their bulk phases have remarkable similarities to the high Tc cuprates as will be shown in the subsequent sections of this chapter. The surface evolution in a system ranging from an unusual superconductor in Sr_2RuO_4 to an antiferromagnetic Mott insulator in Ca_2RuO_4 are explored in the vicinity of broken symmetry due the surface. While the layered structure allows for the creation of pristine [0 0 1] surfaces, the isoelectronic substitution of Ca^{2+} for Sr^{2+} allows the systematic study of surface phases without the complications added due to altering carrier concentrations by doping. To better understand the lattice dynamics and a high temperature tetragonal to low temperature orthorhombic (HTT-LTO) phase transition for the system, inelastic neutron scattering near a *quantum critical point* (QCP) $x = 0.5$ has also been performed. As will be shown, the implications of broken symmetry in this TMO system extends well beyond the surface.

1.1 Background

The discovery of high Tc superconductivity in $La_{2-x}Ba_xCuO_4$ (LBCO) in 1986 spawned a flurry of experimental and theoretical activity in understanding the origins of superconductivity [8]. Within a year after the discovery, other superconducting cuprates were synthesized including $La_{2-x}Sr_xCuO_4$ (LSCO) and $YBa_2Cu_3O_{7-\delta}$ (YBCO) with T_cs reaching well above liquid Nitrogen temperatures [9, 10, 11, 12, 13]. While the first discoveries were with ceramic materials, subsequent studies showed the superconducting property to be intrinsic to bulk crystals [9, 11]. It was clear that a new age of superconductivity had begun. It quickly became evident that the quasi two-dimensional electronic states originating in the planar CuO_2 network was an essential ingredient for high T_c [14, 15]. In the early 1990's high quality YBCO and LSCO crystals were grown and the d-wave nature of superconducting phase was observed [15, 16]. The layered perovskite structure could be formed with

several other transition metals besides copper and a search initiated for other superconductors similar in structure to the cuprates. Eight years after the discovery of LBCO the first perovskite superconductor without copper was finally discovered: Sr_2RuO_4 [17]. While the superconducting ruthenate has the same K_2NiF_4 structure as LSCO, the similarities between the two systems stopped there.

The ruthenate crystals form in alternating layers of Sr/Ca-O and Ru-O planes. The layered structure can take on many different arrangements as they form a Ruddlesden-Popper (RP) series $(Sr, Ca)_{n+1}Ru_nO_{3n+1}$ as shown in Figure 1.1(a) [19, 20]. The ability to form the layered TMO perovskite structures with ruthenium in the RP series was first discovered in the 1950's but the discovery of superconductivity in the cuprates and ruthenates renewed vigor in the investigations of their structure and properties [21]. Several different ruthenates in the RP series ($n = 1, 2, 3, \infty$) have been synthesized and the exhibit a wide array of different electrical and magnetic properties as shown in Figure 1.1(b) [18]. The primary difference between the different structures is the number of RuO_6 interlinked by sharing apical oxygens prior to separation by Ca/Sr-O planes. Dimensionality becomes important throughout the series as exchange interactions per transition metal ion systematically decrease from six for $n = \infty$ down to four for $n = 1$ altering the conductivity perpendicular to the Ru-O plane and emphasizing the importance of the in-plane Ru-O conductivity as n decreases [18]. While the Sr compounds are always metallic with a ferromagnetic component the Ca compounds often involve metal-to-insulator (MIT) transitions and show antiferromagnetic instabilities. Even the exceptions to the rule show instabilities toward the general trends. For example Sr_2RuO_4 is always a paramagnetic metal however magnetic correlations have been observed at low temperatures [22, 23]. Similarly, $CaRuO_3$ is also a paramagnetic metal while slight impurity doping induces antiferromagnetism [24]. With such exotic behavior from the undoped systems, the obvious question arises as to what happens when you combine the two systems. Due to the superconductivity of Sr_2RuO_4, the $n = 1$ system is an obvious place to start but before the bulk $Ca_{2-x}Sr_xRuO_4$ (CSRO) phases are discussed, one must first understand the end members of the family.

1.2 Sr_2RuO_4

To understand the CSRO family it is best to start with Sr_2RuO_4, the most investigated member of the family with well over 400 papes [14]. The structure for Sr_2RuO_4 has been determined by neutron diffraction on powder and single crystals and by x-ray scattering on single crystals [25, 26, 27, 28, 29]. The crystal forms in the *I4/mmm* symmetry and remains in this symmetry from $T \sim 1300K$ down through the superconducting phase transition $T_c = 1.5K$ [30]. The layered perovskite structure of Sr_2RuO_4 is shown in Figure 1.2. Neighboring layer RuO_6 are offset $[a/2, a/2, 0]$ and separated by Sr-O blocks forming a rock-salt type structure. While the transition temperature is significantly different and not as impressive as the cuprates, the character of the superconducting phase is also significantly different but just as impressive as the cuprates. La_2CuO_4, the parent compound for the superconducting series $La_{2-x}M_xCuO_4$ (where M can be Ba, Sr, Ca) is an antiferromagnetic Mott insulator while Sr_2RuO_4 is a paramagnetic metal [30, 31, 32, 33]. While the cuprates require impurities to become metallic and even superconducting, Sr_2RuO_4 is a clean system where superconductivity is achieved without doping and condenses from a metallic state. The unusual properties of the superconducting state are emphasized as doping even a small

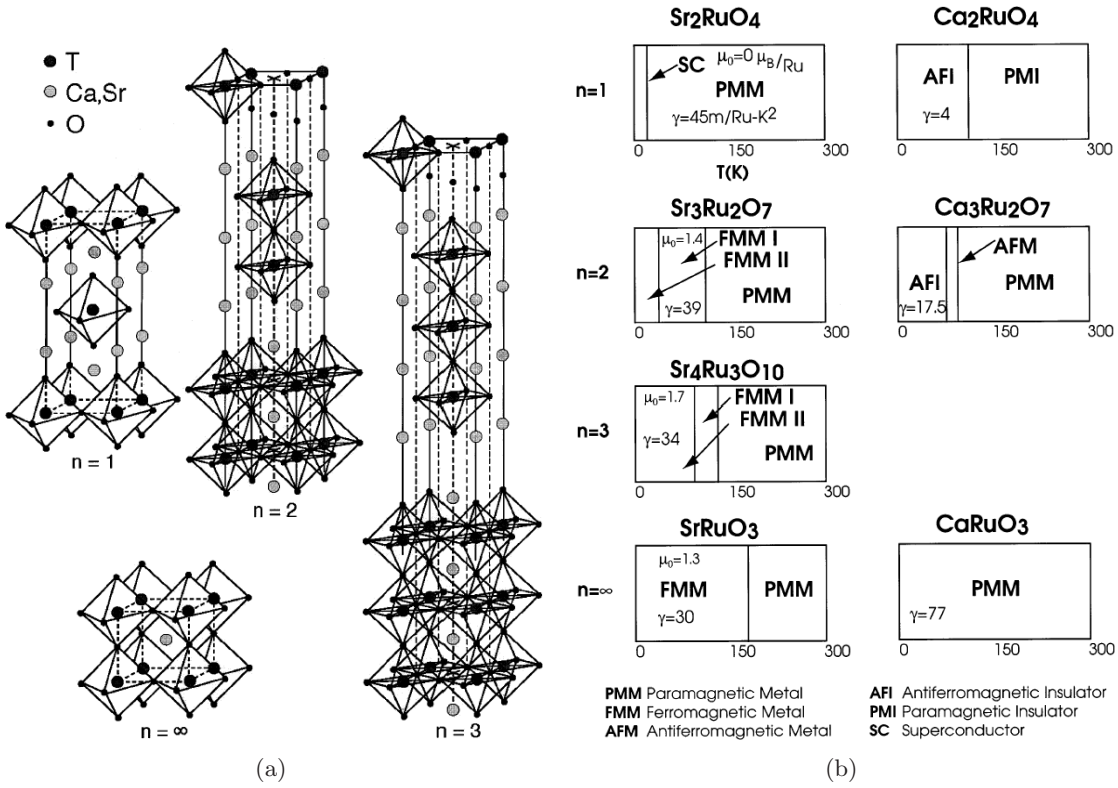

Figure 1.1: Ruddlesden-Popper series (Sr, Ca)$_{n+1}$Ru$_n$O$_{3n+1}$. (a) Crystal structures for various n. T sites are Ru but can be various transition metals. (b) Different phases of undoped members of the series. γ is the electronic specific heat coefficient and μ_o is the magnetic moment. Figures adapted from [18].

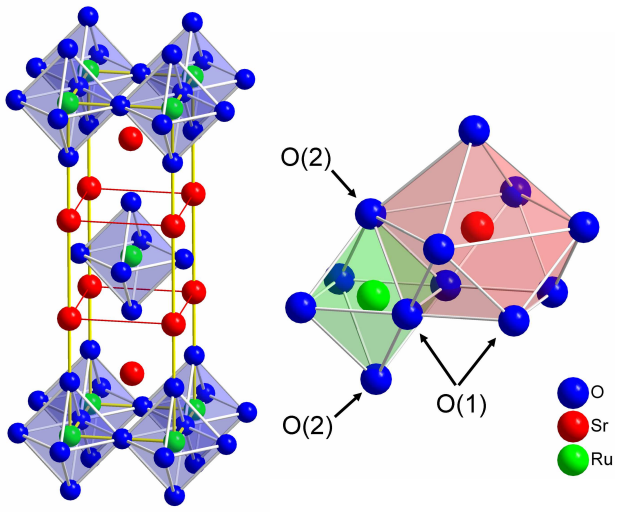

Figure 1.2: Sr_2RuO_4 crystal structure. *I4/mmm* crystal structure (left) with unit cell outlined in yellow. RuO_6 octahedral and CuO_9 triply capped trigonal prism (right).

amount of impurities quickly suppresses the superconducting phase. [34]. The transport properties of Sr_2RuO_4 also show that the low temperature metallic state resistivity has a T^2 dependence, a hall mark of Landau-Fermi liquid theory [17, 30]. Resistivity in both the ab-plane and along the c-axis show this T^2 dependence but with significantly different coefficients. Since this is a clean system without disorder from doping, de Haas-van Alphen measurements could be performed and confirm the Fermi liquid character [35, 36]. The layered structure with offset neighboring RuO_6 reduce the dimensionality of the system from 3 to a quasi 2-dimensional system well described as a 2-dimensional Fermi liquid [30, 37]. The dimensionality is emphasized by the large anisotropy in the resistivity ($\rho_c/\rho_{ab} > 500$). The unusual character of the of the low temperature metallic state and the similarity of the Landau parameters to those of ^{3}He lead theorist to suggest a spin triplet pairing mechanism for the Sr_2RuO_4 superconducting state [14, 38, 39]. Spin triplet pairing has been confirmed experimentally by Nuclear Magnetic Resonance (NMR) Knight-shift and Muon Spin Relaxation (μ-SR) measurements [40, 41]. Spin polarized neutron measurements has observed a lack of reduction in spin susceptibility upon entering the superconducting state also strongly suggesting the odd-parity (p-wave) pairing [42]. Sr_2RuO_4 is not the first heavy fermion superconductor showing odd-parity as UPt_3 and UBe_{13} show similar behavior [41, 42, 43, 44, 45, 46]. However, such spin triplet p-wave character is unexpected from a compound isostrucural with the cuprates where spin singlet d-wave symmetry is observed [14, 41]. For a review of the Fermi liquid normal state and unusual superconducting properties of Sr_2RuO_4 the reader is referred to Refs. [14, 37].

The tetravalent ruthenium takes on a high spin ($S = 1$) $4d^4$ electronic configuration where the atomic configuration has 5 degenerate bands: d_{z^2}, $d_{x^2-y^2}$, d_{xy}, d_{yz}, d_{zx}. The ruthenium ion is surrounded by six oxygens as shown in Figure 1.2 and the crystal field created by the octahedral coordination lifts the degeneracy to create the t_{2g} and e_g subshells as shown in Figure 1.3. Thus the four valence electrons fill the lower energy triply degenerate t_{2g} orbitals: d_{xy}, d_{yz}, d_{zx}. While the Cu-O planes in the cuprates show significant

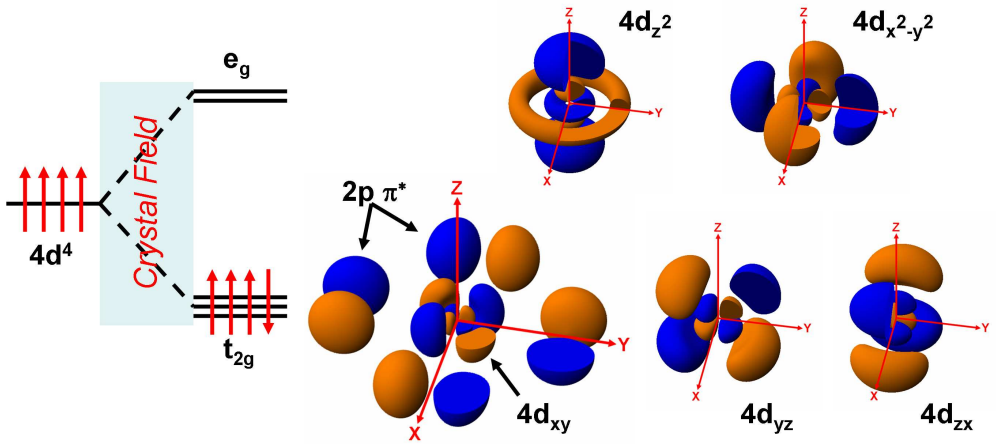

Figure 1.3: Ru electronic configuration. Crystal field splits lifts band degeneracy into subshells as shown. Electronic orbitals occupy e_g and t_{2g} shells as shown. The $4d_{xy}$ orbital is shown with the neighboring oxygen $2p$ π orbitals in an antibonding configuration.

hybridization between the Cu $3d_{x^2-y^2}$ and the O $2p$ σ states leading to strong correlations on the Cu sites, band structure calculations show that it is the O $2p$ π states which hybridize with the Ru d_{xy}, d_{yz}, d_{zx} states at the Fermi level showing antibonding character [49, 50]. Observed and calculated Ru-O bond distances show Ru-O(1) in basal plane is smaller than sum of ionic radii for Ru^{4+} and O^{2-} while Ru-O(2) is larger than the sum. In contrast, the Sr-O(2) bonds appear to be larger than sum of ionic radii. Such a structural configuration shows Sr-O layers are under a tensile stress while the Ru-O planes are compressed. This would lead to the possibility of strong hybridization between the Ru orbitals and the oxygen orbitals in the Ru-O plane [50]. Since the Ru $4d$ states are more extended and delocalized than the Cu $3d$ states, calculations suggest electron correlations are less significant on the Ru sites. While Sr_2RuO_4 is a paramagnetic metal at room temperature, it may not be far removed from the Mott insulating state. Simply replacing the Ru^{4+} with Fe^{4+} generates an isostructural and isoelectronic compound that is an antiferromagnetic semiconductor driven into a metallic state with the application of pressure [35, 51, 52]. The four valence electrons of both compounds occupy the triply degenerate t_{2g} orbitals but the extent of the Ru $4d$ orbitals compared to the Fe $3d$ orbitals changes the character of the hybridization with the neighboring oxygen $2p$ π orbitals altering the transport properties. Specific heat measurements of Sr_2RuO_4 show a linear temperature dependence and measured Fermi velocities by de Haas-van Alphen reveal effective electron mass is enhanced by a factor of 3-5 [17, 30, 35, 36]. Effective mass enhancements and T^2 behavior of resistivity shows Sr_2RuO_4 is well described by Landau Fermi-liquid theory where e-e interactions become significant. Band structure calculations and experimental data show that these active orbitals form three Fermi sheets: the d_{xy} bands form a 2-dimensional electron-like sheet centered at Γ (γ-sheet) and the d_{yz},d_{zx} bands form a quasi 1-dimensional electron-like sheet centered at Γ (β-sheet) and a quasi 1-dimensional hole-like sheet centered at X (α-sheet) as shown in Figure 1.4 [35, 37, 49, 50, 47, 48, 53]. Calculations also show that shifting the Fermi level to slightly higher energies changes the β-sheet from electron-like centered around Γ to hole like centered around X. Thus a saddle point in the band dispersion exists in a quasi-2D

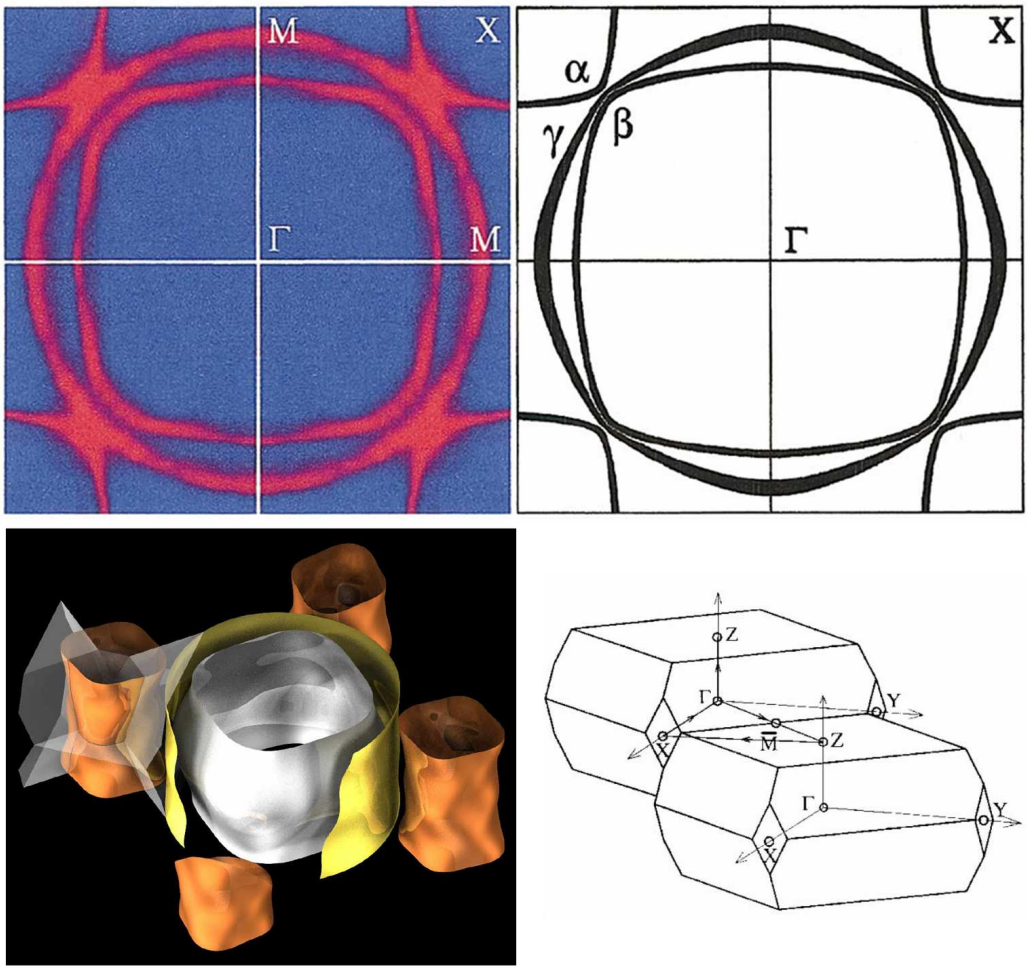

Figure 1.4: Fermi surface of Sr_2RuO_4. Fermi surface as determined from angle resolved photoemission (top left) and de Haas-van Alphen (bottom left) experiments and from LDA calculations (top right). The body centered tetragonal Brillouin zone is shown at the bottom right. Figures adapted from Refs. [15, 37, 47, 48]

system creating a van Hove singularity (VHS). Such a singularity can create a logarithmic divergence in the electronic density of states (DOS) and can be seen as a sharp peak in the DOS calculated by density functional theory (DFT) using the local density approximation (LDA) [50]. While the VHS exists slightly above the Fermi level, slight changes in bandwidth or carrier concentration could move the VHS across the Fermi energy.

The role of magnetism in the superconducting properties of the cuprates has often been debated. While one may hope the appearance of an unusual superconducting state in Sr_2RuO_4 may further the understanding of the role of magnetism, thus far it is not been the case. The role of magnetism in Sr_2RuO_4 has also been debated. Early NMR measurement showed evidence of ferromagnetic (FM) fluctuations [22, 23, 54]. The results were based on the observation of fluctuations and the fact that antiferromagnetic (AFM) spin fluctuations should vanish at magnetically symmetric oxygen sites. The experimental data was supported by LDA calculations favoring FM fluctuations as a possible mechanism for inducing superconductivity in Sr_2RuO_4 [47]. The picture became complicated when further LDA calculations showed a coexistence of both FM and AFM fluctuations [55]. While $SrRuO_3$ is ferromagnetic and Sr_2RuO_4 has remarkable similarities with ^{3}He where FM fluctuations mediate superconductivity, Ca_2RuO_4 is antiferromagnetic [56]. The coexistence of an AFM component is created by a Fermi surface nesting at $\mathbf{Q}= [\pm 2\pi/3\ \pm 2\pi/3]$. The incommensurate AFM spin fluctuations were observed experimentally by inelastic neutron scattering near the theoretically predicted wave vector [57, 58]. The theoretical calculations also showed the coexistence of FM and AFM fluctuations leads to a competition between p-wave and d-wave superconductivity. Further investigations of NMR data suggest that the incommensurate AFM fluctuations, which normally support the d-wave character, are anisotropic lending support to the p-wave character [59]. Thus the role of magnetic fluctuations in the superconductivity of Sr_2RuO_4 is far from clear and work continues to resolve these issues.

Lattice dynamics of Sr_2RuO_4 have also been investigated using inelastic neutron scattering [56]. While the results are still unusual, the complications are not as extensive as the magnetic fluctuations. Phonon dispersion curves taken along the [1 1 0] direction are shown in Figure 1.5. There are two modes particularly important to this work. The Σ_3 mode is a transverse acoustic (TA) mode polarized along [1 $\bar{1}$ 0] and can be described as a rotational mode of the RuO_6 about an axis parallel to the c-axis. The Σ_4 mode is a TA mode polarized parallel to the c-axis and can be described as a tilt mode of the RuO_6 about an axis oriented in the ab-plane. Since La_2CuO_4 has the same structure it will have the same phonon modes, however, there are distinct difference between the two systems. La_2CuO_4 has a pronounced softening of the Σ_4 mode at the Brillouin zone boundary [60]. The soft mode behavior is a precursor to a phase transition involving the static tilt of the CuO_6. The observed dispersion for Sr_2RuO_4 shows the instability of the tilt distortion does not exist for the ruthenate. The acoustic branch of the Σ_4 mode flattens out at the zone boundary and the lowest optic branch is flat across the entire zone. In contrast, the Σ_3 mode does show significant zone boundary softening. The softening is evident in the acoustic and optic branches as a distinct lowering of the phonon energy in the second half of the Brillouin zone. The softening indicates a lattice instability against the rotational distortion of the RuO_6. Surprisingly, the softening does not have any temperature dependence. Most systems exhibiting soft phonon mode behavior as a precursor to a phase transition typically have a distinct temperature dependence as the lowering temperature approaches the

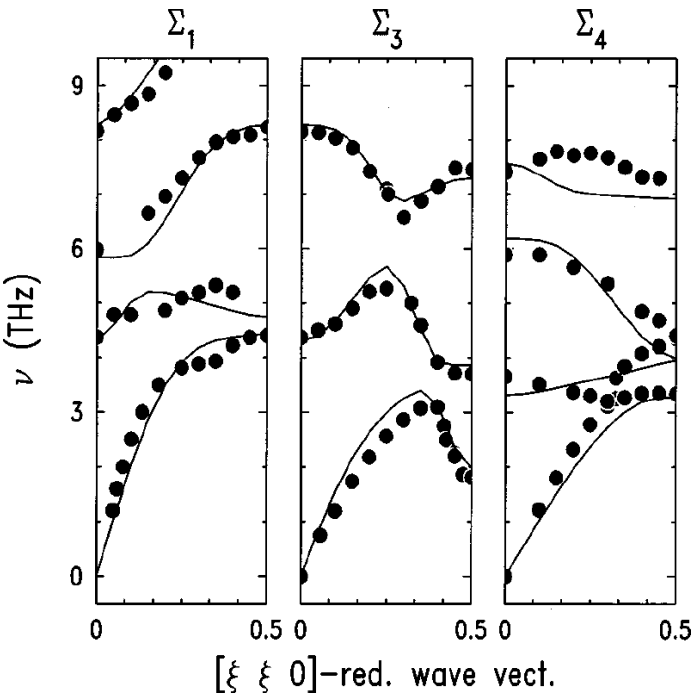

Figure 1.5: Phonon dispersion in Sr_2RuO_4. Phonon dispersion along [1 1 0]. Σ_3 represents a rotational mode of the RuO_6 octahedral. Σ_4 represents a tilt mode of the RuO_6 octahedral. Figure adapted from Ref [56].

phase boundary [61, 62, 63]. While one would expect the zone boundary phonon energy to decrease as the temperature is lowered, the Σ_3 mode energy in Sr_2RuO_4 does not change with temperature. In addition, dispersion along the c-axis is flat and the width of the rotation distortion at the zone boundary does not depend on any c-axis wave vector component. The rotational distortion has distinct 2D character and no rotation correlation is found between nearest neighboring planes. While the cuprates typically do not show phase transition involving static rotations of the octahedral, other compounds similar in structure do show such structural transitions. Sr_2IrO_4 and Sr_2RhO_4 both exhibit structural transitions involving rotations of the transition metal octahedron about an axis parallel to the c-axis [26, 64, 65].

1.3 Ca_2RuO_4

The electronic and magnetic properties of Sr_2RuO_4 arise primarily from the Ru-O plane. Interaction and hybridization of the Ru-4*d* orbitals with the O-2*p* orbitals creates a combination of quasi 1d and 2d bands resulting in the observed electronic and magnetic properties. Since the Sr-O planes seem to play passive roles in the behavior of Sr_2RuO_4, one may expect the substitution of Ca^{2+} for Sr^{2+} would have minor effects on the properties of the system. However, such is not the case as dramatically different properties are the result. While Sr_2RuO_4 is a paramagnetic metal forming in the *I4/mmm* symmetry with unusual superconducting properties at $T_c \sim 1.5K$, Ca_2RuO_4 is an antiferromagnetic insulator forming in the *Pbca* symmetry with a MIT at $T_c \sim 360K$ [66, 67, 68, 69]. The *Pbca* structure, shown in Figure 1.6, is characterized by a static rotation of the RuO_6 about an axis parallel to the c-axis combined with a tilt of the RuO_6 about an axis in the ab-plane. The rotation is $\sim 12^\circ$ and the tilt axis always close to the b-axis. The tilt schemes are similar to those observed in the cuprates, but rotations are typically not found in the cuprates [70, 71]. The RuO_6 can be considered a semi-rigid body as the observed tilt and rotation has minor distortions to the octahedral. In contrast, the CaO_9 trigonal prism is severely distorted due to the structural changes as shown in Figure 1.6.

As the system crosses T_c and enters the insulating phase the resistivity drops ~ 8 orders of magnitude and several structural parameters discontinuously change [68, 70]. The a and b-axis lattice parameters increase while the c-axis lattice parameter decreases creating a step change to a smaller c/a ratio as shown in Figure 1.7. In addition, the RuO_6 tilt increases from $\sim 6^\circ$ to $\sim 12^\circ$ accompanied by enlarged Ru-O(1) bond lengths and reduced Ru-O(2) bond lengths. The net effect is a "flattened" RuO_6 with a larger ($\sim 2\%$ larger volume). A hysteresis of $\sim 20K$ is observed indicating a true first-order structural transition with the MIT. Below T_c, the tilt and b-axis lattice parameter continue to change until the system is cooled to $\sim 180K$, however, no further structural transitions are observed. The MIT in Ca_2RuO_4 is similar to that observed in V_2O_3 [70, 72, 73]. The MIT transition temperature quickly decreases with slight Sr and La doping [74, 75, 76, 77], but increases with pressure. The application of pressure tends to shrink the a and b-axis while elongating the c-axis [78]. Such distortions allow for smaller RuO_6 tilts and drives the system toward the metallic phase. A modest pressures of $P \sim 0.5GPa$ is enough to induce the metallic phase at room temperature.

The structural and electronic degrees of freedom are not the only active participants in the properties of the system. While a MIT $T_c \sim 360K$ is accompanied by a structural phase

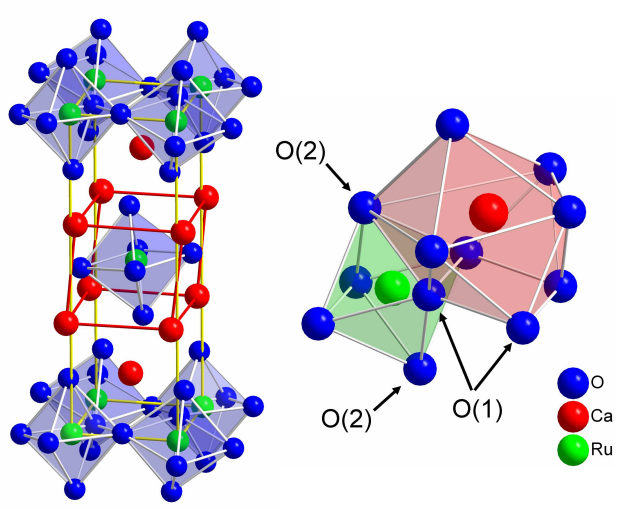

Figure 1.6: Ca_2RuO_4 crystal structure. *Pbca* crystal structure (left) with *I4/mmm* unit cell outlined in yellow for comparison with Sr_2RuO_4 (Figure 1.2). RuO_6 octahedral and CuO_9 triply capped trigonal prism (right).

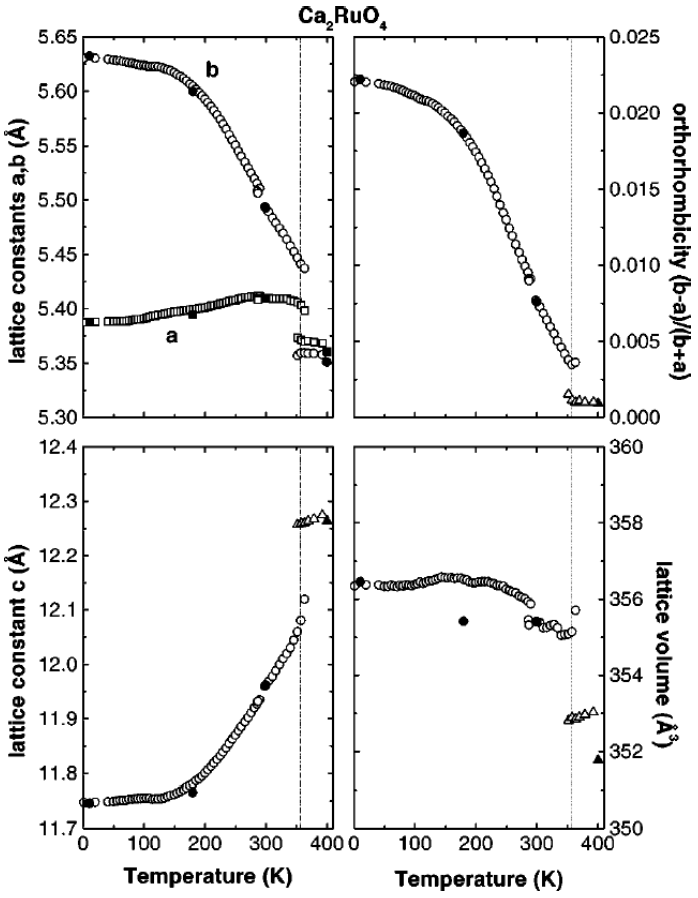

Figure 1.7: Ca_2RuO_4 structural parameters. Dashed line indicates temperature of MIT. Figure adapted from [70].

transition, the system also enters into a $S = 1$ antiferromagnetic phase with $T_N \sim 110K$ and has a Curie-Weiss magnetic susceptibility [66, 68, 70]. While no structural phase transition is observed across T_N, strong magneto elastics are present as structural anomalies are observed [68]. There are two observed magnetic modes observed in Ca_2RuO_4: A-centered and B-centered. The majority phase A-centered mode is similar to La_2CuO_4 with a magnetic ordering propagation vector of $\mathbf{k}$ =(1 0 0), while the minority phase B-centered mode is similar to La_2NiO_4 with a propagation vector $\mathbf{k}$ =(0 1 0) [68, 79, 80, 81]. While the dominant mode can be controlled by pressure, both modes involve Ru moments along the b-axis as the tilt direction seems to determine the spin orientation [78]. The observed magnetic moment is suppressed from the expected Ru^{4+} in a low spin state due to the hybridization between the Ru-4d and O-2p orbitals [82]. While the magnetic ordering is not necessary to induce the insulating phase in Ca_2RuO_4, it has been observed that slight Sr doping can shift T_c and T_N to the same value and it has been suggested that the magnetic ordering is necessary to localize the electrons and create the insulating phase for the lightly Sr doped compounds [70, 75, 76].

In addition to the magnetic degrees of freedom, the orbital degrees of freedom are observed to be active in Ca_2RuO_4. Angle dependent O 1s x-ray absorption spectra suggests the existence of 0.5 holes in the d_{xy} orbital and 1.5 holes in the $d_{yz/zx}$ orbitals [83]. It has been suggested that the hole distribution can lead to strong spin orbit coupling near the MIT. While several groups agree that the orbital degree of freedom is important to the electronic structure, there is no consensus as to the role played by the orbitals. While optical conductivity studies combined with LDA+U theoretical investigations suggest a ferro-orbital ordering ground state [84, 85], other theoretical studies suggest a staggered antiferro-orbital ordering [86]. Alternate optical conductivity studies suggest that ferro and antiferro-orbital ordering could coexist with strong electron-phonon coupling playing an important role in the arrangement [87]. The role of the orbital ordering in the electronic structure of Ca_2RuO_4 is not well understood and further investigation is needed to unravel the entangled degrees of freedom. The convergence of T_c and T_N to the same value for slight Sr dopings emphasizes the importance of spin-orbit coupling in the CSRO family [82, 87].

Doped semiconductors can also exhibit temperature induced MITs. However, while a unified conceptual understanding of the MIT in semiconductors exists, there is no consistent and unified theory for MITs in TMOs [88, 89, 90]. Extended Ru-4d orbitals with significant hybridization with O-2p orbitals combined by intricate balance of coupling degrees of freedom dramatically alter the on-site Coulomb repulsion (U), bandwidths (W), electronic transfer amplitude (t), Hund's coupling (J), and band fillings (n). While it is these parameters determining the electronic state of the semiconductor and TMOs, the TMO picture is clouded by the complexity of the system. Different theoretical models have been proposed emphasizing various aspects of the system as key players in the MIT. Dynamical Mean Field Theory (DMFT) using multiple band Hubbard model shows the possibility of orbital selective Mott transitions occurring at a single T_c when Hund's coupling is absent [91, 92]. Alternate DMFT studies show the interplay of the on-site Coulomb energy lying in between the different bandwidths of the non-degenerate t_{2g} bands can lead to a single Mott transition similar to that observed in our system [93, 94]. Hartree-Fock calculations demonstrate the importance of not only the Coulomb interaction strength U, but the Hund's coupling J combined with electron-lattice interactions to describe the electronic states [95]. While the

theoretical picture is not clear, the various models and descriptions emphasize the interactions of the various degrees of freedom to describe the electronic and magnetic properties of the system. One of the emphasis is on the structure since it is crucial in determining the parameters used to describe the electronic states of the system. To further emphasize the coupling between structure and transport properties of the system, it is necessary to understand the evolution of the family from the *I4/mmm* symmetry of Sr_2RuO_4 to the *Pbca* symmetry of Ca_2RuO_4.

1.4 $Ca_{2-x}Sr_xRuO_4$

Similar to the cuprate compounds, the end members of the CSRO family have dramatically different properties. As a result, mixing Ca_2RuO_4 and Sr_2RuO_4 result in a family of compounds with a wide variety of observed structural, electronic, and magnetic properties. The structural evolution from *I4/mmm* to *Pbca* can be understood as a reduction of symmetry due to static rotations and tilts of the RuO_6 as shown in Figure 1.8 [70, 96]. Starting from Sr_2RuO_4 and decreasing x the system remains in the *I4/mmm* symmetry until $x \sim 1.5$. For $1.5 > x > 0.2$ a second order structural phase transition occurs into the $I4_1/acd$ symmetry. The symmetry can be understood by a static rotation of the RuO_6 resulting in a $\sqrt{2}a \times \sqrt{2}a$ $R45^\circ$ enlarged unit cell in the ab-plane as shown in Figure 1.9. However, the c-axis periodicity of the rotation handedness of the neighboring octahedral layers also doubles the c-axis lattice parameter. As shown in Figure 1.10, there are two possible ways to arrange the rotated RuO_6 along the c-axis: *Acam* and $I4_1/acd$. The difference between the two symmetries is the stacking periodicity resulting in a doubled c-axis lattice parameter for the $I4_1/acd$ symmetry. The super lattice peaks involving the $I4_1/acd$ symmetry become more evident as x is decreased indicating significant disorder in the c-axis periodicity of the RuO_6 rotations. For $x = 1.0$, the coherence length observed in the neutron data is ~ 2 unit cells (~ 50Å) while for $x = 0.5$ very little disorder in the $I4_1/acd$ stacking sequence is observed [70, 96]. Due to the soft phonon behavior of the rotational Σ_3 mode in Sr_2RuO_4, the development of the $I4_1/acd$ phase can be viewed as a freezing of the Σ_3 mode [56, 70, 96].

For $0.5 > x > 0.2$ another second order phase transition is observed [70]. This temperature dependent phase transition is from a high temperature tetragonal (HTT) $I4_1/acd$ phase to a low temperature orthorhombic (LTO) *Pbca* phase and can be understood by a static tilt of the RuO_6 in addition to the already present rotation. The tilting octahedra creates an orthorhombic splitting as the RuO_6 tilt about an axis in the ab-plane. While a similar tilt behavior is observed for the CuO_6 in the cuprates [71], the symmetries are different as ruthenate has already had a tetragonal to tetragonal phase transition involving the static rotation of the RuO_6. While a Σ_4 phonon mode involving the tilting of the RuO_6 is observed in Sr_2RuO_4 with no evidence of zone boundary softening [56], nothing is known regarding the behavior of the Σ_4 phonon as the system is cooled into the LTO phase.

For $x < 0.2$ the system is found in the orthorhombic *Pbca* phase at low temperatures and a tetragonal *Acam* phase at elevated temperatures [70]. A first-order structural phase boundary is established at $x = 0.2$. For all $x < 0.2$, the rotational periodicity of the RuO_6 is always found to be that associated with the *Acam* stacking sequence while for all $x > 0.2$ the stacking sequence of the rotated RuO_6 doubles the c-axis lattice parameter. As the RuO_6 tilt for $x < 0.2$ the periodicity of the tilt is always one lattice parameter. Hence, a possible structural frustration exists for $0.2 < x < 0.5$ as the system is cooled. While

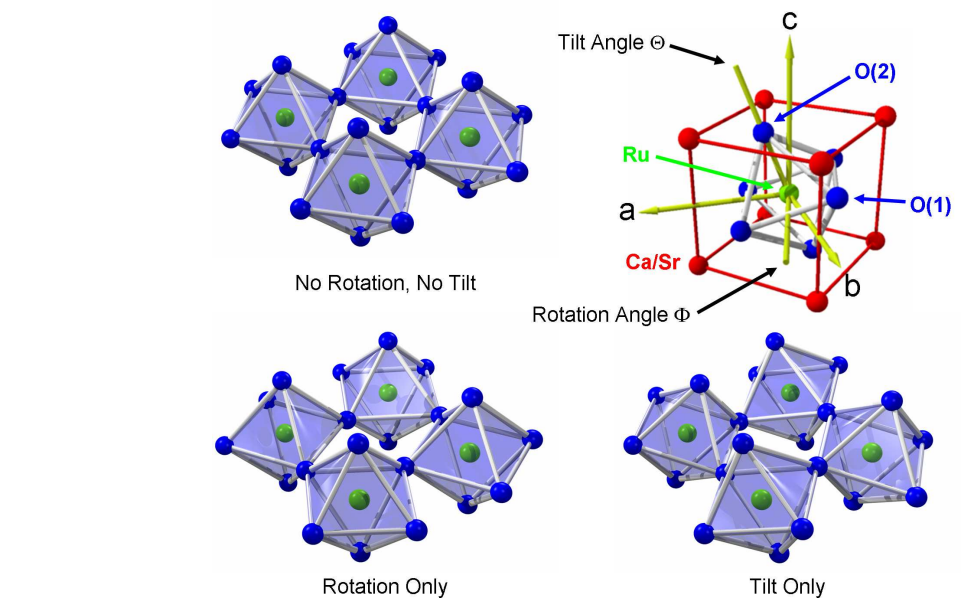

Figure 1.8: RuO_6 distortions found in CSRO. Rotations and tilts found in different symmetries of CSRO family.

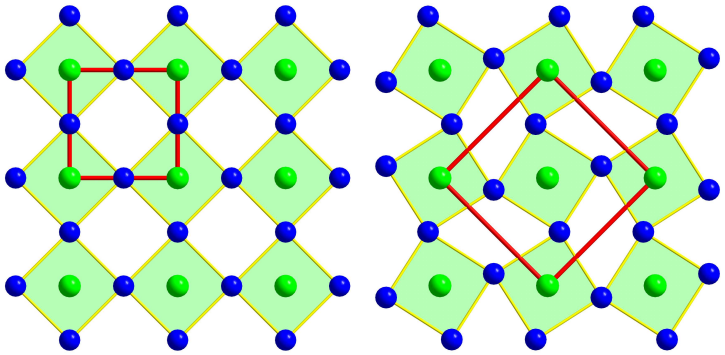

Figure 1.9: Enlarged unit cell from RuO_6 rotation. Ru-O plane showing the unit cells (red) for the $I4/mmm$ (left) and $I4_1/acd + Pbca$ (right) symmetries.

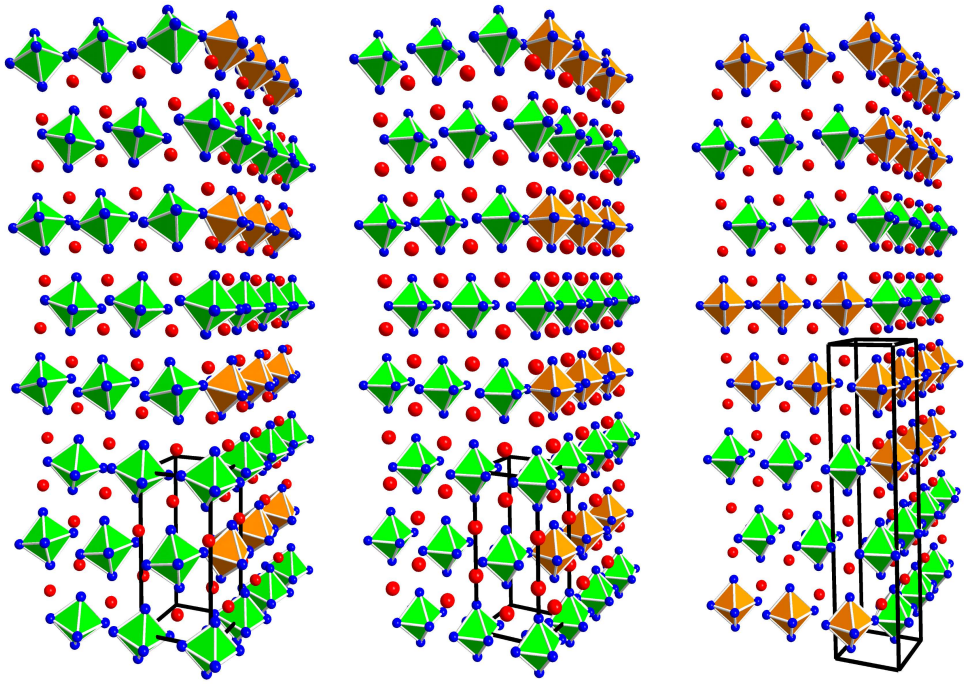

Figure 1.10: RuO_6 stacking in CSRO family. Space groups from left to right: *Pbca*, *Acam* and $I4_1/acd$. The green (orange) octrahedra emphasize the clockwise (counter-clockwise) rotation with respect to the c-axis. Only the RuO_6 and Ca/Sr on the [1 0 0] and [0 1 0] faces are shown. Unit cells are outlined in black.

the rotation prefers a stacking sequence that doubles the c-axis unit cell parameter, the tilt prefers a stacking sequence with half of the periodicity of the rotation.

The electronic and magnetic properties of the CSRO family can be dividend into three distinct regions [74, 75, 76, 97]. For $0 \leq x < 0.2$ the system is described by an AF insulating ground state. As the system is heated, an AF to paramagnetic transition occurs (T_N). In addition, a MIT (T_c) is observed for all $x < 0.2$ as the system is heated further. While T_N and T_c for $x = 0$ are significantly different, they quickly become the same value for modest ($x \sim 0.1$) Sr concentrations. The MIT strongly depends on x as T_c quickly reduces to zero for $x = 0.2$ as shown in Figure 1.11(a). The second region, $0.2 \leq x < 0.5$, is considered a magnetic metallic region showing a peak (T_p) in the magnetic susceptibility. While in the HTT phase the system is a paramagnetic metal, the onset of the LTO phase shows a gradual increase in susceptibility until a peak at T_p. Above T_p, Curie-Weiss behavior exists with AF Weiss temperatures comparable to T_p suggesting AF correlations. While Hund's coupling in the t_{2g} bands should expect $S = 1$ configuration, $S = 1/2$ is evident [76]. The AF correlations remain localized as no long range AF order is established. For regions around $x \sim 0.5$, FM fluctuations also exist and a magnetic cluster glass forms below T_{max}. The final region, $0.5 \leq x \leq 2.0$, is best described as a paramagnetic metal with a concentration dependent FM instability. Low temperature susceptibility exhibits a critical enhancement at $x_c \sim 0.5$ as shown in Figure 1.11(b). The critical enhancement shows a FM state that nearly forms, but never fully develops. For $x < x_c = 0.5$ the enhanced magnetic susceptibility decreases as the short range AF correlations increase. The magnetic frustration near $x_c = 0.5$ results in the appearance of the magnetic cluster glass at low T. The critically enhanced magnetic susceptibility combined with the zero temperature terminus of the HTT-LTO phase transition at $x_c = 0.5$ establishes this point as a *quantum critical point (QCP)* in the phase diagram. In addition to the enhancement of magnetic susceptibility, the $0.5 \leq x \leq 2.0$ region shows heavy mass Fermi-liquid behavior below T_{FL} where a T^2 dependence of specific heat is evident [97]. Extensive experimental and theoretical investigations have revealed how an intricate balance of electronic and orbital configurations directly coupled to the lattice distortions can create the unusual electronic, thermal, and magnetic properties existing throughout the phase diagram shown in Figure 1.12.

The driving force for the different structural transitions observed in CSRO is the relative size of the Ca and Sr cations ($r_{Ca} = 1.18$Å, $r_{Sr} = 1.31$Å) [70, 98]. As Ca is added to Sr_2RuO_4 the lattice parameters shrink due to the smaller cation. The size of the RuO_6 appears robust throughout the family and the shrinking lattice induces a rotation in order to maintain a nearly uniform RuO_6 volume. Due to the narrow Ru-4d orbitals, the rotating RuO_6 dramatically alters the Ru-4d and O-2p hybridization and overlap altering the shape and energy of the electronic bands and the orbital occupations [76, 82]. The bandwidth of the d_{xy} band is dramatically reduced and shifted down in energy while the $d_{yz/zx}$ bandwidths are also reduced but by a lesser amount. The size and energy of the VHS is also shifted due to the band alterations [76]. It is observed that the γ Fermi surface sheet associated with the d_{xy} orbitals changes from electron-like centered at Γ for Sr_2RuO_4 to hole like centered at X in $x = 0.5$ [99]. In addition to altering the bandwidth, LDA+U calculations also suggest that the rotated RuO_6 enhances a FM component [82]. Thus as the static rotation becomes more orderly due to increasing the Ca content, the FM instability observed in the magnetic susceptibility becomes enhanced. The FM ground state is never fully achieved due to the ensuing tilt. As the lattice shrinks further due to increasing Ca content, RuO_6

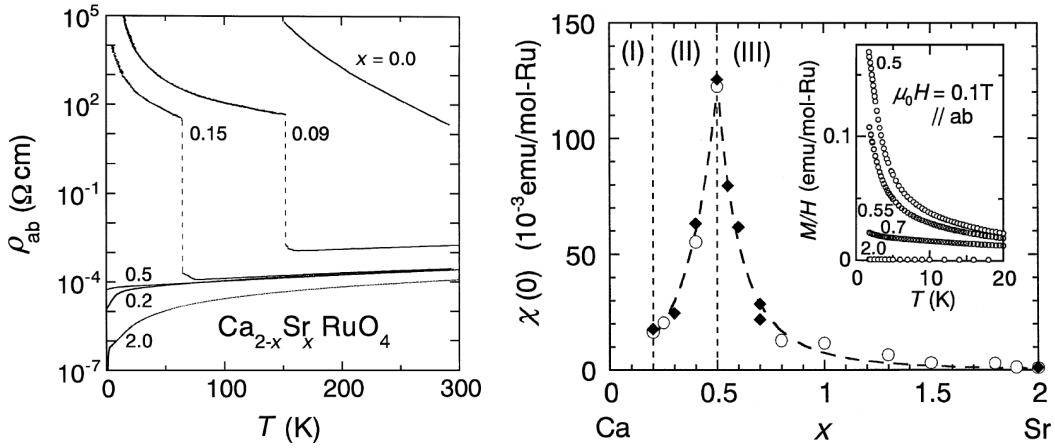

Figure 1.11: Resistivity and magnetic susceptibility in CSRO. (a) Resistivity in Ru-O plane for different x. (b) Magnetic susceptibility in different regions outlined in text. Figures adapted from [75].

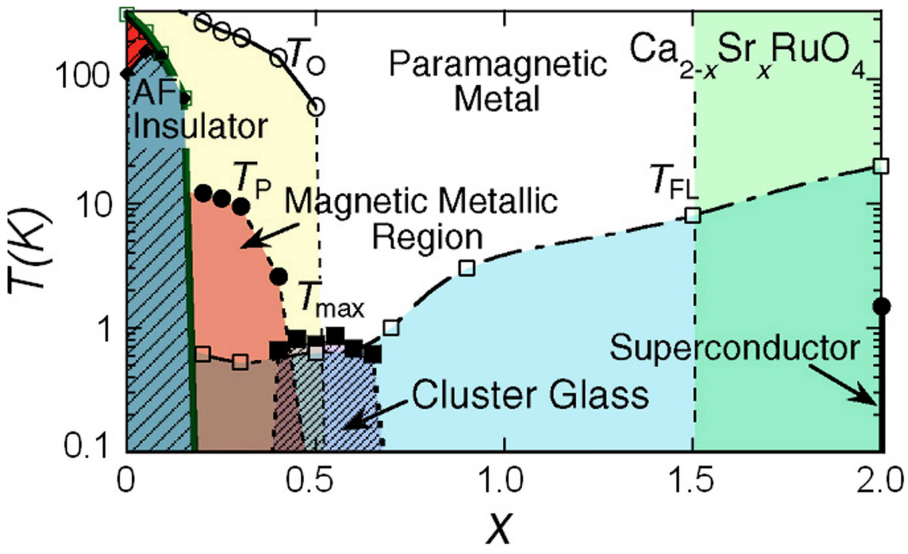

Figure 1.12: Bulk phase diagram for $Ca_{2-x}Sr_xRuO_4$. Different temperatures and transitions are described in the text. Figure adapted from [70, 97]

begins to tilt enhancing a AF component in the system [76, 82]. Thus a competition is established between the FM instability and the AF correlations. The orthorhombic crystal field due to the tilt also lifts the degeneracy of the $d_{yz/zx}$ bands and pushes the d_{xy} bands below the Fermi energy. The result is the band fillings are altered establishing conditions necessary for the Mott MIT. Thus the structural distortions resulting from the shrinking lattice combined with strong coupling between electronic, orbital and magnetic degrees of freedom create the elaborate phase space shown in Figure 1.12. Due to the strong link between structural distortions and electronic/magnetic properties, the question arises as to what happens on the surface where symmetry is broken and the structure relaxes as a result.

1.5 The Surface of Sr_2RuO_4

Surface studies have been performed on Sr_2RuO_4. While bulk studies demonstrate the nearly perfect *I4/mmm* structure surface studies of Sr_2RuO_4 show the first break from bulk trends. While a *p4mm* plane group symmetry pattern is expected for a bulk terminated *I4/mmm* surface, the surface LEED pattern shows a reconstructed *p4gm* surface with a new $\sqrt{2} \times \sqrt{2}$ $R45^\circ$ surface unit cell [100]. A quantitative LEED-IV analysis shows the RuO_6 are rotated by $\sim 9^\circ$ on the surface [101]. The symmetry of the surface RuO_6 layer is equivalent to a bulk terminated *I4 1/acd* unit cell however, the new symmetry appears limited to the topmost RuO_6 surface layer. Due to the soft mode behavior of the Σ_3 RuO_6 rotational mode, the surface reconstruction is attributed to the freezing of the Σ_3 mode at the surface [56, 100, 101]. Theoretical calculations show the rotated RuO_6 should stabilize a FM phase and alternate theoretical studies suggest correlation effects should be enhanced on the surface [100]. However, a FM surface on Sr_2RuO_4 has not been observed experimentally. The new symmetry on the surface folds the electronic bands crossing the Fermi energy into the new surface Brillouin zone as observed by photoemission studies [48, 53].

Surface phonon dynamics have also been investigated on the Sr_2RuO_4 surface utilizing HREELS [102]. The surface reveals four distinct phonon modes as shown in Figure 1.13. Altering the scattering angle reveals all the modes to be dipole active and are identified as $A_{2u}(3)$ or $A_{1g}(2)$ (ω_1), $A_{2u}(2)$ (ω_2), $A_{1g}(1)$ (ω_3), and $A_{2u}(1)$ (ω_4) based on bulk studies [102, 103, 104]. The phonon energies are enhanced $5-8meV$ on the surface compared to bulk and the surface mode energies have very little temperature dependence with an increase $\sim 1meV$ between room temperature and $80K$. Extracting conductivity data from the quasi-elastic peak reveals that the low temperature conductivity in the ab-plane is greater than along the c-axis, which is consistent with bulk data [17, 30]. However, the surface at room temperature reveals an isotropic conductivity counter to the observed bulk trends [102].

One can only wonder what other surprises are revealed by the surfaces of the CSRO family. But first, one must figure out how to look at them.

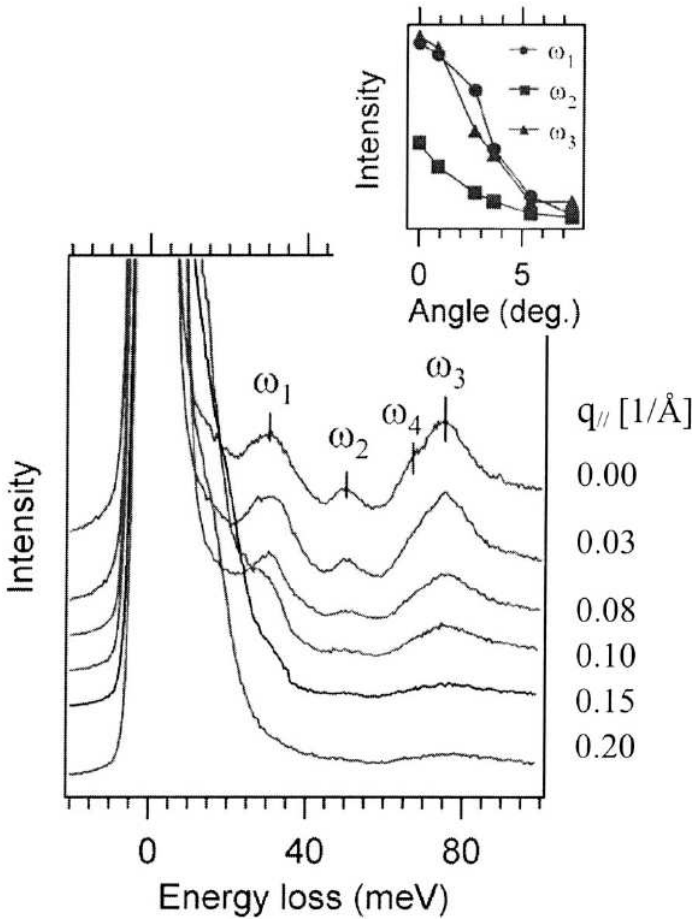

Figure 1.13: HREELS study of Sr_2RuO_4 surface. Data taken at $T = 80K$ showing different momentum transfers $q_{||}$. Intensity of the different modes versus scattering angle is shown in the inset. Figure adapted from [102].

Chapter 2

Experimental Techniques and Analytical Procedures

Shortly after the discovery of the wave-particle duality of light, de Broglie postulated that such a duality should be extended to other things in nature, like electrons, known for their particle like behavior. He postulated that the wavelength of a particle is related to its momentum in a similar way as for a photon:

$$\lambda = h/p = h/mv = h/\sqrt{2mE} \tag{2.1}$$

where λ is the particle's wavelength which has momentum p (with mass m, velocity v and energy E) and h is Planck's constant. Thus a stream of electrons with kinetic energy of 150eV should behave like a wave with a wavelength of 1Å:

$$\lambda_e[\mathring{\mathrm{A}}] = \sqrt{150/E[eV]} \tag{2.2}$$

Due to the dual nature of electrons, such a stream of electrons should diffract from an ordered periodic array of atoms where the interatomic spacing is similar to the wavelength. In 1927, Davisson and Germer discovered (quite accidentally) Low Energy Electron Diffraction (LEED) as they demonstrated how electrons diffract from a Nickel crystal [105, 106, 107]. However, reproducibility of early studies with electrons were hampered by surface adsorbates and serious developments of the technique did not occur until the advent of ultra-high vacuum (UHV) technology in the 1960's [107].

Neutrons also have a dual nature similar to electrons. It was demonstrated in 1936, four years after the discovery of the neutron, that neutrons would also diffract from solids [108, 109]. Serious developments in neutron scattering techniques also had a 30 year incubation from the first demonstration. The reasons are quite different from LEED as neutron scattering does not need UHV. The development of high-flux reactors in the late 1960's and early 1970's produced the necessary incident neutron flux to realize the full potential of neutron scattering [108]. The power of the probe and the valuable information it provided was recognized in 1994 with the awarding of the Nobel Prize in Physics to C. Shull and B. Brockhouse for their contributions to the fields of elastic and inelastic neutron scattering.

While neutrons and electrons can both be used as diffraction probes to understand the structure and dynamics of solids, they are quite different in the way they interact with

matter making them complementary probes. Due to the charge of an electron, interactions between the incident electron and the solid are quite strong. A signal electron will only penetrate a few Angstroms before the interactions with the charged electrons and nuclei in the surrounding solid will significantly alter the trajectory of the signal electron. Thus the shallow penetration depth makes the electron an ideal surface probe as the signal electron will only sample information contained within the first few atomic layers of the solid. In contrast, the charge neutrality of the neutron means the interactions between the signal neutron and the solid are weak. Neutrons will penetrate deep into a solid before interacting making the neutron an ideal probe for bulk studies. The difference in the properties of the probe also require significantly different experimental techniques for establishing a monoenergetic beam of particles. Due to the charge of an electron, electrostatic potentials can be used to set the energy and wavelength of electrons. However, charge neutrality of the neutron requires Bragg scattering off a crystal to be utilized for the creation of monoenergetic signal neutrons. Alignment of monochromator and analyzer crystals are used to establish the desired scattering geometry for extracting the information contained in the scattered signal neutron beam. The majority of data presented here result from fixing the final neutron energy and thus the neutron wavelength:

$$E_f = 14.7meV = \lambda_n = 2.36\text{Å} \tag{2.3}$$

The basic premise of scattering lies in two of the most fundamental concept of physics: Conservation of Energy and Conservation of Momentum, or more formally

$$\begin{aligned} \hbar\omega &= E_f - E_i \\ \mathbf{Q} &= \mathbf{k}_f - \mathbf{k}_i \end{aligned} \tag{2.4}$$

where k=$2\pi/\lambda$ is the wave vector magnitude. The only way for both of the above to be satisfied is if E and k are related by the dispersion relation:

$$E = \frac{\hbar^2 k^2}{2m} \tag{2.5}$$

where m is the appropriate particle mass. Everything that follows is grounded in these seemingly simple concepts. By requiring the incident and scattered particle energies to be the same $E_i = E_f$ (and hence $|\mathbf{k}_i| = |\mathbf{k}_f| = k$) elastic scattering is established and we can extract information about the structure of the material. Particle wavelengths similar to the interatomic spacings within the crystal are necessary to retrieve the structural information as required by Bragg's Law

$$\lambda = 2d\sin\theta_s \tag{2.6}$$

where d is an interplanar spacing and θ_s is the scattering angle. However, if this restriction is lifted information can be extracted about dynamical properties of the material. Due to the mass of the neutron, small neutron energies are required to achieve wavelengths similar to those observed in crystals. As a fortuitous coincidence, the energies of the incident neutrons are similar to excitation energies within the system. Thus neutrons can be used to create (or destroy) lattice vibrations (phonons) within the crystal. By extracting the energy lost (or gained) by the neutron at a particular momentum transfer wavevector $\mathbf{Q}$, information regarding phonon modes is collected. Due to the magnetic moment of the neutron,

interaction with unpaired electrons in a magnetic material can also create magnetic excitations (magnons, spin waves) within the crystal. While magnetic properties are important to understanding the behavior of materials, this study will only focus on lattice excitations.

Electrons can also be used to excite phonons at the surfaces of crystals. By studying electron energy losses at particular momentum transfers dynamical properties of crystalline surfaces can be investigated. High Resolution Electron Energy Loss Spectroscopy (HREELS) is a technique used to study electronic as well as lattice excitations on the surfaces of crystals. In a manner similar to neutrons, electrons can directly interact with nuclei to create phonons (impact regime). However, due to the charge of the electron, long range dipole interactions (dipole regime) can also be used to excite lattice vibrations. The creation of dipoles on the surface require atomic displacements perpendicular to the surface and thus selection rules are established to determine the dipole character of phonon modes observed.

The following sections outline the experimental techniques and analytical procedures used in this work. Section 2.1 describes the use of inelastic neutron scattering to study bulk phonon dynamics in crystalline materials. Section 2.3 describes HREELS and how to use electrons to extract not only lattice dynamics but other quasi-particle excitations as intra-band electronic transitions existing in a typical Drude type metal. Due to the results obtained from the neutron scattering and HREELS measurements, it was evident that the surface structure of the $Ca_{2-x}Sr_xRuO_4$ family must be determined to fully understand the physics of the system. Section 2.2 describes not only the underlying LEED theory but the application of LEED to complex oxide systems. While computer codes used for surface structural determinations can be freely downloaded, the traditional approaches to LEED yield unsatisfactory results for our system. Many of the simplifying assumptions in LEED work well for simple metals and most semi-conductor surfaces but simply do not work for complex oxide systems. Several atoms per unit cell, extended d-orbitals, charge transfer and hybridization between metal cations and oxygen anions are but a few of the reasons why applications of traditional LEED techniques are unable to reliably determine surface structures of complex oxide systems. Section 2.2 is extended to include the theoretical developments and analytical steps necessary to solve complex oxide surface structures.

2.1 Neutron Scattering

Only an outline of neutron scattering theory will be presented here and for more in depth descriptions of the theory and experimental techniques, the reader is directed to Refs. [108, 110]. The instruments used in this work were the HB1 and HB3 triple axis spectrometers at the High Flux Isotope Reactor at Oak Ridge National Laboratory and BT-7 triple axis spectrometer at the NIST Center for Neutron Research at National Institute of Standards and Technology. Several different instrument configurations were utilized including fixing the incident or final neutron energies and performing scans with constant momentum wave vector (constant-Q) or constant energy (constant-E). The configuration that produced the most reliable data consisted of fixing the final neutron energy and performing dispersion measurements with a constant-Q and thus these instrument setups will be outlined here. For more information regarding the triple axis spectrometer or the specific instruments used, the reader is directed to Refs. [108, 111, 112].

2.1.1 Elastic Neutron Scattering

As with any scattering process, we must start from the basic principles of energy and momentum conservation as outlined by Equation 2.4. For elastic scattering where $E_i = E_f$ (and $|\mathbf{k}_i| = |\mathbf{k}_f| = k$) and we are only concerned with Bragg scattering from which we can extract structural information. While momentum conservation must hold we also must consider that there are many different planes existing within our crystal, all of which have a Bragg condition which can be satisfied. Thus we rewrite our energy an momentum conservation in a more useful form:

$$E_f = E_i \tag{2.7}$$

$$\mathbf{Q} = \mathbf{k}_f - \mathbf{k}_i = \mathbf{G}_{hkl} = h\mathbf{b}_1 + k\mathbf{b}_2 + l\mathbf{b}_3 \tag{2.8}$$

where $\mathbf{G}_{hkl}$ is a reciprocal lattice vector labeled by Miller indices h, k, and l with $\mathbf{b}_i$ as the respective axis vectors of the reciprocal lattice. In neutron scattering we are interested in the rate (proportional to the scattering cross section σ) at which neutron incident on the sample are scattered into solid angle $d\Omega$ within a specific energy window dE. For a particular atomic species, the scattering cross section is based on an empirically determined scattering length b. For a single atomic species within a periodic array, the scattered waves will interfere creating a coherent contribution to the scattering cross section(σ_{coh}). Different atomic isotopes can create spatial fluctuations in the scattering length leading to scattered waves which do not interfere coherently thus adding an incoherent contribution to the total scattering cross section (σ_{inc}). Since the different isotopes for the atomic species within our sample do not have significantly varying scattering lengths, we will only consider the coherent scattering cross section ($\sigma_{coh} = \sigma$) as the incoherent contribution is small. In the neutron scattering experiment we are interested in the differential scattering cross section [108]:

$$\frac{d^2\sigma}{d\Omega_f dE_f} = N\frac{k_f}{k_i}\frac{\sigma}{4\pi}S(\mathbf{Q},\omega) \tag{2.9}$$

where N is the number of nuclei and $S(\mathbf{Q},\omega)$ is the scattering function containing information regarding the microscopic properties of the system. For elastic scattering off a crystal containing j atoms per unit cell sitting in positions $\mathbf{d}_j$ then the scattering function can be written in terms of the time average density operator for the lattice:

$$\frac{d\sigma}{d\Omega} = N\frac{(2\pi)^3}{v_o}\sum_{\mathbf{G}}\delta(\mathbf{Q}-\mathbf{G})\left|F_S(\mathbf{G})\right|^2 \tag{2.10}$$

where v_o is the unit cell volume and $F_S(\mathbf{G}) = F_S(hkl)$ is the static nuclear structure factor given by

$$F_S(\mathbf{G}) = \sum_j \bar{b}_j e^{i\mathbf{G}\cdot\mathbf{d}_j}e^{-W_j} \tag{2.11}$$

with $W = 1/2\left\langle(\mathbf{Q}\cdot\mathbf{u}_j)^2\right\rangle$ as the Debye-Waller factor containing information regarding the displacement $\mathbf{u}_j$ from the atomic position $\mathbf{d}_j$. Thus to observe a particular Bragg reflection (hkl) using a monochromatic neutron beam of wavelength λ a scattering angle 2θ

is established from the incident beam and the measured neutron intensity is given by:

$$I = A\frac{\lambda^3 \left|F_S(hkl)\right|^2}{v_o^2 \sin 2\theta} \tag{2.12}$$

For the triple-axis spectrometers used in the experiment the analyzer arm angle is moved in steps twice as large as the sample angle (θ-2θ scan) establishing the scattering conditions necessary to observe elastic Bragg scattering as described by Equation 2.12.

2.1.2 Inelastic Neutron Scattering

The triple axis spectrometer operates within a fixed scattering plane. The incident neutron beam exits the reactor at a specific elevation and the monochromator crystal, sample, analyzer crystal and detector are all at the same elevation. Thus the scattered neutron beam is always maintained within this two-dimensional plane. Different crystallographic axis can be analyzed within a single crystal by rotating the sample within the neutron beam, however constraints are placed on the observable Bragg planes and momentum transfer directions for each sample orientation. The scattering geometry used in these experiments focused in the (hhl) scattering plane by aligning our sample to define our scattering plane with orthogonal axis parallel to the [110] and [001] crystallographic directions. For inelastic scattering, we no longer require the incident and final energies to be the same and no longer require the change in momentum to be equal to a crystal momentum vector defined by a reciprocal lattice vector. Thus if we define our scattering plane as the xy-plane, we can write the general conditions for energy and momentum conservation within the scattering plane:

$$\left(\frac{\hbar^2}{2m}\right)\left(k_{f,x}^2 + k_{f,y}^2 - k_{i,x}^2 - k_{i,y}^2\right) = \hbar\omega \tag{2.13}$$

$$\mathbf{k}_{f,x} - \mathbf{k}_{i,x} = \mathbf{Q}_x = \mathbf{G}_x + \mathbf{q}_x \tag{2.14}$$

$$\mathbf{k}_{f,y} - \mathbf{k}_{i,y} = \mathbf{Q}_y = \mathbf{G}_y + \mathbf{q}_y \tag{2.15}$$

We define the crystal orientation angle Ψ as the angle between the incident neutron beam and one of the principle axis of our scattering plane such as y as shown in Figure 2.1. We define Φ as the scattering angle between $\mathbf{k}_f$ and $\mathbf{k}_i$ also shown in Figure 2.1. Hence we can define relations for $\mathbf{Q}_x$ and $\mathbf{Q}_y$ involving the scattering angles:

$$\mathbf{Q}_x = -\left|\mathbf{k}_i\right| \sin\Psi - \left|\mathbf{k}_f\right| \sin(\Phi - \Psi) \tag{2.16}$$

$$\mathbf{Q}_y = \left|\mathbf{k}_i\right| \cos\Psi - \left|\mathbf{k}_f\right| \cos(\Phi - \Psi) \tag{2.17}$$

So we have established three relations (Equations 2.13, 2.16 and 2.17) between four experimental variables: $|\mathbf{k}_o|$, $|\mathbf{k}_f|$, Ψ, and Φ. An additional constraint must be added in order to meet the above conditions simultaneously. While any of the variables can be fixed, we choose to fix the final energy thus making $|\mathbf{k}_f|$ constant (as is a common practice).

For a crystal with n atoms per unit cell there will exist $3n$ phonon branches with frequencies ω_{js} where s labels a particular mode. Once common practice for measuring phonon dispersion is to fix the momentum wave vector $\mathbf{Q}$ and vary the frequency through a particular dispersion branch. If we subtract out the elastic contribution from $S(\mathbf{Q},\omega)$, then we are left with information regarding fluctuations within the sample as a function of

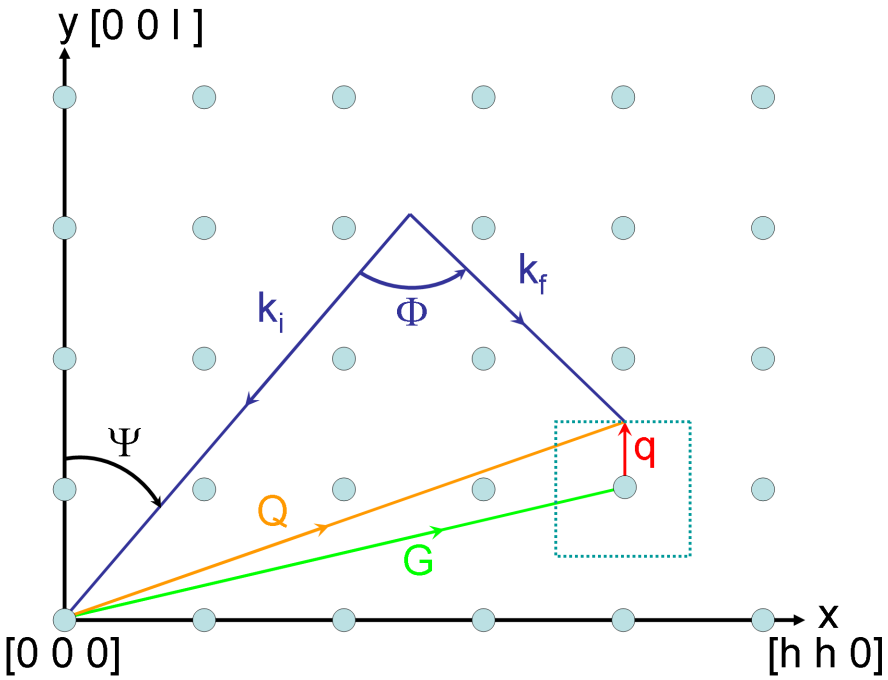

Figure 2.1: Inelastic neutron scattering geometry. Dashed line indicates first Brillouin zone.

momentum and frequency. Thus the scattering cross section for inelastic scattering take the form [108, 113]:

$$\frac{d^2\sigma}{d\Omega_f dE_f} = N\frac{k_f}{k_i}S(\mathbf{Q},\omega) \tag{2.18}$$

From the flux dissipation theorem, we can relate $S(\mathbf{Q},\omega)$ to the dissipative part of a linear response function:

$$S(\mathbf{Q},\omega) = \frac{\chi''(\mathbf{Q},\omega)}{1-e^{\hbar\omega/k_BT}} \tag{2.19}$$

where $\chi''(\mathbf{Q},\omega)$ is the imaginary part of the dynamical susceptibility. If we consider a scattering process where a single phonon is created or destroyed we can write

$$\chi''(\mathbf{Q},\omega) = \frac{1}{2}\frac{(2\pi)^3}{v_o}\sum_{\mathbf{G},\mathbf{q}}\delta(\mathbf{Q}-\mathbf{q}-\mathbf{G})\sum_s \frac{|F_D(\mathbf{Q})|^2}{\omega_{\mathbf{q}s}} \times [\delta(\omega-\omega_{\mathbf{q}s})-\delta(\omega+\omega_{\mathbf{q}s})] \tag{2.20}$$

where $F_D(\mathbf{Q})$ is the dynamic structure factor given by

$$F_D(\mathbf{Q}) = \sum_j \frac{\bar{b}_j}{\sqrt{m_j}}(\mathbf{Q}\cdot\xi_{js})\, e^{i\mathbf{Q}\cdot\mathbf{d}_j}e^{-W_j} \tag{2.21}$$

where m_j is the mass of the j^{th} atom and ξ_{js} is the polarization vector for the j^{th} atom for a particular mode s. For a triple-axis spectrometer the factor k_f/k_i in Equation 2.18 becomes unity and we can write the measured inelastic intensity as:

$$I = A\frac{1}{\omega_{\mathbf{q}s}}|F_D(\mathbf{Q})|^2 \times \left[n_{\mathbf{q}s}+\frac{1}{2}\pm\frac{1}{2}\right] \tag{2.22}$$

where the + sign is used for neutron energy loss and − sign is used for neutron energy gain and n_{qs} is the Bose factor:

$$n_{\mathbf{q}s} = \frac{1}{e^{\hbar\omega_{\mathbf{q}s}/k_BT}-1} \tag{2.23}$$

The Bose factor emphasized the expected phonon intensities due to lowering temperatures. As the crystal is cooled, fewer phonons will be populated and the scattering intensity for a particular mode will decrease. As shown in Figure 2.2, the Bose Factor can significantly alter low energy phonon mode intensities at elevated temperatures. The dynamical structure factor can often be calculated using force constants derived from models or from first principles calculations. However the process is not straight forward for complex unit cells with multiple atoms per unit cell. The $\mathbf{Q}$ dependence of $F_D(\mathbf{Q})$ depends on the polarization vectors for the different atoms and is difficult to predict. The periodicity for which $F_D(\mathbf{Q})$ varies is dramatically different for a system with multiple atoms per unit cell. When one considers doped compounds with atomic structural positions that are not simple fractions of the unit cell, $F_D(\mathbf{Q})$ may never repeat increasing the challenge of finding zones where phonon intensities can be systematically measured throughout the Brillouin zone [108]. The dynamical structure factor and phonon scattering intensities have been calculated for Sr_2RuO_4 [56]. Zones can be searched based on the Sr_2RuO_4 results however, several alternate zones must be systematically investigated due to the increased complexity.

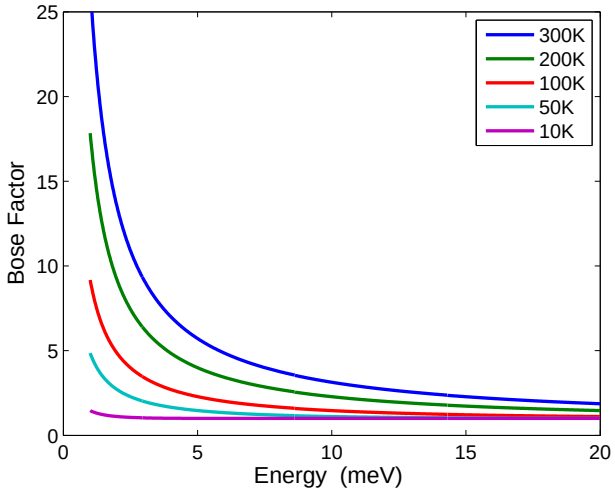

Figure 2.2: Bose factor correction for phonon intensities.

2.2 Low Energy Electron Diffraction

The fundamental theory of Low Energy Electron Diffraction (LEED) presented here follows the developments set forth by Pendry and Van Hove [114, 115, 116]. If we consider for a moment only elastic scattering then $E_i = E_f$ and that also means that $|\mathbf{k}_i| = |\mathbf{k}_f| = k$. If we consider a monoenergetic stream of electrons incident on our crystal then we can represent the incident electron beam as an incident plane wave:

$$A_i = A_o e^{-i\mathbf{k_i}\bullet\mathbf{r}} \tag{2.24}$$

with A_o as the constant incident electron beam amplitude traveling with momentum vector $\mathbf{k}_i$ and $\mathbf{r}$ is a space vector. For the sake of simplicity, lets consider a 1-dimensional case where our beam is traveling in the x direction and is incident on a semi-infinite row of identical atoms separated by a distance d with $x = 0$ as the position of the first atom. Then our incident plane wave can be simplified as:

$$A_i = A_o e^{-ik_i x} \tag{2.25}$$

2.2.1 Kinematic Approximation

Lets then assume that the transmission or reflection from an atom in any layer can be represented by complex transmission and reflection coefficients where:

$$T^*T + R^*R = 1 \tag{2.26}$$

If we assume that the scattering from any particular atom is weak (ie kinematic approximation) than we can further restrict the relationship between T and R. If we have perfect transmission then $|T| = 1$ and the argument of T must vanish, i.e. T becomes real. Lets assume that scattering is weak enough that T remains real even when $|T| < 1$. Then we

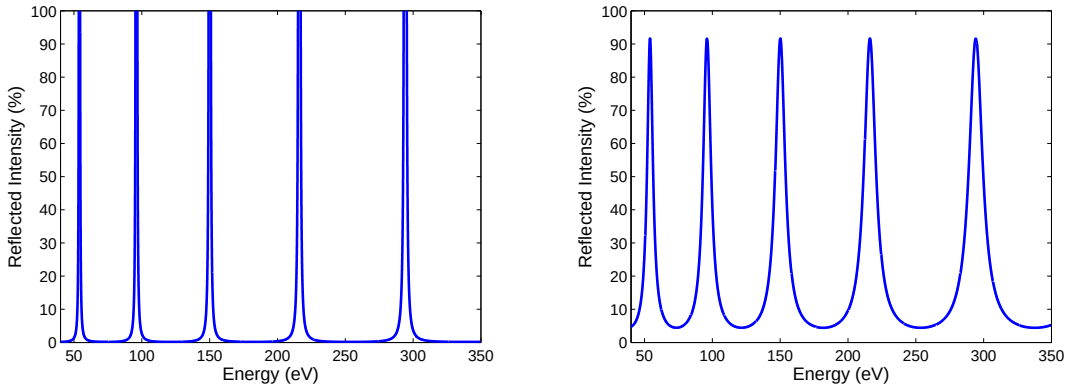

(a) (b)

Figure 2.3: Kinematic 1-D Bragg scattering. (a) Infinite Bragg peaks due to assumption that incident wave is transmitted only once through each site ($d = 2.5$Å, $T = 0.99$). (b) Kinematic 1-D Bragg scattering corrected for multiple transmittance through each site ($d = 2.5$Å, $T = 0.85$).

can establish:

$$R = i\sqrt{1 - T^2} \tag{2.27}$$

In our simple 1-dimensional case, we only have one beam reflected from the surface and it is the sum of all the reflected beams from each layer and we can write the scattered beam amplitude as:

$$A_s = A_o \sum_{j=0}^{\infty} R e^{ik2d_j} e^{-ikx} = A_o \frac{i\sqrt{1 - T^2}}{1 - e^{ik2d}} e^{-ikx} \tag{2.28}$$

with the index j labeling each atom in our row. Figure 2.3(a) shows the scattered beam intensity ($I = |A|^2$) for our simple case. The scattered intensity is negligible until a Bragg condition is met (i.e. $k2d = 2\pi n$ with $n = 1, 2, 3\ldots$). At each Bragg intensity we have an infinite intensity which clearly violates current conservation. To correct for the discrepancy we must realize that the wave traveling through the crystal is transmitted twice through each atom j: once from the wave propagating from the crystal surface to atom $j + 1$ and then again as the reflected wave from atom $j + 1$ travels back to the surface. Thus the correct scattered wave amplitude is:

$$A_s = A_o \sum_{j=0}^{\infty} R T^{2j} e^{ik2dj} e^{-ikx} = A_o \frac{i\sqrt{1 - T^2}}{1 - T^2 e^{ik2d}} e^{-ikx} \tag{2.29}$$

Figure 2.3(b) shows how the correction doesn't shift the positions of the peaks, as nothing has changed our Bragg condition, but it prevents the Bragg reflections from reaching infinite intensity since $|T| < 1$. The above argument is still not entirely correct as we have neglected multiple reflections from each layer. However, for weak scattering where $|T|$ is close to 1 Equation 2.29 is approximate and can be useful for illustration purposes.

In real materials the above argument is much too simplistic as there are other physical factors which must be considered. If we assume each of our atoms is an identical metallic

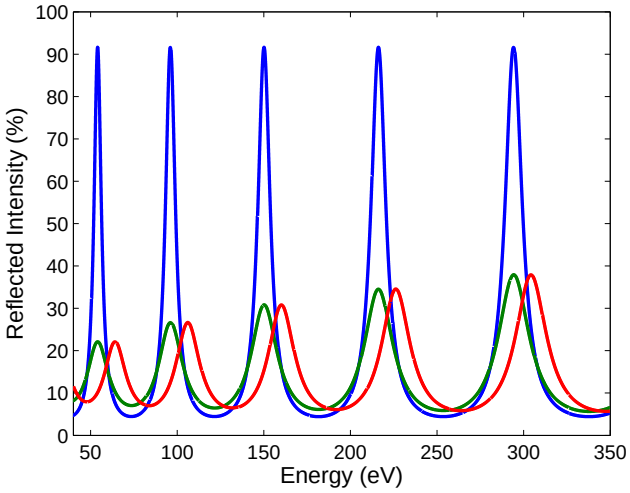

Figure 2.4: Kinematic 1-D Bragg scattering with V_{or} and V_{oi}. Interlayer spacing $d = 2.5$Å and transmission coefficient $T = 0.85$ with $V_{or} = V_{oi} = 0$ (Blue); $V_{or} = 0$, $V_{oi} = -5eV$ (Green); and $V_{or} = 10eV$, $V_{oi} = -5eV$ (Red).

species and if we allow our interlayer spacing to be somewhat realistic for actual metals, then the interstitial space between each layer would have a non-zero charge density due to the conduction electron wavefunctions extending beyond neighboring atoms. This non-zero charge density will lead to a non-zero potential which will alter the energy of our electron wave. In addition, the electron beam will be attenuated due to inelastic scattering events. Electrons are charged and interact inelastically with the crystal environment yielding a fairly short mean free path (typically 10-20Å). Thus LEED is a surface sensitive probe and such attenuation affects must be accounted for in our models. To understand the implications of the crystal environment on our electron beam traveling through the crystal we can add a complex inner potential existing inside our crystal: $V_o = V_{or} + iV_{oi}$. This inner potential will alter the electron's energy and thus its momentum:

$$k = \sqrt{\frac{2m(E - V_o)}{\hbar^2}} = 2\pi\sqrt{\frac{E - V_{or} - iV_{oi}}{150[eV]}} \tag{2.30}$$

Figure 2.4 shows the effects of constant real and imaginary parts of the inner potential. In our simple kinematic model, the real part simply has the effect of shifting the position of the Bragg peaks. The imaginary component shows the effects of attenuation as the Bragg peak intensities are dramatically reduced and the width increases. Experimental and theoretical investigations have revealed that a constant $V_{or} \sim 10eV$ and $V_{oi} \sim -4eV$ work well for simple metals and have typically been held constant. However, such a constraint doesn't work well with complex transition metal oxide materials as will be discussed below. Thus far we have only considered the case where scattering from each atom is weak. Hence, the backscattered beam only includes reflections from each layer and does not include effects of multiple reflections, or multiple scattering.

2.2.2 Multiple Scattering

In X-ray scattering incident photons interact weakly with the solid. Hence there is a low probability of interacting with the crystal and the kinematic approximation works well. It can be assumed without loss of accuracy that any backscattered photon will have encountered only a single scattering event prior to exiting the crystal. In contrast, electron interactions with the crystal are much stronger. While experimental observations show that $\sim 1\%$ of the incident electrons are backscattered, an electron backscattered from an atomic plane inside the crystal still has to pass the above planes prior to exiting the surface. The backscattered electron can interact with one of the above planes and undergo another scattering event. The electron interactions with the solid are strong enough that multiple scattering events are probable and kinematic theory breaks down. To account for multiple reflections within the crystal we shift from our kinematic model to one derived by normal mode analysis. Figure 2.5 shows schematically how the wave amplitudes add at each interstitial region between the atoms. For a reference point half way between any two atoms we can write down the wave amplitude resulting from transmission and reflection of the wave from the neighboring atoms:

$$a_n^+ = (Ra_n^- + Ta_{n-1}^+)e^{ikd} \tag{2.31}$$

and

$$a_{n-1}^- = (Ra_{n-1}^+ + Ta_n^-)e^{ikd} \tag{2.32}$$

While normal mode analysis can determine wave amplitudes within any part of the crystal, we are only interested in the amplitude of the wave field exiting the surface (a_o^-), but this amplitude includes all of the internal reflections occurring within the crystal. It can be shown that the exiting wave from the crystal surface has the amplitude:

$$A_s = \frac{k_o(1 + a_o^+/a_o^-) + k(1 - a_o^+/a_o^-)}{k_o(1 + a_o^+/a_o^-) - k(1 - a_o^+/a_o^-)} \tag{2.33}$$

where

$$a_o^+/a_o^- = \frac{i}{\sqrt{1-T^2}}[i\sin(kd) \pm \sqrt{T^2 - \cos^2(kd)}] \qquad \text{if} \quad T^2 > \cos^2(kd) \tag{2.34}$$

and

$$a_o^+/a_o^- = \frac{i}{\sqrt{1-T^2}}[i\sin(kd) \pm i\sqrt{\cos^2(kd) - T^2}] \qquad \text{if} \quad T^2 < \cos^2(kd) \tag{2.35}$$

Figure 2.6 shows a comparison between the kinematic approximation and the more exact normal mode analysis. For the case of high transmission and large attenuation (large T and large V_{oi} as in Figure 2.6(a)) both methods yield similar results as these parameters represent weak scattering with few multiple reflections, where the kinematic approximation holds.

While for a row of identical atoms the normal mode analysis is exact, the crystals we are interested in are not quite as simple. We must extend our method into 3-dimensions and allow for different types of atomic species within the crystal. Thus we must account for the fact that each atomic species will scatter the electron differently and we also must account

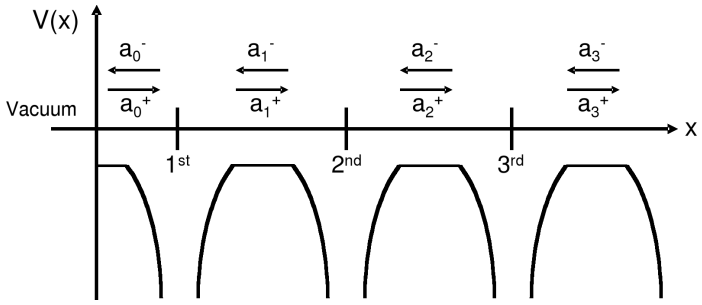

Figure 2.5: Schematic diagram of multiple scattering. Each number represents an atom in the row and the surface is at $x = 0$.

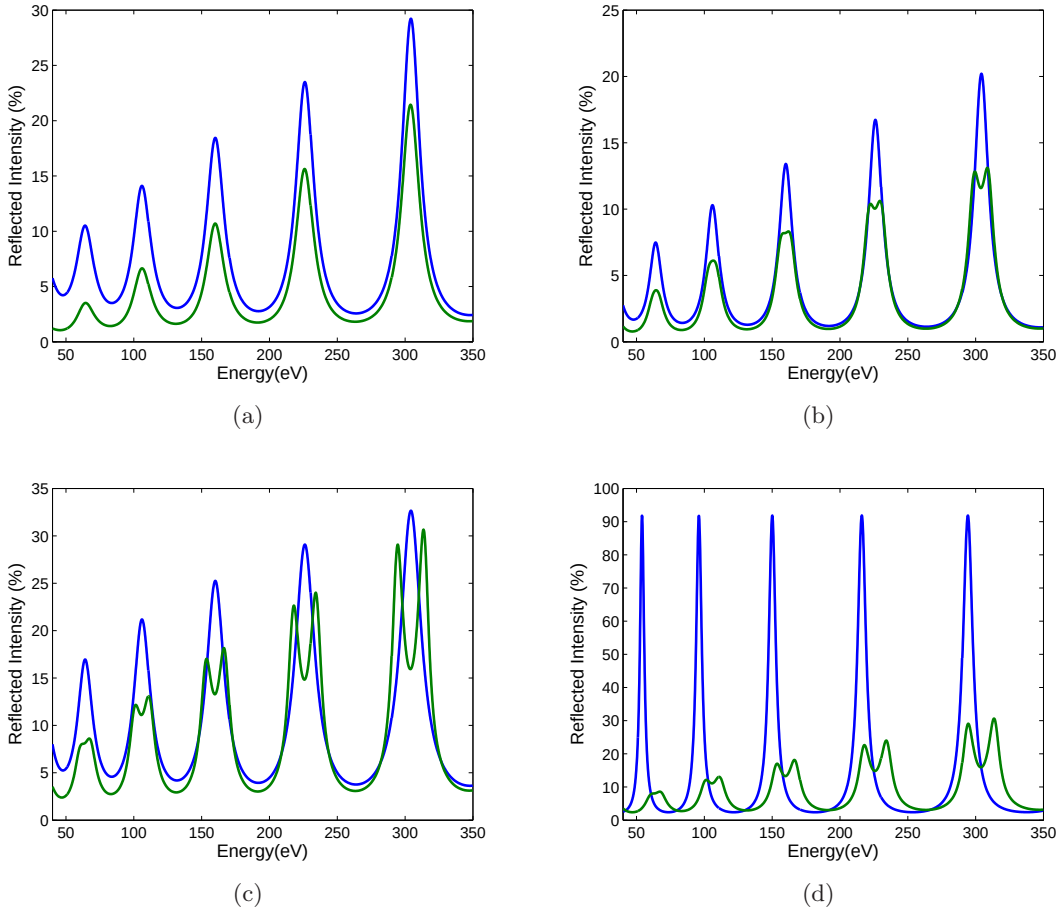

Figure 2.6: Kinematic VS multiple scattering. Kinematic shown in blue and multiple scattering shown in green with $d = 2.5$Å for different parameters. (a) $T = 0.99$, $V_{or} = 10eV$, $V_{oi} = -8eV$. (b) $T = 0.95$, $V_{or} = 10eV$, $V_{oi} = -5eV$. (c) $T = 0.85$, $V_{or} = 10eV$, $V_{oi} = -5eV$. (d) Kinematic model: $T = 0.85$, $V_{or} = 0$, $V_{oi} = 0V$; Multiple scattering model: $T = 0.85$, $V_{or} = 10eV$, $V_{oi} = -5eV$.

for multiple scattering effects within a single 2-dimensional layer in addition to multiple transmissions and reflections between layers. The reader is directed to Refs. [114, 115] for the extension of the kinematic approximation and normal mode analysis into higher dimensions. Computer codes have been written to analyze LEED data and I will simply outline the construction and application of the codes. The codes used in this work are modified versions of the SATLEED codes from Barbari and Van Hove [117]. Modifications have been incorporated to more accurately model IV spectra from our crystals. The physics and justification for each modification will be discussed in more detail.

2.2.3 LEED-IV

To understand how to determine surface structure from LEED data we must first understand the LEED pattern. Due to the constructive (and destructive) interference of the scattered waves emanating from the crystal surface, only certain exit beams are allowed and these exit beams contain information regarding the symmetry of the atomic scatters within the periodic crystal array. To better envision the crystal symmetry encoding we can refer to the Ewald construction and how it applies to our observed LEED pattern as shown in Figure 2.7. For x-ray scattering where the kinematic approximation is an accurate description we can envision a sphere with radius k_o existing inside the reciprocal space lattice and everywhere the sphere touches a reciprocal space lattice point, the Bragg condition is satisfied and a Bragg reflection results:

$$\mathbf{Q} = \mathbf{k} - \mathbf{k}_o = \mathbf{G}_{hkl} = h\mathbf{b}_1 + k\mathbf{b}_2 + l\mathbf{b}_3 \tag{2.36}$$

where $\mathbf{G}_{hkl}$ is a reciprocal lattice vector labeled by Miller indices h, k and l with $\mathbf{b}_i$ as the respective axis vectors of the reciprocal lattice. In the case of LEED, since the incident electron wave strongly interacts with the first few atomic layers the periodicity parallel to the direction of the incident wave becomes ill defined. For a perfectly 2-dimensional surface with the incident beam normal to the surface the periodicity along the plane normal becomes infinite thus in reciprocal space $|\mathbf{b}_3|$ becomes zero. Thus our reciprocal space lattice no longer takes the shape of distinct lattice points but becomes rods extending infinitely in the direction normal to the surface. Momentum in directions parallel to the surface is still conserved and thus we can identify planar symmetries existing along the surface. Thus in our Ewald construction we must project the wave vectors onto a surface perpendicular to the rods and the Ewald sphere becomes a circle. From this projection we can connect points touching the intersection of the circle and the rod and establish the 2-dimensional Bragg condition:

$$\mathbf{Q}_{||} = \mathbf{k}_{||} - \mathbf{k}_{o||} = \mathbf{G}_{hk} = h\mathbf{b}_1 + k\mathbf{b}_2 \tag{2.37}$$

Since momentum conservation is lost normal to the surface, the Laue condition normal to the surface can never be met and the diffraction spots are evident at all incident wave energies. Since the incident electron beam does indeed penetrate the surface of the crystal (albeit only within a few atomic layers) our reciprocal space Bragg rods are not infinite and we do probe crystallographic information for the first few atomic layers. Park and Farnsworth found that the intensity of the diffracted beams modulates as a function of incident beam energy (IV specta) and this modulation encodes information regarding the geometrical atomic structure near the surface region of the crystal [118].

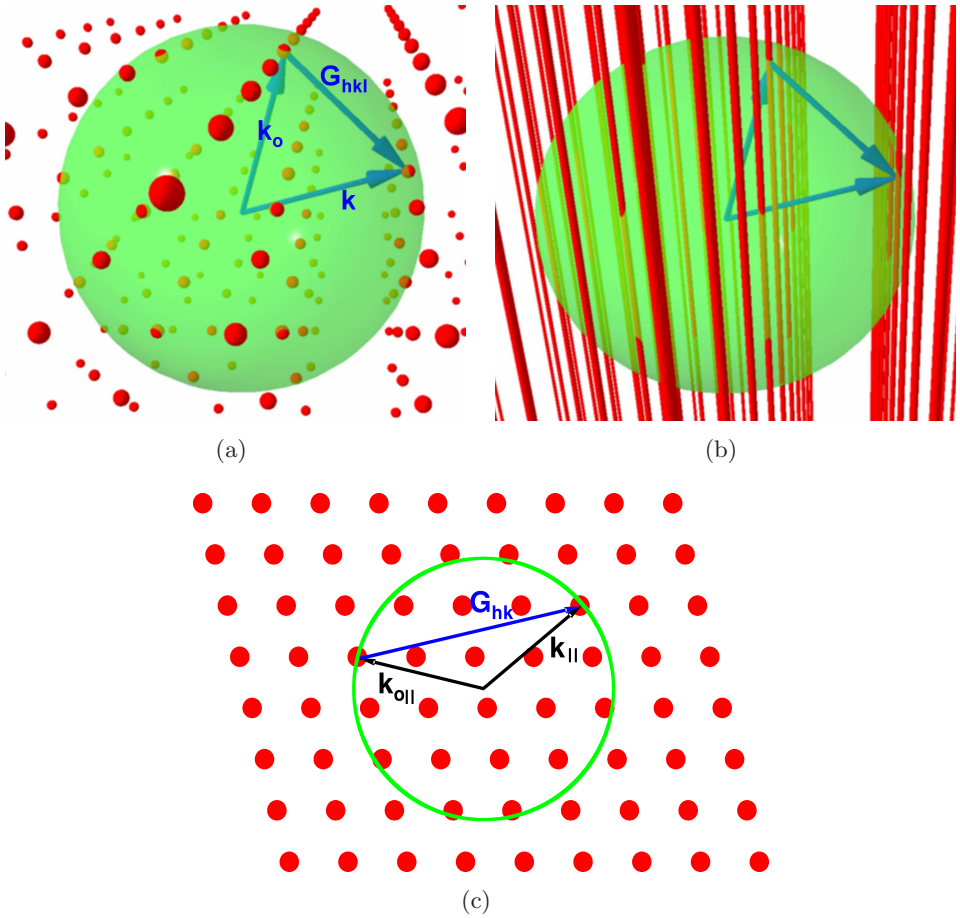

Figure 2.7: Ewald construction. (a) 3-D Ewald sphere construction through Bragg spots. (b) 3-D Ewald sphere construction through Bragg rods. (c) 2-D projection of Ewald sphere parallel to Bragg rods.

Due to the multiple scattering processes the intensities from the diffracted beams can not be directly inverted to reveal the real space structure of the crystal surface. Thus LEED is an iterative process where one starts with a model (reference structure) of the surface and IV spectra is calculated for this model. Then small deviations in atomic positions are created (trial structure) and perturbations to the IV spectra are then calculated and compared to experimental data. Correlation between the theoretical IV curves and experimental curves are evaluated with the use of a reliability factor. Thus LEED is an optimization process where different trial structures are generated and compared with experimental data. The trial structure which generates the lowest reliability factor (best correlation with experimental data) is accepted as the true real space configuration of the atoms near the crystal surface. Thus in LEED one must start with an idea of the surface structure and evaluate the feasibility of a particular model. Calculation of IV spectra is not a trivial process even for simple metals with one atom per unit cell. For simple materials, approximations and assumptions can be invoked to make the calculations more tractable. However, for more complex materials involving several atomic species and numerous atoms in a unit cell ($I4_1/acd$ structure has 56 atoms in its unit cell), some of our simplifying assumptions and approximations no longer hold and more detailed descriptions of the crystal potential from which our incident wave scatters must be employed.

In general the interactions between the incident LEED electrons and the crystal surface are non-local and contain electrostatic as well as exchange and correlation effects. In addition to the non-local interactions, the crystal potential can be quite complicated as it is made up of overlapping atomic orbitals of different sizes and shapes. The addition of multiple atomic species and several atoms per unit cell further complicates the shape of the crystal environment in which the electrons scatter. To make the calculations tractable the general procedure for LEED is to start with a *muffin-tin* (MT) potential approximation. In this procedure each atom is assumed to be a spherical well potential with a flat interstitial potential connecting each scattering center. The interstitial potential accounts for the valence electron sea existing outside the atomic cores. Thus the scattered wave function $\psi(\mathbf{r})$ can be written using a partial wave expansion while in the interstitial region it takes the form of a simple plane wave. There are different methods for choosing muffin-tin radii however caution must be used as the overlapping of neighboring spherical potentials can create artificial resonant effects in the scattering wavefunctions. Thus a muffin-tin radii is chosen to ensure adjacent spheres do not overlap and the potential inside the muffin-tin spheres are adjusted to account for the electronic orbital overlap in the real crystal. While this method has proven successful for close packed metals, there is some question as to its accuracy when one starts to deal with transition metals with extended d orbitals and complex metal oxides with significant hybridization between the metal cation and oxygen orbitals. Different methods for calculating muffin-tin radii and the extension of LEED theory to include the energy dependence of the interstitial region will be discussed in subsequent sections of this Chapter. As a first step in modeling the crystal potential, we start with modeling how an electron wave scatters with an individual spherical atomic core.

2.2.4 Atomic Phase Shifts

Detailed descriptions of scattering theory for an incident electron scattering off a spherical muffin-tin potential $V_{mft}(\mathbf{r})$ with radius r_{mft} is covered in most quantum mechanics textbooks [119, 120]. The wave function $\psi(\mathbf{r})$ for an electron with energy E and momentum $\mathbf{k}$

scattering from a spherical well can be found from solving the time-independent Schrödinger equation and for large distances from the scattering center takes the asymptotic form:

$$\psi(\mathbf{r}) \underset{\mathbf{r}\to\infty}{\to} e^{i\mathbf{k}\bullet\mathbf{r}} + f(k,\theta,\phi)\frac{e^{i\mathbf{k}\bullet\mathbf{r}}}{r} \tag{2.38}$$

where $f(k,\theta,\phi)$ is the scattering amplitude into polar angle θ (scattering angle) and azimuthal angle ϕ. Since the scattering potential is spherically symmetric it does not depend on ϕ and by using the method of partial-waves the wave function and scattering amplitude can be expanded in Legendre polynomials $P_l(\cos\theta)$ and we are left with solving the one-dimensional radial Schrödinger equation:

$$\left(-\frac{\hbar^2}{2m}\frac{1}{r^2}\frac{d}{dr}\left(r^2\frac{d}{dr}\right) + \frac{\hbar^2}{2m}\frac{l(l+1)}{r^2} + V_{mft}(r)\right)R_l = ER_l \tag{2.39}$$

for which the solutions in regions $r > r_{mft}$ is given by:

$$R_l(k,r) = A_l(k)j_l(kr) + B_l(k)n_l(kr) \tag{2.40}$$

where j_l and n_l are the spherical Bessel and Neumann functions respectively. Using this method allows us to expand the scattering amplitude into Legendre polynomials for the scattering angle θ between $\mathbf{k}$ and $\mathbf{r}$

$$f(k,\theta) = 4\pi\sum_{l=0}^{\infty}(2l+1)t_l(k)P_l(\cos\theta) \tag{2.41}$$

where $t_l(k)$ is the t-matrix element given by:

$$t_l(k) = \frac{e^{2i\delta_l(k)}-1}{4k} = \frac{1}{2k}e^{i\delta_l(k)}\sin\delta_l(k) \tag{2.42}$$

with the *phase shifts* $\delta_l(k)$ representing the atomic scattering inside the muffin-tin spheres. We can then determine the total scattering cross-section into solid angle $d\Omega$

$$\frac{d\sigma(k,\theta)}{d\Omega} = |f(k,\theta)|^2 \tag{2.43}$$

with the total flux given by an integration over all angles

$$\sigma_T(k) = \int |f(k,\theta)|^2\, d\Omega = \frac{4\pi}{k^2}\sum_{l=0}^{\infty}(2l+1)\sin^2\delta_l(k) \tag{2.44}$$

Thus the entire scattering process is reduced to determining phase shifts for our muffin-tin spheres and the importance of phase shifts in LEED becomes evident.

To calculate the phase shifts we start by calculating the one-electron scattering potentials for a free atom by performing a relativistic Hartree-Fock (Dirac-Fock) calculation for each atomic species. Figure 2.8(a) shows the radial electronic density for each atomic species in our system from which an atomic potential $V_{at}(r)$ can be calculated based on solving Poissons equation subject to the boundary condition $V_{at}(r \to \infty) = 0$. Construction of

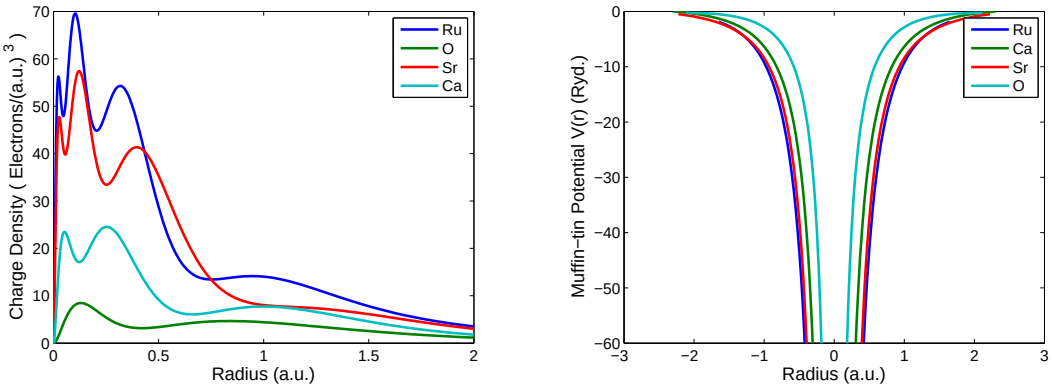

(a) (b)

Figure 2.8: Free atomic charge density and muffin-tin potential. (a) Free atom charge density results from Driac-Fock calculation. (b) Muffin-tin potentials calculated from Mattheiss prescription.

the muffin-tin potentials follows the Mattheiss prescription [121, 122]. A bulk terminated surface is assumed and the free atom electronic densities are superimposed on bulk unit cell coordinates. Thus the atomic electronic densities and potentials on a particular site overlap neighboring sites. For a particular unit cell site a spherical shell of neighboring atoms are determined and the electronic density from the shell is determined. The process is repeated for next nearest neighboring atom shell and superposition procedure continues for larger shells until a predetermined electronic density limit is reached. A monopole is calculated from the overlapping electronic densities due the different shells and added to the atomic electronic density at the particular site from which spherical potentials are calculated by solving Poissons equation. In addition a local *Slater-like exchange* term [123]

$$V_{ex}(r) = -3\alpha \left(\frac{3\rho(r)}{8\pi} \right)^{1/3} \tag{2.45}$$

is added to the electrostatic spherical potential to create the muffin-tin potential $V_{mft}(r)$ at a particular site. The exchange parameter α is different for different elements but typically takes on values between 2/3 and 1 [124]. The spatial average of the interstitial regions are used to determine the muffin-tin zero potential and the spherical muffin-tin potentials are renormalized to the muffin-tin zero. Muffin-tin potentials for the atomic species in our system are presented in Figure 2.8(b). Phase shifts are determined by solving the one-dimension radial Shrödinger Equation 2.39 for the muffin-tin potential subject to the boundary conditions that the wave function and its derivative must be continuous at the muffin-tin radius r_{mft}:

$$\tan \delta_l(k) = \left(\frac{kr_{mft} j_l^{'}(kr_{mft}) - \beta_l j_l(kr_{mft})}{kr_{mft} n_l^{'}(kr_{mft}) - \beta_l n_l(kr_{mft})} \right) \tag{2.46}$$

where $j_l^{'}$ and $n_l^{'}$ are derivatives of the spherical Bessel and Neumann functions evaluated at $r = r_{mft}$ and β_l is

$$\beta_l = \left[\frac{r}{R_l(kr)} \frac{dR_l(kr)}{dr} \right]_{r=r_{mft}} \tag{2.47}$$

Free atom atomic charge densities and phase shifts were calculated using the Barbieri-Van Hove phase shift package [117].

The partial wave sum given in Equation 2.41 runs over all l however the sum is truncated for some l_{max} as the higher order phase shifts contribute less to the scattering cross-section. In general the forward scattering cross section grows at high energies for larger l while the back scattering cross sections decreases at high energies for larger l. To determine the appropriate l_{max} it is usually best to plot out the scattering cross section for different l_{max} to evaluate the appropriate cutoff as shown in Figure 2.9. However, as an estimate one can use the classical analog where a particle is orbiting a spherical potential with angular momentum l while having a linear momentum k [114]. Thus the closest the particle would approach the center of the potential would be with a radius r_l where $l = kr_l$. The maximum possible angular momentum for a classical particle orbiting our muffin-tin sphere would be $l_{max} = kr_{mft}$. If the particle passed by the spherical potential with a larger momentum or at a larger radius, it simply would not "see" the potential.

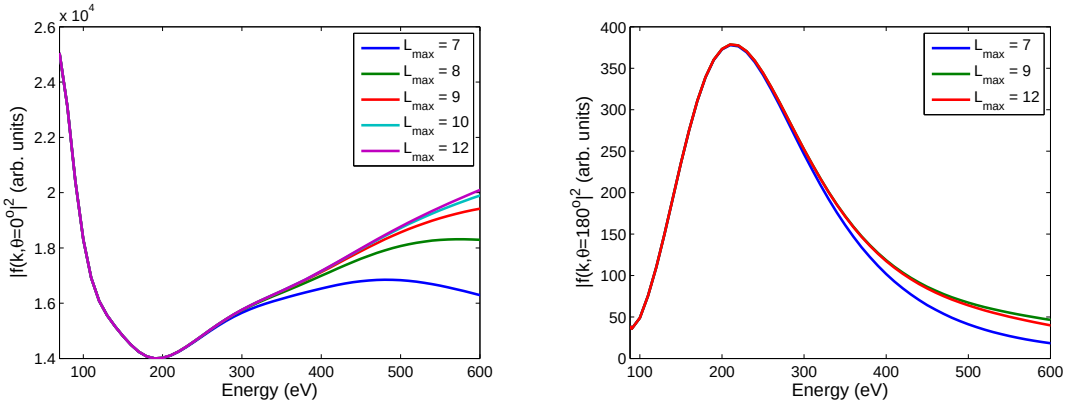

Figure 2.9: Forward scattering and back scattering amplitude for Ru for different L_{max}. (a) Forward scattering. (b) Back scattering.

2.2.5 The Optical Potential

As discussed above, the incident signal electrons strongly interact with the first few atomic surface layers of the crystal. As a result, multiple scattering effects become important and the incident electron beam is attenuated within the first few atomic layers due to inelastic scattering. To accurately model the scattering phenomena one must account for these effects when calculating theoretical IV curves of diffracted beams. The calculation of IV spectra from the model crystal potential assumes non-overlapping MT spheres surrounded by a flat interstitial region. The flat region represents the electron sea from the valence and conduction bands surrounding the ion cores. Due to the non-local extent of these bands the signal electron will encounter an averaged potential in the interstitial region arising from overlapping orbitals of the many surrounding ion cores. As a result a flat averaged interstitial potential is typically a good approximation for metallic systems. Thus the inner potential is typically modeled as a constant (V_{or}) within which the ion cores are periodically distributed.

In addition, to model the electron attenuation due to inelastic scattering events, an imaginary component to the inner potential is assumed which accounts for the mean free path of the electron. As the signal electron propagates through the material there is a finite probability of scattering inelastically and thus there is a finite lifetime, or finite path length, it will travel before encountering such an event. It is typically assumed that the electron will have a similar lifetime or mean free path no matter which trajectory the electron traverses through the sample. Due to the periodic nature of the material such an assumption holds as one unit cell of the crystal is identical to all other unit cells and thus the mean free path should not vary as the electron scatters elastically through several of such unit cells. Thus the inner potential is given an imaginary component (V_{oi}) which is constant and accounts for the mean free path of the electron throughout the crystal.

Hence in LEED the optical potential is typically modeled as a constant with a real and imaginary component ($V_o = V_{or} + iV_{oi}$). Theoretical predictions and experimental experience has shown that V_{or} takes on typical values of $\sim 10eV$ while the imaginary component V_{oi}

takes on values of -4 to -5 eV [114]. During the optimization process, V_{or} is taken as a non-structural fit parameter and is optimized in the process. Due to the periodic nature of the material the assumed spatial average is a good approximation, however, due to the strong interactions between the signal electron and the crystal, one must consider the dependence of the signal electron energy on these assumed constant potentials. Will a $50eV$ electron propagating through system behave the same as a $500eV$ electron?

2.2.5.1 V_{oi}

The implications of adding an imaginary component to the optical potential were shown in Figure 2.4. The introduction of an imaginary component to the optical potential (V_{oi}) establishes the lifetime of an electron (τ) with energy E for the intensity of the electron wave function:

$$\tau = -\frac{1}{2V_{oi}} \tag{2.48}$$

where $\hbar = 1$. Thus the uncertainty principle implies the minimum width a feature can be observed in the diffraction intensity as given by

$$\left(\frac{\Delta E}{2}\right)^2 \left(\frac{1}{2V_{oi}}\right)^2 \geq \frac{1}{4} \tag{2.49}$$

or

$$\Delta E \geq 2|V_{oi}| \tag{2.50}$$

Hence the peak width observed in the IV spectra is directly related to V_{oi} [114]. Information regarding the penetration depth of the signal electron can be extracted by analyzing the width of peaks in the IV spectra. While $V_{oi} = constant$ works for most simple metals the absorption or inelastic scattering of incident electrons will depend on their incident energy. To better understand how to model the energy dependence of V_{oi}, ignore the atomic potential and write the energy of the electrons inside the crystal as:

$$\frac{\hbar^2 k_s^2}{2m} = E + V_{or} + iV_{oi} \tag{2.51}$$

Since k_s is complex, we can write it as $k_s = k_s^r + ik_s^i$ and separate Equation 2.51 into its real and imaginary components:

$$E + V_{or} = \frac{\hbar^2}{2m}\left[(k_s^r)^2 - (k_s^i)^2\right] \tag{2.52}$$

and

$$V_{oi} = 2\left(\frac{\hbar^2}{2m}\right)(k_s^r)(k_s^i) \tag{2.53}$$

Combining Equations 2.52 and 2.53 to eliminate k_s^i we can write

$$E + V_{or} = \frac{\hbar^2 (k_s^r)^2}{2m} - \frac{V_{oi}^2}{4\left(\frac{\hbar^2 (k_s^r)^2}{2m}\right)} \tag{2.54}$$

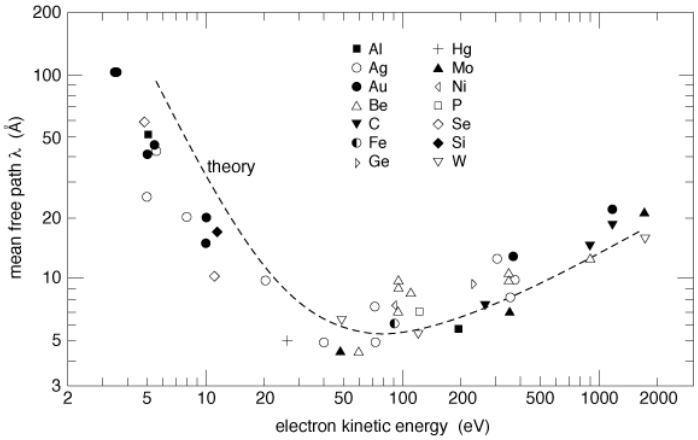

Figure 2.10: "Universal curve" of electron mean free path in various metals. Figure adapted from Ref. [125].

Since our incident beam energies are much higher than the imaginary part of the optical potential

$$V_{oi}^2 << \left(\frac{\hbar^2 k_s^r}{2m}\right)^2 \tag{2.55}$$

and we can write the real part of the inner potential inside the crystal as:

$$k_s^r = \sqrt{\frac{E + V_{or}}{\hbar^2/2m}} \tag{2.56}$$

Substituting this expression into Equation 2.53 for V_{oi} and we obtain:

$$k_s^i = \frac{V_{oi}}{2(\hbar^2/2m)\sqrt{\frac{E+V_{or}}{\hbar^2/2m}}} \tag{2.57}$$

If we write the wavefunction inside the crystal as

$$\psi_s = Ae^{i(k_s^r + ik_s^i)x} = Ae^{ik_s^r x}e^{-x/\lambda} \tag{2.58}$$

where λ is the mean free path of the electrons inside the crystal which can be written a

$$\lambda = 1/k_s^i = \frac{2(\hbar^2/2m)\sqrt{\frac{E+V_{or}}{\hbar^2/2m}}}{V_{oi}} \tag{2.59}$$

Thus we have established a relation between the mean free path of the signal electron at energy $E + V_{or}$ and V_{oi}. To model V_{oi} we can consider the "Universal Curve" of electron mean free path in various metals as shown in Figure 2.10 and establish a phenomenological form for V_{oi} that reproduces the curve through the relationship in Equation 2.59. For the energy ranges used in LEED it is found that a simple phenomenological form for V_{oi} that

reproduces the "Universal Curve" is [114, 126]:

$$V_{oi} = C\left(\frac{E}{200/27.21 + V_{or}}\right)^{1/3} \tag{2.60}$$

The SATLEED codes were modified to incorporate this phenomenological form for V_{oi}, where the constant C takes the those values normally assumed for a constant imaginary part of the optical potential (typically -4 or -5eV).

2.2.5.2 V_{or}

During the construction of the MT potentials the overlapping orbitals from neighboring sites were added to the spherical potential on a particular site. In addition, a Slater-like exchange term was added to the MT potential to account for exchange and correlation effects. However, since our probe is an electron we must consider exchange and correlation effects between our signal electron and the surrounding electron sea between the ionic cores. It has been shown that an electron propagating through a jellium model for an electron gas will encounter exchange and correlation effects with the surrounding gas. The strength of this interaction depends on the difference between the energy of the signal electron and the Fermi energy of the surrounding gas. Thus this exchange potential has an energy dependence. If the signal electron travels through the gas with relatively high energies, the electron gas of the jellium will relax too slowly to accompany the electron by an exchange-correlation hole. However for low energy electrons, like the ones in LEED, the exchange potential can become important as the overall effect lowers the energy of our signal electron. Here we follow the development of the exchange-correlation potential and $V_{or}(E)$ by Hedin and Lundqvist as outlined by Rundgren [127, 128, 129, 130].

If we consider local density theory then the signal electron propagating through the jellium electron gas will contribute the following energy to the system:

$$p^2(r_s) + \Sigma[p(r_s), r_s] = \varepsilon + k_F^2(r_s) + \mu_{xc}(r_s) \tag{2.61}$$

With the left hand side of the equation representing the local momentum p and local density self-energy Σ of the signal electron. The right hand side of the equation represents the excitation energy ε of the signal electron with the local Fermi momentum of the electron gas k_F along with the local ground state exchange-correlation energy μ_{xc}. In LEED the excitation energy is the energy of the signal electron relative to the local potential generated by the spherically averaged superposition of atomic potentials $\varepsilon = E - V_{sw}(r)$ for $r < r_{mft}$. Hence we can consider the excitation energy as the signal electron energy relative to our constant interstitial potential for regions outside the MT spheres $\varepsilon = E - V_{or}$ for $r > r_{mft}$. The parameter r_s is the interelectron spacing based on the local electron density. Thus if one considers the local electron density ρ anywhere within the crystal then r_s is the radius of a sphere containing one electron with such a density

$$r_s = \left(\frac{4}{3}\pi\rho\right)^{-1/3} \tag{2.62}$$

In LEED we can identify the local exchange potential V_{xc} with the self-energy of the signal electron $V_{xc} = \Sigma$. In this way, one can make use of two different data bases for the self-energy of and excited state electron in the electron gas to determine the energy dependence of the inner potential. Following the development by Hedin and Lundqvist we can start with the Kohn-Sham-Gáspár exchange potential [127, 131]

$$\mu_x(r_s) = -\frac{e^2 k_F}{\pi} = -\frac{e^2}{\pi}(3\pi^2\rho)^{1/3} = -\left(\frac{2}{\pi}\right)\left(\frac{9}{4}\pi\right)^{1/3} r_s^{-1} Ryd \tag{2.63}$$

where Rydberg atomic units ($m_e = 1/2$, $\hbar = 1$, $e^2 = 2$) are used. Thus we can express the Fermi momentum as

$$k_F(r_s) = \left(\frac{9}{4}\pi\right)^{1/3} r_s^{-1} \tag{2.64}$$

and determine the ground state exchange-correlation potential by multiplying the exchange potential by an enhancement factor β based on correlation energy data determined by Singwi [132]

$$\mu_{xc}(r_s) = \beta(r_s)\mu_x(r_s) \tag{2.65}$$

with

$$\beta(r_s) = 1 + 0.7734x\ln(1 + x^{-1}) \qquad x = \frac{1}{21}r_s \tag{2.66}$$

If we consider the limits that as the excitation energy tends toward zero $\varepsilon \to 0$ and $p \to k_F$ then the electron self-energy must become the ground state exchange-correlation potential $V_{xc} = \Sigma \to \mu_{xc}$. Due to the inaccuracies in the self-energy calculations these limits do not hold for the existing databases and it is suggested that the self energy data be scaled accordingly [127, 128]:

$$V_{xc} = \left(\frac{\Sigma(p, r_s)}{\Sigma(k_F, r_s)}\right)\mu_{xc}(r_s) \tag{2.67}$$

Starting from this limit we can determine the energy dependent exchange potential V_{xc} for any electron density starting from $p^2 = \varepsilon + k_F^2$ and then solving Equation 2.61 for p^2 and determining V_{xc} from the existing data bases as the signal electron energy increases [127, 133]. Since V_{xc} depends on the local momentum p, equation can be solved iteratively until self-consistently for increasing signal electron energies. Figure 2.11 shows the energy dependence of the exchange potential $V_{xc}(E)$ versus incident electron beam energy for $r_s = 2$, typical for metallic charge densities. Since the exchange potential is defined relative to the interstitial potential, we add $V_{xc}(E)$ to our inner potential and keep a constant potential V_{oc} which is an optimized non-structural fit parameter $V_{or}(E) = V_{oc} + V_{xc}(E)$. The electron self-energy and $V_{or}(E)$ have been calculated for several systems and it is found that $V_{or}(E)$ takes on a phenomenological form:

$$V_{or}(E) = c_0 + \frac{c_1}{\sqrt{E + c_2}} \qquad (c_0 < 0, c_1 < 0) \tag{2.68}$$

where c_0, c_1 and c_2 are r_s dependent parameters [129].

Since $V_{xc}(E)$ is determined based on the local electron density ρ through the interelectron spacing r_s, in principle one could fit $V_{xc}(E)$ based on the experimental data. Starting from the theoretical model for $V_{xc}(E)$ and solving the structural parameters, one could then

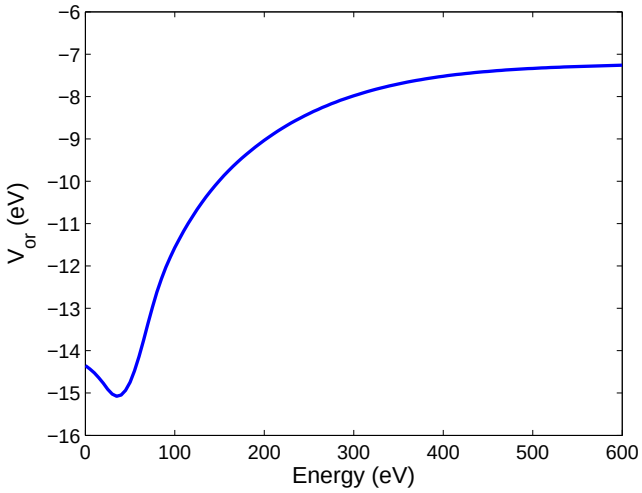

Figure 2.11: Energy dependence of optical potential for $r_s = 2$.

optimize r_s to fit $V_{xc}(E)$ to the experimental data holding the structural parameters fixed. Since $V_{xc}(E)$ is determined by the local electron density and assuming it behaves as an electron gas, the self-consistent ground state electron density must be determined prior to calculating $V_{xc}(E)$. Using the pseudo charge density generated from LDA calculations $V_{xc}(E)$ could be modeled from the charge density existing at the determined MT radii.

To understand the effects of an energy dependent inner potential we can use our one-dimensional illustrative example described in Section 2.2.2. Figure 2.12 shows our one-dimensional model with a constant V_o where V_{or} and V_{oi} take on typical values ($V_{or} = -10eV$ and $V_{oi} = -4eV$). For comparison, the same IV was calculated with $V_{or}(E)$ assuming the energy dependence calculated for Cu and $V_{oi}(E)$ assuming the phenomenological form [134]. As can be seen from such a simplistic model (with a physically exaggerated T=0.85), the energy dependence of the optical potential can have pronounced effects on the positions and shapes of the IV spectra even for such a simplistic example. When the complexity of multiple atoms per unit cell and multiple types of atoms per unit cell are included in the system the importance of accurately modeling non-structural parameters becomes amplified. Even for simpler systems as Cu where an unusual surface layer contraction was determined, the incorporation of $V_{or}(E)$ improved the solution and showed the anomalous contraction was due to the improper modeling of the inner potential [135].

While it is evident that accurate modeling of V_{or} can have important consequences on theoretical IV spectra, the approach outlined above was not explored as further improvements can be made to the determination V_{or} and MT radii and improve phase shift calculations. The SATLEED codes were modified to incorporate the energy dependence of $V_{or}(E)$*.

*The SATLEED code modification implementing the phenomenological form for $V_{or}(E)$ were written by V. B. Nascimento.

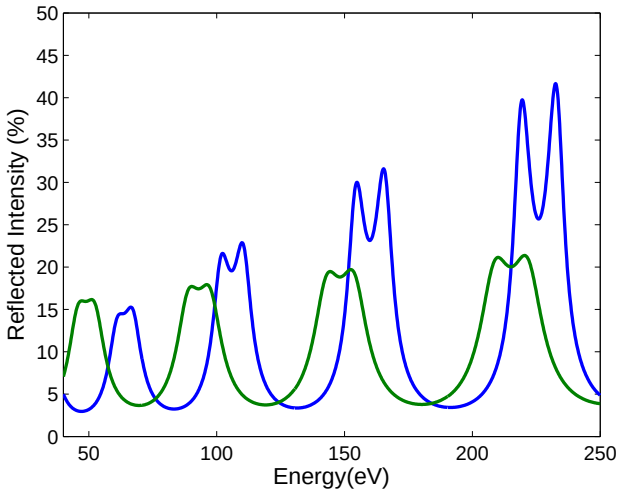

Figure 2.12: V_o versus $V_o(E)$ for 1-D scattering. 1-D normal mode scattering model with V_o is shown in blue, $V_o(E)$ is shown in green.

2.2.6 Muffin-Tin Radii

One of the ingredients in the calculation of the muffin-tin (MT) potentials is the MT radius r_{mft}. The radii for each atomic species within each layer have to be input manually. Typically, one starts by assigning empirically determined ionic radii depending on the coordination of atom. To ensure undesired resonant effects from overlapping spheres are avoided the empirical radii are scaled according to the model unit cell. The atomic size ratio between neighboring atoms and relative distances between neighboring sites are calculated. The empirical radii are scaled to ensure the MT spheres touch at the midpoint between neighboring sites but do not overlap. The scaling also ensures that the size ratio between neighboring species is maintained. Using this procedure phase shifts for $Ca_{1.9}Sr_{0.1}RuO_4$ are calculated for a model based on bulk neutron scattering data at $T = 300K$ [70]. Starting from empirically determined ionic radii found in the literature and scaling according to the dimensions of the model system the MT radii used in the phase shift calculation were: Ru^{4+}= 1.2075$a.u.$; Ca^{2+}= 1.8424$a.u.$; Sr^{2+}= 2.1542$a.u.$; O^{2-}= 2.4566$a.u.$ [98, 136]. While this procedure works well for close packed metals, questions arise as to the validity when dealing with extended transition metal d-orbitals and strong hybridization between metallic cations and oxygen anions. Oguchi and Singh show how for CSRO there appears to be a strong hybridization between the Ru 4d orbitals and the O 2p orbitals [49, 50]. Plus Fang and others show that orbital occupation changes with concentration as the structure of the CSRO family changes [82, 87, 84]. Such a strong hybridization, charge transfer, and orbital occupation could change the effective MT radii in our system.

2.2.6.1 Muffin-tin Radii from First Principles Calculations

To better understand the distribution of charge in our system density functional theory (DFT) calculations were performed. Self consistent DFT calculations utilizing the local density approximation (LDA) with a plane wave pseudo potential basis were performed with the Quantum–ESPRESSO package [137]. While an all-electron *ab initio* calculation may be more suited for such a complex system [138], Fang has shown that Vanderbuilt ultra-soft pseudo potentials works well for our CSRO system [82]. Model system based on bulk neutron scattering data for Sr_2RuO_4 and $Ca_{1.9}Sr_{0.1}RuO_4$ were used to calculate the pseudo charge densities in our system. While the $Ca_{1.9}Sr_{0.1}RuO_4$ coordinates were used, each atomic site was assumed to contain Ca. Self-consistent calculations were performed using an Energy cutoff of $30Ryd$ on a $10\times10\times10$ Monkhorst-Pack Grid (216 k-points for $Ca_{1.9}Sr_{0.1}RuO_4$ and 125 k-points for Sr_2RuO_4). Starting from bulk coordinates and holding the experimentally determined unit cell parameters fixed the internal coordinates were allowed to fully relax. From the model system, pseudo charge densities were plotted out from which MT radii were determined. Figure 2.13 shows the calculated total pseudo charge density for the Ru-O(1) plane for $Ca_{1.9}Sr_{0.1}RuO_4$ while Figure 2.14 shows the pseudo charge density profiles between different atomic sites. Minimums in charge density between atomic sites were used to determine the MT radii. Although we assume spherically symmetric potentials, it is easy to see that the charge density minimums between Ru-O(1) and Ru-O(2) sites are different. The different charge density minimums question the accuracy of modeling the crystal potential as MT spheres in such a complex system but the methods employed here ensure spherically symmetric potentials. Thus to ensure that adjacent muffin-tins did not overlap, the smaller of the resulting distances were used. While the empirical determined ionic radii for Ru

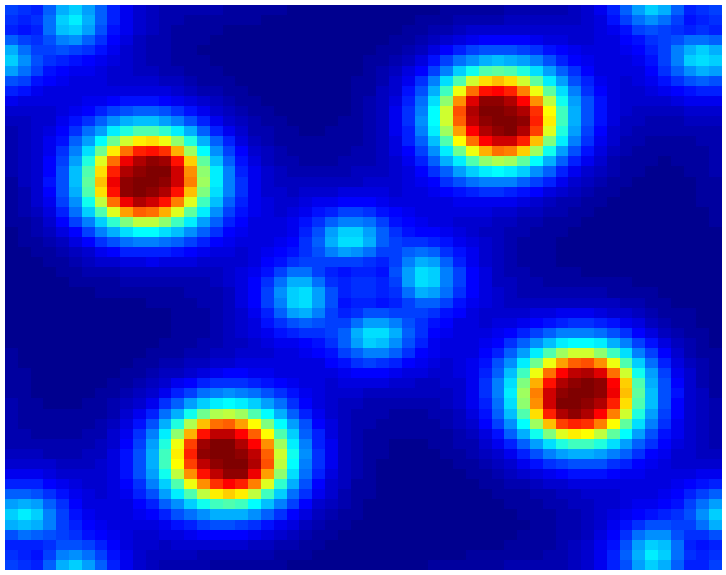

Figure 2.13: LDA psuedo charge density for Ru-O(1) plane in $Ca_{1.9}Sr_{0.1}RuO_4$. Ru atom is at the center of the figure.

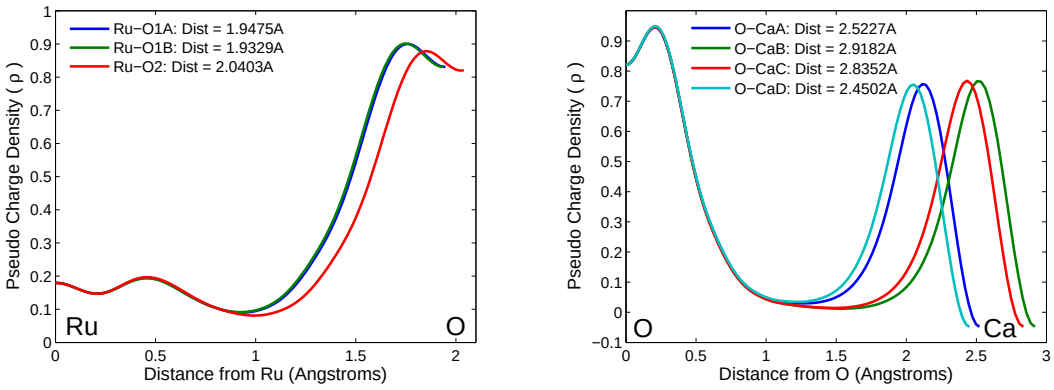

(a) (b)

Figure 2.14: Ru-O and Ca/Sr-O pseudo charge density profile in $Ca_{1.9}Sr_{0.1}RuO_4$. Total Ru-O pseudo charge density (a) and total Ca-O pseudo charge density (b) from LDA calculation.

and O are significantly different, the *ab initio* calculations show that the charge density minimum occurs near the center between the atomic sites. Similar calculations have been performed for TiO_2 and similar results were obtained where the Ti and O MT radii were similar to each other [139]. While the TiO_2 work employed different methods for calculating phase shifts and the scattering crystal potential, the method described here simply shows the effects of MT radii on phase shifts calculated using the Matthesiss prescription. The MT radii determined from the *ab initio* calculations were: Ru^{2+}= 1.7435$a.u.$; Ca^{2+}= 2.5181$a.u.$; Sr^{2+}= 2.3800$a.u.$; $O(1)^{2-}$= 1.9211$a.u.$; and $O(2)^{2-}$= 2.1121$a.u.$ MT potentials and phase shifts utilizing these radii were determined as outlined above. Phase shifts for Ru calculated using this procedure are shown in Figure 2.15.

2.2.6.2 Optimized Muffin-Tin Radii

The calculation of phase shifts as outlined above requires the crystal potential to be modeled by non-overlapping spherical potentials connected by a flat interstitial potential. In complex systems this can arise to problems of continuity at the muffin-tin radii. As can be seen from Figure 2.8(b) the size of the spherical wells in our system vary for the different atomic species. As we truncate the spherical wells to form muffin-tins small steps can develop at r_{mft} between the spherical wells and the interstitial potential. Such steps can have resonant features appearing in our phase shifts. These resonant features often appear as oscillations in the phase shifts. Such oscillations, observed in Figure 2.15, are inaccuracies arising from the modeling process and can lead to inaccuracies in the theoretical LEED IV spectra. Since the interstitial potential has an energy dependence as show above, the flat potential connecting the MT spheres changes as the energy of the incident electron changes. Thus V_{xc}(E) will lead to energy dependent step heights creating more systematic errors in our muffin-tin potential approach. To overcome such systematic errors and to include existing XPS data for surface core-level shifts, Rundgren has proposed an optimized surface-slab excited-state muffin-tin potential from which phase shifts can be calculated [129]. The development presented here follows closely the method proposed by Rundgren.

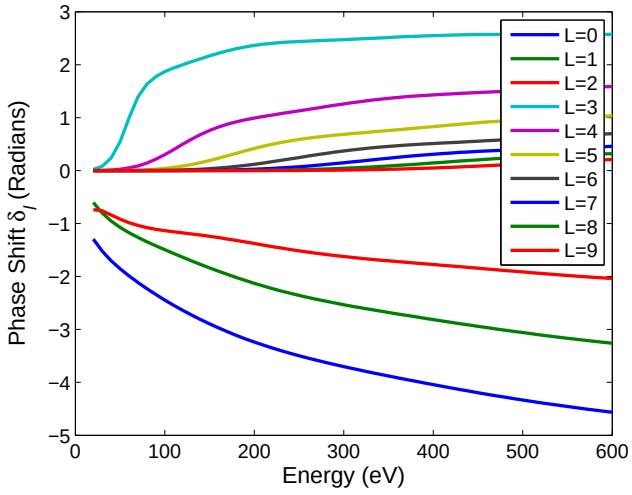

Figure 2.15: Phase shifts for Ru. Phase shifts calculated using MT radii determined from LDA pseudo charge density calculations.

The total potential $\mathrm{U}_i(E,r)$ (where the subscript i distinguishes the different types of atomic sites within the unit cell) for the incident electron beam with primary energy E is written as:

$$U_i(E,r) = V_{fei}(r) + V_{xci}(E,r) \tag{2.69}$$

where $V_{fei}(r)$ is a "fast electron potential," the potential observed by electrons too fast to develop an exchange-correlation hole and V_{xci} is the energy dependent exchange-correlation potential described above. The contributions to the fast electron potential are:

$$V_{fei}(r) = V_{swi}(r) + V_{Mi}(r) + V_{CLi}(r) \tag{2.70}$$

with V_{swi} being the spherical well from the monopolar superposition of free-atom potentials, V_{Mi} is a Madelung correction for nonzero valence and V_{CLi} is a potential correction from empirical surface-core level shifts developed from XPS data. To determine the total potential $U_i(E,r)$ for each site we must consider the atomic sphere at each site as a charge sphere such that the electron density from the superposition of overlapping free-atom densities $\rho_{swi}(r)$, $r < R_i$, accounts for the nuclear charge Z_i and the valence v_i at each site:

$$4\pi \int_0^{R_i} \rho_{swi}(r) r^2 dr = Z_i + v_i \tag{2.71}$$

Thus the interstitial potential between the muffin-tin spheres arises from the charge existing outside the muffin-tin which is still contained within the atomic sphere $r_{mfti} < r < R_i$, i.e.

$$V_{or}(E) = \sum_{i=1}^{N} w_i \int_{r_{mfti}}^{R_i} [V_{fei}(r) + V_{xci}(E,r)] 4\pi r^2 dr \tag{2.72}$$

where the sum runs over the atoms in the surface slab N and w_i is a normalization factor to account for equivalent sites within the surface slab

$$w_i = N_{eq}(i) \left[\frac{4\pi}{3} \sum_{j=1}^{N} N_{eq}(j)(R_j^3 - r_{mftj}^3) \right]^{-1} \tag{2.73}$$

Since $V_{xci}(E,r) \to 0$ as $E \to \infty$ then $V_{or}(E)$ can be separated into its constant and energy dependent components:

$$V_{or}(\infty) = V_{oc} = \sum_{i=1}^{N} w_i \int_{r_{mfti}}^{R_i} V_{fei}(r) 4\pi r^2 dr \tag{2.74}$$

and

$$V_{xc}(E) = \sum_{i=1}^{N} w_i \int_{r_{mfti}}^{R_i} V_{xci}(E,r) 4\pi r^2 dr \tag{2.75}$$

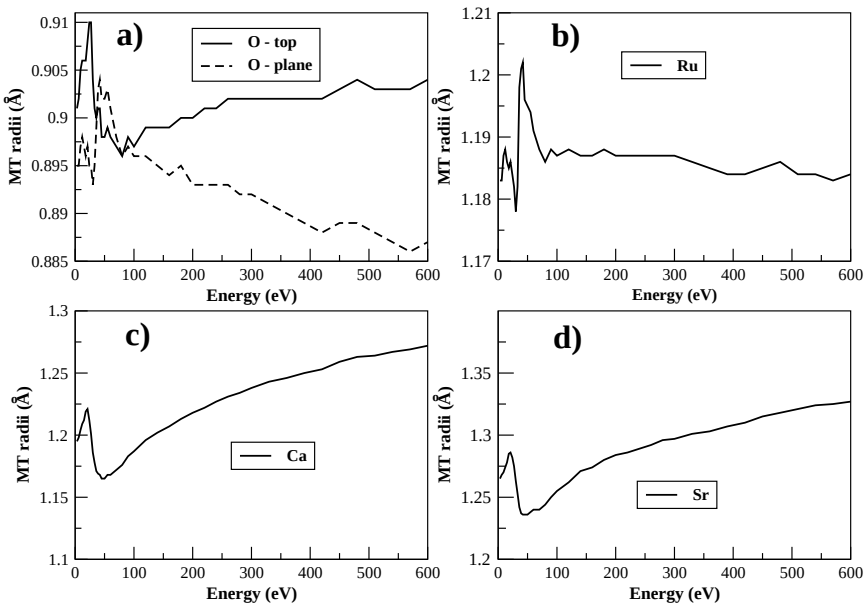

Figure 2.16: Muffin-tin radii generated from Optimized MT method for $Ca_{1.5}Sr_{0.5}RuO_4$. The radii for the different atomic species are shown: (a) O(1) and O(2) (plane and top respectively), (b) Ru, (c) Ca, and (d) Sr.

While the above accounts for the exchange-correlation contribution to the interstitial potential, it also generates an energy dependent potential step at the muffin-tin boundary r_{mft}

$$s_i(E) = U_i(E, r_{mfti}) - V_{oc} - V_{xc}(E) \tag{2.76}$$

To minimize the artificial structure generated in the phase shifts due to the potential step at each muffin-tin boundary, the muffin-tin radii (r_{mfti}) are optimized at each energy E to minimize the potential step $s_i(E)$. The adjustable r_{mfti} alters the limits of the integrals in Equations 2.72, 2.74 and 2.75 and thus the N-dimensional optimization produces optimum muffin-tin radii as well as an optimized interstitial potential $V_{or,optimum}(E)$. Figure 2.16 shows the optimum muffin-tin radii and Figure 2.17 shows the optimum $V_{or}(E)$ generated for $Ca_{1.5}Sr_{0.5}RuO_4$.[†] Figure 2.18 shows the phase shifts for Ru generated by the optimized MT approach and by using the Mattheiss prescription and MT radii generated from LDA calculations. Comparing Figure 2.18(a) with Figure 2.18(b) shows the optimized muffin-tin procedure produces smoother phase shifts than the traditional techniques modified to incorporate r_{mft} generated from LDA charge density calculations.

2.2.6.3 Comparison of Muffin-Tin Radii and V_o vs. $V_o(E)$

To illuminate the importance of incorporating $V_o(E)$ and the effects of MT radii on phase shift calculations structural optimizations were performed on $Ca_{1.9}Sr_{0.1}RuO_4$ data utilizing different methods for calculating phase shifts. The experimental IV used in the comparison was collected at $T = 90K$ and details of the data collection and IV generation can be found

[†]The data presented in Figure 2.16, Figure 2.17 and Figure 2.18(a) were calculated by J. Rundgren. Figures 2.16 and 2.17 were created by V. B. Nascimento.

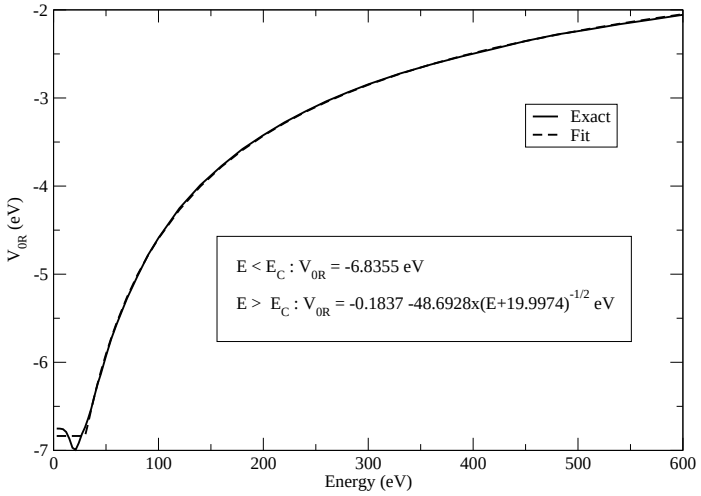

Figure 2.17: $V_{or}(E)$ generated from Optimized MT method for $Ca_{1.5}Sr_{0.5}RuO_4$. The inset shows the fit parameters when fit the the phenomenological form for $V_{or}(E)$.

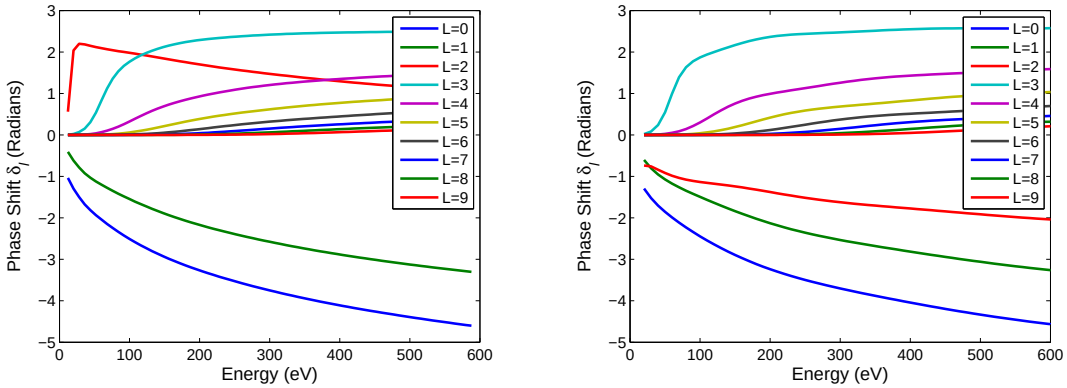

(a) (b)

Figure 2.18: Comparison of Ru phase shifts. (a) Ru phase shifts generated from Rundgren's optimized MT potential method. (b) Ru phase shifts generated from Mattheiss prescription using MT radii generated from LDA pseudo charge density.

Table 2.1: Comparison of different phase shifts. Phase shifts calculated using different methods (see text). Both the LDA MT and Optimized MT methods incorporate $V_o(E)$.

	Traditional	LDA MT	Optimized MT
R_p	0.29	0.24	0.19
RuO_6 Rotation (Degrees)	26	16	15.6
O(1) Tilt (Degrees)	5.1	9.3	8.8
O(2) Tilt (Degrees)	7.2	6.7	6.5
Ru-O(2) Bond Length (Å)	2.08	2.06	2.05
Ru-O(1) c-axis Disp. (Å)	0.032	0.007	0.007
Top Ca/Sr c-axis Disp. (Å)	0.11	0.08	0.07
V_{oc} (eV)	5.0	8.3	8.8

in Section 5.2. The refinements utilized the Rigid RuO_6 Optimization simulated annealing method outlined in Section 2.2.10 with the fit parameters described in Section 5.2 and listed in Table 5.1. All reference models in this Section were calculated from bulk $T = 300K$ coordinates determined from neutron data [70]. The first model (Traditional) used phase shifts calculated the traditional way. Using empirical MT radii listed in Section 2.2.6 phase shifts were calculated using the Barbieri-Van Hove phase shift package [117]. The energy dependence of the inner potential was neglected in this model with both V_{or} and V_{oi} assumed to be constant. While $V_{or} = V_{oc} = 10eV$ was allowed to vary and optimized during the refinement process, $V_{oi} = -4eV$ and remained static during refinement. The second model (LDA MT with $V_o(E)$) incorporated MT radii calculated from first principles calculations described in Section 2.2.6.1. The phase shifts were once again calculated using the Barbieri-Van Hove phase shift package using the newly determined MT radii. In the second model the energy dependence of the inner potential was incorporated in the theoretical model. $V_{or}(E)$ was calculated as described in Sections 2.2.5.2 and 2.2.6.2 while $V_{oi}(E)$ was calculated using the phenomenological form described in Section 2.2.5.1. The third model (Optimized MT with $V_o(E)$) utilized the optimized MT potentials as described in Section 2.2.6.2. The third model also incorporated the same energy dependence of the inner potential as used in the second model. The difference between the second and third models is the method used to calculate the phase shifts. The results from the comparison are shown in Table 2.1.

The importance of using smooth phase shifts and incorporation of the energy dependent inner potential for complex oxide systems becomes clear. The second and third models yield essentially the same structural results however the phase shifts calculated using the optimized MT method have a noticeable improvement in R-factor ($\Delta R_p = 0.05$) over the phase shifts calculated using the Mattheiss prescription and the MT radii calculated from first principles. The dangers of using robust global optimization algorithms with poorly defined crystal scattering potentials for complex oxide systems is realized by the comparison of the Traditional model with the other two. The use of empirical ionic radii and neglecting the energy dependence of the inner potential leads to an pathological and unphysical solution. The phase shifts calculated using the traditional methods have more significant oscillations leading to R_p oscillations of the 14-dimensional hyper-surface in parameter space. While the hyper-surface for the second and third methods are smooth with a well defined minimum, the minimum is still shallow as emphasized in Section 2.2.9. Calculating the R_p by using the solution generated by the third method with the crystal potential generated by the

first method yields $R_p = 0.35$. Oscillations in the phase shifts and maintaining V_o constant yields oscillations of the hyper-surface creating pathological minimums more shallow than the physical solution. While there is little difference between the two hyper-surface minima, the ability of simulated annealing to find the global minimum leads to an unphysical solution.

Based on these results, the solutions presented in Chapter 5 were all determined utilizing phase shifts and $V_{or}(E)$ calculated from the optimized muffin-tin method as described in Section 2.2.6.2. The phenomenological form of $V_{oi}(E)$ present in Section 2.2.5.1 was also employed. Due to the improved accuracy of the crystal scattering potential, no parameter constraints were introduced during the simulated annealing optimization. All solutions presented are true global minimums as determined by simulated annealing.

2.2.7 Renormalized Forward Scattering

Refer to Figure 2.9(b) where the backscattering amplitude for Ru is presented. Backscattering at moderate electron energies is significant and therefore the kinematic approximation (weak backscattering) breaks down and we must address multiple scattering. It is therefore necessary to develop a mathematical formalism for handling multiple scattering of electrons beyond the first scattering event.

The general procedure for calculating LEED spectra is to first calculate the scattering amplitude (or t-matrix) for each atom as described above. The second step is to calculate the 2-dimensional layer-diffraction matrix using the matrix inversion method [140]. Lastly we have to perform multiple scattering calculations to account for the multiple reflections occurring between the layers. While the first two steps are exact in angular-momentum space (l-space), computationally efficient perturbation methods have been developed for interlayer scattering. Since we can describe the scattering in the interstitial regions using a plane wave basis, interlayer scattering is perturbational in k-space. The preferred method for calculating interlayer multiple scattering is the Renormalized Forward Scattering (RFS) method which is much faster than alternate methods such as the Layer Doubling method [114, 115, 116, 141]. Due to the 2-dimensional periodicity within a single layer, there exists a discrete set of beams exiting each layer defined by the plane wave vector $\mathbf{k}$. In the RFS method backscattering is assumed weak (but non-negligible) and the perturbation is based on expanding total reflectivity in terms of number of multiple reflections of the exit beams. As shown in Figure 2.19 the first order perturbation assumes only one reflection from each layer while the second order perturbation assumes 3 reflections of the incident beam between each layer (only under odd number of reflections will the incident electron beam exit the surface). While the method is fast there can be issues of convergence for the perturbation. If the reflectivity of the surface is too high or if the interlayer distance between successive 2-dimensional layers is too small (typically less than 1 Å), the method will fail to converge. In the CSRO system, the buckling of the Ru-O(1) plane and Ca/Sr-O(2) planes due to the tilt of the RuO_6 creates 2-dimensional cation and oxygen layers with little interlayer spacing. The RFS method can still be used if these layers are combined into larger composite layers as outlined in Figure 2.20. Within each composite layer, the exact layer-diffraction matrix is calculated and the perturbational RFS method is used for multiple scattering between composite layers. The combination of single layers into composite layers is computationally costly, but allows for the use of the efficient RFS method for multiple scattering by eliminating the convergence instabilities due to the small interlayer

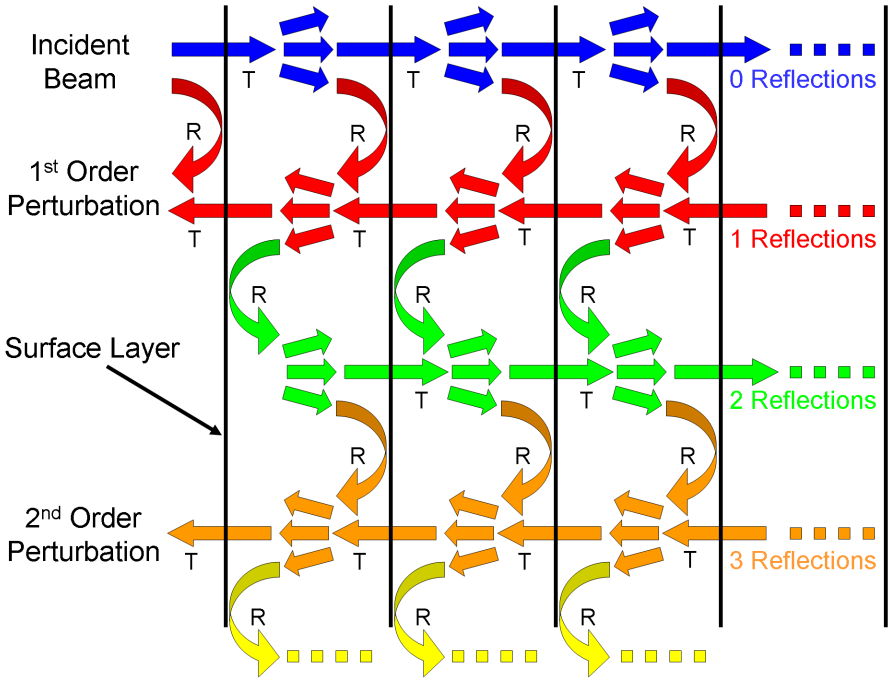

Figure 2.19: Schematic of Renormalized Forward Scattering. Vertical black lines represent layers of the crystal. T and R are transmitted and reflected beams, respectively.

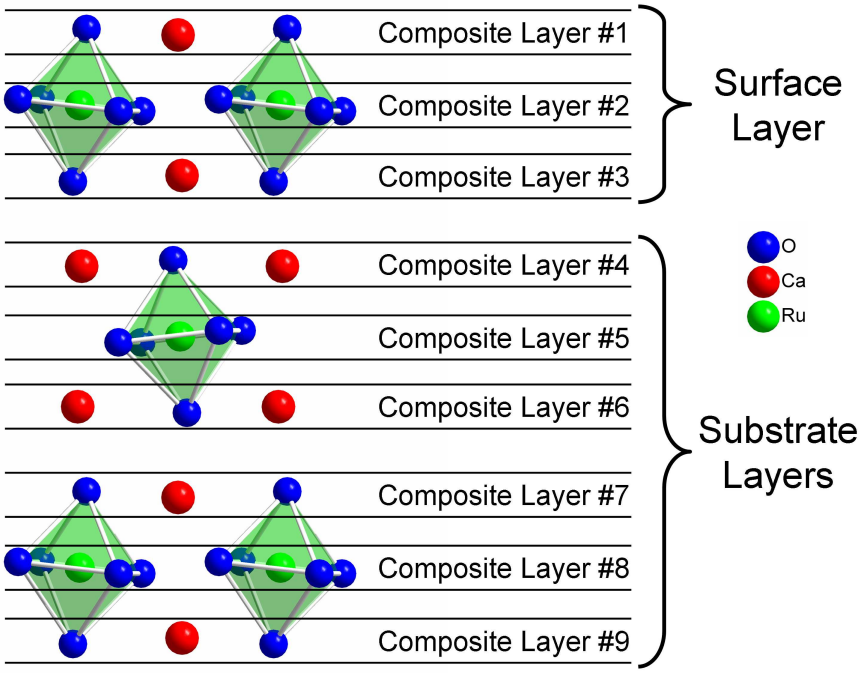

Figure 2.20: Composite layers for LEED calculation. Composite layers for $Ca_{1.9}Sr_{0.1}RuO_4$ are shown.

spacing. Typically the RFS series usually converge after three orders of iterations with 20 penetration layers, but it was necessary to increase the number of penetration layers to 30 to ensure convergence over the wide energy range encountered with the CSRO system.

Since we are addressing a doped system, it is desirable to determine the structure for a wide range of concentrations. The obvious consequence of the doping is that each Ca/Sr site could be occupied either by Ca or Sr. In order to account for the different concentrations the Average T-Matrix Approximation (ATA) method was employed [142, 143]. In this method, the t-matrix for a Ca atom and a Sr atom are calculated at the Ca/Sr site and the two t-matrices are averaged together weighted proportional to the existing concentrations of each atomic species. Such an approximation is a mean field approach in the sense that each Ca/Sr site is assumed identical with the resultant scattering amplitude dependent on the relative cation concentrations. While the ATA approach neglects local effects and inhomogeneities in the concentration, the number of sites probed by the coherent incident electron beam is sufficient enough to assume such local effects would be averaged out in the experimentally observed exit beams.

2.2.8 Tensor-LEED Approximiation

As outlined above, LEED is a trial-and-error optimization procedure. While x-ray diffraction techniques allow for direct methods where crystal structures can be automatically determined from diffraction data, in the present state of LEED, one will always need to start from a best guess model of the surface structure. For this reference structure full dynamical calculations are performed and the theoretical IV spectra are compared to experimentally observed spectra via a reliability factor. Full dynamical calculations are computationally costly and a perturbational tensor LEED (TLEED) approximation has been developed and implemented by Rouse and Pendry [144, 145, 146, 147]. In the TLEED approximation, atomic displacements from the reference structure are assumed small thus distortions to the IV spectra can be determined using perturbation theory. Thus for a trial structure deviated from the reference structure the scattering amplitude A is calculated as a perturbation from the scattering amplitude of the reference structure A_o:

$$A = A_o + \delta A \tag{2.77}$$

the perturbation δA is assumed to be a liner function of the displacement $\delta \mathbf{r_j}$ ($j = 1, 2, \ldots N$ atoms) from the reference structure. To calculate δA we consider the effects of the displacement on the scattering of electrons:

$$\hat{t}_j = t_j + \delta t_j(\delta \mathbf{r}_j) \tag{2.78}$$

where t_j is the t-matrix for the individual atom and δt_j is the change to the t-matrix due to the displacement of atom j. If we consider the exact state of the diffracted electron beam with parallel momentum $\mathbf{k}_{||}$ as $\left|\mathbf{k}_{||}\right\rangle$ for the reference structure, then for the distorted trial structure we have

$$\delta A \approx \left\langle \mathbf{k}'_{||} \right| \delta t_j \left| \mathbf{k}_{||} \right\rangle = \sum_j \sum_{lm,l'm'} T_{j;lm,l'm'} \delta t_{j;lm,l'm'} \tag{2.79}$$

with lm and $l'm'$ as the angular momentum for the reference and trial structures respectively. The advantage of such a formalism is that the tensor $T_{j;lm,l'm'}$, depends on the scattering potential of the reference structure and not on the actual atomic displacements. Hence $T_{j;lm,l'm'}$, acts as a form factor and we can determine the scattering intensity for the trial structure as

$$I \propto |A + \delta A|^2 \tag{2.80}$$

In essence, by calculating perturbations to the atomic t-matrix the changes in the scattering potential of the reference structure are determined without a full dynamical calculation for the atomic displacements of the trial structure. The tensor LEED approximation holds as long as atomic displacements from the reference structure are small ($\delta \mathbf{r}_j < 0.2$Å). The advantage of the tensor LEED approximation is the efficiency in which trial structures are evaluated. Several thousand trial structures can be evaluated in a fraction of the computation time required for one full dynamical calculation.

2.2.9 Reliability Factors

Once the theoretical IV spectra for a reference structure or a trial structure have been calculated, the spectra are compared to experimental IV curves to determine how accurately the model structure IV represents the experimental IV. While it is often useful to plot out both the theoretical and experimental IV curves and compare them visually, more formal and systematic procedures must be employed to reliably determine what model best matches the experimental data. In LEED reliability factors (R-factors) are used to evaluate the goodness of fit between the theoretical and experimental IV. While there are several R-factors developed for LEED and no consensus in the LEED community as to which is the best, the R-factor used in this work is one developed by Pendry [148]. The advantage of the Pendry R-factor (R_p) is the emphasis on relative peak positions and the importance of smaller peaks. Such structure in the IV spectra is a direct consequence of the geometrical configuration of atoms on the surface. Pendry considers both the small peaks and large peaks to be important and wants to treat all peaks and minima with equal weight. To accomplish this weighting the R_p is based on logarithmic derivatives of the IV spectra intensity $I(E)$:

$$L = \frac{1}{I(E)} \frac{dI(E)}{dE} \tag{2.81}$$

When the IV curve is near a minima with $I(E) \approx 0$, a singularity occurs in the logarighmic derivative. To avoid such singularities, a Y function is introduced:

$$Y = \frac{L}{1 + V_{oi}^2 L^2} \tag{2.82}$$

where V_{oi} is the imaginary part of the optical potential that is used to keep the function finite within the range of $\pm 1/2 V_{oi}$. While an energy dependence of $V_{oi}(E)$ is introduced in the calculation of the theoretical IV spectra as outlined above, a constant average value ($V_{oi} = -4eV$) is assumed in the calculation of R_p. For a particular IV beam the R_p is defined as

$$R_p = \frac{\int (Y_{\text{exp}} - Y_{th})^2 dE}{\int (Y_{\text{exp}}^2 + Y_{th}^2) dE} \tag{2.83}$$

where Y_{exp} and Y_{th} are the Y functions for the experimental and theoretical beams respectively. To calculate the total R_p for the set of N inequivalent beams, the R_p for each beam is weighted based on the energy range (ΔE) for the beam:

$$R_p^{Total} = \frac{\sum_{i=1}^{N} (R_p)_i (\Delta E)_i}{\sum_{i=1}^{N} (\Delta E)_i} \tag{2.84}$$

The total Pendry R-factor depends on the number of inequivalent beams and the total kinetic energy range of the LEED data set. Thus a $R_p = 0$ shows perfect correlation between the theoretical and experimental beams and $R_p = 1$ signifies no correlation between the trial structure IV and the experimental IV. The greater number of beams and the larger energy range typically yields the most reliable structural solution, however there is no set rule for what R_p constitutes a "good solution." In general, the LEED community accepts a R_p below ~ 0.3 as a reliable solution for systems containing a few atoms per unit cell. As more complex systems are evaluated with LEED this acceptable value may be raised as the complexity of the system induces more technical and theoretical inaccuracies.

Once a global minimum of the R_p has been determined, the trial structure for the global minimum is taken as the actual surface structure. It is often prudent to run a full dynamical calculation for the best trial structure and rerun the analysis starting from this new reference structure to ensure the convergence onto the global minimum. To evaluate the uncertainty in the LEED-IV analysis the variance of the total R_p is calculated as proposed by Pendry [148]:

$$\sigma = (R_p^{Total})_{\min} \sqrt{\frac{8|V_{oi}|}{\Delta E}} \tag{2.85}$$

where the R_p is for the global minimum and ΔE is the total energy range of the experimental data set. Thus the error bar for each structural parameter in the LEED calculation is determined by the structural deviation from the global minimum required to generate $R_{perror} = R_{pmin} + \sigma$ as shown in Figure 2.21. Reliability factors allow the ability to quantitatively evaluate a particular trial solution. Atomic coordinate deviations from the reference structure are generated to create trial solutions for which the R_p is calculated.

2.2.10 Structural Optimization

The search for the surface structural solution has been reduced to finding the global minimum of the R_p in the N^3 dimensional structural parameter space (3 spatial dimensions for N atoms). While systems with only a few atoms per unit cell the LEED problem can be solved by manually adjusting atomic parameters to map out the R_p hyper-surface in the given parameter space. As systems become more complex, the size of the structural parameter space quickly becomes too large for manual optimization. For $Ca_{1.5}Sr_{0.5}RuO_4$ there are 56 atoms per unit cell. Due to the layered structure, the first iteration of the LEED structural analysis assumes only the top layer (14 atoms) relax and/or reconstruct due to the broken symmetry at the surface. While this assumption greatly reduces the number of fit parameters, there still exists a total of 43 fit parameters (14x3 structural fit parameters + V_{oc}). With such a large dimensional parameter space, pathological solutions with physically

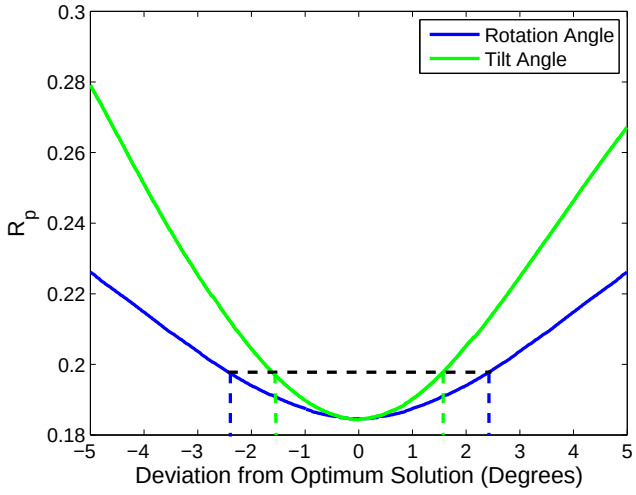

Figure 2.21: Error associated with R_p. Error for RuO_6 rotation and O(2) tilt angles.

unrealistic structures can easily result. To increase the accuracy of the final solution and to reduce the number of fit parameters methods have been developed to take advantage of the observed surface symmetry to restrict the motion of the surface atoms. Taking advantage of symmetry operations such as mirror-planes and n-fold rotation axis observed in the LEED pattern, the fit parameter space can be greatly reduced and generated trial structures are required to maintain the symmetry observed in the LEED pattern. Such constraints allow the use of minimum seeking search algorithms to automate the search process and minimize the acceptance of pathological and unphysical solutions. Current methods employed in the SATLEED codes takes advantage of symmetry operations within a 2-dimensional layer and have a variety of search algorithms to automate the process. Unfortunately, the current state of the codes does not allow for glide plane symmetries and the symmetry operations are only defined for the surface overlayer. In the CSRO system, the RuO_6 octahedral is considered as a semi-rigid body and as can be seen from Figure 2.20 the octahedral extends through three composite layers with the second composite layer having a glide plane symmetry. While the Sr_2RuO_4 system has a $\sqrt{2} \times \sqrt{2}$ $R45°$ reconstruction involving the static rotation of the RuO_6 octahedra [101], such a rotation can be viewed as a surface analog to the surface layer of the $I4_1/acd$ symmetry. For all the other members of the CSRO family, a p(1x1) reconstruction is observed indicating that the surface symmetry is identical to the bulk where only non-symmetry breaking relaxations are allowed. Thus we can take advantage of the symmetry of the bulk to reduce the search parameters and use global search algorithms to find the structure of the surface.

2.2.10.1 Coordinate Calculations and Group Symmetry

To outline the construction of the structural optimization algorithms lets consider the surface structure of $Ca_{1.9}Sr_{0.1}RuO_4$. From neutron scattering experiments the bulk structure has been solved [70]. The bulk forms according to space group *Pbca* as shown in Figure 1.6. The bulk structure is well described by a static rotation plus tilt of the RuO_6 from the *I4/mmm* structure found in Sr_2RuO_4. However, the c-axis coordination of the rotations and tilts from layer to layer is well defined and the unit cell encodes the positions for two RuO_6 octahedral layers. While the RuO_6 can be considered as a semi-rigid body distortions to the octahedral do exist. First, the tilt axis can be defined in two ways: the tilt angle of the Ru-O(2) bond relative to the c-axis and the tilt angle of the Ru-O(1) basal plane relative to the c-axis. While both tilts are about the same axis in the ab-plane, they can be different according to the *Pbca* symmetry and indeed they are different. In addition, a Jahn-Teller distortion elongates the RuO_6 basal plane such that the O(1)-Ru-O(1) distances are different. This distortion creates two different Ru-O(1) bond distances, which is also allowed by the *Pbca* space group. In addition, the Ca/Sr site is no longer required to have $x = y = 0$ crystal coordinates and indeed the Ca/Sr site moves to relieve strain induced by the RuO_6 tilt. While the *Pbca* space group allows for significant distortions to the RuO_6 and Ca/Sr positions, group symmetry allows us to define the atomic coordinates for the entire system based on a few atomic parameters through the use of symmetry generators. As will be discussed in Section 5.2, the observed LEED pattern for $Ca_{1.9}Sr_{0.1}RuO_4$ shows no symmetry changing reconstruction, therefore bulk-like structural parameters and symmetry generators can be used to define the surface structural fit parameters. Figure 2.22 shows

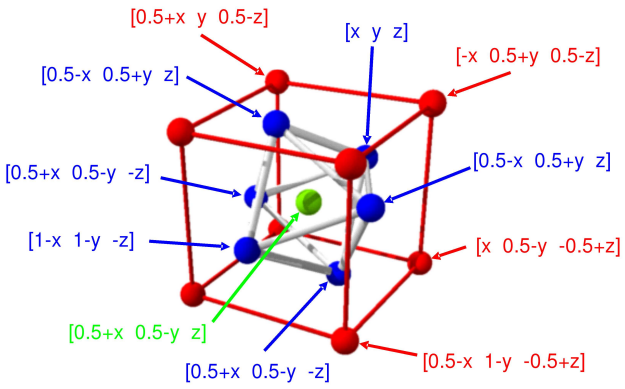

Figure 2.22: Symmetry generators used to define surface layer coordinates. Symmetry generators for $Ca_{1.9}Sr_{0.1}RuO_4$ are listed. Additional symmetry generators used but not shown: Ru [x y z], O(2) [x y z] and O(2) [-x -y -z].

the symmetry generators used to define coordinate positions of a single layer of the crystal system. Based on the allowed symmetry observed in the LEED pattern, two different methods were developed to encode the allowed structural distortions for the surface layer.

The first method (Rigid RuO_6 Optimization) uses the observation that the bulk RuO_6 acts as a semi-rigid body with very minor distortions observed throughout the CSRO family. The surface layer of the bulk unit cell not only contains multiple types of atoms, but each atomic plane and composite layer contains multiple atoms of the same type as shown in Figure 2.20. Since LEED is less sensitive to in-plane atomic distortions, the first method neglects the Jahn-Teller distortion of the Ru-O(1) bonds and treats the RuO_6 as a rigid body. Starting from a bulk terminated reference structure trial structures are generated by allowing rigid body rotations and tilts of the RuO_6 octahedral. One structural fit parameter is assigned to the RuO_6 rotation and all ab-plane O(1) coordinates are generated from a rigid rotation of the RuO_6. While the RuO_6 is rotated the O(1) atoms are assumed to be equidistant from neighboring Ru atoms thus neglecting distorted Ru-O(1) bonds due to the Jahn-Teller effect. Since the O(2) tilts can be different from the basal plane O(1) tilts, two different fit parameters generate the two different allowed tilts. Since LEED intensities arise from Bragg rods, the bulk symmetry along the c-axis can be destroyed without affecting the observed LEED pattern. As such, the apical O(2) positions have an inversion symmetry about the central Ru atom in the bulk but some of the information encoding the inversion symmetry is lost in the LEED pattern. Hence the Ru-O(2) top and Ru-O(2) bottom bond lengths can be different but it is assumed that the O(2) bottom–Ru–O(2) top atoms remain on a straight line. Similarly, the Ru c-axis coordinate and the c-axis coordinate of the O(1) basal plane origin are no longer restricted to be the same. Multiple atoms exist within the unit cell for the Ca/Sr planes and while the a and b-axis coordinates of the top and bottom Ca/Sr planes must be symmetrically defined, coupling is lost between the top and bottom Ca/Sr planes in the LEED pattern and thus a, b, and c-axis coordinates are defined for the

Ca/Sr sites in top and bottom Ca/Sr planes of the surface layer. Symmetry generators are then used to define the coordinates of the second Ca/Sr site within each Ca/Sr plane. Thus the 42 spatial parameters defining the coordinates of the surface layer have been reduced to a maximum of 13 structural fit parameters used in the structural search. The fit parameters are listed in Table 2.2. Due to the layered structure of the crystal and due to the encoding of multiple layers within each bulk unit cell, the question arises as to how broken is the symmetry on the surface? It is noted that the surface layer accounts for $^1/_2$ of the bulk unit cell for the *Pbca* symmetry while it accounts for $^1/_4$ of the bulk unit cell for the $I4_1/acd$ symmetry. To better understand the correlation of surface layer coordinate relaxations to bulk coordinate locks are created to further restrict the fit parameters. Locks are provided to restrict the Ru and O(1) basal plane origin c-axis coordinate to the same value, to restrict the O(1) and O(2) tilts to the same value, and to correlate the a and b-axis coordinates of the top and bottom Ca/Sr planes. Thus the total number of structural fit parameters can be further reduced to 8. Each fit parameter can also be held at a fixed value and not optimized during the search process. Hence the optimization procedures allow from 0-13 structural fit parameters plus an optional non-structural fit parameter for V_{oc}.

A second optimization method (Group Symmetry Optimization) was developed to take full advantage of the symmetry group of the surface layer. The primary difference between the Group Symmetry Optimization and the Rigid RuO_6 Optimization methods is the generation of the Oxygen coordinates. As discussed above, the *Pbca* allows for in-plane distortions of the O(1) basal plane and distortions are observed in the bulk. To investigate the existence of basal plane distortions leading to differing Ru-O(1) bond lengths a, b, and c-axis fit parameters are used to generate the O(1) coordinates. Similarly, additional fit parameter are used to generate the a, b, and c-axis coordinates of the apical O(2) oxygens. To account for the possibility of c-axis relaxations allowing for different inter-planar displacements for the different atomic layers, fit parameters for asymmetric coordinates are also created. While the variation of the c-axis coordinate of the top and bottom Ca/Sr planes allows for motions of the atoms into or out of the surface, the oxygen atoms have an inversion symmetry about the origin of the basal plane and the symmetry generators will only define coordinates maintaining this inversion symmetry. To account for relaxations parallel to the c-axis asymmetric fit parameters are c-axis displacements added to the oxygen coordinates after they are generated by the symmetry generators. To prevent distortions of the apical oxygens, the asymmetric fit parameter is adjusted to ensure the coordinate remains on the Ru-O(2) bond line determined by the symmetry generators. While the Ru symmetry generators defines the Ru atom as the center of the basal plane, motions along the c-axis are allowed without disrupting the observed LEED pattern. Hence, an asymmetric displacement fit parameter is created for the Ru atoms of the surface layer. The Group Symmetry Optimization method allows for a maximum of 16 structural fit parameters and one non-structural fit parameter (V_{oc}) that are listed in Table 2.2. Once again, locks are provided between different fit parameters to better understand the implications of broken symmetry and fit parameters can be held at predefined values allowing anywhere from 0-16 structural fit parameters during the optimization process.

2.2.10.2 Simulated Annealing

The simulated annealing (SA) algorithm used in this work is based on a procedure developed by Corana and implemented by Goffe [149, 150]. Other SA approaches have been applied

Table 2.2: Optimization fit parameters. Fit parameters for both optimization methods used in the analysis.

Rigid RuO_6 Optimization	Group Symmetry Optimization
RuO_6 Rotation (Degrees)	O(1) a-axis Crystal Coord. (x)
O(1) Tilt (Degrees)	O(1) b-axis Crystal Coord. (y)
O(2) Tilt (Degrees)	O(1) c-axis Crystal Coord. (z)
Top Ru-O(2) Bond Length (Å)	O(1) Asymmetric c-axis Disp. (Å)
Bottom Ru-O(2) Bond Length (Å)	O(2) a-axis Crystal Coord. (x)
Ru c-axis Disp. (Å)	O(2) b-axis Crystal Coord. (y)
O(1) Basal Plane c-axis Disp. (Å)	O(2) c-axis Crystal Coord. (z)
Top Ca/Sr a-axis Crystal Coord. (x)	Top O(2) Asymmetric c-axis Disp. (Å)
Top Ca/Sr b-axis Crystal Coord. (y)	Bottom O(2) Asymmetric c-axis Disp. (Å)
Top Ca/Sr c-axis Crystal Coord. (z)	Ru Asymmetric c-axis Disp. (Å)
Bottom Ca/Sr a-axis Crystal Coord. (x)	Top Ca/Sr a-axis Crystal Coord. (x)
Bottom Ca/Sr b-axis Crystal Coord. (y)	Top Ca/Sr b-axis Crystal Coord. (y)
Bottom Ca/Sr c-axis Crystal Coord. (z)	Top Ca/Sr c-axis Crystal Coord. (z)
V_{oc} (eV)	Bottom Ca/Sr a-axis Crystal Coord. (x)
	Bottom Ca/Sr b-axis Crystal Coord. (y)
	Bottom Ca/Sr c-axis Crystal Coord. (z)
	V_{oc} (eV)
Maximum Fit parameters = 14	Maximum Fit parameters = 17

to LEED but they all stem from the same idea set forth by Kirkpatrick [151]. The method uses thermodynamic principles to determine the likeliness of a solution to be the global solution. To start one must define a vector $\mathbf{X}$ containing the fit parameters x_i and initial step lengths for each parameter $\mathbf{V} = v_i = \delta x_i$. The function minimized during the process is the Pendry R-factor (R_p) described in Section 2.2.9 which is used to evaluate how correlated IV spectra for a particular trial solution is to the experimental data. In the SATLEED code one must define a perturbation to a reference structure by defining coordinate deviations for each atomic position in the overlayer. To maintain symmetry coordinate deviations are determined by the two methods described in Section 2.2.10.

An initial R_p function evaluation is calculated $f(\mathbf{X}) = R_p(x_i)$ starting from the reference structure (or some predetermined trial structure). Trial solutions are generated by varying one of the fit parameters $f(\mathbf{X}') = R_p(x_i')$ where $x_i' = x_i + r * v_i$ and r is a random number [-1 1]. The initial step lengths (v_i) used in the procedure are defined depending on the type of fit parameter: Angles = 2°; Crystal Coordinates = 0.02; Coordinate Displacements = 0.05Å. If $\Delta f = f' - f < 0$ the new trial solution is accepted as the starting point for the next iteration. If f' is the minimum R_p found thus far, it is accepted as the current global solution. If $\Delta f > 0$ then the acceptance or rejection for the trial solution being the starting point for the next iteration is based on the Metropolis criterion:

$$P = e^{-\Delta f/T} \tag{2.86}$$

P is compared to a uniformly distributed random number P' and if $\Delta P = P - P' > 0$ then the point current is accepted as the new starting point from which steps (v_i) are taken and the algorithm moves uphill starting from a solution with a R_p greater than the current global solution. After a user determined number of iterations ($N_S = 20$) for each fit parameter, the step lengths are adjusted in attempts to make 50% of all steps accepted. The process continues for another N_S iterations before another step length adjustment is made. Two factors influence the probability of an uphill move, the temperature T and Δf which depends on the step length. After a user determined number of step length adjustments ($N_T = 5$), the temperature is reduced by a user defined reduction factor $T' = r_T * T$ ($r_T = 0.5$). As the temperature is reduced, an uphill trial solution is less likely and thus the step length gets reduced. The process continues until the temperature is low enough shrinking the step size until all functional values from two successive temperature reductions are within a user defined limit $R_p = R_{pmin} + \varepsilon$ ($\varepsilon = 0.0001$) of the global optimum.

Global optimization methods including simulated annealing have been previously applied to LEED structural searches with success [152, 153, 154]. As outlined in Section 2.2.6.3 caution must be taken as inaccurate models of crystal scattering potential for complex systems combined with numerous fit parameters can lead to pathological and non-physical structural solutions. The robust nature of simulated annealing for finding global minimums does not guarantee the correct physical solution will be found. More accurate models of the scattering potential will help ensure the correct physical solution is found but steps must be taken to ensure the optimum solution is indeed the physical solution. The Traditional method outlined in Section 2.2.6.3 generated pathological solutions which were easy to identify. The inaccuracies in the model scattering potential generated fluctuations in the R_p hyper-surface. Many different global minimum solutions were created by locking various fit parameters or holding a particular fit parameter at a certain value. Different global minimums were also created by manually varying non-structural parameters such as V_{oc} and

Debye Temperatures. The idea of different global minimum solutions means that no identifiable correlation is observed between the solution generated with all fit parameters free and the solution generated with the constrained fit parameters. For example, using the Traditional method of Section 2.2.6.3 and optimizing the structure by constraining $V_{oc} = 10eV$ generated significantly different RuO_6 tilt values (difference $> 3°$) and RuO_6 rotation value (difference $> 9°$). In contract, attempting the same exercise with the Optimized MT potential approach yielded the same structural solution with only a slightly degraded R_p. When one parameter was constrained, all other parameters still yielded similar values compared to the case where all parameters were free. Several different combinations of structural and non-structural fit parameters were used to test the robust nature of the results presented in Chapter 5. The Optimized MT potential approach presents itself as an accurate model of the true crystal potential as only one structural solution was evident with the various combinations of fit parameters used. As such there was no need to set upper and lower bounds for the fit parameters used in the structural searches.

While simulated has been previously applied to LEED, this is the only study employing the method developed by Corana and implemented by Goffe [149, 150]. While this algorithm uses a flat distribution of random numbers which are multiplied by the step length v_i, other algorithms use different probability distributions to accelerate the convergence to the global minimum [153, 154, 155, 156]. Even with a flat random number distribution, the employed method with 14 fit parameters typically found the minimum solution within 25,000 functional evaluations taking ~30 minutes using a 3GHz Pentium IV PC.

2.3 High Resolution Electron Energy Loss Spectroscopy

In the LEED experiment we considered the case of elastically scattered electrons where the electron energy E and wave vector magnitude k did not change during the scattering event. However, not all of the electrons scattered from the surface meet these requirements. Due to the symmetry of the surface, elastically scattered electrons exited the surface in discrete beams that contain structural information about the surface. When a LEED pattern is observed, one will notice a relatively uniform background of intensity which surrounds the discrete beams. The background intensity is primarily due to two major contributions: a) disorder on the surface (a perfect crystal is not a realistic crystal) where the lack of periodicity destroys the in-plane Laue conditions and no formation of a Bragg rod and b) inelastic events where the scattered electron energy and wave vector are not the same as the incident electron. While the elastically scattered electrons contain information regarding surface structure, the inelastically scattered electrons contain information regarding quasiparticle excitations on the surface such as: adsorbate vibrations, lattice vibrations (phonons), surface plasmons, and interband electronic transitions. If we consider a monoenergetic beam of electrons with energy E_i and momentum $\mathbf{k_i}$ incident on the sample surface at an angle θ_i, the electron can be inelastically backscattered into the vacuum with energy E_s, momentum $\mathbf{k_s}$ at an angle θ_s as shown in Figure 2.23. Thus we can rewrite our general conservation laws of Equation 2.4 to reflect the inelastic conditions:

$$E_s(\mathbf{k}_s) = E_i(\mathbf{k}_i) - \hbar\omega_\nu(\mathbf{q}_{||}) \tag{2.87}$$

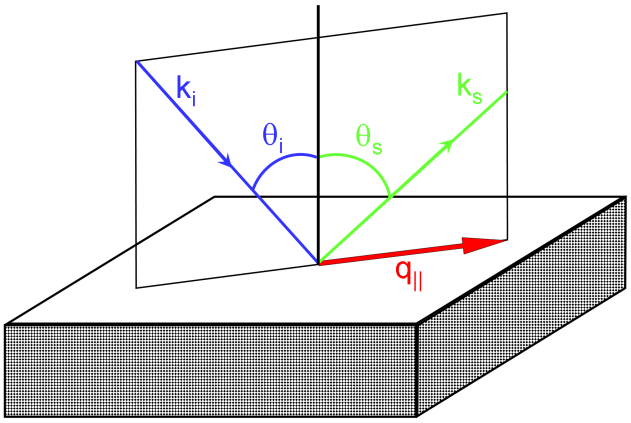

Figure 2.23: HREELS scattering geometry.

where $\Delta E = \hbar\omega$ is the energy of the surface excitation and $\mathbf{q}_{||}$ is the momentum transfer parallel to the surface satisfying our momentum conservation law:

$$\mathbf{k}_{s||} = \mathbf{k}_{i||} - \mathbf{q}_{||} \pm \mathbf{G}_{h,k} \tag{2.88}$$

where $\mathbf{G_{h,k}}$ is a two-dimensional reciprocal lattice vector parallel to the surface. The energy of the excitations are typically in the range of tens of millivolts making the energy losses relatively small. As such, highly monochromatic incident beams and meV energy resolution are required. The technique to study inelastically scattered electrons to understand the dynamics of a surface is known as High Resolution Electron Energy Loss Spectroscopy (HREELS). The energy of the incident electrons is small making HREELS a surface sensitive technique similar to LEED.

A detailed description of HREELS theory is presented in Refs. [157, 158] and only intuitive highlights will be presented here. The most common geometry in a HREELS experiment is to restrict the incident and scattered electrons to a plane and thus only momentum transfer parallel to the incident momentum are measured. This allows us to write down a simple expression describing the momentum transfer parallel to the surface:

$$\mathbf{q}_{||} = \frac{\sqrt{2m_e}}{\hbar}\left(\sqrt{E_i}\sin\theta_i - \sqrt{E_i - \hbar\omega_\nu}\sin\theta_s\right) \pm \mathbf{G}_{h,k} \tag{2.89}$$

From Equation 2.89 one can set a specific momentum transfer by adjusting the incident electron energy along with the incident and scattered angles. Inelastically scattered low energy electrons can be divided into two conceptually different regimes [157]. The first regime, dipole scattering, is described as vibrations excited by the long-range electric field of the incoming incident electron. The dipole interactions can occur prior to or after reflection from the surface but are characterized by forward scattering events. Hence, the dipole scattering results in scattering events observed by a specular geometry where the scattered angle is similar to the incident angle ($\theta_s \sim \theta_i$). The second regime, impact scattering, is inelastic scattering arising from the direct interaction of the incident electron with the

atomic ion cores. The interaction of electrons and ion cores are described in Section 2.2 however, the requirement for elastic scattering events is no longer a constraint. The cross section for inelastic scattering events is a function of the ion core potential and the atomic coordinates of the surface region. Due the differences in the scattering mechanism, selection rules are developed to allow one to distinguish between the two different regimes.

2.3.1 Dipole Scattering Regime

To understand the concept of dipole scattering it is convenient to follow the development set forth by Persson describing the interaction of an electron with a molecule bound to a perfectly conducting surface [159, 160]. The adsorbed molecule with dipole moment μ will interact with the electric field $\mathbf{E}$ at the adsorption site generated by the incident electron and its image charge:

$$U = -\mu \bullet \mathbf{E} \tag{2.90}$$

The scattering cross section (probability of scattering into solid angle $d\Omega$) for a transition from an incident state $|\psi_i\rangle$ to a final scattered state $|\psi_s\rangle$ is given by:

$$\frac{dS}{d\Omega} = \left(\frac{4m\mu e}{\hbar^2}\right)\frac{v_s}{v_i}\frac{1}{\cos\theta_i}\left|2\pi^2\left\langle\psi_s\right|\frac{z}{|\mathbf{x}|^3}\left|\psi_i\right\rangle\right|^2 \tag{2.91}$$

where $\mu = \langle f|\,\mu_z\,|0\rangle$ is the expectation value of the dipole moment operator normal to the surface between the ground state $|0\rangle$ and excited state $|f\rangle$ of the molecule, v_s and v_i are the scattered and incident electron velocities and $z/|\mathbf{x}|^3$ is the dipolar field at the adsorption site generated from the incident electron and its image. For the simplifying case where plane waves are used to describe the incident and final electron states, the matrix element in Equation 2.91 can be written as:

$$\left|2\pi^2\left\langle\psi_s\right|\frac{z}{|\mathbf{x}|^3}\left|\psi_i\right\rangle\right|^2 = \left(\frac{q_{||}}{(k_{i,z}-k_{s,z})^2+q_{||}^2} - \frac{q_{||}}{(k_{i,z}+k_{s,z})^2+q_{||}^2}\right)^2 \tag{2.92}$$

Figure 2.24 shows a plot of the dipole scattering cross section as a function of scattering angle ($\Delta\theta = \theta_s - \theta_i$) for different incident electron energies. It is observed that the dipole scattering cross section is sharply peaked around the specular direction ($\theta_i = \theta_s$) where the cross section quickly becomes negligible for small off-specular angles ($\Delta\theta \geq 2°$). It is noted from Equation 2.91 that only excitations between states with non-zero μ_z will lead to a non-zero cross section. Thus a dipole regime selection rule is established for HREELS: *only vibrations with a dipole moment normal to the surface can be excited.* Conversely, this also means that in-plane vibrations will not be excited by dipole scattering. While the above equations were derived for electrons confined to the half space above the surface, allowing electrons to penetrate the surface generates a $1/k_i$ term indicating that the dipole cross section decays roughly as the square root of the incident energy [157][‡].

[‡]This is contrary to the general trend observed in Figure 2.24 which is presented to emphasize the necessity of small scattering angles.

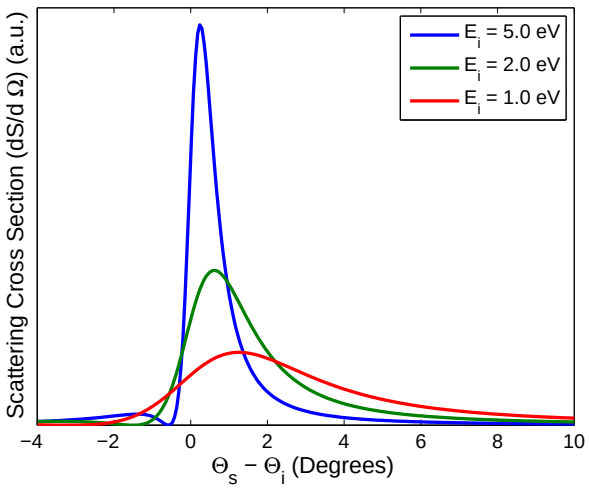

Figure 2.24: HREELS dipole cross section. Cross section calculated for different incident electron energies. Calculation assumes incident angle = 45° and loss energy = $100meV$.

2.3.2 Impact Scattering Regime

In general, impact scattering is not necessarily peaked in the forward scattering direction and can often be observed for large deviations from the specular scattering geometry [157, 161]. Since impact scattering does not have the requirement of $\mu_z \neq 0$, vibration modes not accessible by dipole scattering can still be excited by impact scattering. The impact scattering cross section for a particular vibrational mode Q_v is [157]:

$$\frac{dS(\mathbf{k}_i, \mathbf{k}_s)}{d\Omega} = \frac{mE_i \cos^2(\theta_s)}{2\pi^2\hbar^2 \cos(\theta_i)} A \left| M(\mathbf{k}_i, \mathbf{k}_s; \mathbf{Q}_\nu) \right|^2 \tag{2.93}$$

where A is the surface area of the sample and M is the matrix element given by;

$$M(\mathbf{k}_i, \mathbf{k}_s; \mathbf{Q}_\nu) = \sqrt{1 + n_\nu} \sqrt{\frac{\hbar}{2N\omega_\nu}} \left(\frac{\partial f}{\partial \mathbf{Q}_\nu} \right) \tag{2.94}$$

where N is the number of atoms in the unit cell, n_ν is the number of phonons present and

$$\frac{\partial f}{\partial \mathbf{Q}_\nu} = \sum_{j,\alpha} \left(\frac{\partial f}{\partial R_{j,\alpha}} \right)_0 u_{j,\alpha}(\mathbf{Q}_\nu) \tag{2.95}$$

where α is the Cartesian components, $R_{j,\alpha}$ is the atomic position of the j^{th} atom and $u_{j,\alpha}(Q_\nu)$ is the displacement vector of the j^{th} atom for phonon mode Q_ν. It is noted that the atomic displacements $u_{j,\alpha}(Q_\nu)$ for a particular mode Q_ν contains factors which eliminate the dependence of the cross section on the surface area. Based on Equation 2.95 we can establish a selection rule for impact scattering considering the atomic displacements for a particular mode $u_{j,\alpha}(Q_\nu)$. *If the scattering plane coincides with a mirror plane of the surface, then all modes with atomic displacements odd with respect to the mirror plane will not be excited.* If the symmetry of $u_{j,\alpha}(Q_\nu)$ is odd under reflection in the mirror plane then $\partial f / \partial Q_\nu$ is identically zero causing the cross section to vanish. Odd modes are polarized completely within the surface plane as out of plane displacements will be even under reflection. In general, it has also been observed that higher incident electron energies increase the impact scattering cross section [157]. Hence, by increasing the incident electron energy and moving off-specular, the dipole scattering cross section decreases while the impact scattering cross section increases. By controlling the scattering geometry, one can emphasize the desire scattering regime and excite different vibrational modes.

Chapter 3

Soft Σ_4 Phonons in $Ca_{2-x}Sr_xRuO_4$

Several of the RP compounds exhibit structural phase transitions displacive in character [62, 60]. $SrTiO_3$ and La_2CuO_4 are classic examples where soft phonon behavior drives structural instabilities near the transition temperature. Displacive phase transitions are typically associated with a soft phonon mode that freeze at a critical temperature to become a static lattice distortion [61]. For example, the energy of the Σ_4 tilt mode reduces to zero at the Brillouin zone boundary in La_2CuO_4 at the temperature of the HTT-to-LTO phase transition [60]. The Σ_4 tilt mode lattice vibration involves the rotation (in-plane tilt) of the CuO_6 octahedron about an axis parallel to the ab-plane [162], where the c-axis is perpendicular to the layers. The Σ_4 mode is a transverse acoustic mode of the CuO_6 octahedron. Since $Ca_{2-x}Sr_xRuO_4$ has the same oxygen octahedron structure, and undergoes an HTT-to-LTO phase transition ($0.2 < x < 0.5$), one would expect similar softening behavior in the CSRO family. However, there are significant differences in symmetry for the LSCO and CSRO systems. The CSRO has already undergone a structural transition at $x \approx 1.5$ associated with the in-plane rotation of the RuO_6 octahedral. Thus the HTT-to-LTO transition in CSRO (LSCO) is from space group $I4_1/acd$ to $Pbca$ ($I4/mmm$ to $Cmca$). One obvious consequence of the different space groups is that there is no change in the shape of the Brillouin zone during the HTT-to-LTO phase transition in CSRO.

As Ca is substituted for Sr in CSRO, the smaller Ca cation radius induces local strain in the lattice. To relieve the strain, bulk phonons soften and eventually freeze into a new structural phase[75, 76, 70]. Little is known about the tetragonal-to-tetragonal phase transition in CSRO that occurs at $x \approx 1.5$. The transition is from the space group $I4/mmm$ to $I4_1/acd$, caused by the rotation of the octahedral about the c-axis. It is believed that this transition is a result of the Σ_3 phonon mode reducing to zero energy at the zone boundary for $x \approx 1.5$. This is based on the observation of a soft zone boundary Σ_3 phonon mode in the undoped Sr_2RuO_4 [56]. Although this mode does not demonstrate typical softening behavior with temperature, it is anticipated that the correct temperature behavior would be observed for a Ca concentration closer to the phase transition. For $0.5 \leq x < 1.5$ a second order structural phase transition into the $I4_1/acd$ phase is observed[70, 96]. Although the symmetry is $I4_1/acd$, disorder in the c-axis periodicity of the RuO_6 rotation is observed. Such disorder results in a mixture of the preferred $I4_1/acd$ symmetry with an $Acam$ symmetry. As x is decreased, the disorder in the c-axis periodicity is reduced and a more perfect $I4_1/acd$ phase is formed [70, 96]. The RuO_6 orientations for different structural phases of the CSRO family are shown in Figure 1.10.

3.1 The Neutron Scattering Experiment

Inelastic neutron scattering measurements were performed using the HB1 and HB3 triple-axis spectrometers at the High Flux Isotope Reactor at ORNL and the BT-7 triple-axis spectrometer at the NIST Center for Neutron Scattering. The HB1 and HB3 instrument configuration consisted of a fixed focus PG (002) monochromator and a flat PG (002) analyzer with instrumental collimations of 48'-40'-40'-240,' while the BT-7 instrument configuration consisted of a variable focus PG (002) monochromator and PG (002) analyzer with collimations of open-50'-40'-open. All measurements employed a fixed final neutron energy of 14.7 meV with a PG filter placed in the scattered beam. Samples were mounted in the (hhl) scattering plane and indexed in a manner consistent with the unit cell of pure Sr_2RuO_4. Due to the static RuO_6 rotation a glide plane symmetry is established and the (1.5 1.5 2) Bragg peak (using the *I4/mmm* indexing scheme) is extinguished. This region in q-space corresponds to a zone boundary for both the *I4/mmm* and *I4 1/acd* symmetries. Figure 1.9 shows the relation between the *I4/mmm* and the *I4 1/acd* unit cells. Due to the rotation of the RuO_6 the *I4 1/acd* unit cell is rotated 45° with the side lengths increasing to $\sqrt{2}a$ with respect to the *I4/mmm* unit cell. Hence we can establish the relations between reciprocal space vectors and the indexing scheme for both symmetries:

$$\begin{aligned}
\left[\vec{b}_1\right]_{I4_1/acd} &= \tfrac{1}{2}\left[\vec{b}_1\right]_{I4/mmm} - \tfrac{1}{2}\left[\vec{b}_2\right]_{I4/mmm} \\
\left[\vec{b}_2\right]_{I4_1/acd} &= \tfrac{1}{2}\left[\vec{b}_1\right]_{I4/mmm} + \tfrac{1}{2}\left[\vec{b}_2\right]_{I4/mmm} \\
\left[\vec{b}_3\right]_{I4_1/acd} &= 2\left[\vec{b}_3\right]_{I4/mmm}
\end{aligned} \tag{3.1}$$

and

$$\begin{aligned}
h_{I4_1/acd} &= h_{I4/mmm} - k_{I4/mmm} \\
k_{I4_1/acd} &= h_{I4/mmm} + k_{I4/mmm} \\
l_{I4_1/acd} &= 2l_{I4/mmm}
\end{aligned} \tag{3.2}$$

According to Equation 3.2 the (1.5, 1.5, 2) reciprocal lattice position in the *I4/mmm* symmetry becomes the (3, 0, 4) reciprocal lattice position in the *I4 1/acd* symmetry. However, the Bragg condition for *I4 1/acd* requires for (h, 0, l) that $h, l = 2n$ (where $n = 1, 2, 3, \ldots$) making the (3, 0, 4) position a zone boundary for the *I4 1/acd* symmetry. For consistency and easy comparasion with La_2CuO_4 we will adapt the *I4/mmm* indexing scheme. As the Σ_4 tilt mode phonon energy tends to zero, the ensuing static distortion results in the appearance of this extinguished Bragg peak as this q-space position becomes a zone center for the orthorhombic *L-Pbca* phase. To study the Σ_4 phonon we focus our efforts in the (110)/(001) scattering geometry with measurements concentrated in the region of the extinguished Bragg peak. The Σ_4 phonon propagates in the [1 1 0] direction but the motion of the oxygen atoms due to the static rotation results in mixed longitudinal and transverse components such that the Σ_4 phonon dispersion can be measured in several regions of q-space in the (hhl) scattering plane. Due to the necessity to study both the longitudinal and transverse components, several Brillouin zones were examined. Regions around the (1.5 1.5 2) and (0.5 0.5 6) reciprocal lattice points provided clean Σ_4 phonon measurements due to structure factor considerations.

Single crystalline $Ca_{2-x}Sr_xRuO_4$ samples used in this study were grown using an NEC SC-M5HD image furnace. For feed-rod preparation, a mixture of $CaCO_3$, $SrCO_3$, and RuO_2

with the appropriate molar ratio (i.e. for $x = 0.6$ the ratio was: 1.40:0.60:1.15), was pre-reacted in air at 1000 ^{o}C for 12 h. After regrinding, the powder was pressed into rods and heated in air at 1100 ^{o}C for another 12 h. Single crystals were grown using a feed rate of 30mm/h and a growth rate of 15 mm/h in an atmosphere of 10% oxygen and 90% argon. Shiny black crystals were produced with the correct Ca:Sr concentrations as determined by energy dispersive X-ray analysis.

The neutron beam incident upon our sample in a triple axis spectrometer is generated from a single crystal monochromator. Taking advantage of Bragg scattering, a graphite crystal (PG) is used to generate a monochromatic beam of neutrons. By focusing on the (002) reflection from the PG crystal a single wavelength of neutrons is selected from the Maxwellian reactor spectrum. This Bragg reflection is used as the monoenergetic incident neutron beam with which we perform our scattering experiments. However, since we are taking advantage of Bragg's Law when scattering off a monochromator crystal, we must also consider the consequences of higher order Bragg scattering. If the scattering condition allows for our desired wavelength λ then, higher order wavelengths (λ/N) are also allowed. In our triple-axis measurement we determine counting integration times by setting a fixed number of monitor counts for each data point. The monitor is positioned in the incident beam prior to the sample. As such, the monitor counts include the neutrons from the monochromator with the desired wavelength plus all higher order reflections. Monitor counts from the higher order reflections is a systematic error effectively shortening the neutron count time for each data point. After scattering off our sample, the scattered neutron beam passes through a PG filter to remove the higher order wavelengths prior to reaching the analyzer. The amount of higher order contamination in the incident beam is a function of incident energy due to creating a monoenergetic incident beam from the Maxwellian reactor spectrum. Thus in fixed final energy experiments, the scattered intensities must be corrected for the monitor contamination.

In addition to the monitor contamination from higher order Bragg scattering, corrections must be made for the fixed focused monochromator and analyzer. During the instrument alignment process, elastically scattered Bragg peaks off powder samples and our crystalline sample are utilized. Instrument angles are adjusted in order to achieve the maximum neutron throughput for the Bragg peaks. In addition sample parameters and sample alignment are adjusted to ensure the sample can be translated from one Bragg reflection to another and achieve optimum resolution for all reflections. The neutron optics are designed to maximize the number of neutrons focused on the sample and to maintain optimum instrumental resolution as the sample is rotated from one Bragg reflection to another. However, in the inelastic scattering regime used to study lattice and magnetic excitations, the scattering geometry is altered to establish the desired energy/momentum transfer to the sample. As such, the fixed focal points of the neutron optics are no longer optimally aligned resulting in a smearing of the scattered neutron beam that reaches the analyzer. As a result, the inelastic neutron counts from the analyzer are erroneously altered and the error is dependent on the energy transfer. Measurements have been made at HFIR to determine the effects of fixed focus on the HB1 and HB3 instruments used in these experiments and the inelastic data corrections are shown in Figure 3.1.*

*The HB1 and HB3 instrument correction parameters were determined by HFIR instrument scientists. Codes for calculating intensity corrections provided courtesy of M. D. Lumsden.

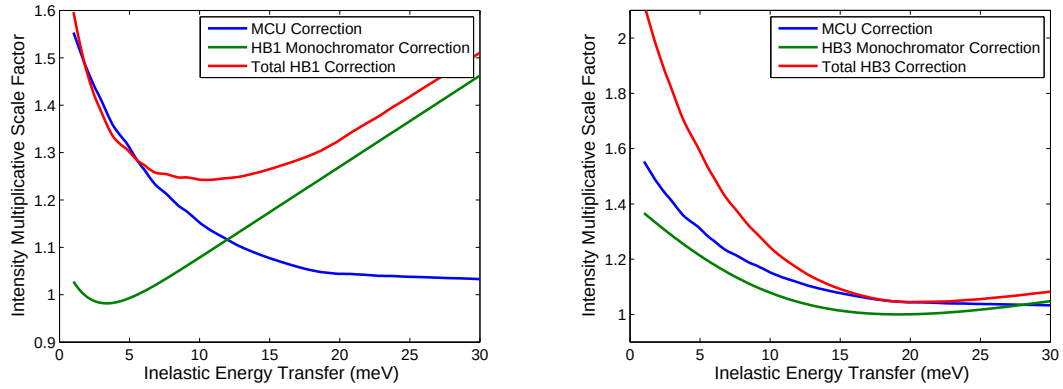

(a)

(b)

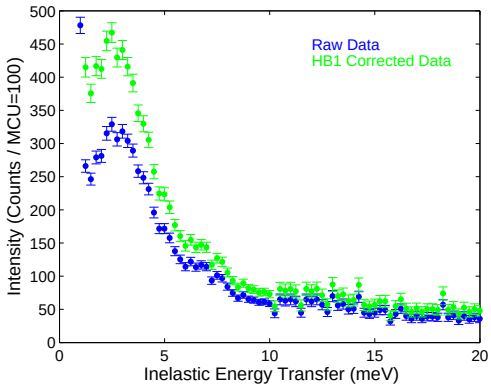

(c)

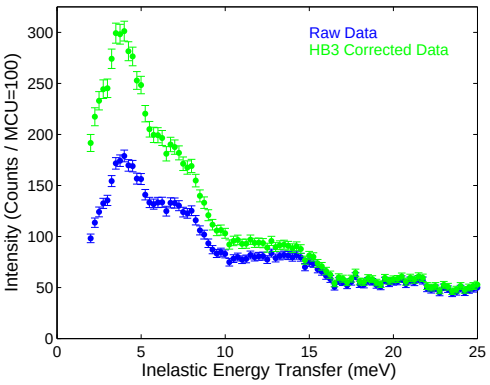

(d)

Figure 3.1: HB1 and HB3 instrument corrections. (a) HB1 instrument corrections. (b) HB3 instrument corrections. (c) HB1 corrected data $x = 0.4$, q =(1.5 1.5 2). (d) HB3 corrected data $x = 0.6$, q =(1.5 1.5 2).

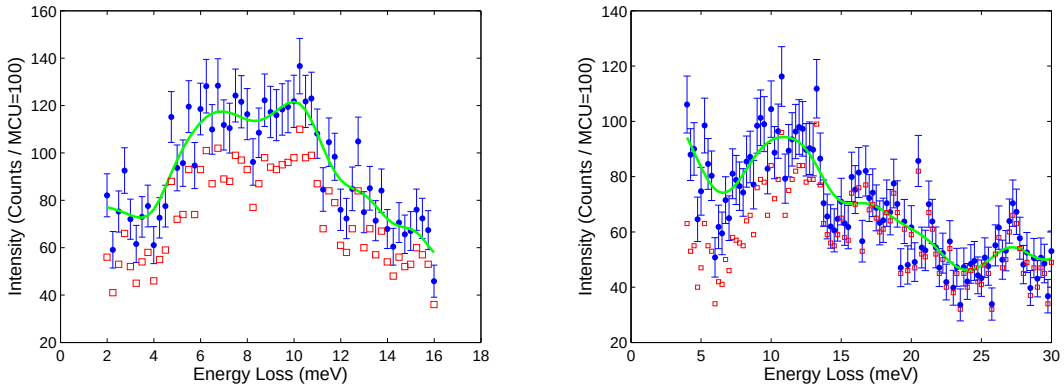

(a) (b)

Figure 3.2: Wavelet denoising of inelastic data. (a) HB1 data for $x = 0.4$ and q =(0.35 0.35 6). (b) HB3 data for $x = 0.6$ and q =(1.6 1.6 2). The red squares are raw data with the blue circles showing data with instrument corrections. The green line shows data after wavelet smoothing.

Phonon dispersion curves were determined by comparing the individual constant wavevector scans to multiple Gaussian peaks. To better estimate the low energy background and instrumental energy resolution, scans through the incoherent elastic peak were combined with inelastic data and a Gaussian assumed for the incoherent peak plus one for each mode observed. To improve the quality of the fits and to allow all fit parameters to be unrestricted during analysis, the data were first smoothed using translation invariant wavelet shrinkage (Haar Wavelet basis) from the WaveLab software package [163]. The wavelet denoising analysis used the Haar wavelet basis with 4 non-vanishing moments ($L = 4$) and soft thresholding ($thr = \sqrt{2 * log(N)}$ where N is the minimum dyadic length to encompass the data). Figure 3.2 shows an inelastic scans for $x = 0.4$ and 0.6 with the smoothed data. While wavelet shrinkage has been proven successful in removing statistical Poisson noise from many different types of data [164, 165, 166, 167], it has never been systematically tested with neutron data. Thus a final fit was performed using monitor and instrument corrected raw data starting from the fit parameters generated with the smoothed data.

3.2 Inelastic Scattering Data for $Ca_{1.4}Sr_{0.6}RuO_4$

Inelastic scattering measurements for $x = 0.6$ were performed on the HB3 spectrometer at HFIR. The sample consisted of a single crystalline rod ($m_{x=0.6} \approx 4g$) with mosaic measured as < 30 minutes indicating a high quality single crystalline sample. Inelastic neutron spectra for (1.5, 1.5, 2), (0.5, 0.5, 6) and (1.25, 1.25, 2) are shown in Figure 3.3. The scans show several spectral features with the lowest energy feature being the Σ_4 mode as labeled in Figure 3.3(a). In addition to the Σ_4 mode, higher energy phonon modes not explored in this work are present plus an extra feature labeled as an anomalous mode in Figure 3.3(a). The anomalous mode appears in all Brillouin zones where the Σ_4 mode is present and its behavior mimics the Σ_4 mode. Figures 3.3(a) and 3.3(b) are at the zone boundary and Figure 3.3(c) is half way to the boundary where the energy of the Σ_4 mode is nearly

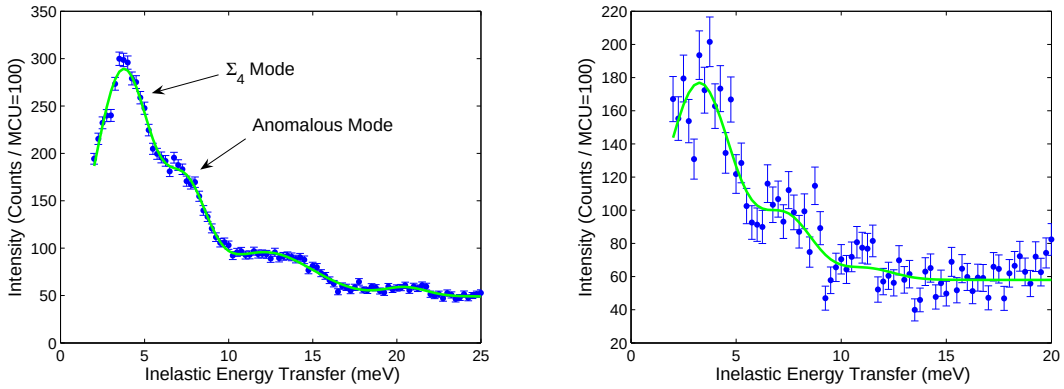

(a)

(b)

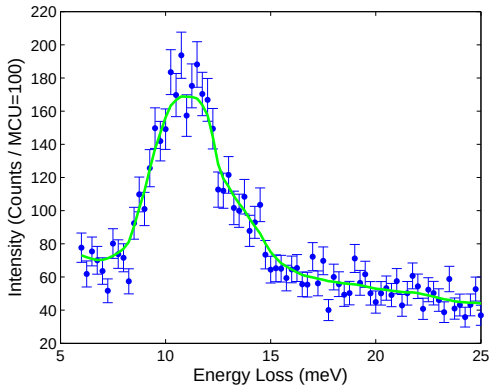

(c)

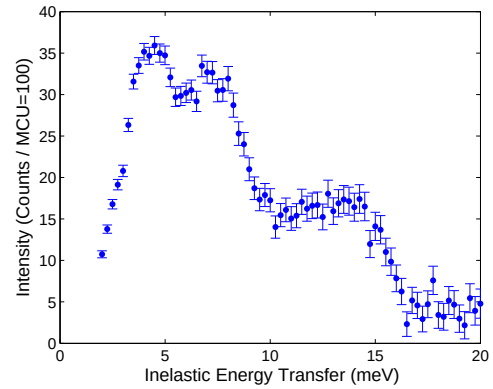

(d)

Figure 3.3: Inelastic data for $Ca_{1.4}Sr_{0.6}RuO_4$. (a) $T = 300K$, $q = (1.5\ 1.5\ 2)$. (b) $T = 200K$, $q = (0.5\ 0.5\ 6)$. (c) $T = 200K$, $q = (0.25\ 0.25\ 6)$. (d) Same data as in (a) with background subtracted and Bose corrected. The green lines are result of wavelet smoothing.

maximum and energy separation of the anomalous mode is small. While the anomalous mode is more obvious in Figure 3.2(b) at q = (0.35 0.35 6), at the center of the Brillouin zone it appears as an asymmetric shoulder on the Σ_4 mode. Near the zone boundary where the two modes are obvious, the Gaussian model phonon width for the $\Sigma_4 = 3.2 \pm 0.3meV$ while the width for the anomalous mode $= 3.4 \pm 0.5meV$. In addition to the asymmetric lineshape, modeling the inelastic peak at the zone center as two Gaussian modes resulted in model widths consistent with the other data points. For reduced wave vector (ζ ζ 0) with $\zeta < 0.2$ the inelastic peak has a more symmetric shape with a width of $\sim 4.2meV$ and thus modeled with a single Gaussian. This anomalous mode is not expected from normal mode analysis and the fundamental reasons for its existence must be explored to fully understand the physics of the system.

To check the homogeneity and purity of the sample the first experiments looked at the temperature dependence of the diffraction spots that should be extinguished due to the glide plane symmetry in the $I4_1/acd$ tetragonal structure caused by the clockwise-anticlockwise in-plane rotation of the octahedra. In the Brillouin zone of the $I4/mmm$ Sr_2RuO_4 parent compound the indexing is (1.5, 1.5, 2). Figure 3.4 shows the normalized scattering intensity, peak width and scattering angle at the location of this "missing Bragg peak." The low temperature data in Figure 3.4(a) is what would be expected for the "central peak" as the temperature is lowered and fluctuations into the near by *Pbca* orthorhombic phase grow [97]. But the constant non-zero intensity at high temperatures combined with the anomalous peak width and incommensurate shifting of the reflection angle indicates a potential problem with the sample. The high temperature data is used to extract a peak shape and then the low temperature data fitted using two Gaussians. Figure 3.5(a) shows the single Gaussian fit at high temperatures and Figure 3.5(b) shows the low temperature data fit with two Gaussians. Assuming the two Gaussian model, the central peak intensity and width are extracted as shown in Figures 3.5(c) and 3.5(d). The data presented in Figure 3.4 can be explained as resulting from a temperature independent Bragg peak and a temperature dependent central peak associated with the structure of the nearby orthorhombic *Pbca* phase. X-ray data suggest a Rutile RuO_2 impurity phase accounts for approximately 2% of our sample [168]. The position of the temperature independent Bragg peak is consistent with the strong [1 2 1] reflection of Rutile RuO_2 and the peak intensity is consistent with the expected 2% impurity phase. The constant intensity and width of the RuO_2 impurity phase Bragg reflection does not change as the HTT-LTO phase boundary is approached suggesting that the impurity phase has no significant effect on the phase transition or physical properties of the sample. The second order character of the HTT-LTO phase transition is evident as one investigates the central peak behavior in Figure 3.5(c). As the phase boundary is approached scattering intensity at the central peak is enhanced. Neutron scattering intensity at the central peak remains near the background level until $\sim 110K$. Below this temperature the central peak intensity increases approximately linearly as the temperature is lowered. Due to the random distribution of the dopant cations, inhomogeneities can create local phase fluctuations. As such, the central peak enhancement is typical for a second order phase transition.

3.3 Inelastic Scattering Data for $Ca_{1.6}Sr_{0.4}RuO_4$

Inelastic scattering measurements for $x = 0.4$ were performed on the HB1 spectrometer at HFIR and the BT-7 spectrometer at NIST. The sample consisted of two co-aligned

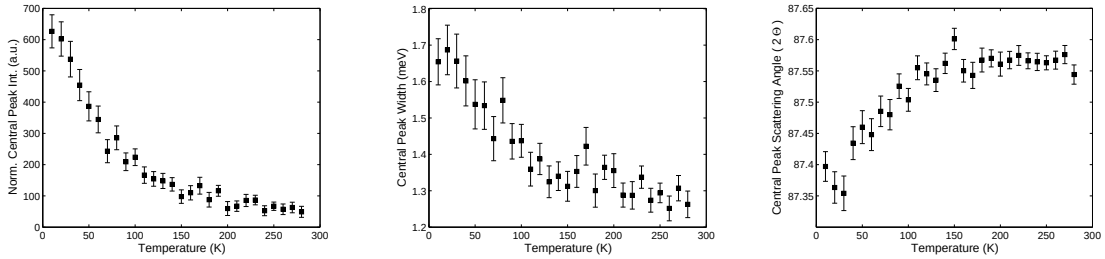

(a) (b) (c)

Figure 3.4: Central peak behavior for $Ca_{1.4}Sr_{0.6}RuO_4$. (a) Intensity normalized to (1 1 2) Bragg peak. (b) FWHM assuming single Gaussian model. (c) Central peak scattering angle.

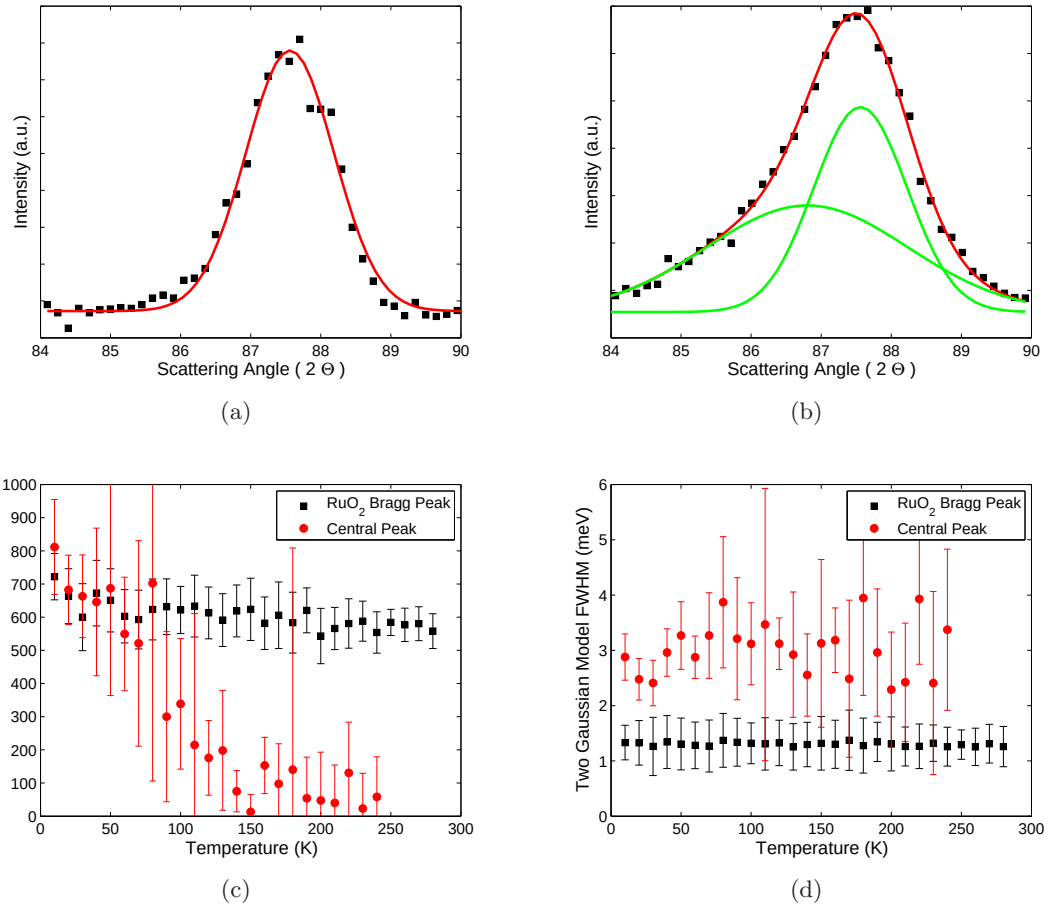

(a) (b) (c) (d)

Figure 3.5: Central peak for for $Ca_{1.4}Sr_{0.6}RuO_4$ with impurity RuO_2 phase. (a) High temperature data with single Gaussian model. (b) Low temperature data with two Gaussian model. (c) Two Gaussian model Intensity. (d) Two Gaussian model FWHM.

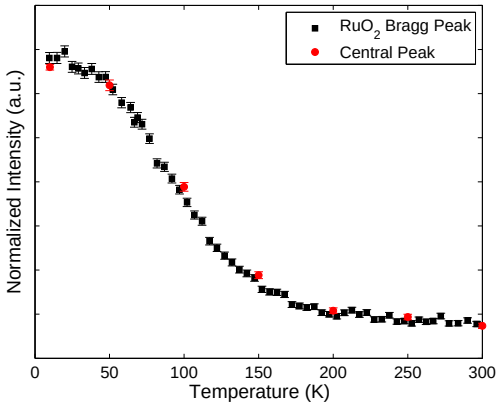

Figure 3.6: HTT-LTO phase transition order parameter for $Ca_{1.6}Sr_{0.4}RuO_4$.

single crystalline rods (total $m_{x=0.4} \approx 3g$) with mosaic measured as <30 minutes after co-alignment of the two rods. Using the (1.5 1.5 2) Bragg peak intensity as an order parameter, it is revealed that the phase transition temperature for our $x = 0.4$ crystal is $T_c \sim 155K$, consistent with previous studies [75, 76, 70]. Investigation of the q =(1.5 1.5 2) reciprocal space position indicated the presence of small amounts of an impurity RuO_2 phase in this crystal as well. The intensity of the [1 2 1] Bragg peak for the impurity phase was much smaller than the previous sample. No x-ray data is available to indicate the extent of the rutile RuO_2 impurity phase, but from the size of the existing Bragg peak it estimated to account for $\sim 1\%$ of the sample volume. No hysteresis for the order parameter is observed consistent with the expected second order phase transition as shown in Figure 3.6.

Constant wave-vector scans for $x = 0.4$ are shown in Figure 3.7. The scans are similar to those for $x = 0.6$ (Figure 3.3) showing several spectral features with the lowest energy feature being the Σ_4 mode as labeled in Figure 3.7(a). Similar to the results from $x = 0.6$, an additional slightly higher energy anomalous phonon mode is also found as shown in Figure 3.7(a). Once again, near the zone boundary the anomalous mode is easily observed but near the zone center it appears as an asymmetric shoulder to the Σ_4 mode as shown in Figure 3.7(b). The dispersion of the two modes can easily be seen from the raw data scans for different wave-vectors throughout the zone as shown in Figure 3.7(c). The anomalous mode still appears in all Brillouin zones where the Σ_4 mode is present and its intensity and wave-vector modulation mimics the Σ_4 mode for both $x = 0.4$ and $x = 0.6$.

Part of the experiment explored the phonon softening in the presence of a magnetic field. A crystal was aligned inside a superconducting magnet in the (110)/(001) scattering geometry. Due to the size of the bore, we were unable to co-align samples inside the magnet so we looked at the largest grain of one of the two crystals used during the softening measurements. The magnet was ramped to 5 Tesla and data compared with those at 0 Tesla. Some inelastic scans show that the only observed affect is a lowering of overall inelastic intensity (Figure 3.8(a)) while other scans suggest a slight down shift ($\sim 1meV$) in the phonon energy (Figure 3.8(b)). However, most elastic scans of the incoherent peak show distortions to the elastic intensity peak (Figure 3.8(c)). While some of the data suggests an interaction between the phonon softening and magnetic field, the consistency throughout the Brillouin zone is questionable and thus inconclusive.

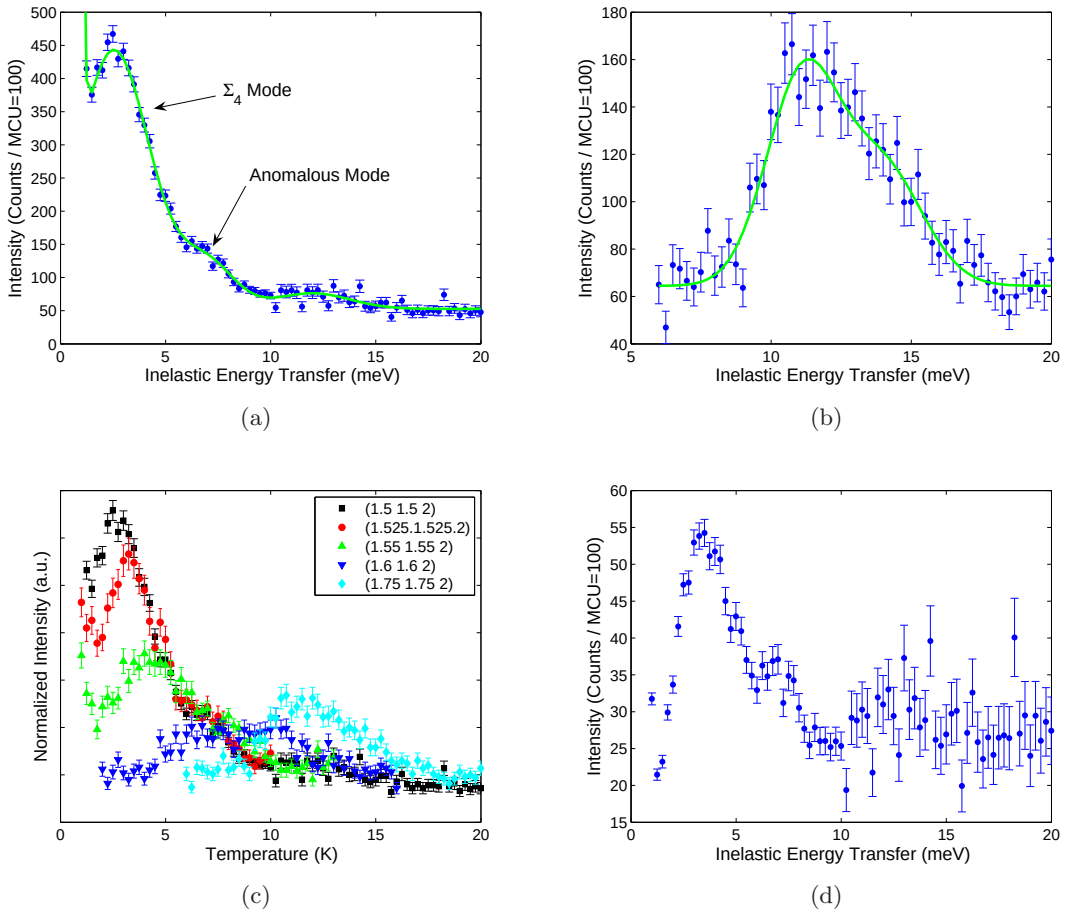

Figure 3.7: Inelastic data for $Ca_{1.6}Sr_{0.4}RuO_4$ at $T = 270K$. (a) q = (1.5 1.5 2). (b) q = (1.75 1.75 2). (c) Raw data at different q showing phonon dispersion. (d) Same data as in (a) with background subtracted and Bose corrected. The green lines are result of wavelet smoothing.

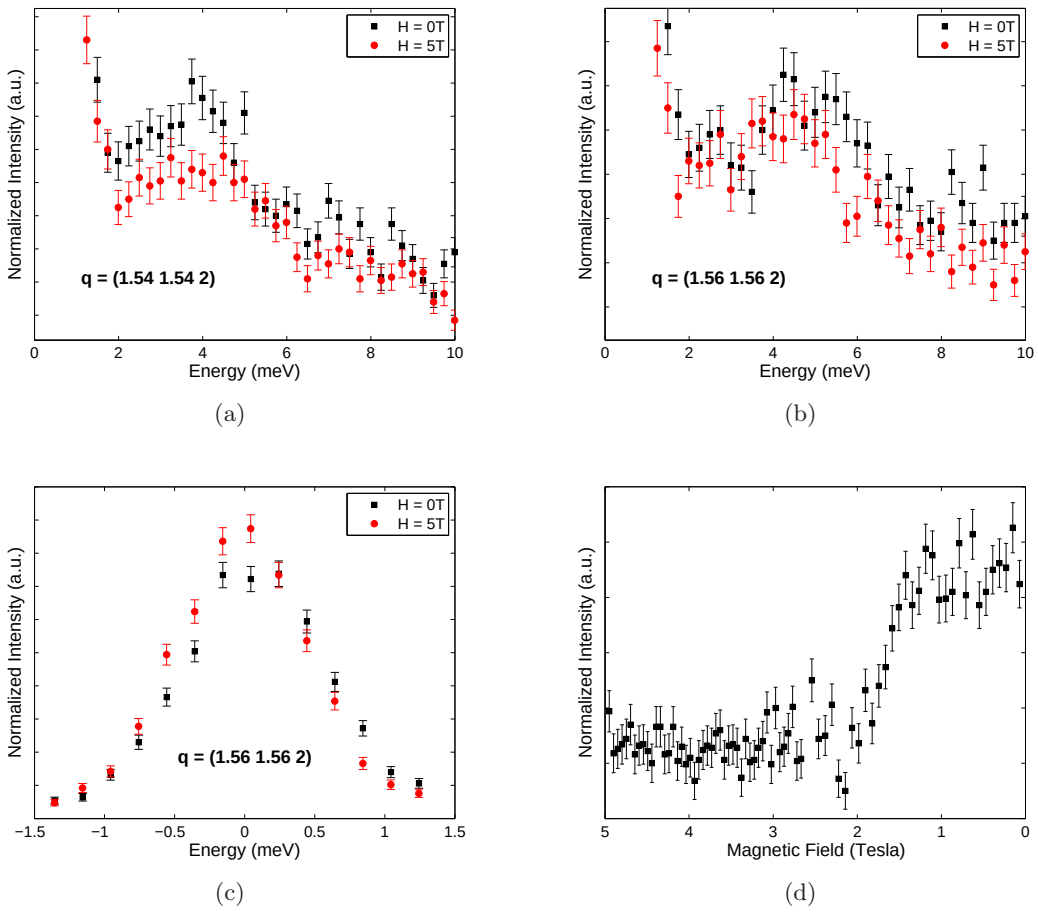

Figure 3.8: Effects of magnetic field on $Ca_{1.6}Sr_{0.4}RuO_4$ at $T = 225K$. (a) Inelastic data at $q = (1.54\ 1.54\ 2)$. (b) Inelastic data at $q = (1.56\ 1.56\ 2)$. (c) Elastic data at $q = (1.56\ 1.56\ 2)$. (d) Ramping magnetic field while counting at $q = (1.5\ 1.5\ 2)$.

As the magnet was ramped down to zero field, the instrument was set up to sit at (1.5 1.5 2) and count (MCU = 10, $\sim$ 15 seconds per data point). As shown in Figure 3.8(d), there is a large drop in scattering intensity at $\sim 1.5T$. It is unclear as to what caused this change. It is likely that the PG filter used to reduce $\lambda/2$ scattering before the analyzer was moved due to the field. The mount was loose and there appeared to be a slight angle when at 5T (although the filter is encased in aluminum). This could be the reason for the distortions to the elastic peak and reduced counts during the inelastic scans. However, if the filter was mis-aligned in the field, then it should let more $\lambda/2$ scattering through (i.e. more of the (3 3 4) Bragg peak should make it through to the analyzer and detector). It this were true, then one would expect the change in counts at 1.5T to be in the opposite direction, more $\lambda/2$ counts making it through at high fields, not fewer counts. The field was parallel to the ab-plane during the entire experiment due to the (hhl) scattering plane alignment. It would be preferred to have the field parallel to the c-axis, but it is not possible to align the crystal with this orientation AND measure the phonon softening simultaneously. Thus the data under magnetic field remains strange and suggestive but questionable and inconclusive.

3.4 Dispersion Results

The resulting measured dispersion for the Σ_4 is shown in Figure 3.9. The dispersion is plotted in the $I4/mmm$ Brillouin zone for comparison with the soft phonon behavior in La_2CuO_4 [60]. Starting from the Γ point in $x = 0.6$ the Σ_4 mode energy increases linearly with wave vector consistent with an acoustic phonon mode. The energy increase continues until the center of the zone where a maximum is reached. While an acoustic mode dispersion would continue to increase reaching a maximum at the zone boundary, the Σ_4 mode reaches a peak energy of $\sim 11meV$ at the zone center and begins to decrease as the wave vector is increased. Such behavior is typical of a soft phonon mode. The Σ_4 energy continues to decrease until near the zone boundary where it reaches a minimum energy of $\sim 3.5meV$ at the boundary for $T = 200K$. In contrast to La_2CuO_4, one immediately recognizes the phonon splits into two distinct modes near the zone center. The dispersion of the anomalous mode mimics the Σ_4 mode starting from the zone center and continuing until the zone boundary. The energy difference between the two modes ($\Delta E \sim 4meV$) remains almost constant throughout the second half of the Brillouin zone. The Σ_4 phonon mode is doubly degenerate with two possible tilt modes around $[0\bar{1}0]$ and [100] and the two distinct modes could be due to a lifting of the phonon degeneracy. While a lifting of the phonon degeneracy is not expected from the tetragonal symmetry of the system the observed symmetry and dispersion of the anomalous mode strongly suggests the Σ_4 mode degeneracy has been lifted. Further zone boundary softening occurs as the HTT-LTO phase boundary is approached via cooling as shown in Figure 3.10. For $x = 0.6$ the Σ_4 phonon energy never reaches zero at the zone boundary as the crystal remains in the tetragonal phase. Once again the anomalous mode follows the Σ_4 behavior with a similar softening, maintaining the constant energy difference between the two modes and both modes showing a $\frac{d\hbar\omega}{dT} = 6.3(7)\mu eV/K$ temperature dependence between $300 > T > 10K$.

A similar dispersion relation is also observed for $x = 0.4$ also shown in Figure 3.9. Once again the Σ_4 energy peaks at $\sim 11meV$ near the zone center and begins to soften as the wave vector is increased. A minimum energy is reached at the zone boundary however, the minimum energies achieved are lower than those observed for $x = 0.6$. Such is to be expected

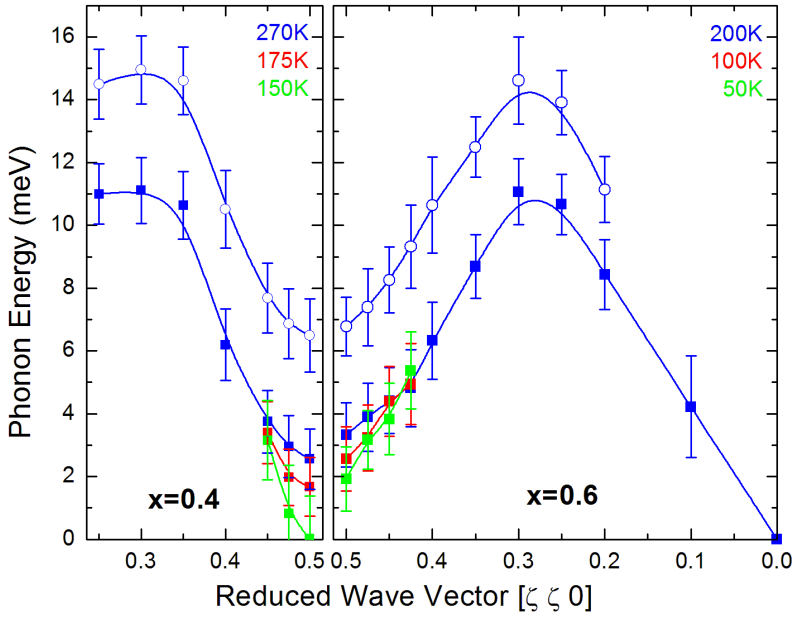

Figure 3.9: Dispersion of Σ_4 and anomalous phonon modes near QCP. The squares represent the Σ_4 phonon mode and the open circles represent the anomalous mode.

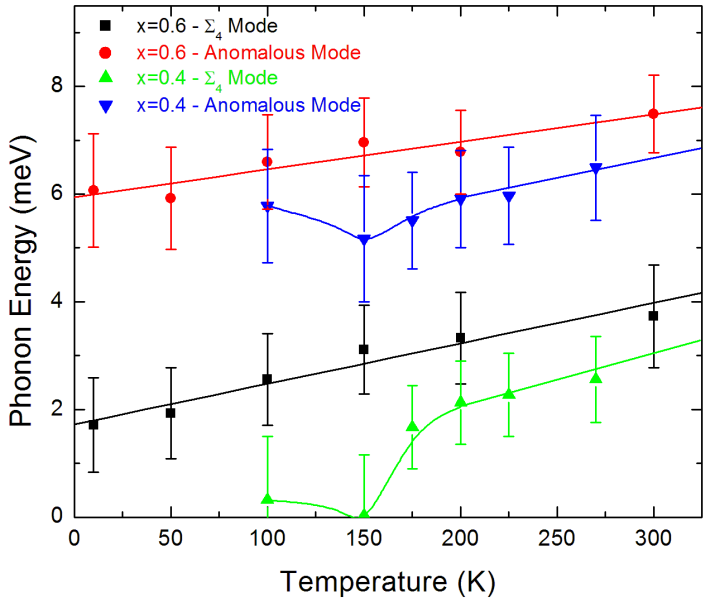

Figure 3.10: Zone boundary phonon softening for the Σ_4 and anomalous modes.

as $x = 0.4$ at $T = 270K$ is much closer to the phase boundary than $x = 0.6$ at $T = 200K$. While $x = 0.6$ never reaches the phase boundary, the significant softening observed even at room temperature shows the instability of the system against the RuO_6 tilt distortion. As the system is cooled, a linear temperature dependence for both modes is once again observed with a slightly larger slope: $\frac{d\hbar\omega}{dT} = 9(1)\mu eV/K$. This liner temperature dependence persists to $T \sim 200K$, below which the softening is significantly enhanced down to $T_c = 155K$. The Σ_4 mode quickly decreases to zero energy at the phase boundary while the upper anomalous mode branch never drops below $5meV$. Remarkably, the anomalous branch maintains the $\Delta E \sim 4meV$ energy difference over the Σ_4 branch down until $T \sim 200K$ below which the anomalous branch flattens out while the Σ_4 branch freezes at the phase boundary.

3.5 Simulation and Discussion

The thesis of O. Friedt [96] reports similar observations for x $\sim$ 0.6, both of the soft Σ_4 phonon mode and the anomalous branch suggesting the anomalous phonon mode is not due to sample problems but is intrinsic to the system. We propose a simple description of disorder, primarily along the c-axis to explain the anomalous mode. As the Σ_4 mode freezes into a static tilt distortion a specific stacking sequence is imposed. It is noted that for $x < 0.2$ the *Pbca* phase shows the preferred c-axis rotation and tilt periodicity is one lattice parameter while the $I4_1/acd$ c-axis parameter is doubled due to the doubled periodicity of the RuO_6 rotation as shown in Figure 1.10. However, if the Σ_4 degeneracy is lifted due to phonon-phonon interactions resulting from a doubling of the c-axis lattice parameter as the octahedra tilts, one would expect that both modes would soften to zero energy across the LTO phase boundary, but this is not the case. It has been observed in 2D systems that disorder can alter phonon softening and prevent the freezing phonon from reaching zero energy at the phase transition[169, 170, 171, 172]. If the anomalous mode is due to disorder in the quasi 2D layered system then one could expect that such a mode would soften to a finite temperature at the phase boundary as the Σ_4 mode reduces to zero energy. The intensity of the Σ_4 and anomalous modes near the zone boundary are similar for $x = 0.6$ as shown in Figure 3.3(d) while the relative intensity of the anomalous mode is significantly lower for $x = 0.4$ as shown in Figure 3.7(d). It is noted that the background has been subtracted and the data Bose corrected for both Figures to reveal the true relative intensities of the Σ_4 and anomalous phonon modes. If the anomalous mode is due to stacking faults, it can be assumed that the anomalous mode intensity is proportional to the number of faults. It has been previously reported that the coherence length for elastic scattering is dependent upon x [70, 96]. While the symmetry for $0.5 < x < 1.5$ is $I4_1/acd$, a coherence length of approximately two unit cells is observed for $x \sim 1.0$ [96]. It has also been observed that as more Ca is added to the system, a more perfect $I4_1/acd$ symmetry forms resulting in fewer faults and an increased coherence length. The disorder in the c-axis periodicity of the RuO_6 rotation can be viewed as a mixing of two symmetries: $I4_1/acd$ and *Acam*. The lifting of the phonon degeneracy is likely due to faults in the $I4_1/acd$ stacking sequence. While inter-layer coupling along the c-axis is assumed weak, it must occur for the well coordinated RuO_6 rotations and tilts to exist along the c-axis. It is noted that the $I4_1/acd$ unit cell encodes the positions for four octahedra layers. In addition, the decreased anomalous mode intensity for $x = 0.4$ is consistent with the existence of fewer faults and a more perfect $I4_1/acd$ symmetry as expected. An orthorhombic splitting is observed as

the system enters the LTO phase due to the induced RuO_6 tilt [70]. For $x < 0.2$ in the *Pbca* phase, lattice elongation is observed perpendicular to the tilt and the Ca/Sr cations move off their high symmetry positions in order to reduce the Ca/Sr-O bond shrinkage [70]. Disorder in the stacking periodicity of the RuO_6 rotation also results in disorder in the tilt axis orientation creating strain at the fault interface altering the Ca/Sr-O interaction across the interface. Such structural frustration could lift the phonon degeneracy near the fault boundary.

For $x > 0.2$, all of the structural phase transitions appear to be second order in character [75, 76, 70]. While the $I4_1/acd$ phase is preferred for $0.2 < x < 1.5$ the question still remains as to how many stacking faults exist in $Ca_{1.4}Sr_{0.6}RuO_4$. Starting from the $I4/mmm$ symmetry, there are two possibilities for establishing the stacking sequence for the system as the RuO_6 is rotated. Although $Ca_{1.4}Sr_{0.6}RuO_4$ is in the $I4_1/acd$ phase, an alternative stacking sequence is encoded by the *Acam* spacegroup. When looking along the [1 0 0] face of the two systems in Figure 1.10, the difference is noted in the handedness of the RuO_6 rotations. Along the face the *Acam* symmetry shows an alternating pattern of clockwise and anti-clockwise octahedron rotation while the $I4_1/acd$ symmetry prefers to have two neighboring octahedral layers with the same handedness. The periodicity of the stacked RuO_6 is doubled in the $I4_1/acd$ symmetry thus doubling the unit cell. Any disorder in the stacking sequence would result in a mixing of the two symmetries. To better understand how layer stacking faults affect the experimental neutron data, LDA calculations and Monte Carlo simulations were performed.

Since the CSRO family is a layered perovskite structure, quasi-2D material properties are anticipated. The question arises as to the effects of stacking faults within the crystalline structure. To better understand the implications of a stacking fault existing within a unit cell, total energy first principle calculations employing the Local Density Approximation (LDA) were utilized. The self-consistent *ab initio* calculations were performed using a plane wave basis with Vanderbuilt ultrasoft pseudo potentials [137]. The model calculation started from the experimental parameters for $Ca_{1.5}Sr_{0.5}RuO_4$ at $T = 300K$ from previously reported neutron results [70]. As a model calculation, all of the Ca/Sr sites were assumed to occupied by Ca. Hence the model system consisted of Ca_2RuO_4 in the $I4_1/acd$ symmetry. Calculations were performed starting with a $20Ryd$ cutoff on a $2 \times 2 \times 2$ Monkhorst-Pack grid. Due to the smaller Ca cation radius, large inward stresses were observed. The unit cell parameters and volume were manually optimized to minimize the observed stresses. After each manual unit cell optimization, the internal coordinates were allowed to fully relax. As a result of the 100% Ca occupation, the optimized unit cell volume decreased $\sim 3\%$ and after the internal coordinates were allowed to fully relax, the RuO_6 rotation increased to $\sim 18^\circ$. It should be noted that while the RuO_6 rotation increased, no tilt was ever induced or observed during any relaxation iteration. After optimization, the total energy of the ideal unit cell was calculated. To simulate a stacking fault, the third octahedral layer was rotated with the same magnitude but with the opposite handedness and total energy calculations once again performed performed. After initial results, the K-point mesh was gradually increased by increments of $\Delta 2 \times \Delta 2 \times \Delta 2$ and subsequently the total energy was systematically increased by $\Delta 5 Ryd$ for each K-point mesh increment. At each iteration, the unit cell volume was once again manually optimized to minimize the stress and the internal coordinates allowed to fully relax. At each iteration step total energy for the ideal and faulty unit cell were calculated. The idea was to optimize the model structure and

perform the calculations for a more accurate energy cutoff and K-point mesh (the goal was a 30Ryd cutoff on a $10 \times 10 \times 10$ Monkhorst-Pack grid), however, the 56 atom unit cell was too large for to be run on our existing PC with the desired parameters. Nevertheless, while fluctuations in the final total energy were observed for each iteration step of the convergence tests, the difference between the total energy for the ideal and faulty models systems never varied more than $\sim 1meV$ with the faulty system always higher in energy. While the calculation should be completed on a larger computer system to ensure accuracy, a final energy cutoff of $25Ryd$ on a $6 \times 6 \times 6$ grid was achieved and the consistency of each iteration step the suggest that stacking faults in our layered system cost very little in total energy. Such a result is not a surprise due to the layered structure, but the question is raised as to how the experimentally observed symmetries exist if randomness in RuO_6 rotations cost so little in energy.

Two different Monte Carlo simulations were performed utilizing two different methods for creating model crystal structures [173, 174]. The first method defined a single RuO_6 layers to construct models. Since the $I4_1/acd$ symmetry defines four octahedral layers, four different layers were created and labeled as A, B, C, and D as shown in Figure 3.11(a). While Figure 3.11(a) shows the preferred orientation for the $I4_1/acd$ symmetry, the $Acam$ symmetry can be constructed by alternating A and B layers or C and D layers (i.e. ...ABABAB... or ...CDCDCD... versus ...ABCDABCD...). Thus the four layers can be stacked together to define both symmetries. Super-cells consisting of $20 \times 20 \times 1$ RuO_6 unit cells were constructed for the four layers. It is noted that Figure 3.11(a) shows a $20 \times 20 \times 4$ super-cell defined using the individual RuO_6 layer method. As individual super-cell layers are stacked along the c-axis a probability P is defined as the probability of the next created layer having the correct orientation relative to the previous layer. Due to the staggered positions of the octahedra, only layers B or D can follow layer A (layer B being correct and layer D having a faulty rotation handedness). Similar inter-layer constraints are established for the other layers to ensure only the rotations change and not the ab-plane positions of the RuO_6. Hence $P = 98\%$ indicates that the next layer created in the model has a 98% chance of being Layer C if the last created layer was Layer B (and a 2% chance it will be Layer A). The idea is to get a crude model for nearest neighbor coupling strength for RuO_6 rotations and see how varying such a coupling strength will affect the experimental data. It is noted that this is a VERY crude model for several reasons: a) an actual coupling strength is not defined, only a probability of generating a layer with a faulty rotation handedness, b) the next layer generated in the model structure only takes into account the previous created layer thus any nearest neighbor coupling is highly asymmetric at best, c) real crystals grow parallel to be ab-plane and not parallel to the c-axis. Despite its crude nature, it is noted that if there existed no structural inter-layer coupling then the RuO_6 rotations would be completely random and assigning $P = 50\%$ for every layer generated should yield the correct structure. Plus if there were perfect coupling, then $P = 100\%$ for every layer generated and a model system with perfect $I4_1/acd$ symmetry is indeed created. Model crystals are thus created by stacking 600 layers and adjusting P for neighboring layers (creating a crystal with dimensions of $20 \times 20 \times 150$ $I4_1/acd$ unit cells). Using this stacking scheme, perfect $I4_1/acd$ and $Acam$ symmetries are created and powder diffraction patterns are simulated as shown in Figure 3.12(a). In addition, setting $P = 50\%$ generates a random stacking sequence also shown in Figure 3.12(a). The scattering angles chosen show that the $I4_1/acd$ and $Acam$ symmetries are easy to identify and completely different from a randomly stacked

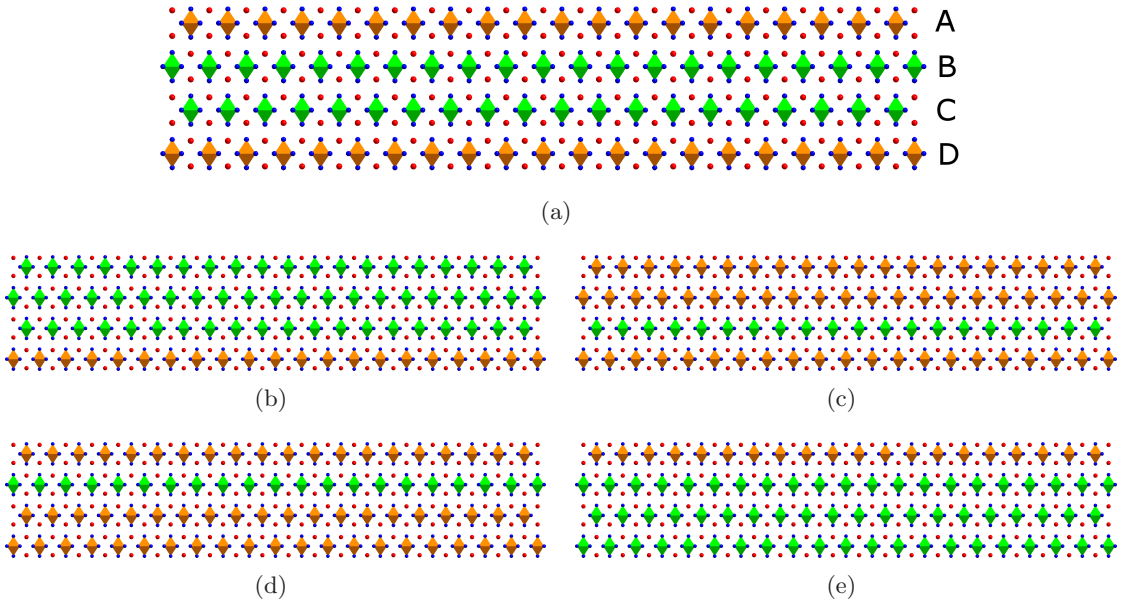

Figure 3.11: Stacking faults for Monte Carlo simulations. All figures show the [1 0 0] face of 20x20x1 super-cells used in the simulations. The green (orange) octahedra show the clockwise (counter-clockwise) handedness of the RuO_6 rotation. (a) Perfect 20x20x1 super-cell showing preferred orientation of the four $I4_1/acd$ RuO_6 layers. Each layer is given a letter designator shown to the right of the respective layer. The other four figures show the super-cell with one faulty layer rotated with the opposite handedness: (b) Layer A rotated with opposite handedness. (c) Layer B rotated with opposite handedness. (d) Layer C rotated with opposite handedness. (e) Layer D rotated with opposite handedness.

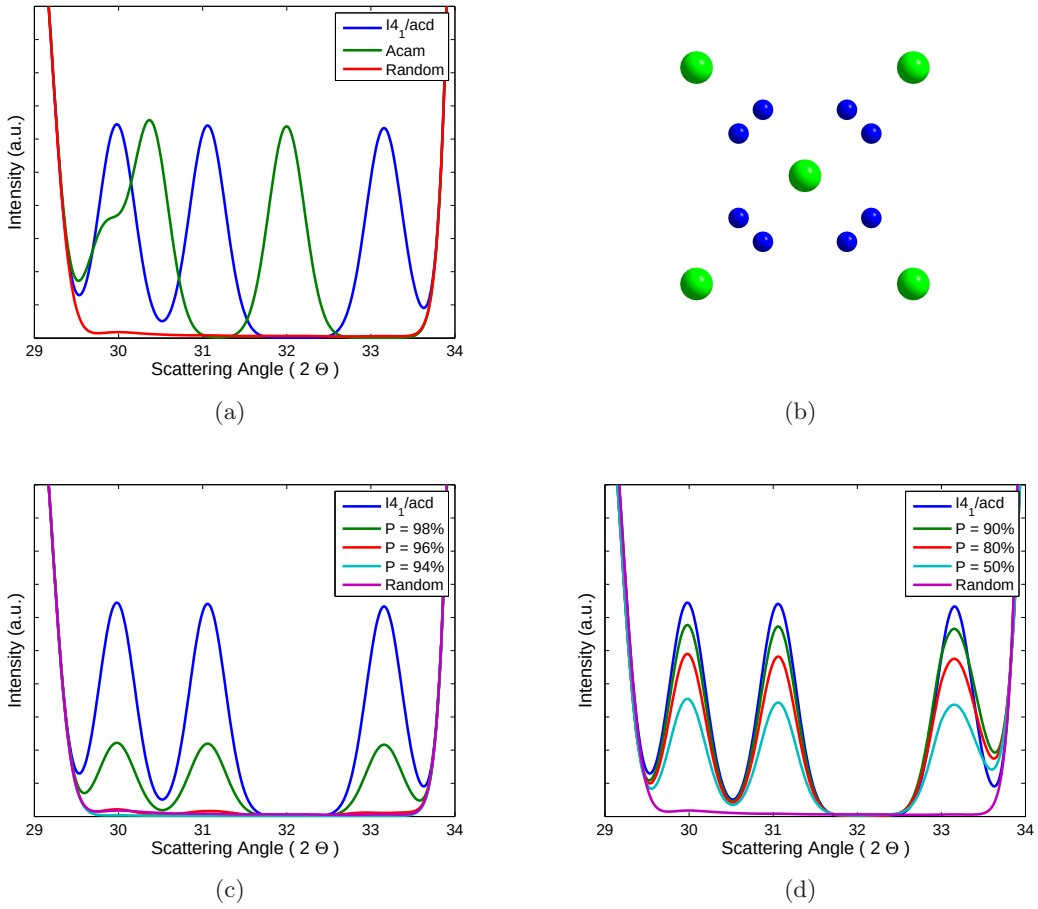

Figure 3.12: Monte Carlo simulations of diffraction patterns. All powder diffraction patterns generated with $\lambda = 1.23$Å, $a = b = 5.34$Å and $c = 25.0$Å. (a) Simulated powder diffraction patterns for different symmetries and randomly stacked RuO_6 layers. (b) Ru-O(1) plane in the *Cmca* symmetry showing the Ru atoms (green) with the O(1) atoms (blue) in the 16*g* Wyckoff positions. (c) Simulated powder diffraction patterns for stacking individual layers (see text). (d) Simulated powder diffraction patterns for stacking individual unit cells (see text).

sequence. The randomly stacked layers lose all O(1) correlations parallel to the c-axis and the diffraction pattern shows a different symmetry. Modeling the random sequence as the *Cmca* symmetry having the O(1) sitting in the 16*g* Wyckoff position with 50% occupancy yields a similar diffraction pattern. While this model for the random sequence is not exactly correct as O(1) correlations in the ab-plane exist within each layer, the net result exemplifies the change in symmetry for the random sequence. To extend the model, different structures were generated by varying P and simulating powder diffraction patterns. Surprisingly, the $I4_1/acd$ and *Acam* symmetries are both easily destroyed when very few stacking faults are generated using this scheme as shown in Figure 3.12(c). For the $P = 98\%$ case, the resulting crystal showed the following stacking sequence character:

....16 Perfect Unit Cells....$CDABCD|CDABCD$....35 Perfect Unit Cells....

with the vertical bar showing the position of the stacking fault. While the entire model crystal is not shown the general character is evident. Around the stacking fault, two *Acam* unit cells are evident (CDCD) with the perfect $I4_1/acd$ unit cells on each side of the fault displaced by 1/2 of a unit cell relative to each other. While the method is not an accurate representation of nearest neighbor coupling, it is suggestive as the existence of the fault does not penetrate into the neighboring domains any further than the nearest neighbor layer away from the fault line. The model suggests that no more than a few percent of the unit cells can be faulty or the $I4_1/acd$ symmetry in the powder diffraction pattern is lost due to the 1/2 unit cell relative shift between neighboring domains.

The above model was generated to test the idea of how nearest neighbor coupling affects the diffraction pattern for the $I4_1/acd$ symmetry. As an alternative, another model system was generated to test for the idea of inter-layer structural coupling extending beyond the nearest neighboring RuO_6 layers. In such a model, the existence of a layer with the wrong handedness does not necessarily destroy the stacking sequence of the entire unit cell. For example, we can start with a perfect $20 \times 20 \times 1$ unit cell super-cell $I4_1/acd$ layer. From this perfect super-cell, we can assume that there exists one layer with the wrong handedness. Since there are four RuO_6 encoded in the $I4_1/acd$ symmetry, then there are four possible layers which can have the wrong handedness. The possible super-cell layers with one layer having the wrong rotation are shown in Figure 3.11. The central idea is that if structural coupling extends for several layers, a single layer having the wrong rotation handedness will not destroy the relative orientations of the other layers within the unit cell. The idea is extended to allow for two, three, or all four layers to have the wrong RuO_6 rotations. Model crystals are generated by stacking the unit cells (each consisting of 4 RuO_6 layers) and defining a probability P of the next unit cell super-cell having the correct stacking sequence. If we assume inter-layer coupling extends beyond the nearest neighbor layers, then the probability of having a unit cell with two faulty layers is less than a unit cell with one faulty layer. Similarly, a unit cell with three faulty layers is less probable than two faulty layers, and so on. Thus $1 - P$ defines the probability of having one faulty layer and the probability of having multiple faulty layers is assumed to be: 2 fault layers $= (1 - P)/2$, 3 faulty layers $= (1 - P)/4$, 4 faulty layers $= (1 - P)/8$. It is noted that four faulty layers is once again the $I4_1/acd$ symmetry simply shifted 1/2 a unit cell from the previous layer, the difference from the previous model being that the relative shift does not extend beyond the single faulty unit cell (unless multiple faulty cells with 4 faulty layers are stacked adjacent to each other). The results for stacking different model crystals by

varying P are shown in Figure 3.12(d). Remarkably, the results are opposite of the previous model, where a significant number of faulty cells can exist without destroying the $I4_1/acd$ symmetry observed in the diffraction pattern. While stacking faults in our real crystals are most likely some combination of the two above models the general conclusion is the same. Stacking faults which shift neighboring domains by 1/2 of a unit cell quickly destroy the observed symmetry. Such faults would be characteristic of nearest neighbor coupling. To maintain the observed symmetry pattern, long range correlations between the large domains adjacent to faults must exist. Inter-layer structural coupling must be present for the $I4_1/acd$ symmetry to exist and the coupling must extend beyond nearest neighboring RuO_6 layers since the symmetry encodes the positions for four octahedral. If no coupling existed, the RuO_6 layers would stack with random rotation orientations and the observed symmetry would be neither $I4_1/acd$ nor $Acam$. While our phonon measurements were taken on a single crystal and no data was taken for a direct comparison between the simulations and experiment. The scattering angles plotted in the simulations can be compared with data existing from previous experiments [70]. Ideally, since the intensity in the peaks defining the $I4_1/acd$ symmetry vary depending upon the number of faults, one could use simulations to perform a quantitative analysis for the number of faults existing within a crystal. However, the above models are more for illustration purposes and further investigations for more accurate representations of stacking faults should be explored.

While arguments have been set forth showing how disorder in the stacking periodicity combined with inter-layer coupling is most likely responsible for the lifting of the Σ_4 phonon mode degeneracy, an alternate explanation exists based on surface structural studies to be presented in Chapter 5. While the arguments regarding disorder and breaking of symmetry in a quasi 2-dimensional system still apply, one must look at the implications of breaking translational symmetry within the ab-plane. The surface structural studies suggest the existence of tilt domains forming on the surface of the crystals. The surfaces of $0.2 \leq x \leq 0.5$ show majority and minority tilt domains as the surface is cooled below the HTT-LTO phase transition boundary. The observed symmetry suggests the minority tilt domains involve RuO_6 tilt axis which lies nearly parallel to the a-axis contrary to the majority tilt domains that have the expected tilt axis near the b-axis. It is possible that the broken symmetry at the surface cause the RuO_6 tilt axis to be ill defined as it is cooled. However, crystals cleaved well below T_c also show the existence of tilt domains. The cleaving of the layered crystal inducing domains of different tilts is very unlikely and the tilt domains observed on the surface are most likely due to tilt domains existing in the bulk prior to cleaving. The existing minority tilt domains probably account for a small fraction of our crystalline sample. A single orthorhombic splitting is observed as the system is cooled suggesting well defined a and b-axis. Thus any RuO_6 tilting around an axis nearly parallel to the a-axis would be in a highly asymmetric configuration and could easily be responsible for the higher energy mode observed. The existence of tilt domains within the ab-plane implies that grain boundaries exist with line defects involving broken octahedra. Since all of the RuO_6 are connected within the ab-plane, breaking an octahedra or removing an octahedra is the only conceivable way for multiple tilt axis to exist. Even if the minority tilt domains make up a small fraction of the crystal, phonon interactions across the broken symmetry of the grain boundary and with the grain boundary itself combined with the crystal distortions at the grain boundary could extend into the majority tilt domains interfering with the propagating Σ_4 phonon also lifting its degeneracy. The existence of a minority tilt phase can be seen

using neutron scattering. As in LEED, within the minority tilt domain the opposite glide line would be destroyed thus creating a central peak at (1.5 -1.5 2). The size of this central peak should give an indication of the fraction of the sample in the minority tilt phase. Since we knew where to look from previous experiments and existing crystallography data to observe the correct central peak and study the softening phonon behavior, looking for non-extinguished Bragg peaks along the opposite glide line was never performed. The LEED results were discovered after the neutron experiments, so the possibility of tilt domains was never checked using neutrons. The literature never mentions tilt domains of different axis for this system, but most crystallography data was performed on powder samples where the minority tilt domain would simply be another randomly oriented powder domain and never appear in the data. Future experiments should explore the possibility of tilt domains.

3.6 Conclusions

In summary, inelastic neutron scattering experiments have been performed to measure the dispersion of the Σ_4 tilt mode phonon near the QCP in $Ca_{2-x}Sr_xRuO_4$ ($x = 0.4, 0.6$). The Σ_4 mode demonstrates typical soft phonon behavior similar to La_2CuO_4, but a new anomalous phonon mode appears. The anomalous mode mimics the Σ_4 dispersion and softening characteristics. Both modes demonstrate a linear temperature dependent softening behavior at the zone boundary. Remarkably the slopes of temperature dependence for both modes are nearly identical and persist until within $\sim 50K$ of the phase boundary. At the phase boundary, the Σ_4 mode quickly softens to zero energy while the anomalous mode never softens below $5meV$ in $x = 0.4$. The nearly identical wave vector modulation and zone boundary softening of the anomalous indicates it is most likely the result from a lifting of the doubly degenerate Σ_4 mode. The lifting of degeneracy is most likely due to disorder in the layered stacking sequence of the crystal. The CSRO family is characterized by two different symmetries with the primary difference being the stacking periodicity of the rotated RuO_6. Both symmetries require some degree of inter-layer coupling to establish the c-axis correlations of the rotations. Simulations show that randomly stacked RuO_6 layers quickly extinguishes powder diffraction peaks which identify both symmetries. The breaking of symmetry at a stacking fault line combined with the existing inter-layer coupling of the rotated layers is most likely responsible for lifting the phonon degeneracy. Previous studies have illustrated the degree of disorder in the stacking sequence for different x in the CSRO family. Relative intensities of the Σ_4 and anomalous modes agree with the previously determined trends. Recently discovered LEED data suggests the possibility of tilt domains existing within the a single ab-plane. While crystal domains of RuO_6 tilting around axis rotated $\sim 90^\circ$ with respect to each other could easily lift the degeneracy of the Σ_4 phonon modes, further studies must be performed to show the extent of tilt domains in our bulk single crystalline sample.

The surface science community has demonstrated the potential effects broken symmetry has on lattice vibrations. As will be shown in Chapter 4 and in previous experiments [102], breaking translational symmetry by the creation of a surface on the CSRO system can increase the lattice vibrational energy by $\sim 5meV$. While the creation of a stacking fault is not the same as creating a surface as all of the crystal field and restoring forces above the fault line are not suddenly removed, symmetry is nonetheless broken. Not only is the crystal field altered by the existence of the fault but the displacement of neighboring

Ca/Sr cations in the rocksalt inter-layer can be severely distorted by neighboring RuO_6 layers tilting around ill defined axis. While no anomalous mode was observed in La_2CuO_4, phases involving simple rotations of the CuO_6 about an axis parallel to the c-axis are also not encountered. In general, the $La_{2-x}M_xCuO_4$ compounds, where M can be Ba, Sr, or Ca, typically do not form phases with c-axis octahedral rotations [31, 32]. However, other similar compounds, like Sr_2IrO_4 and Sr_2RhO_4, do form phases with metal cation octahedral rotations [26, 64, 65]. While disorder in the c-axis periodicity of these other compounds has also been observed the implications of breaking symmetry on lattice dynamics has not been fully explored.

Unusual magnetic behavior has been observed at low temperatures for $0.2 < x < 0.5$ [75, 76, 70, 30, 97, 175, 176]. Theoretical studies have also shown that the rotation of the RuO_6 enhances a ferromagnetic component in the system while the tilt of the RuO_6 enhances an antiferromagnetic component[82]. For the *Pbca* phases ($x < 0.2$) where the RuO_6 are statically tilted, the unit cell periodicity along the c-axis is half of the $I4_1/acd$ periodicity. Thus for $0.2 < x < 0.5$, stacking faults would create a pseudo structural glassy phase as the tilt direction becomes frustrated due to the ill defined c-axis periodicity. Such structural frustration could induce magnetic frustration responsible for the unusual magnetic behavior. In such a system where magnetic and electronic properties are closely linked with subtle changes in structural properties, disorder in structure could easily disrupt the other properties. Further investigation is required to fully understand the role of defects and stacking faults in the CSRO family.

Chapter 4

Surface Lattice Dynamics on $Ca_{1.9}Sr_{0.1}RuO_4$

Discovery of High Tc superconductivity and colossal magnetoresistance in perovskite-like cuprates and manganites has renewed vigor in the experimental and theoretical study of strongly correlated materials [88]. The coupling of charge, lattice, orbital, and spin degrees of freedom in strongly correlated materials leads to competing ground states of similar energy and a rich array of exotic phases. Due to the established links between superconductivity and the Mott metal-insulator transition (MIT) [72, 88], understanding the insulating phase and its fluctuations in the metallic phase has become paramount for understanding coupling mechanisms in these highly correlated systems. The recognition of the importance of electron-phonon (e-p) interaction [177, 178], orbital ordering [84, 86, 87, 88] and reduced dimensionality [179, 180] at the MIT in transition-metal oxides (TMOs) makes MITs fascinating and challenging for both experimentalists and theorists.

Cleaving layered perovskite systems can be used to study correlation effects and possibly new phases by breaking the symmetry (surfaces) without altering the stoichiometry of the sample. The surface of Sr_2RuO_4, an unconventional p-wave superconductor is reconstructed by breaking the translational symmetry [56, 101]. The stress at the surface freezes out a soft bulk zone-boundary phonon resulting in a rotation of the RuO_6 octahedra. It is also observed that the rotation of the RuO_6 octahedra changes the phonon spectrum from the bulk resulting in increased phonon energies [102].

HREELS is a highly surface sensitive technique utilized to probe the electronic and lattice dynamics at the crystal surface [157]. Substitution of isovalent Sr^{+2} with Ca^{+2} distorts the crystal structure without manipulating the carrier concentration. The smaller radius of the Ca cations causes a rotation and tilt of the RuO_6 octahedra from the ideal K_2NiF_4 type structure allowing an opportunity to control the bandwidth of the system [70]. Changing the bandwidth in this highly correlated system creates a wide array of bulk phases from the unconventional superconductor at $x = 2$ to an Antiferromagnetic Mott insulator in bulk crystals for $x < 0.2$ [75]. The bulk MIT temperature strongly depends on doping. In Ca_2RuO_4 the MIT transition temperature (T_c) and the magnetic ordering Neel temperature (T_N) differ by nearly 200K, while for $Ca_{1.9}Sr_{0.1}RuO_4$, T_c and T_N are nearly identical. The rotation and tilt of the RuO_6 octahedra creates an orthorhombic structure with *Pbca* crystal symmetry for both $x = 0.0$ and $x = 0.1$ both above and below T_c.

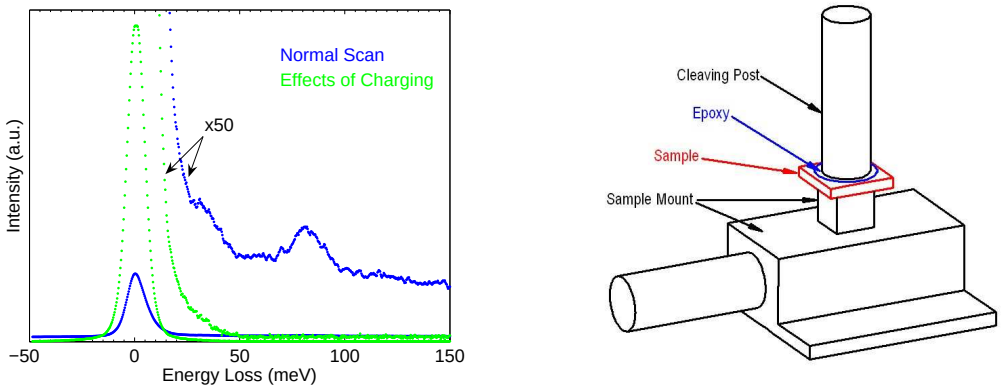

(a) (b)

Figure 4.1: Effects of charging on HREELS data. (a) Comparison of normal HREELS scan with charging peak. (b) Sample stage design to minimize epoxy exposure to incident electron beam after cleaving.

4.1 The HREELS Experiment

In our study we use well-characterized single $Ca_{1.9}Sr_{0.1}RuO_4$ crystals grown by the optical floating zone technique. The crystal is secured to a sample stage using a silver epoxy and an aluminium post attached to the top of the sample using the same epoxy.* After curing the epoxy at 150C for one hour in atmosphere, the sample is placed in a vacuum chamber load lock and pressure reduced to UHV conditions prior to cleaving. The cleaving process involves knocking off the aluminium post while at room temperature thus exposing a new crystal surface while in UHV conditions. The cleaving process produces a pristine [001] crystal surface that has never been exposed to atmospheric contaminants. After cleaving, the sample is transferred to an HREELS chamber and maintained at a base pressure of $2x10^{-10}$ Torr during HREELS measurements.

Charging of the sample and silver epoxy interface appear as a problem during the initial experimental trials. The charging is evident by an order of magnitude increase in HREELS spectral count rate with low counts in a featureless inelastic spectrum as shown in Figure 4.1(a). Charging of similar silver epoxies has been observed before during HREELS measurements of high-temperature superconductors [181]. The problem is avoided by coating the silver epoxy and sample stage with a solution of colloidal suspension of graphite to ensure sufficient conductivity between the sample, epoxy, and sample stage. In addition, a sample stage is designed to avoid epoxy exposure to the incident electron beam as shown in Figure 4.1(b).

Prior to HREELS measurements, LEED images are obtained to ensure the quality of the cleaved surface and the absence of contamination. The surface of the $Ca_{1.9}Sr_{0.1}RuO_4$ crystal has a p(1x1) structure without reconstruction. A detailed quantitative LEED analysis of the $Ca_{1.9}Sr_{0.1}RuO_4$ surface is presented in Chapter 5. HREELS measurements are performed over a temperature range from 300K to 80K. Incident electron energy is $20eV$ and

*Epoxy used was an all solids silver epoxy (H31D) from Epotek. This epoxy was chosen as it is strong and has negligible outgassing in UHV conditions.

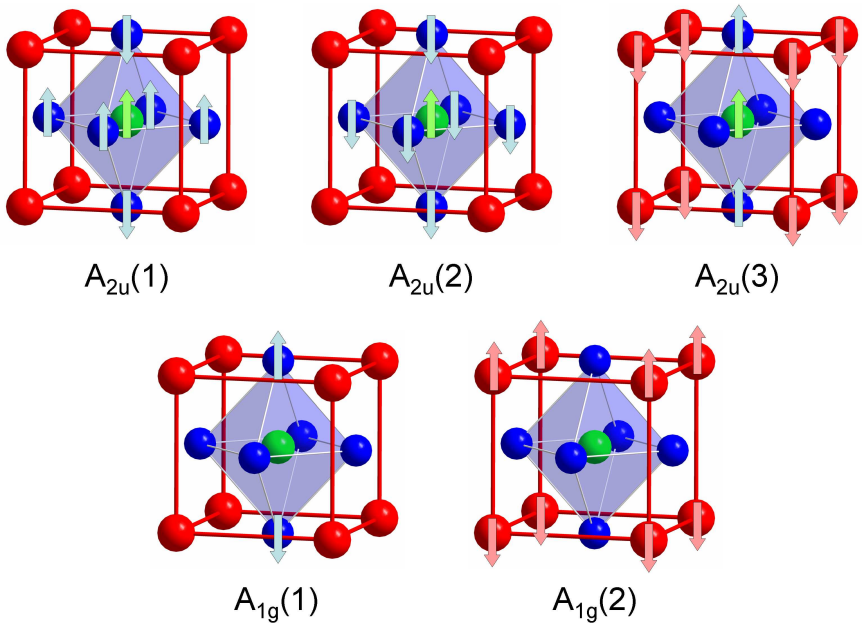

Figure 4.2: Surface dipole active optic phonon modes for K_2NiF_4 structure. Eigenvector for each mode is shown below the respective mode.

all data were taken in a specular arrangement with an incident angle of 45° and instrument resolution of $5 - 7meV$. Similar HREELS analysis of Sr_2RuO_4 reveals four dipole active optical phonons: $A_{2u}(3)$, $A_{2u}(2)$,$A_{2u}(1)$, and $A_{1g}(1)$. The atomic displacements of the four modes are shown in Figure 4.2. Since the instrument is maintained in a specular arrangement, only dipole active modes with atomic displacements perpendicular to the surface are observed. As shown in Figure 4.3, only the A_{1g} mode is visible on the $Ca_{1.9}Sr_{0.1}RuO_4$ surface. Due to the similarity between the Sr_2RuO_4 and $Ca_{1.9}Sr_{0.1}RuO_4$ surfaces, plus the similarity in the observed phonon energies, mode assignment is based on previous Sr_2RuO_4 results [102]. The tilt of the RuO_6 octahedra makes an ill defined a-b crystalline plane in the layered material resulting in rough cleaved surfaces with multiple terraces as observed in an optical microscope compared to the Sr_2RuO_4 surface without a RuO_6 tilt. Although LEED patterns remain sharp, the rough surface creates a wide range of incident electron angles that degrades the inelastic spectrum. As a result, only the strongest A_{1g} mode is apparent and instrument spectral count rate and resolution is reduced. The incident angle can be changed as much as ~ 5 degrees without significant loss in the spectral count rate. To minimize the number of terraces created during the cleave process, small crystals (typically $\sim 3mm$) were used in the analysis. Cleaving smaller crystals yielded smoother surfaces with fewer observable terraces and improved instrument resolution.

4.2 HREELS Results

Typical HREELS data for various temperatures are shown in Figure 4.4. HREELS directly probes the dielectric response of the surface through quasi-particle excitations such as phonons and plasmons plus intra-band transitions in a Drude metal. The changes in

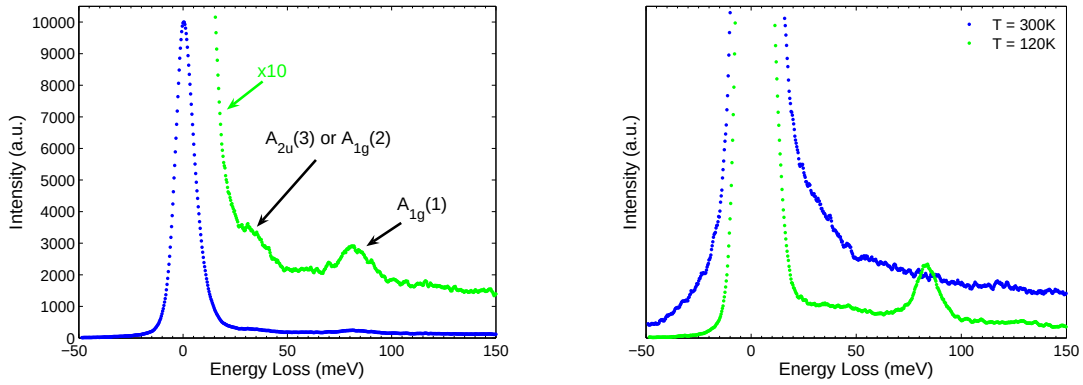

(a) (b)

Figure 4.3: HREELS raw data. (a) Data at $T = 200K$ showing observed phonon modes. (b) Data at $T = 300K$ and $T = 120K$ emphasizing decrease in Drude weight as temperature is lowered.

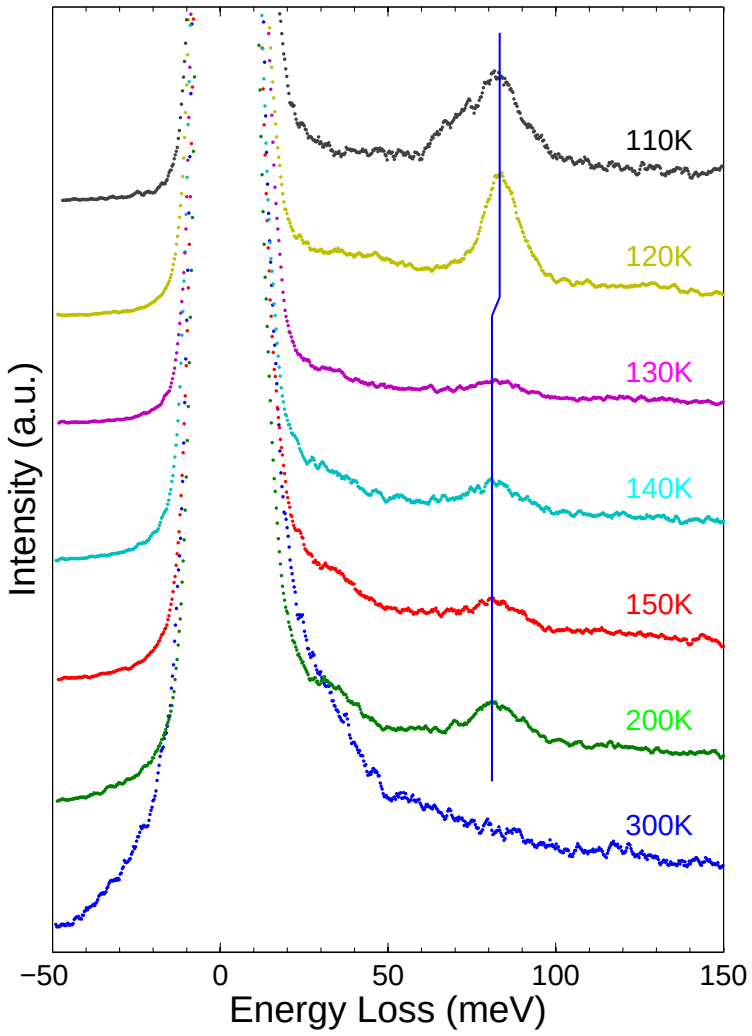

Figure 4.4: HREELS data at different temperatures. The data have been vertically displaced for clarity. The vertical line emphasizes the upward shift in phonon energy below $T = 130K$.

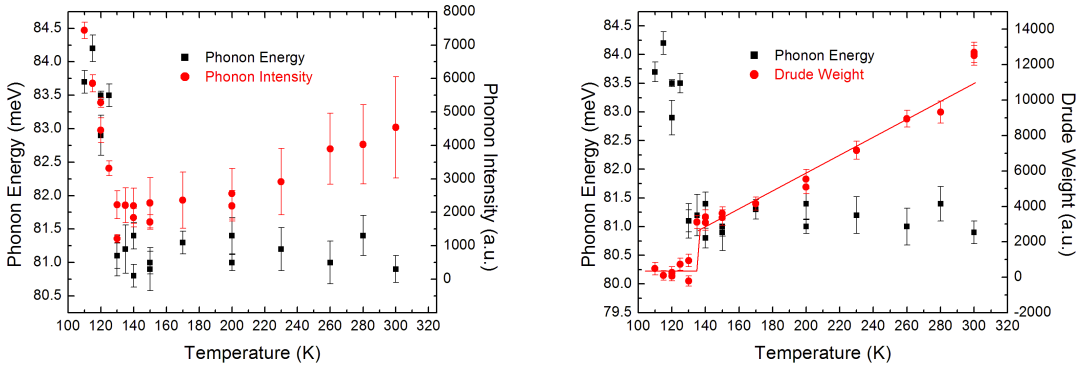

(a) (b)

Figure 4.5: HREELS $Ca_{1.9}Sr_{0.1}RuO_4$. (a) A_{1g} phonon mode energy and intensity. (b) A_{1g} phonon mode energy and integrated Drude tail weight. Line acts as a guide to the eye to show approximate linear decrease of Drude weight with T.

surface conductivity can be measured by tracking the spectral weight in the Drude tail. There are several models which can accurately describe the quasi-particle spectrum and are used to determine phonon dynamics and extract the spectral weight in the Drude tail. Since the Drude tail makes the spectral peak asymmetric, a Lorentz model is used to fit the left side of the spectral peak. In addition, a Lorentz model is used to fit the A_{1g} phonon for each temperature scan. Since the inelastic spectrum in the region around the phonon is a convolution of the Drude tail and the A_{1g} phonon, a linear term is used to fit the Lorentz baseline for the phonon. For the instrument resolutions used and the energy of the A_{1g} phonon relative to the spectral peak, it is found that a linear term is sufficient for the Drude tail in the immediate region around the phonon. Once the spectral peak and phonon are determined, they are subtracted from the data. The remaining inelastic data is an accurate representation of the spectral weight in the Drude tail and thus integrated for a qualitative description of the surface conductivity. Although quantitative conductivity measurements can be inferred from the data, we are only interested in the changes in conductivity over the temperature range of interest.

The phonon energy and intensity as a function of temperature are shown in Figure 4.5(a). It is found that the phonon intensity decreases from room temperature down to $130K$ while the energy remains constant at $81meV$. Below $130K$, the phonon intensity is significantly enhanced while the energy increases by $\sim 2meV$. In addition to the phonon energy shift, the linewidth of the phonon abruptly changes from $\sim 20meV$ above $130K$ to $7meV$ below. Figure 4.5(b) shows the evolution of surface conductivity as a function of temperature. As expected with a Drude metal, the conductivity decreases approximately linearly with temperature down until $130K$. Below $130K$, simultaneously with the changes in phonon character, the dielectric response shows a discontinuous decrease in surface conductivity. Above $130K$, the A_{1g} phonon energy is $\sim 6meV$ higher than that observed on the surface of Sr_2RuO_4 [102]. The slight upshift in surface phonon energy can be understood by the shrinkage of the Ru-O(2) bond length ($\Delta L = 0.02$Å) observed between $x = 2.0$ and $x = 0.1$ in the bulk. However, while the phonon energy remains nearly constant on the

surface of Sr_2RuO_4 between $T = 300K$ and $80K$, a distinct transition is observed on the $Ca_{1.9}Sr_{0.1}RuO_4$ surface.

4.3 HREELS Conclusions and Discussion

Although LEED images at various temperatures show the surface exhibits no change in symmetry through the temperature range of the HREELS measurements, the crystal is apparently near a structural instability. The crystal remains intact during bulk conductivity meaurements however, the crystal often crumbles during the HREELS experiments near $100K$. The strain induced by the cyrstal/epoxy interface is enough to destroy the crystal as the bulk undergos a structural phase transition. As shown in Figure 4.4, it was possible to continue HREELS measurements at $100K$ and below. The sample which remains attached to the sample stage is no longer a single crystal with a well defined surface and tuning HREELS is extremely difficult and the results are unreliable as the spectral count rates are decreased by an order of magnitude and the phonon peak appears inconsistently asymmetric. As with the Mott transitions in bulk crystals, a thermal hysteresis is observed in the surface conductivity and phonon energy. However, due to difficulties tuning HREELS on degraded samples, detailed characterization of the hysteretic behavior is not determined.

Due to the crystal instabilities when attached to a sample stage, several crystals are used for the experiment. Figures 4.3(b) and 4.4 show a typical spectra however, there is one occasion where a phonon is evident at room temperature and the data is included on Figure 4.5. The phonon is evident on all samples at $280K$ and below. The appearance of the phonon is accompanied by a large decrease in surface conductivity. This behavior is possibly due to a change in conductivity along the c-axis. Similar behavior is observed with Sr_2RuO_4 as the c-axis conductivity significantly decreases and the crystal becomes a quasi 2-D metal when the temperature is lowered [17, 30, 102].

The sudden decrease in surface conductivity below $130K$ is consistent with the Mott MIT observed in the bulk. Similar phonon dynamics have been observed in bulk Ca_2RuO_4 for the A_{1g} phonon mode across the bulk MIT [85]. Raman data also show an enhancement in the phonon intensity and a $\sim 2meV$ shift in the B_{1g} phonon energy across the MIT transition temperature [182]. The B_{1g} phonon mode is also associated with vibrations of the apical oxygens. The breaking of symmetry at the surface could distort the lattice stabilizing the metallic phase and creating a MIT which is $\sim 20K$ lower than the bulk MIT. The increase in the A_{1g} phonon mode intensity below $130K$ is consistent with a reduction in electron screening resulting from electron localization in the insulating phase. In addition, Scanning Tunneling Spectroscopy (STS) data reveal an insulating gap on the surface opening up at $130K$ [183]. Thus the combination of the HREELS and STS data suggest the surface MIT $T_c = 130K$. The bulk MIT is accompanied by a structural phase transition. As the bulk enters the insulating phase the RuO_6 tilt increases while the Ru-O(2) bond lengths decrease. Due to the distinct bulk structural characteristics associated with the insulating phase in the CSRO family, the question arises as to what is the surface structure of $Ca_{1.9}Sr_{0.1}RuO_4$. Quantitative surface structure analysis for the CSRO family is the topic of the Chapter 5.

Chapter 5

Surface Structural Analysis

The discovery of superconductivity in Sr_2RuO_4 renewed vigor in the search for and study of superconductors similar in structure in cuprates. It was eight years between the discovery of the high T_c cuprates and Sr_2RuO_4 but the unusual superconducting properties of the ruthenate offers opportunity for new insights into correlated electron systems [8, 14, 17, 30]. While Sr_2RuO_4 is a paramagnetic metal entering into a two dimensional Fermi liquid state at temperatures just above T_c, substituting Ca^{2+} for Sr^{2+} generates an antiferromagnetic insulating ground state [30, 68]. The discovery of the MIT transition coupled to a structural phase transition in Ca_2RuO_4 at $T_c \sim 360K$ combined the paramagnetic to antiferromagnetic transition at $T_N \sim 110K$ shows the ruthenates exhibit exotic phases with intricate coupling between structural, electronic, and magnetic degrees of freedom. Links between MITs and superconductivity have been investigated in the cuprates and the $Ca_{2-x}Sr_xRuO_4$ family offers an alternative system to investigate the evolution from and antiferromagnetic insulating ground state to superconductivity [88, 90]. The phase diagram of the CSRO family shown in Figure 1.12 indeed shows numerous structural, electronic and magnetic phases similar to the cuprates [70, 97]. While the superconducting dome existing in the cuprate phase diagram is not present in the ruthenate phase diagram, the zero temperature terminus of the HTT-LTO phase transition accompanied by a critically enhanced magnetic susceptibility labels $x_c = 0.5$ as a QCP where a magnetic cluster glass phase has been observed. The unusual behavior near the QCP qualitatively appears where one would expect to observe the superconducting dome in the cuprate phase diagram. Understanding the differences between the two systems could lead to valuable insight in to understanding the superconducting phase.

Structure plays an key role in the CSRO phase diagram. Experimental and theoretical studies have revealed how the structural evolution by doping tunes the Ru-4d bands [50, 68, 70, 76, 82, 97, 99]. The rotation and tilt of the RuO_6 not only alter degeneracy, band energies, and band widths, but also alters the magnetic component of the Ru ion. Finding new ways to control the structure of the system allows opportunity to tune observed phases and possibly create new ones. Surface studies of Sr_2RuO_4 reveal how breaking symmetry alters the structural, magnetic and electronic properties of the system. The creation of a surface generates a surface reconstruction described by a $\sim 9^\circ$ rotation of the RuO_6 [101, 100]. The reconstruction further emphasizes the instability of the CSRO family against the rotation distortion and the importance of structure on the electronic bands [56, 48, 53]. As shown in Chapter 3, the CSRO family has a similar instability against the RuO_6 tilt

distortion. The second order HTT-LTO phase transition is governed by a Σ_4 soft phonon involving a tilting RuO_6. Bulk studies have also shown the importance of the RuO_6 tilt on the electronic and magnetic properties of the system [97, 76, 75, 82, 68]. The need to study the surfaces of the CSRO family is apparent. The manifestations of breaking symmetry in this correlated electron system offers an opportunity to not only better understand the intricate couplings observed in the bulk but an opportunity to search for new phases and new physics.

5.1 The LEED Experiment

The sample preparation for the LEED analysis is similar to that outlined for the HREELS experiment in Section 4.1. The primary difference in the sample preparation is due to the desire to cleave samples at different temperatures. While all of the crystals for the HREELS measurements were cleaved at room temperature, several of the crystals used in the LEED analysis were cleaved at lowered temperatures. The sample was still prepared in atmosphere and placed in a load lock where UHV conditions were established. To accomplish the low temperature cleaves, the sample was transferred from the load lock into the LEED chamber prior to cleaving. The sample temperature was established and time allotted for thermal equilibrium prior to cleaving. The cleaving still consisted of knocking off the attached aluminum post however since the sample was on the cryostat coldfinger, the sample remained at the desired temperature after the cleaving process.

The sample was positioned in front of the LEED optics and aligned to normal incidence. Normal incidence was achieved by adjusting tilt and cant angles while monitoring the intensity of symmetrically equivalent beams. For the CSRO system, the four equivalent (1,1) beams were used to align the samples. To ensure normal incidence the intensity of symmetrically equivalent beams was tracked during data acquisition. All (1,1) beams agreed within an $R_p < 0.03$ for all surfaces analyzed. Data was collected using commercial LEED optics with a homebuilt LabVIEW based video-leed data acquisition system. The video-leed system was based around a high resolution 16-bit/pixel ccd camera necessary to analyze the weak fractional order spots. After data acquisition and generation of IV curves the data was normalized to the measured sample current. All available beams were collected and typical energy ranges of $75 - 600eV$ were encountered. The energy ranges varied slightly from surface to surface and from concentration to concentration, but total energy ranges used in the analysis were typically $> 3000eV$.

Surface structural analysis was performed utilizing a modified version of the SATLEED codes [117]. The codes were modified to incorporate the energy dependence of the real and imaginary parts of the inner potential ($V_{or}(E)$ and $V_{oi}(E)$). While such energy dependence can often be neglected for simple metallic or semiconductor surfaces, it has been shown that such assumptions are less reliable for complex transition metal oxide surfaces. The modifications to the SATLEED codes are described in Section 2.2.5. Phase shifts were determine utilizing the optimized muffin tin approach proposed by Rundgren [129] as outlined in Section 2.2.6.2.* A comparison between different methods for determining phase shifts is presented in section 2.2.6. The advantage of the optimized muffin tin approach for complex oxide materials is evident and all analysis presented here take advantage of the improved

*The phase shifts used in this analysis were actually calculated by J. Rundgren.

phase shifts. All structural parameters were determined utilizing a simulated annealing algorithm as outlined in Section 2.2.10.2. Two different methods for defining atomic coordinates were developed to minimize the number of structural fit parameters and to ensure the symmetry observed in LEED pattern is not violated. The development of the optimization methods employed are presented in Section 2.2.10. Section 2.2.6.3 shows how the use of global optimization methods combined with the use of phase shifts calculated using more traditional techniques can easily lead to bogus unphysical and pathological solutions for complex oxide materials. However, due to the improved optimized muffin tin potential approached combined with the incorporation of an energy dependent inner potential, no parameter constraints were necessary for the results presented in this chapter. All presented solutions are the true global minimums found during the simulated annealing process.

It is often observed that optimizing surface Debye temperatures can lead to improved R_ps. While often taken as a non-structural fit parameter, it is found that the improved fit does not lead to different structures. Use of the SATLEED codes requires significant computational time to manually optimize Debye temperatures as a new reference structure calculation must be performed for different temperatures. Since numerous surfaces encompassing numerous concentrations were analyzed during this study, optimization of Debye temperatures was not performed. Debye temperature were assumed to be bulk values determined from the mean square atomic displacements observed by neutron studies (Ru: $T_D = 325K$, O: $T_D = 605K$, Ca: $T_D = 237K$, Sr: $T_D = 237K$) [70].

5.2 The Surface of $Ca_{1.9}Sr_{0.1}RuO_4$

The bulk structure of $Ca_{1.9}Sr_{0.1}RuO_4$ forms in the *Pbca* space group [70]. This subgroup of the *I4/mmm* structure is characterized by a static tilt and rotation of the RuO_6. While both the high temperature and low temperature bulk $Ca_{1.9}Sr_{0.1}RuO_4$ structures form in the *Pbca* space group, there are distinct structural differences intrinsically linked to the bulk transport properties. For Ca_2RuO_4 two distinct phase transitions observed upon cooling. In addition to the metal-to-insulator transition (MIT) there is an additional magnetic transition that occurs at slightly lower temperatures ($T_c \sim= 357K$, $T_N \sim 170K$) [75, 76, 74, 69]. While Ca_2RuO_4 and $Ca_{1.9}Sr_{0.1}RuO_4$ form similar structures, the addition of small amounts of Sr dramatically lowers the MIT T_c and it is found that the magnetic transition occurs at similar temperatures (T_N=$T_c \sim 154K$). For both $x = 0$ and $x = 0.1$ distinct structural changes are observed as the system enters into the insulating phase. Larger RuO_6 tilts (increases of $\sim 5°$), shorter Ru-O(2) bond lengths (decreases of ~ 0.05Å), and a smaller c/a axis ratio (decreases of $\sim 5\%$) characterize the low temperature insulating structures. Such structural distortions narrow the d_{xy} bands and pushes them below the Fermi energy. In addition, a gap between the $d_{yz/zx}$ bands forms and becomes wide enough that the electronic density of states reduces to zero at the Fermi energy. Thus the structural distortions alters U/W and the band filling to form a half-filled Mott insulating state. Since the cation substitution is isoelectronic, the carrier concentration is not altered upon Sr doping and it is these structural distortions driving the orbital occupations, bandwidths and thus the electron localization.

It has been observed in Chapter 4 that the creation of a surface drives T_c to a lower temperature. While traditional expectations may suggest that the broken symmetry should favor an insulating state and raise T_c, it is also unexpected that an insulating state would

form on the top of a conducing bulk crystal [93]. Regardless of what one would expect, the surface of $Ca_{1.9}Sr_{0.1}RuO_4$ remains metallic for $\sim 20K$ after the bulk has entered the insulating phase. It is well known that crystalline surfaces reconstruct when symmetry is broken due to the existence of a surface. Since structure plays such a critical role in determining the properties of the system, the obvious question arises: What is the surface structure of $Ca_{1.9}Sr_{0.1}RuO_4$? To answer this question, surface structural analysis for $Ca_{1.9}Sr_{0.1}RuO_4$ has been performed utilizing the LEED-IV technique.

A typical LEED pattern for $Ca_{1.9}Sr_{0.1}RuO_4$ is shown in Figure 5.1. For comparison, a LEED pattern generated from the $\sqrt{2}x\sqrt{2}$ $R45°$ reconstruction on Sr_2RuO_4 is also shown in Figure 5.1. The surface reconstruction on Sr_2RuO_4 arises from the rigid rotation of the RuO_6 octahedron resulting in a *p4gm* plane group symmetry [101]. As a result of the lateral oxygen displacements two perpendicular glides are created resulting in the extinguishment of fractional order beams (±0.5, ±0.5), (±1.5, ±1.5), (±2.5, ±2.5), etc. (indexing using the *p4mm* plane group symmetry of a bulk terminated Sr_2RuO_4 surface). For $Ca_{1.9}Sr_{0.1}RuO_4$, one immediately recognizes that one direction of the missing fractional order spots are now present. To understand the change in surface symmetry it is important to understand the bulk symmetry of $Ca_{1.9}Sr_{0.1}RuO_4$. While the rigid RuO_6 rotation observed on the surface of Sr_2RuO_4 also exists in the bulk phases for $x < 1.5$, an additional tilt of the RuO_6 is observed in the bulk phases for $x < 0.2$. As a consequence of the tilt, lateral and vertical displacements of the oxygens are induced. Since the *p4gm* plane group symmetry does not allow for buckling of atoms of the same type, the tilt lowers the surface plane group symmetry [101, 184]. The tilt also destroys the glide line symmetry parallel to the tilt axis and the resulting surface symmetry is *pg*. Thus the observed LEED pattern is consistent with a bulk terminated surface and represents a p(1x1) surface of the bulk *pg* plane group. However, surface relaxations are allowed which do not break the observed symmetry. As a result of the p(1x1) surface, bulk symmetry generators shown in Figure 5.2 were used to determine atomic positions as outlined in Section 2.2.10.

As observed in Figure 1.10 the RuO_6 tilts along the [0 1 0] face are all in the same direction. As a result, different surface terminations resulting from step terraces will not destroy the glide line symmetry. While the angle of the tilt axis with respect to the b-axis will vary from terrace to terrace due the rotation of the RuO_6, the tilt axis is always near the b-axis and the tilt angles are correlated from layer to layer. Thus the observed LEED pattern for $Ca_{1.9}Sr_{0.1}RuO_4$ allows for multiple terraces. In order to destroy the opposite glide line, the tilt axis of the RuO_6 must be rotated by 90°. Since all the RuO_6 are connected in the basal plane, any change in tilt axis would result in the breaking of octahedra and the formation of tilt domains. While the majority of surfaces analyzed show a single glide line, disorder in tilts and the formation of domains has been observed. Figure 5.3 shows three images of LEED patterns all taken from the same surface. After taking the image shown in Figure 5.3(a), the sample was moved laterally through the incident electron beam. As the sample was moved a clear indication of multiple tilt domains is observed as shown in Figure 5.3(b) with both glide lines destroyed and a resulting *pm* plane group symmetry resulting. As the sample was moved further, the *pg* symmetry returns with the glide line appearing 90° rotated from the original orientation. The diameter of the incident electron beam is $\sim 1mm$ and the lateral translation of the sample between images a and c was $\sim 2mm$. Thus millimeter sized domains of different tilt axis orientations are observed. While this is the only surface showing multiple tilt domains, subsequent cleaves of a single

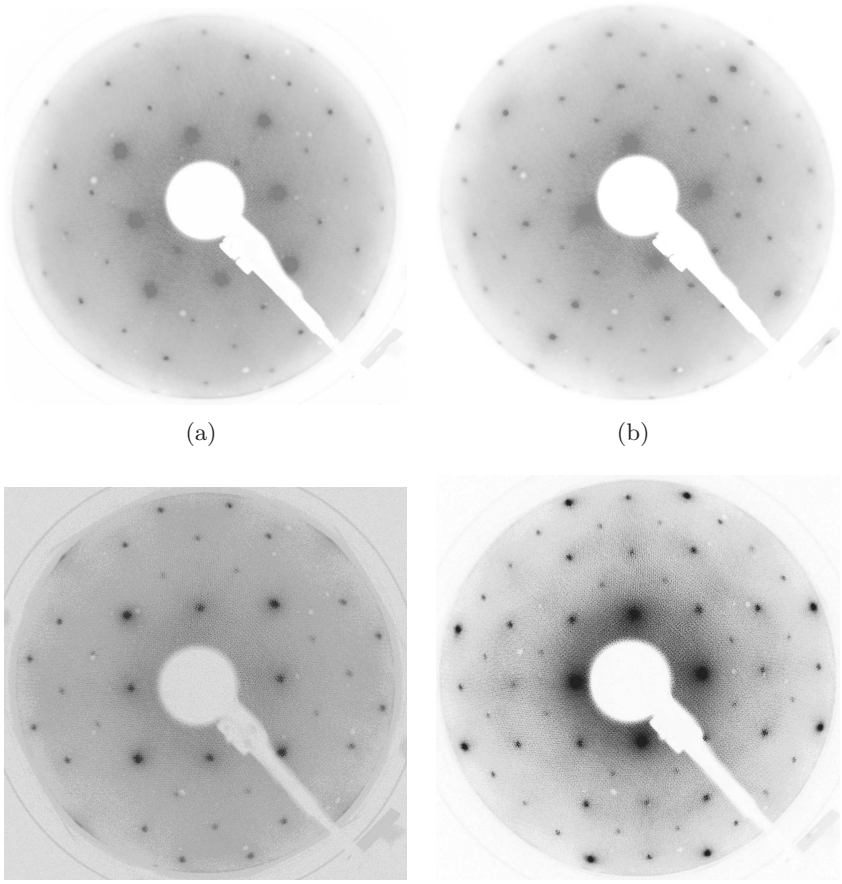

(a) (b)

(c) (d)

Figure 5.1: LEED pattern for $Ca_{1.9}Sr_{0.1}RuO_4$. Typical LEED pattern observed for $Ca_{1.9}Sr_{0.1}RuO_4$ at (a) 176eV and (b) 265eV. Typical LEED pattern observed for Sr_2RuO_4 at (c) 134eV and (d) 200eV. The image contrast has been adjusted to emphasize the weaker spots.

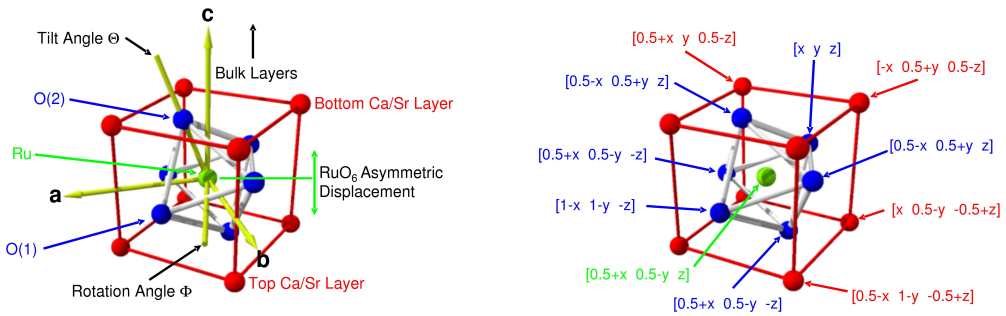

(a) (b)

Figure 5.2: Surface layer parameters for $Ca_{1.9}Sr_{0.1}RuO_4$. (a) Anatomy of a surface layer. Bulk layers are generated along the +c-axis direction. (b) Symmetry generators used in optimization method #2. Additional symmetry generators not listed: Ru [x y z], O(2) [x y z] and O(2) [-x -y -z].

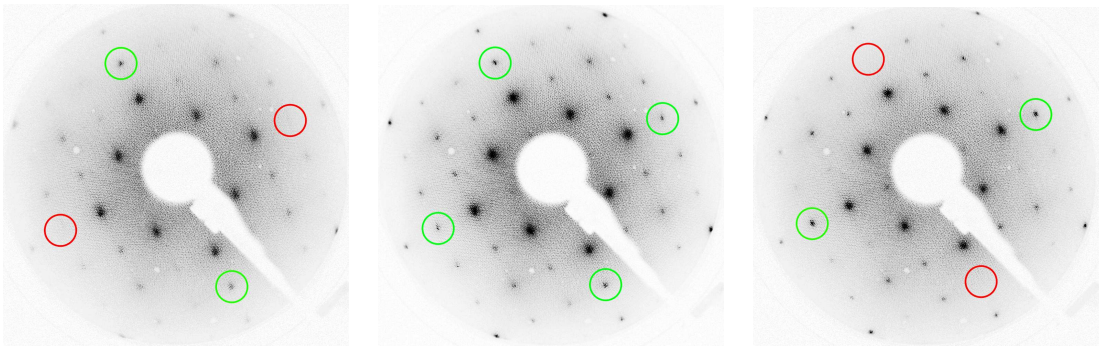

(a) (b) (c)

Figure 5.3: Tilt domains in $Ca_{1.9}Sr_{0.1}RuO_4$. (a) LEED pattern at 176eV. Green circles emphasize existing spots, Red circles emphasize extinguished spots due to glide plane symmetry. (b) Image of same surface after sample translation of ∼1mm from Image (a). (c) Image of same surface after sample translation of ∼1mm from Image (b).

sample have also demonstrated a rotated tilt axis by the flipping of the glide line from one cleaved surface to the next. Due to the orthorhombic splitting it is expected that the strain induced by the alternate tilt phase domain would create favorable conditions for cleaving the crystal at the tilt domain boundaries. While domains of different tilt axis have been observed, these two cases are the only evidence from numerous cleaved samples. It is assumed that any domains with a tilt axis near the a-axis form a minority phase and constitute a very small fraction of the sample. All IV data taken were on single domains with one glide line evident.

To analyze the surface structure, IV curves were collected between $50 - 600eV$ in $1eV$ increments. A total of 16 nonequivalent beams were used in the analysis: (2,0), (0,2), (3,0), (4,0), (0,4), (1,1), (2,2), (4,4), (1,2), (2,1), (1,3), (3,1), (1,5), (5,1), (2,4), (4,2). All symmetrically equivalent beams were recorded and averaged to produce the experimental IV data and all beams were normalized to the sample current. Due to the importance of the in-plane parameters for the O(1) oxygen in the basal plane and to better determine true error in structural parameters, multiple surfaces were analyzed. A total of four surfaces were analyzed at different temperatures both above and below the MIT. The first surface (⧫) consisted of an *in situ* cleave at room temperature and only consisted of collecting IV data at room temperature. The second surface (•) was a subsequent cleave of the same crystal at room temperature and then cooled to analyze the structure across the MIT. The third surface (★) was a new crystal cleaved at room temperature and analyzed at room temperature and at temperatures just above and below the surface MIT. The fourth surface (▼) consisted of a third crystal cleaved at 170K and then analyzed both above and below the MIT. A total of 11 different sets of IV curves were collected and analyzed encompassing 8 different temperatures: 300K, 160K, 150K, 140K, 110K, 100K, 90K, 80K. The experimental IV curves were smoothed using no more than two iterations of a weighted 5-point adjacent averaging method. The total energy ranges for the different IV sets varied from 3982 to 4669eV. The smaller energy ranges were typically encountered for the higher temperature IV sets due to thermal effects.

While the use of bulk symmetry generators greatly reduced the number of fit parameters for the 14 atoms in the surface layer, several fit parameter constraints may be incorporated and parametric searches were run to determine how different fit parameters affected the final results. The creation of a surface obviously breaks translational symmetry but it is desirable to understand just how broken is the symmetry in such layered compounds. Parametric searches allowed for an intuitive understanding of the implications of broken symmetry on the surface layer. Bulk data suggests that the RuO_6 behaves as a rigid object, but the *pg* plane group allows for numerous distortions to the octahedron without breaking the symmetry observed in the LEED pattern. For example, the Ru atom exists at the center of the O(1) basal plane in the bulk but vertical motions of the Ru atom or the O(1) plane are allowed without disrupting the observed pattern. In addition, the two Ru-O(2) bond lengths are identical in the bulk, but interlayer distances between the top O(2) top and the Ru plane are allowed to be different than the interlayer distances between the bottom O(2) plane and the Ru plane. Such a distortion would allow for different Ru-O(2) bond lengths. To understand the implications of breaking symmetry parametric searches were performed on two of the four surfaces (5 of the 11 IV data sets) using different combinations of fit parameters utilizing both optimization methods. It is found that allowing different Ru-O(2) bond lengths improves the R_p of the final result by ~ 0.0002 where the final bond lengths varied by ~ 0.005 Å (much smaller than the accuracy of the analysis). There was also no consistency between which bond tended to be longer. As a result, the top and bottom Ru-O(2) bond lengths were assumed identical and the corresponding fit parameters constrained during subsequent fits. Similar results were obtained when the Ru vertical displacement was assumed independent of the vertical origin of the O(1) basal plane. No trend was observed in the relative displacements of the two parameters and the improvement in the R_p was negligible (~ 0.0002). Thus the Ru atom was always assumed to be in the center of the O(1) basal plane. However, it was observed that vertical displacements of the entire RuO_6 from the symmetrically defined positions did improve the final fit and thus are allowed for in the analysis. In addition, allowing the O(1) tilt to be different than the O(2) tilt made significant improvements to the final results ($\Delta R_p \sim 0.025$) and thus separate tilt angles were allowed optimization parameters. While different O(1) and O(2) tilt angles are observed in the bulk, the sensitivity of the analysis to the constrained tilt angles is unexpected.

A single a-axis and b-axis coordinate define the in-plane positions for all of the Ca/Sr sites, surprisingly an improvement to the final R_p of ~ 0.01 was observed if separate a and b parameters were defined for the top and bottom Ca/Sr planes. In addition, a distinct trend in the coordinate variations was observed with the addition of the two extra fit parameters. The addition of these two fit parameters is a distinct breaking of bulk symmetry, but *pg* plane group symmetry is not broken as both the top and bottom Ca/Sr planes adhere to the *pg* symmetry with coordinates defined by the symmetry generators of the bulk. While the bottom Ca/Sr coordinates remained close to bulk values, the top Ca/Sr a-axis coordinate was always sufficiently larger than bulk values. Although the LEED analysis is less sensitive to in-plane coordinates, such a distinct trend with an appreciable improvement to the final results must not be ignored and separate a and b-axis coordinates were allowed for the top and bottom Ca/Sr planes. A summary of the final fit parameters for both optimization methods is listed in Table 5.1. The primary difference between the two optimization routines is the definition of the in-plane O(1) coordinates. While the first method defines octahedral

Table 5.1: $Ca_{1.9}Sr_{0.1}RuO_4$ fit parameters. Fit parameters for both optimization methods used in the analysis.

Rigid RuO_6 Optimization	**Space Group Optimization**
RuO_6 Rotation Angle (Degrees)	O(1) a-axis Crystal Coord. (x)
O(1) Tilt Angle (Degrees)	O(1) b-axis Crystal Coord. (y)
Ru-O(1) Basal Plane c-axis Disp. (Å)	O(1) c-axis Crystal Coord. (z)
O(2) Tilt Angle (Degrees)	O(2) a-axis Crystal Coord. (x)
Ru-O(2) Bond Length (Å)	O(2) b-axis Crystal Coord. (y)
	O(2) c-axis Crystal Coord. (z)
	RuO_6 Asymmetric c-axis Disp. (Å)
Top Ca/Sr a-axis Crystal Coord. (x)	Top Ca/Sr a-axis Crystal Coord. (y)
Top Ca/Sr b-axis Crystal Coord. (y)	Top Ca/Sr b-axis Crystal Coord. (y)
Top Ca/Sr c-axis Crystal Coord. (z)	Top Ca/Sr c-axis Crystal Coord. (z)
Bottom Ca/Sr a-axis Crystal Coord. (x)	Bottom Ca/Sr a-axis Crystal Coord. (x)
Bottom Ca/Sr b-axis Crystal Coord. (y)	Bottom Ca/Sr b-axis Crystal Coord. (y)
Bottom Ca/Sr c-axis Crystal Coord. (z)	Bottom Ca/Sr c-axis Crystal Coord. (z)
Voc (eV)	Voc (eV)
Number of Fit Parameters = 12	Number of Fit Parameters = 14

tilts and rotations and assumes all Ru-O(1) bond lengths to be equivalent, the second method uses bulk symmetry generators to define the O(1) coordinates and thus allows for basal plane distortions and a variation of the Ru-O(1) bond lengths. While both methods always yielded the same structural parameters for the rotation, tilts, Ru-O(2) bond lengths and Ca/Sr parameters, the second method consistently yielded R_p improvements of ~ 0.01. Thus the results from the second optimization method which allows for in-plane relaxation of the O(1) basal plane are presented in Figures 5.4, 5.5, 5.6, 5.7 and Table 5.2. The bulk data presented in these figures is derived from Refs. [70, 96].

The most dramatic reconstruction on the surface involves a inward motion the top Ca/Sr plane c-axis coordinate. As can be seen from Figure 5.4(a), the distance between the Ru plane and the top Ca/Sr plane is ~ 0.06 Å smaller than the distance between the Ru plane and the bottom Ca/Sr plane. While the bottom Ca/Sr plane c-axis coordinate remains close to those values observed in the metallic bulk phase, the top Ca/Sr plane c-axis coordinate is closer to those values observed in the insulating bulk phase. Such a large displacement of the top Ca/Sr plane would result in an asymmetric compression of the surface layer along the c-axis. The compression is asymmetric as only the top half of the surface layer appears to have a compressed interlayer distance between the Ru and Ca/Sr planes.

When the surface is cooled, Figure 5.4(b) shows an asymmetric displacement of the RuO_6 into the surface. This displacement is added to the c-axis coordinates of the Ru and all 6 octahedral oxygens after their coordinates are determined by the symmetry generators. Thus the asymmetric displacement is a deviation from the symmetrically defined positions. The RuO_6 is observed to move toward the bulk crystal ~ 0.02 Å as the system is cooled. The top Ca/Sr c-axis coordinate is also observed to move toward the bulk by ~ 0.02 Å. Such a movement appears as a decrease in the c-axis coordinate relative to the symmetrically defined Ru coordinate upon cooling. In addition, the bottom Ca/Sr plane c-axis coordinate relative to the symmetrically defined Ru coordinate appears to increase, indicating a downward vertical movement into the bulk crystal. The net result is there appears to be a thermal contraction of the surface layer, but one which does not alter the existing compression due to the creation of the surface. The RuO_6 and both Ca/Sr planes move into the surface by ~ 0.02 Å resulting in the c-axis distance between the top Ca/Sr plane and bottom Ca/Sr plane to remain unaltered during the cooling process. It is likely the observed displacement is due to a thermal contraction of the bulk crystal resulting in an observed downward motion and compression of the interlayer distances between the surface layer and the bulk.

Significant deviations from bulk trends are also observed for the Ca/Sr a and b-axis coordinates as shown in Figure 5.5. While at room temperature, the bottom Ca/Sr plane a and b-axis coordinates take on values similar to those observed in the metallic bulk phase, however, they remain static at these bulk metallic phase values as the surface is cooled through the MIT. The top Ca/Sr plane a-axis coordinate shows a $+0.06$ Å deviation from bulk values at room temperature while the b-axis coordinate shows a -0.06 Å deviation. The result of such a relaxation is a 0.1Å decrease in the minimum Ca/Sr-O(2) bond length over those found in the bulk. As the surface is cooled, the b-axis coordinate takes on values close to the bulk metallic phase coordinates while the a-axis coordinate always remains greater than the bulk values and increases ~ 0.02 Å upon cooling. While a 0.1Å in-plane motion is near the limits of the LEED analysis, all surfaces analyzed are consistent and agree with 0.03Å of each other.

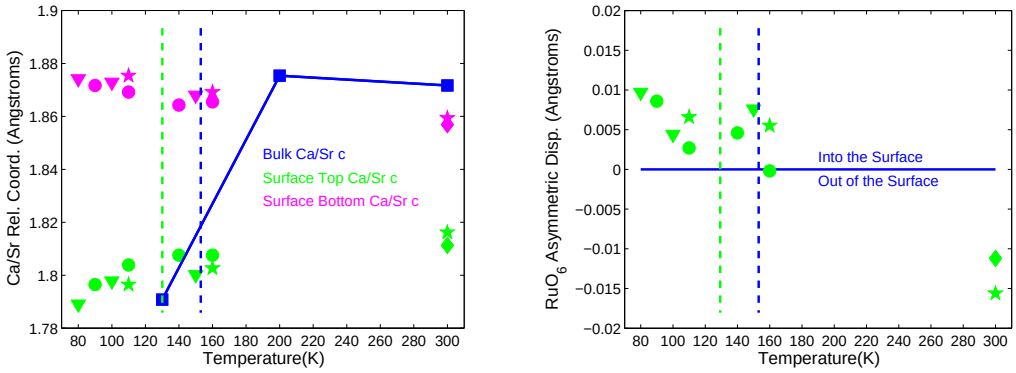

(a) (b)

Figure 5.4: RuO_6 and Ca/Sr c-axis relative coordinates. (a) Absolute value of [x y $\pm 0.5 \mp$z] Ca/Sr c-axis coordinate relative to Ru at origin [0 0 0]. (b) RuO_6 c-axis displacement from coordinates generated by symmetry. Blue and green dashed lines are bulk and surface MIT temperatures respectively. Bulk Data is from Ref. [70].

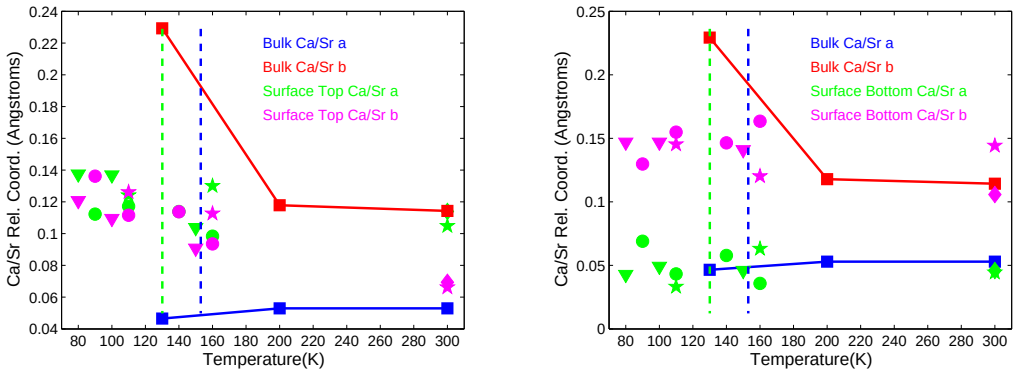

(a) (b)

Figure 5.5: Ca/Sr a and b-axis relative coordinates. (a) Top [x y -0.5+z] Ca/Sr a and b-axis coordinate relative to Ru at origin [0 0 0]. (b) Bottom [x y 0.5-z] Ca/Sr a and b-axis coordinate relative to Ru at origin [0 0 0].

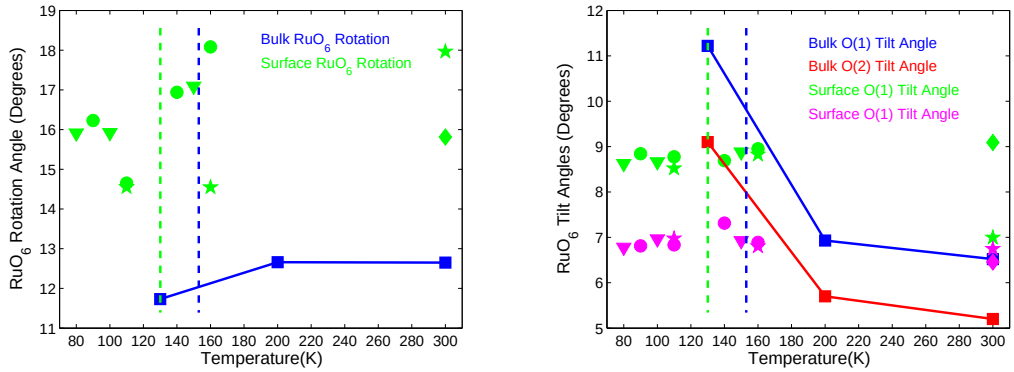

(a) (b)

Figure 5.6: RuO_6 rotation and tilt angles. (a) RuO_6 rotation angle. (b) O(1) and O(2) tilt angles.

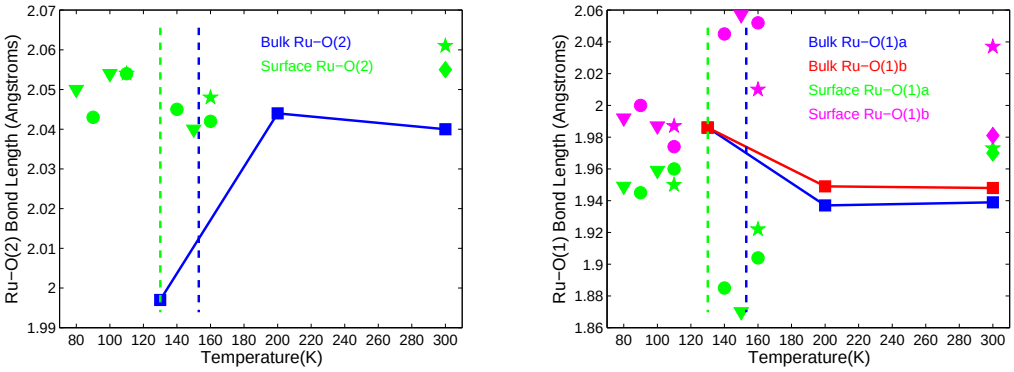

(a) (b)

Figure 5.7: Ru-O(1) and Ru-O(2) bond lengths. (a) Ru-O(2) bond lengths. (b) Ru-O(1) bond lengths.

Table 5.2: $Ca_{2-x}Sr_xRuO_4$ ($x = 0.1, 0.5$) Structural Refinement. All fit parameters are given in crystal coordinates unless otherwise specified. Associated errors are given in parenthesis. Coordinates generated using bulk 300K unit cell parameters. For $x = 0.1$: a=5.3494Å; b=5.3420Å; c=12.3219Å. For $x = 0.5$: a=b=5.3395Å; c=25.1498Å [70].

Concentration (x)	0.1	0.1	0.1	0.5
Temperature (K)	300	140	90	300-80
Total Energy Range (eV)	4162	4315	4530	3729
R_p	0.244	0.211	0.193	0.240
Vc (eV)	8.89(10)	9.14(8)	9.03(8)	10.37(11)
Top Ca/Sr x	0.021(5)	0.021(5)	0.021(5)	0
Top Ca/Sr y	0.013(7)	0.021(7)	0.026(6)	1/4
Top Ca/Sr z	0.3530(7)	0.3533(6)	0.3542(4)	0.5536(6)
O(1) x	0.181(12)	0.196(10)	0.185(9)	0.187(16)
O(1) y	0.321(11)	0.326(9)	0.323(7)	x + 1/4
O(1) z	0.018(3)	0.017(2)	0.018(2)	1/8
O(2) x	-0.042(7)	-0.042(6)	-0.040(6)	0
O(2) y	-0.011(8)	-0.024(8)	-0.022(7)	1/4
O(2) z	0.166(2)	0.165(1)	0.165(1)	.4566(5)
RuO_6 c-axis Disp. (Å)	-0.011(6)	0.005(5)	0.009(4)	0.00(3)
Bottom Ca/Sr x	0.009(8)	0.011(7)	0.013(7)	0
Bottom Ca/Sr y	0.019(10)	0.027(9)	0.024(8)	1/4
Bottom Ca/Sr z	0.3493(10)	0.3487(8)	0.3481(8)	0.5485(10)
Ca/Sr-Ca/Sr||c (Å)	3.67(2)	3.67(1)	3.67(1)	3.72(3)
Top Ca/Sr-O(max) (Å)	3.02(6)	3.03(5)	3.02(5)	2.68(2)
Top Ca/Sr-O(min) (Å)	2.35(6)	2.36(5)	2.37(5)	2.68(2)
Bottom Ca/Sr-O(max) (Å)	2.96(9)	2.98(9)	2.97(8)	2.68(2)
Bottom Ca/Sr-O(min) (Å)	2.42(9)	2.41(9)	2.41(8)	2.68(2)
Rotation (Degrees)	15.8(2.3)	16.9(2.1)	16.2(2.0)	14.1(4.0)
O(1) Tilt (Degrees)	9.1(0.9)	8.5(0.8)	9.0(0.7)	0.0(5)
O(2) Tilt (Degrees)	6.5(0.7)	7.3(0.6)	6.8(0.5)	0.0(5)
Ru-O(1) (Å)	1.97(6)	1.89(6)	1.95(5)	1.95(7)
	1.98(6)	2.04(6)	2.00(5)	1.95(7)
Ru-O(2) (Å)	2.06(3)	2.05(2)	2.05(2)	2.05(2)
O(1)-O(1)||a (Å)	2.81(6)	2.83(5)	2.82(5)	2.75(7)
O(1)-O(1)||b (Å)	2.77(5)	2.73(5)	2.76(4)	2.75(7)
RuO_6 Volume ($Å^3$)	10.68	10.56	10.64	10.34

While significant relaxations are observed for the Ca/Sr coordinates due to the creation of a surface, the primary structural parameters describing the bulk MIT involve the RuO_6. As can be seen in Figure 5.6(a) the RuO_6 rotation is always a few degrees larger than the bulk values. In addition, it remains constant (within error) through out the measured temperature range and across the MIT. The observed tilts on the surface are also slightly larger than room temperature bulk values as seen in Figure 5.6(b). Surprisingly, the surface tilts also appear to be fixed and do not change across the surface MIT compared to the bulk tilts which nearly double across the MIT. The surface O(1) and O(2) tilts take on values which are in between the bulk metallic phase and insulating phases and remain fixed at these values as both the bulk and surface enter into the insulating phase. The Ru-O(2) bond takes on similar values to those observed in the bulk metallic phase and surprisingly, remain at a fixed bond length through the surface MIT as shown in Figure 5.7(a) . While the bulk Ru-O(2) bond length shows a dramatic reduction through the MIT, the surface Ru-O(2) bond remains near lengths expected in the metallic phase even after the surface has entered into the insulating state. The largest changes to the RuO_6 observed upon cooling involve the Ru-O(1) bond lengths shown in Figure 5.7(b). As the system approaches T_c, the Ru-O(1) bond lengths significantly deviate from their average value. At temperatures just above T_c, the bonds deviate ~ 0.08 Å from the average value. Just below the phase transition, the Ru-O(1) bonds are significantly closer to the average value. Such a deviation indicates the basal plane becomes significantly distorted just before the surface phase transition.

It is unexpected that the surface structure would remain near the bulk metallic phase coordinates at temperature down to $80K$. As a check, different reference structures were used in the structural determination. Reference structures from bulk data of $200K$ and $130K$ were calculated and fits generated based on these models [70]. The $200K$ reference structural model generated the same solution as the $300K$ model and final fit R_p's were very similar. Such a result is expected since the bulk $200K$ structure is similar to the $300K$ structure. In contrast, fits generated from the insulating $130K$ bulk reference structural model were poor in comparison. While the final structural parameters were near those observed in the bulk insulating phase, the best fit ($R_p > 0.6$) structural parameters proved unreliable. When the optimized surface structural parameters utilizing the bulk $300K$ reference structure were held static and compared to the bulk $130K$ reference structure a $R_p = 0.74$ resulted. The significant difference in R_p when comparing the insulating and metallic bulk reference structures further supports the accuracy of the bulk metallic model describing the data and emphasized the static nature of the surface structure as the system enters the insulating phase both in the bulk and on the surface.

Based on these observations, three distinct surface structures for $Ca_{1.9}Sr_{0.1}RuO_4$ are defined: $300K$, $160 - 140K$, $110K - 80K$. IV curves for the low temperature surface phase are presented in Figure 5.8. Structural parameters for three different temperatures are listed in Table 5.2. While the error for individual scans were determined as outlined in Section 2.2.9, the consistency and reliability of analyzing multiple surfaces allowed for a reduction in the true error through statistically combining the results within the three temperature ranges. A comparison of bulk and surface structures is presented in Figure 5.9.

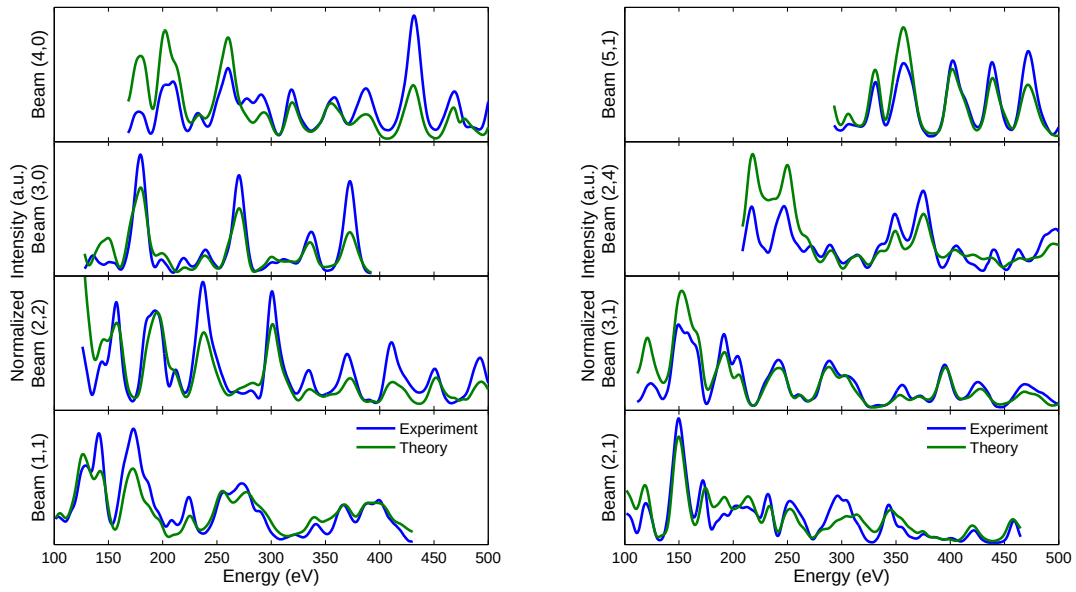

(a) (b)

Figure 5.8: Selected $Ca_{1.9}Sr_{0.1}RuO_4$ IV curves at 90K. (a) Beams (1,1), (2,2), (3,0), (4,0). (b) Beams (2,1), (3,1), (2,4), (5,1).

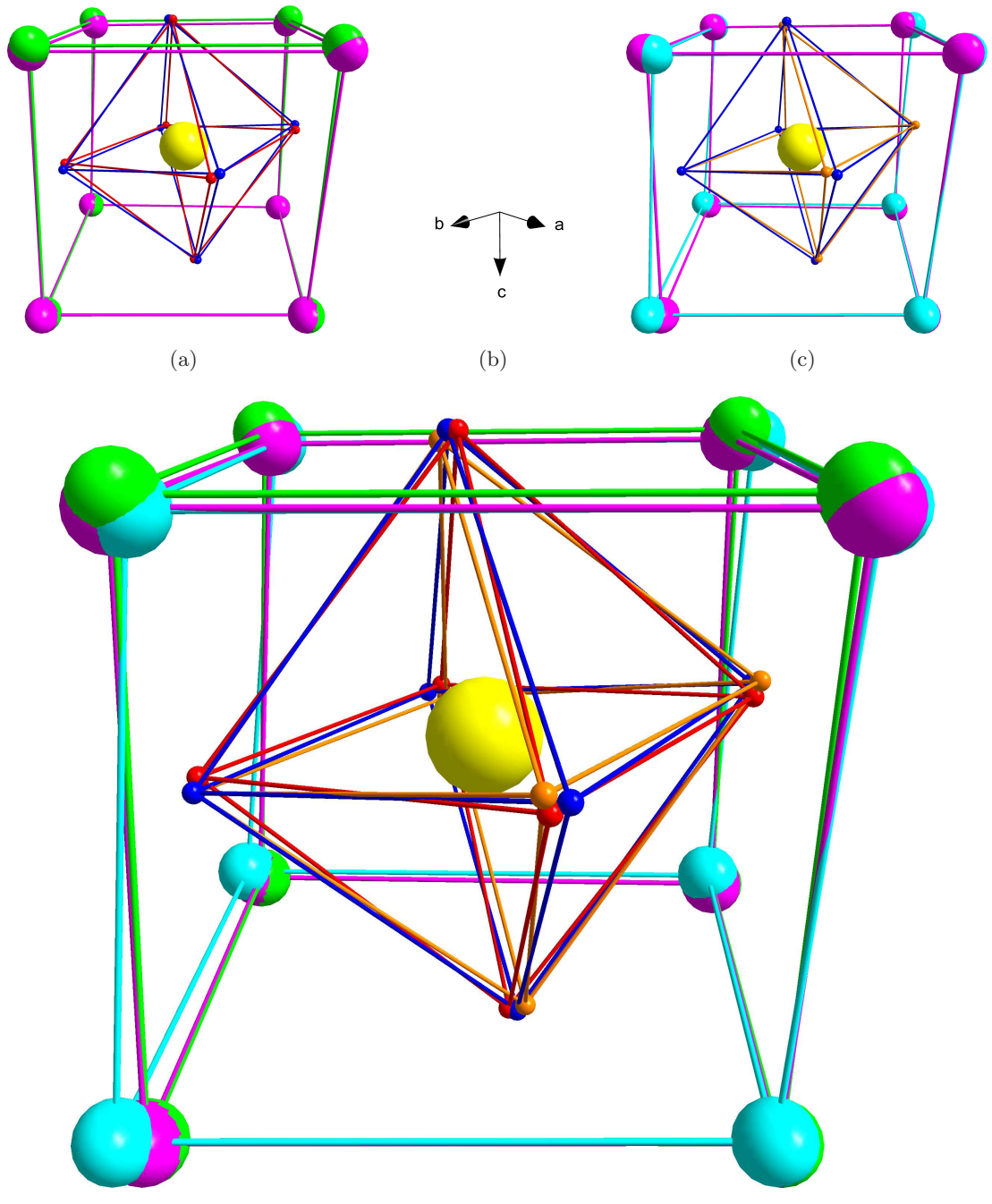

(a) (b) (c)

(d)

Figure 5.9: Surface structural comparison for $Ca_{1.9}Sr_{0.1}RuO_4$. (a) Surface structure (blue and purple) at $T = 90K$ compared with bulk $300K$ reference structure (red and green). (b) Coordinate axis for structures shown. (c) Surface structure (blue and purple) at $T = 90K$ compared with bulk $10K$ reference structure (orange and cyan). (d) Same comparison and color coding enlarged for clarity.

5.3 Discussion of $Ca_{1.9}Sr_{0.1}RuO_4$ Results

The structural refinement data of $Ca_{1.9}Sr_{0.1}RuO_4$ overwhelmingly supports a static surface structure throughout the temperature range analyzed. The largest surface relaxation involves an inward motion of the top Ca/Sr plane while the rest of the surface remains bulk-like. Surprisingly, this structure remains static across both the bulk and surface MIT. While the bulk insulating phase is well characterized and it is well understood how the observed structural distortions can create a half-filled Mott insulating state, similar structural distortions are simply not observed on the surface. While there are further structural relaxations evident as the surface is cooled they are all subtle and continuous, nothing like the first order structural phase transitions observed in the bulk as the system enters into the insulating phase. The largest structural changes across the surface T_c involve the distortion of the O(1) basal plane encountered just prior to the MIT. However, caution must be taken as the in-plane oxygen structural parameters still have the largest associated error even after statistical combination of different measurements. Plus, the combination of RuO_6 structural parameters results in static average Ru-O(1) bond lengths, average Ru-O(2) bond lengths and even static average O(1)-O(1) bond lengths. The surface parameters appear to be a mixture of the bulk metallic and insulating parameters. In addition to the top Ca/Sr plane c-axis coordinate taking on values similar to the bulk insulating phase, the slightly larger RuO_6 rotation combined with slightly larger tilts make the observed O(1)-O(1) bond distances and the Ru-O(1) bond distances more akin to those in the insulating phase [70]. As a result, the surface RuO_6 volume has increased to values similar to those observed in the insulating phase. On the contrary, the observed tilts never reach the values observed in the insulating phase and the Ru-O(2) bond lengths remain at their metallic bulk values. Even in the insulating phase, the bulk structural parameters continue to change as the system is cooled further. The b-axis and c-axis lattice constants continue to shrink while the O(1)-O(1) bond distances continue to increase. To better understand what is changing on the surface in the insulating phase, it is necessary to look at the LEED patterns. Figure 5.10 shows LEED patterns taken below the surface T_c. In addition to the normally observed LEED pattern, additional spots are easily observed. While the positioning of these spots suspiciously look like a p(3x1) reconstruction, there is no consistency in the appearance of additional spots nor the locations of the additional spots from one surface to another. However, the streaking observed does appear on all the surfaces. Below $T_c \sim 130K$, weak streaking appears between the spots and the intensity of the streaking increases as the surface temperature is lowered. Between $130K > T > 110K$ the streaks appear parallel to the direction of the glide line with an intensity that gradually increases with the lowering T. Below $T \sim 100K$ streaks start to appear perpendicular to the glide line with sudden jumps in streak intensity often occurring. The streaking is attributed to surface degradation. Below $T \sim 90K$ the majority of the samples crumble with large portions of the crystal falling to the bottom of our LEED chamber. The appearance of additional spots is typical of crystal twinning and the formation of large cracks. While the streaking is most likely due to small structural defects appearing parallel to the a and b-axis but with irregular intervals between the defects. The appearance of the streaks are non-reversible and subsequent warming of the sample usually results in crumbling. Thus investigating hysteretic behavior becomes difficult and unreliable. The spot width and profile remains unchanged and the alignment of the sample remains normal as the R_p between equivalent beams never exceeds

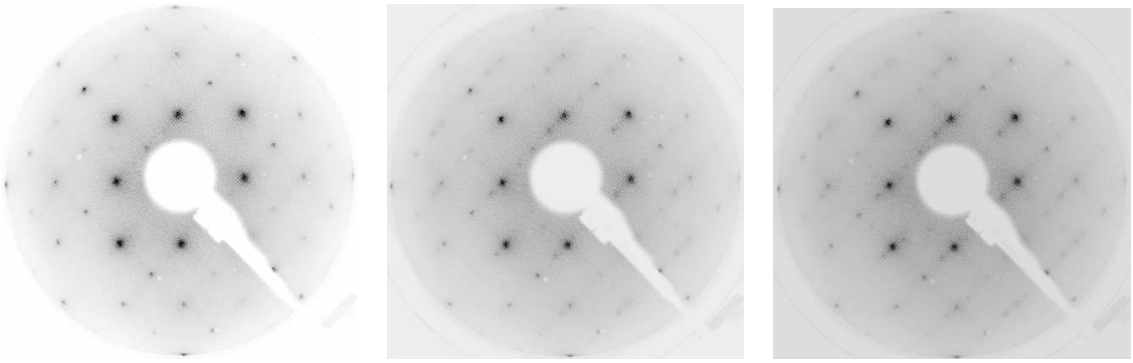

(a) (b) (c)

Figure 5.10: Structural instability of $Ca_{1.9}Sr_{0.1}RuO_4$ surface. Data shown at (a) 110K, (b) 100K and (c) 90K.

0.03. As such the R_p of the final refinements are not affected by the appearance of the surface defects. Similar structural instability and crumbling of single crystalline samples has also been observed during bulk studies [70, 96].

5.4 The Surface of $Ca_{1.5}Sr_{0.5}RuO_4$

It is found that the RuO_6 on the surface of Sr_2RuO_4 are rotated by $\sim 10^\circ$ [101]. The breaking of symmetry by the creation of a surface freezes the Σ_3 rotational phonon mode of the RuO_6. The bulk system is unstable against the rotational distortion as evident by the soft phonon behavior of the Σ_3 mode near the Brillouin zone boundary [56]. As shown in Section 3.3, the bulk CSRO system is also unstable against the RuO_6 tilt distortion as similar soft phonon behavior is observed for the Σ_4 phonon mode. As the phase boundary between the HTT and LTO phases is approached, the Σ_4 mode monotonically decreases in energy at the zone boundary until the RuO_6 freeze into a displacive structural phase transition with a static non-zero tilt. Due to the similarities between the rotational and tilt soft phonon modes, the question arises as to what surface structure one should expect to observe on the surface of the CSRO family near the HTT-LTO phase transition. While a 25% Ca concentration is required to freeze the Σ_3 mode in the bulk, simply cleaving the layered crystal structure is enough to induce the rotation distortion on the surface. The proximity of $Ca_{1.5}Sr_{0.5}RuO_4$ to the HTT-LTO phase boundary could be considered much closer in phase space than the $x = 2.0$ scenario. Thus LEED studies were performed on $Ca_{1.5}Sr_{0.5}RuO_4$ to investigate a surface induced tilt distortion.

A typical LEED pattern for $Ca_{1.5}Sr_{0.5}RuO_4$ is shown in Figure 5.11. As can be seen in the figure, the LEED pattern appears identical to that observed for Sr_2RuO_4. However, the bulk symmetry between the two systems is different. While bulk Sr_2RuO_4 forms in the highly symmetric *I4/mmm*, $Ca_{1.5}Sr_{0.5}RuO_4$ forms in a lower symmetry subgroup $I4_1/acd$. Thus for a bulk terminated Sr_2RuO_4 one would expect to see a LEED pattern from the *p4mm* plane group but the surface reconstruction exists and a *p4gm* LEED pattern is experimentally observed. The $\sqrt{2}$x$\sqrt{2}$ $R45^\circ$ surface reconstruction results from the rigid rotation of the RuO_6 octahedron. The bulk structure for $x = 0.5$ already has such a rigid

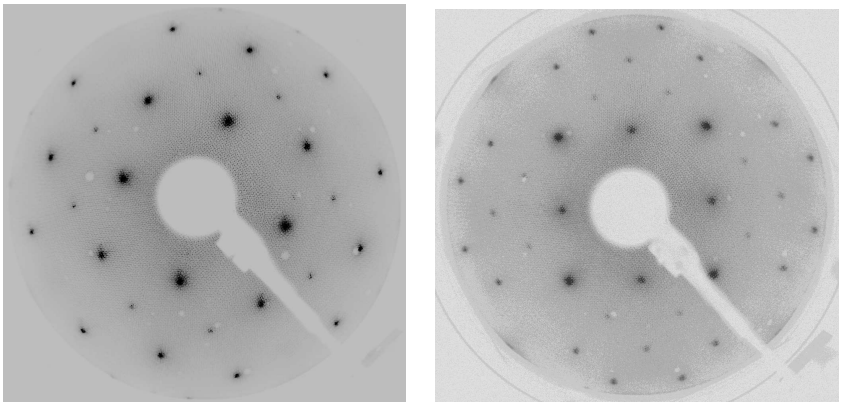

(a) (b)

Figure 5.11: LEED pattern for $Ca_{1.5}Sr_{0.5}RuO_4$. (a) Typical LEED pattern at 125eV. (b) LEED pattern for Sr_2RuO_4 at 134eV.

RuO_6 rotation and thus the LEED pattern for a bulk terminated crystal would be expected to be similar to that observed for Sr_2RuO_4. The difference in bulk symmetry increases the unit cell size and resulting Brillouin zone and thus the surface of $Ca_{1.5}Sr_{0.5}RuO_4$ shows a p(1x1) surface reconstruction. The important observation is that the LEED patterns show two glide lines rotated 90° with respect to each other. Since the glide lines are encoded by the rotation of the Ru-O(1) basal plane, destruction of the glide lines would occur if the Ru-O(1) plane either rotated back to zero angle, or tilted. Thus the simple fact that both glide lines are evident is an indication that the RuO_6 are not tilted.

Due to the different symmetry observed on the surface of $Ca_{1.5}Sr_{0.5}RuO_4$, several parameters in the optimization routines can be constrained. No tilt of the RuO_6 and the resulting buckling of the O(1) plane is allowed. In addition, the Ca/Sr sites remain fixed in their positions and are not free to move in the ab-plane. Therefore of the 17 possible fit parameters in the optimization routines listed in Table 2.2, we are restricted to 8 maximum. However, there still exists possible distortions to the RuO_6 allowed without breaking the observed symmetry. The Ru layer and the O(1) layer are not required to maintain the same c-axis coordinate plus the top and bottom Ru-O(2) bond lengths are not required to be the same. Parametric searches with different combinations of fit parameters were performed to better estimate the distortions existing to the RuO_6. The parametric searches were performed on four different IV data sets: two different crystals, each at 300K and at $80K$. The parametric searches yielded similar results to those obtained for $Ca_{1.9}Sr_{0.1}RuO_4$. Both $x = 0.1$ and $x = 0.5$ data suggest the top and bottom Ru-O(2) bond lengths remain equal. In addition, both concentrations suggest the Ru c-axis coordinate remains in the center of the O(1) basal plane. Based on these results, the final fit parameters for $x = 0.5$ are presented in Table 5.3. Due to the observed *p4gm* symmetry a constraint is placed on the O(1) b-axis coordinate in the Space Group Optimization method: $y = x + 1/4$. Therefore only one coordinate is used to define the RuO_6 rotation and Ru-O(1) bond length. This means that both optimization methods have the same number of fit parameters and are simply different ways of defining the same atomic coordinates. The use of the different optimization methods does not provide any additional information, but it serves as a check

Table 5.3: $Ca_{1.5}Sr_{0.5}RuO_4$ fit parameters. Fit parameters for both optimization methods used in the analysis.

Rigid RuO_6 Optimization	**Space Group Optimization**
RuO_6 Rotation Angle (Degrees)	O(1) a-axis Crystal Coord. (x)
Ru-O(2) Bond Length (Å)	O(2) c-axis Crystal Coord. (z)
Ru-O(1) Basal Plane c-axis Disp. (Å)	RuO_6 Asymmetric c-axis Disp. (Å)
Top Ca/Sr c-axis Crystal Coord. (z)	Top Ca/Sr c-axis Crystal Coord. (z)
Bottom Ca/Sr c-axis Crystal Coord. (z)	Bottom Ca/Sr c-axis Crystal Coord. (z)
Voc (eV)	Voc (eV)
Number of Fit Parameters = 6	Number of Fit Parameters = 6

to ensure the robust nature of the final results (i.e. both optimization methods should find the same results if the solution is the true global minimum solution).

The final fits were generated by including 11 non-equivalent beams: (1,1), (2,2), (3,3), (4,4), (2,0), (4,0), (2,1), (3,1), (4,1), (5,1), (4,2). Similar to the $x = 0.1$ analysis, all equivalent beams were collected and averaged to generate the experimental input data. The energy ranges for the different IV sets ranged from 3256 to 3729eV. The final results for all four surfaces analyzed yielded essentially identical results. While systematic changes were observed for $x = 0.1$ as the temperature was changed, the final fits for $x = 0.5$ at $T = 300K$ and $80K$ were well within error of the analysis and considered to be the same structure. Such a similar structure at the two refined temperatures shows the stability of the system against the tilt distortion. In contrast, bulk Sr_2RuO_4 is significantly far away in phase space from any structural phase transitions and a surface reconstruction involving the RuO_6 rotation is observed. IV curves for the resulting fit at $T = 80K$ are shown in Figure 5.12 and refinement results are listed in Table 5.2.

The most dramatic reconstruction from bulk structure for $Ca_{1.5}Sr_{0.5}RuO_4$ once again involves the inward motion of the Ca/Sr plane. Similar behavior was observed for $x = 0.1$ but the inward motion is even more pronounced for $x = 0.5$. While the RuO_6 remains undistorted, the final solution indicates a slightly larger rotation but the bulk rotation is well within the error of the rotation fit parameter. Remarkably, the Ru-O(2) bond lengths maintain their bulk values even with such a large displacement of the top Ca/Sr layer. In addition, the Ru-O(1) plane and bottom Ca/Sr planes remain near their bulk positions. Similar to $Ca_{1.9}Sr_{0.1}RuO_4$ the inward motion of the top Ca/Sr plane is analogous to an asymmetric uniaxial compression, a compression affecting primarily the upper half of the surface RuO_6. The lack of a tilt on the surface of $Ca_{1.5}Sr_{0.5}RuO_4$ suggests the system is more stable against the tilt distortion and a tilt must be harder to induce. The system is more prone to the rotation distortion as evident both in the surface structural data and the bulk structural data. While the tilt remains zero on the surface similar to the bulk, all of the $x = 0.5$ surface refinements show a slightly larger rotation than bulk. Similar trends are observed in the bulk as the doping becomes more Ca rich. For $0.2 < x < 1.0$ the bulk rotation increases as the Ca concentration increases. In addition, the unit cell parameters

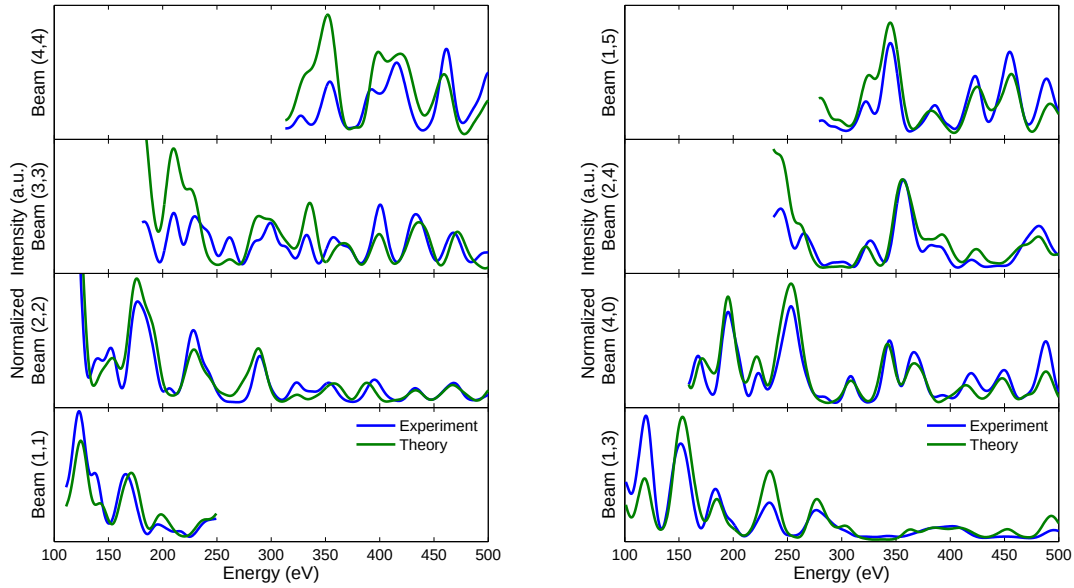

(a) (b)

Figure 5.12: Selected $Ca_{1.5}Sr_{0.5}RuO_4$ IV curves at 80K. (a) Beams (1,1), (2,2), (3,3), (4,4). (b) Beams (1,3), (4,0), (2,4), (1,5).

shrink with increasing Ca, causing a systematic decrease in the unit cell volume. Under the conditions of a shrinking unit cell due to a chemical pressure induced by the smaller Ca^{2+} cation radii, the rotation angle increases to minimize distortions to the RuO_6. While the surface a and b-axis unit cell parameters are fixed by the bulk substrate, the c-axis compression by the inward motion of the top Ca/Sr plane reduces the volume enclosing the surface RuO_6 and an increased rotation angle could be the result.

5.5 The Surfaces of $Ca_{2-x}Sr_xRuO_4$

In order to better understand the instability against the tilt distortion for the CSRO family, several different surfaces between $0.2 \leq x \leq 0.5$ were studied. All surfaces created by room temperature cleaves for this concentration range yielded identical LEED patterns to those observed for $x = 0.5$. Following a procedure similar to that for $Ca_{1.5}Sr_{0.5}RuO_4$, room temperature IV spectra were collected for the same inequivalent beams used in $x = 0.5$ analysis over similar energy ranges (50-550eV). Due to the similarities in bulk structure a reference structure for the LEED analysis was based on bulk parameters for $x = 0.5$ at $300K$. The surface refinements for the different concentrations yielded similar results as those obtained for $x = 0.5$ as shown in Figure 5.13. The general trend is the same: a dramatic inward motion of ~ 0.12 Å for the top Ca/Sr plane. All of the RuO_6 rotations were slightly larger than bulk values with the bulk value within the error of the analysis. However, it should be noted that single crystal bulk data tends to have slightly larger rotations than those for powder bulk data also shown in Figure 5.13 for comparison [70, 96]. Surprisingly, $x = 0.1$ is the only concentration that shows a RuO_6 tilt. In bulk studies, the single crystal $x = 0.2$ data shows no tilt while the powder bulk data shows a tilt exists. Due to the proximity of the $x = 0.2$ surface to the HTT-LTO phase transition, one might expect to see a tilt due to the system instability against the tilt distortion. However, the two different $x = 0.2$ surfaces studied showed no signs of a tilt at $T = 300K$. As shown in Figure 5.13(c), all of the Ru-O(2) bond lengths were similar to bulk values.

For comparison, an independent analysis of the same data using parametric grid searches were performed for $x = 0.5$, $x = 0.4$, and $x = 0.3$.[†] The grid search results are also presented in Figures 5.13. In general, the grid searches yielded the same results as the simulated annealing algorithms. The grid searches do show slightly smaller rotation angles, closer to bulk angles, for the three concentrations but the simulated annealing algorithms typically had a slightly smaller final R_p than the grid searches (typically ~ 0.02) most likely due to the lack of refinement of the grids to smaller and smaller step sizes which would require excessive computational time. The solutions using both refinement methods are well within error of each other and considered as the same structure. Such a comparison shows the robust nature of the simulated annealing algorithms to find the true global optimum solution. The advantage being computational time as exhaustive grid searches typically take days to complete while the simulated annealing procedure finds the same solution within a half-hour (both procedures were run on 3GHz Pentium IV PC's running Linux with Intel Fortran compilers).

To further investigate the robust nature of the top Ca/Sr contraction, surface structural analysis was performed on $x = 1.0, 1.5$ and 2.0. Both surfaces showed the same LEED

[†]The grid searches were performed by V. B. Nascimento.

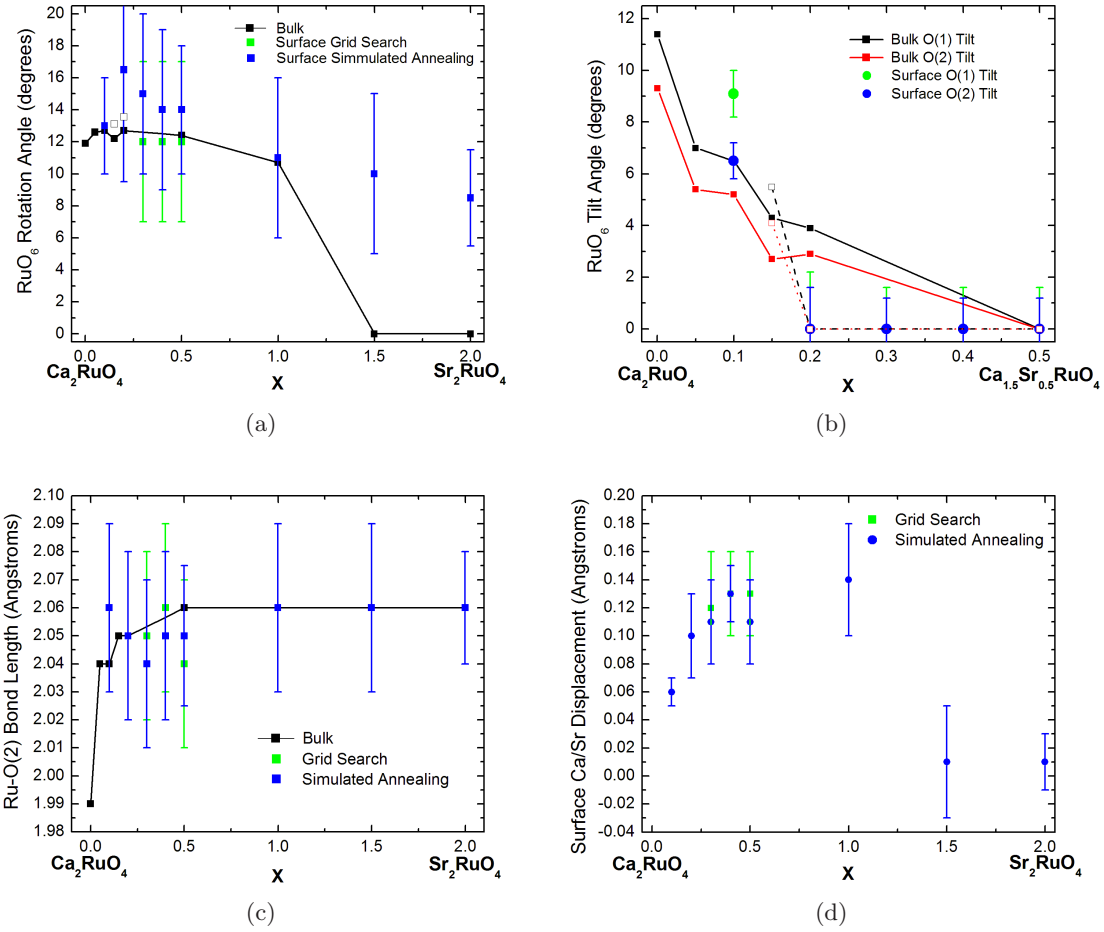

Figure 5.13: LEED refinement results for $Ca_{2-x}Sr_xRuO_4$ at $T = 300K$ for different x. The closed squares and solid lines are from bulk powder data while the open squares and dashed/dotted lines are from bulk single crystal data. (a) RuO_6 rotation angle. (b) RuO_6 tilt angles. (c) Ru-O(2) bond lengths. (d) Top Ca/Sr layer inward displacement.

pattern as $x = 2.0$ and $x = 0.5$ as expected. IV spectra were once again collected for the same set of inequivalent beams over similar energy ranges (100-500eV). The reference structure for $x = 1.0$ was a $300K$ bulk terminated model of the same concentration, once again generated from neutron data. However, for $x = 1.5$, the bulk forms in the $F4/mmm$ symmetry with no evidence of a RuO_6 rotation. Since the $x = 1.5$ LEED pattern shows a rotation similar to the surface of $x = 2.0$, a reference structure was generated with bulk parameters using neutron data for $x = 1.5$ with the exception that the surface layer RuO_6 was rotated by 12° similar to the rotation angles observed for $x < 1.5$. The refinement results are also shown in Figure 5.13. While the RuO_6 for both $x = 1.0$ and 1.5 show rotation angles similar to those observed for $x \sim 0.5$, only $x = 1.0$ shows a large inward displacement of the top Ca/Sr plane. The $x = 1.5$ data suggests the top Ca/Sr plane remains near bulk values with only a very slight inward motion evident. The $x = 2.0$ results are similar to those reported previously [101].

While the inward motion of the top Ca/Sr plane could be considered analogous to a uniaxial surface compression, it is worth noting the differences between bulk structure under pressure and the observed surface structure [78]. Under pressure, the bulk unit cell volume is observed to decrease. Surprisingly, it is the a and b-axis shrinkage in the bulk which drives the decrease in unit cell volume, as the c-axis unit cell length increases with increasing pressure. For Ca_2RuO_4, the shrinking a and b-axis with an increased c-axis results in smaller tilt angles. Even under modest pressures ($P \sim 0.5GPa$) the Ca_2RuO_4 system can be driven into the metallic phase characterized by smaller tilt angles and increased Ru-O(2) bond lengths. Since increasing the c-axis allows for the RuO_6 tilt angle to decrease, one might expect the asymmetric motion of the top Ca/Sr plane to induce a tilt, but such a trend is not observed. What is observed is the inward motion of the top Ca/Sr plane is much smaller for $x = 0.1$ than for $0.2 > x > 0.5$. The inward motion of the top Ca/Sr plane for the surface with a tilted RuO_6 is half the value of those surfaces with no tilt. The results suggest the inward motion of the top Ca/Sr plane may interfere with the tilting RuO_6.

5.6 The Surface HTT-LTO phase transition

It is rather unexpected that the surface of Sr_2RuO_4 shows a rotational distortion of the RuO_6 while Ca concentration increases up to $x = 0.2$ still shows no evidence of a surface RuO_6 tilt distortion at room temperature. The surface reconstruction for $x = 2.0$ involves the freezing of the Σ_3 phonon mode in the surface layer. This same phonon mode shows significant softening near the Brillouin zone boundary in bulk Sr_2RuO_4 evidence of the instability of the system against the rotational distortion. Similarly, the static tilt distortion involves the freezing of a Σ_4 phonon mode. Inelastic neutron studies presented in Sections 3.2 and 3.3 show typical soft mode behavior for the Σ_4 phonon. Softening at the Brillouin zone boundary becomes enhanced as the temperature is lowered and the HTT-LTO phase boundary is approached. With such similar softening behavior in the bulk for the rotation and tilt phonon modes, one might expect to see similar behavior on the surface inducing static rotations and tilts by freezing the associated phonon modes. However, such is not the case as the creation of a surface does not induce a tilt distortion for $x \geq 0.2$. To better understand the tilt instability on the surface, several surfaces were analyzed for $0.2 \leq x \leq 0.4$ across the HTT-LTO phase transition.

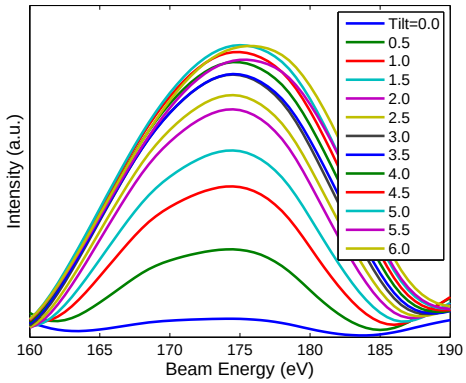

Figure 5.14: HTT-LTO LEED order parameter. Variation of Beam (3,0) intensity for different RuO_6 tilt angles. Theoretical IV calculated assuming RuO_6 rotation is 12° with O(1) and O(2) tilt angles equal.

The first study involved cleaving crystals at room temperature and traversing the phase boundary by cooling and subsequent warming of the samples. As outlined in Sections 3.1 and 5.2 the tilt distortion changes the symmetry of the system resulting in the destruction of a glide line and the appearance of Bragg reflections. The new Bragg reflections are evident in neutron scattering experiments and on the surface of $Ca_{1.9}Sr_{0.1}RuO_4$. The appearance of the extinguished Bragg reflection was used as an order parameter in the neutron studies to understand the nature of the phase transition. The appearance of the (3,0) beam in the LEED pattern is the same Bragg reflection used as an order parameter in the neutron investigation. As such, the appearance of the (3,0) beam in our LEED patterns can be used as an order parameter to investigate the surface HTT-LTO phase transition. As shown in Figure 5.14, tilting the RuO_6 extinguishes the glide line creating the appearance of the (3,0) beam at ∼175eV. The intensity of the IV spectra between $170 - 180eV$ is proportional to the tilt angle and thus used as an order parameter for our investigations. The (3,0) beam intensity was determined by integrating the IV spectra between $165 - 185eV$. Due to slight variations in the incoherent diffuse scattering from surface to surface, a flat background was subtracted determined from the IV minimums occurring at $\sim 160eV$ and $\sim 187eV$. The beam intensity was then normalized to the (2,2) beam intensity integrated between $110 - 115eV$. Due to multiple scattering effects in the LEED IV spectra, the tilt angle can affect the IV intensity of all the back scattered beams. This energy range for the normalization was chosen as model IV shows the tilt angle to have little effects on the (2,2) beam within this range.

The LEED and HREELS chambers are connected on our system with a manipulator to transfer the sample form one chamber to the other. As such, the sample is mounted on the end of a cryostat $\sim 1m$ in length attached to the manipulator. Due to the length of the cryostat, thermal contraction from modest temperature changes will move the sample through the $\sim 1mm$ incident electron beam from the LEED gun. Thus it is difficult to monitor a single sample position as the surface is cooled through the phase transition. Intensity fluctuations were noted for the (3,0) beam from one sample position to the next inducing systematic errors in the measurement. To determine the true character of the phase transition several spectra were taken at each temperature, each at a different sample

position in the incident LEED beam. In addition, sufficient time was allotted between different temperatures to ensure the sample and cryostat were in thermal equilibrium prior to taking the IV spectra.

The first system studied was $x = 0.3$ due to its moderate phase transition temperature ($T_c \sim 190K$) in the bulk [185]. As the surface is cooled below room temperature weak (3,0) beam intensity first appears at $\sim 240K$, some $50K$ above the bulk phase transition temperature. Surprisingly, weak intensity also appears around the (0,3) beam as shown in Figure 5.15. As such, it is hard to distinguish the true a and b-axis on the surface and the spot with the strongest intensity is assigned to the (3,0) beam. As the system is cooled further, the (3,0) and (0,3) beam intensity remains constant until $\sim 160K$. After this temperature, both beams begin to increase intensity until ~100K as shown in Figure 5.16 and Figure 5.17. Below $200K$, the intensity increase for both the (3,0) and (0,3) beams is similar to that observed for our bulk $Ca_{1.6}Sr_{0.4}RuO_4$ phase transition data. However, a deviation between the surface and bulk phase transition is observed upon heating. As shown in Figure 3.6 the bulk phase transition is second order as expected from previous studies. In contrast, a small thermal hysteresis is observed as the surface is subsequently heated. While a thermal hysteresis was observed for every surface phase transition measured, the systematic error of our system prevents accurate measurement of the hysteresis loop. As such it is only estimated that a $10 - 20K$ hysteresis exists between cooling and heating of the surface. Subsequent cooling and heating of the same surface traces out the same hysteresis loop within error. The IV curves shown in Figure 5.16 are an average of data collected at all sample positions for each temperature. However, to prevent underestimating the systematic error in the measurement, the different sample positions were not averaged in Figure 5.17 and thus each data point and associated statistical error are presented in the results. Based on these results, the phase transition temperature is defined as the temperature at which a dramatic increase in Beam (3,0) intensity is first encountered and established as $T_c = 170 \pm 10K$. While the breaking of symmetry at the surface induces the rotational distortion, the tilt distortion is not induced until temperatures $\sim 20K$ below the bulk phase transition temperature.

To better understand differences between the bulk and surface phase transition, phase transitions for $x = 0.2, 0.4$ and 0.5 were investigated. While bulk neutron powder diffraction data shows the $x = 0.2$ system to be in the *Pbca* phase, single crystal neutron data shows the system to be in the $I4_1/acd$ symmetry. The LEED pattern for the surface of our $x = 0.2$ single crystals cleaved at room temperature is consistent with that of an $I4_1/acd$ symmetry with only a rotational distortion and no evidence of a tilt as shown in Figure 5.18(a). However, upon cooling, weak (3,0) and (0,3) beams appear at $\sim 285K$. The weak intensity remains until $\sim 250K$ where the beam intensity increases similar to that observed for $x = 0.3$. Due to the systematic errors in our system preventing accurate measurements of the hysteresis loops, such loops were not investigated for $x = 0.2$. Similar measurements were performed on $Ca_{1.6}Sr_{0.4}RuO_4$ where a larger separation between bulk and surface T_c is found. While our neutron studies show the bulk $T_c \sim 155K$ as presented in Section 3.3, LEED data at $T = 100K$ shown in Figure 5.18(b) shows only weak diffuse scattering at the (3,0) position. The crystals analyzed in the LEED experiment was the same crystal used in the neutron scattering experiment. The weak diffuse scattering first appears around $T \sim 120K$, but IV taken at $T = 80K$ still shows no sign of an intensity increase signaling the start of the phase transition. While lower temperature spectra were not taken for $x = 0.4$,

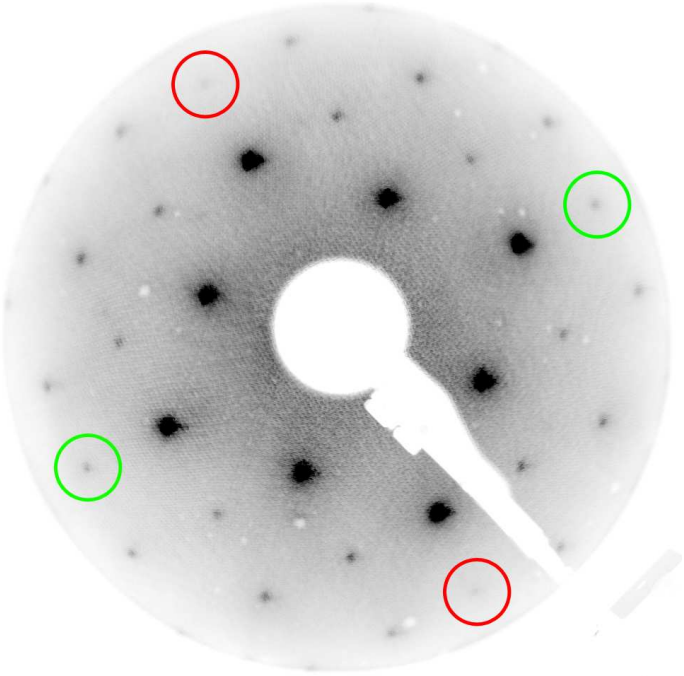

Figure 5.15: Tilt domains on $Ca_{1.7}Ca_{0.3}RuO_4$. Green (red) circles show Beam(3,0) (Beam(0,3)) on the surface at 132eV.

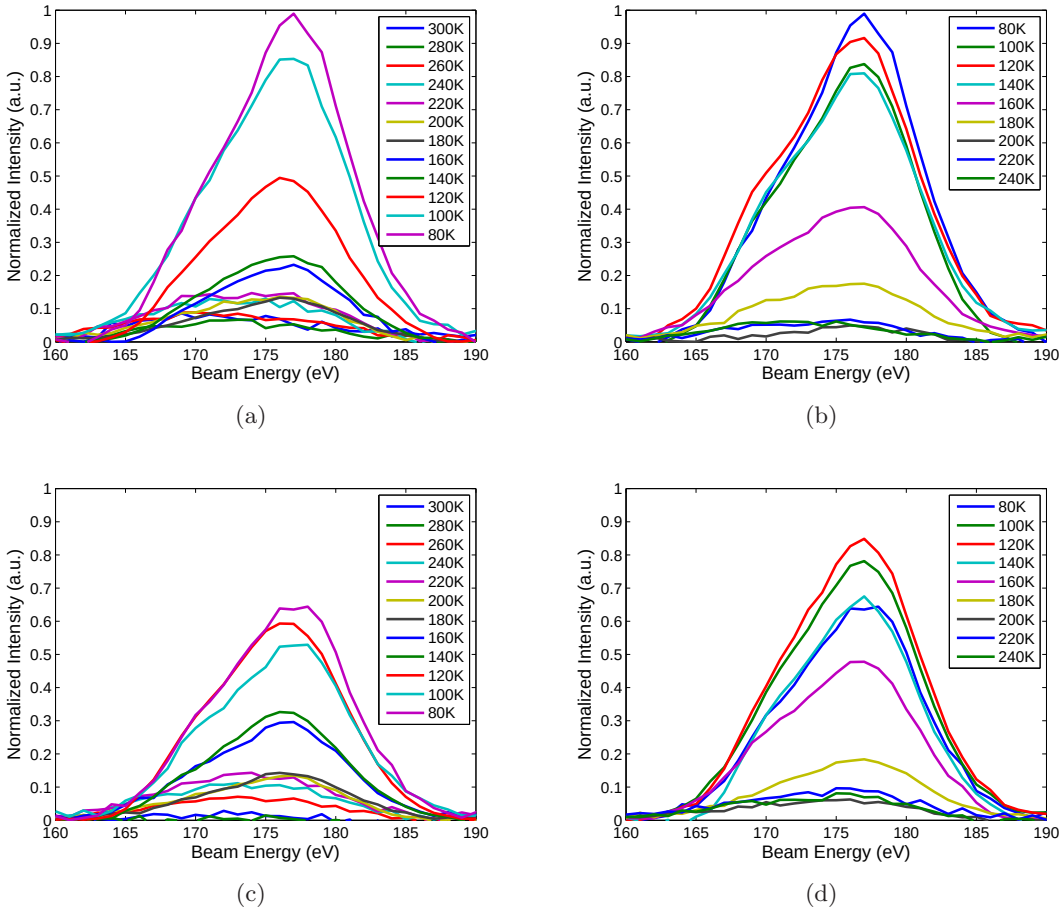

Figure 5.16: Experimental IV data for $Ca_{1.7}Sr_{0.3}RuO_4$ through phase transition. All IV data have been averaged and normalized at each temperature. (a) Beam (3,0) data upon cooling. (b) Beam (3,0) data upon warming. (c) Beam (0,3) data upon cooling. (d) Beam (0,3) data upon warming.

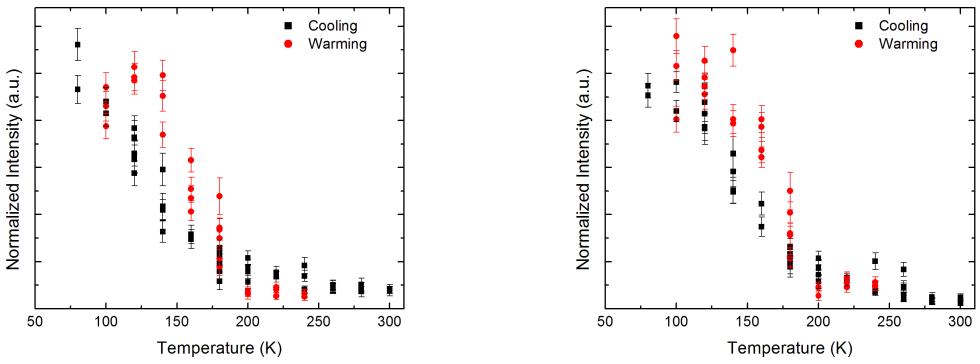

(a) (b)

Figure 5.17: Experimental HTT-LTO order parameter for $Ca_{1.7}Sr_{0.3}RuO_4$ surface. Data shown for (a) Beam (3,0), and (b) Beam (0,3).

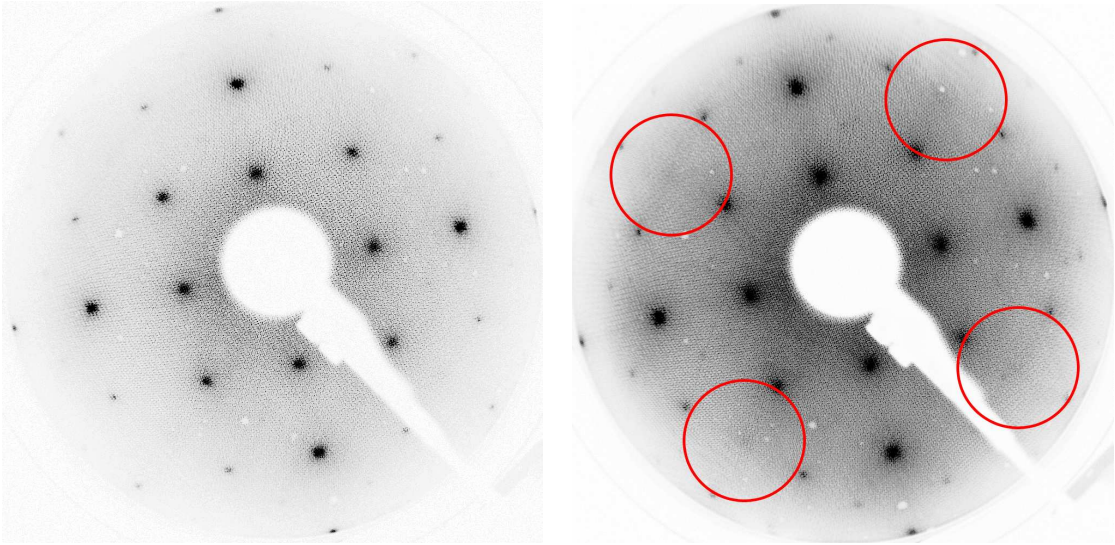

(a) (b)

Figure 5.18: LEED patterns for $Ca_{1.8}Sr_{0.2}RuO_4$ and $Ca_{1.8}Sr_{0.2}RuO_4$ surfaces. (a) LEED pattern for $x = 0.2$ at $T = 300K$ showing no evidence of tilt distortion. (b) LEED pattern for $x = 0.4$ at $T = 80K$ showing only weak diffuse scattering at (3,0) and (0,3) positions.

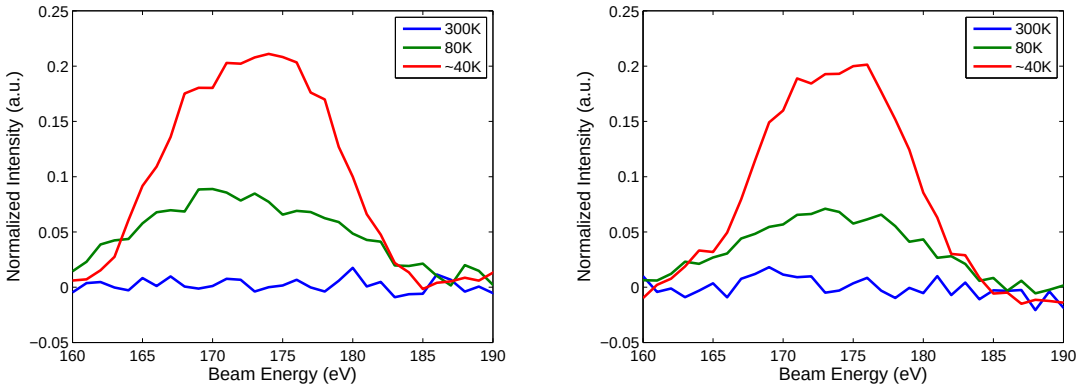

(a) (b)

Figure 5.19: Experimental HTT-LTO order parameter IV for $Ca_{1.5}Sr_{0.5}RuO_4$ surface. Data shown for (a) Beam (3,0), and (b) Beam (0,3).

it is anticipated that T_c should exist between $60 - 75K$ based on trends established from $x = 0.2$ and $x = 0.3$.

Measurements were also performed on $Ca_{1.5}Sr_{0.5}RuO_4$ where it is found that intensity in the (3,0) and (0,3) beams first appears $\sim 75K$. Cooling the system further shows the surface of $Ca_{1.5}Sr_{0.5}RuO_4$ undergoes the HTT-LTO phase transition in contrast to the bulk. While $x = 0.5$ is the bulk terminus for the HTT-LTO phase transition and labeled as a quantum critical point, the breaking of symmetry by the creation of a surface alters the quantum criticality of the surface and the phase transition appears. Our experimental apparatus did not include a radiation shield around the sample inducing error in our surface temperature measurement and thus the transition temperature for $x = 0.5$ is estimated between $30 - 45K$. While the (3,0) and (0,3) beam intensity at the lowest achievable temperatures for our system ($\sim 35K$) indicate that the phase transition is not complete, the intensity is significant enough to show the surface is below the phase transition temperature as shown in Figure 5.19.

The appearance of the (0,3) beam is unexpected and must be investigated further. In the *Pbca* phase, the tilts are well correlated from layer to layer with all the tilts along the [0 1 0] phase appearing with the same handedness as shown in Figure 1.10. Plus the tilt axis is always near the b-axis creating an orthorhombic splitting of the a and b-axis unit cell parameters as the system enters into the tilted phases by changing Ca concentration. A similar orthorhombic splitting is observed for $0.2 < x < 0.5$ as the bulk system enters into the LTO-phase. Such data would suggest that the tilts in the LTO phase would also be well correlated from layer to layer. To better understand the tilt axis disorder observed on the surface upon cooling through the LTO phase transition, single crystals of $x = 0.3$ were prepared and cooled to $T = 80K$ prior to cleaving. While bulk behavior would suggest that a single tilt axis exist for surfaces created in the LTO phase, tilt axis disorder is evident as intensity in the (3,0) and (0,3) beams exist for crystals cleaved in the LTO phase. The same behavior is observed for $x = 0.2$ crystals cleaved below the LTO phase boundary.

While the surfaces for $0.2 < x < 0.5$ show disorder in the tilt axis orientation, the intensity in the (3,0) and (0,3) beams were typically different. Numerous samples were

observed and normally one of the beams had an enhanced intensity over the other. Only one case was observed where both beams had identical intensity and only once case was observed where the (0,3) beam was completely extinguished. Such observations suggest the formation of tilt domains on the surface. A majority tilt axis giving rise to the more intense (3,0) beam and a minority tilt axis domain creating the (0,3) beam intensity. The formation of tilt domains is surprising as it requires breaking of the RuO_6. Scanning Tunneling Microscopy images of Sr_2RuO_4 reveal line defects that preferentially align along the [1 0 0] and [0 1 0] directions as shown in Figure 5.20. While the surface topology of the doped samples are difficult to observe due to nanoscale electronic inhomogeneities [186], it is expected that similar defects occur on the surfaces of the doped samples. The disorder of the tilt axis upon cooling through the LTO phase boundary would suggest that such defects could involve broken octahedra. The length scale of the line defect is consistent with a missing Oxygen atom necessary to break the octahedral. While it could be argued that such defects occur only on the surface and are induced due to the cleaving process. It is unlikely that cleaving such a quasi 2-dimensional layered material would induce the defects AND create disorder in the RuO_6 tilt axis as the tilt is already induced below T_c. The appearance of the (0,3) beam in the LEED pattern from the low temperature cleaved surfaces for $x = 0.2$ and $x = 0.3$ is most likely due to disorder existing in the bulk prior to cleaving. Strain induced by a disordered layer could create amenable conditions for creating a surface from cleaving making the disordered layers more likely to appear as surfaces. The disorder is most likely present prior to the creation of the surface. Attempts were made to refine the surface structure of $x = 0.3$ below T_c. LEED-IV spectra were collected on a sample surface that showed similar intensity for the (3,0) and (0,3) beams. The IV collected showed a 4-fold symmetry for all the collected beams. While only a 2-fold degeneracy is observed for most of the $x = 0.1$ beams due to the presence of the single glide line. Two different reference models were utilized for the refinement. The first model consisted of the $I4_1/acd$ model used for $x = 0.3$ high temperature studies. The difference being the O(1) and O(2) tilts were not constrained to zero during the parameter search. The theoretically calculated beams were averaged together to maintain the 4-fold degeneracy observed in the LEED spectra. While the high temperature refinements yielded a $Rp = 0.28$ for $x = 0.3$, the low temperature structure refinement yielded a $R_p = 0.55$. As a second model, the $x = 0.1$ *Pbca* structure was used. If multiple tilt domains of equal size are assumed, then the domains with the tilt axis rotated by 90° would produce a LEED pattern rotated by 90°. Thus to emulate the observed IV spectra theoretical IV for beams overlapping by the 90° rotation were averaged together. For example, all eight (±2,±1) were averaged together. This procedure generated the correct beam degeneracy observed and the refined tilt values simply corresponded to identical tilt values in both domains, tilting around their respective axis. The final fit produced a marginal $R_p = 0.35$, but it is a distinct improvement over the previous model. The refined search produced parameters similar to those observed for $x = 0.1$: RuO_6 rotation = 13(6)°; O(1) tilt = 8(4)°; O(2) tilt = 5.5(3.5)°; with Ru-O(2) bond lengths = 2.04(4)Å. While the errors are large and the final fit parameters should be considered with skepticism, it is interesting to note that the refinement showed an inward displacement of the top Ca/Sr plane of 0.81(35)Å, some 0.3Å less than the high temperature phase.[‡]

[‡]However, it is noted that the high temperature Ca/Sr displacement is within the error of the refinement.

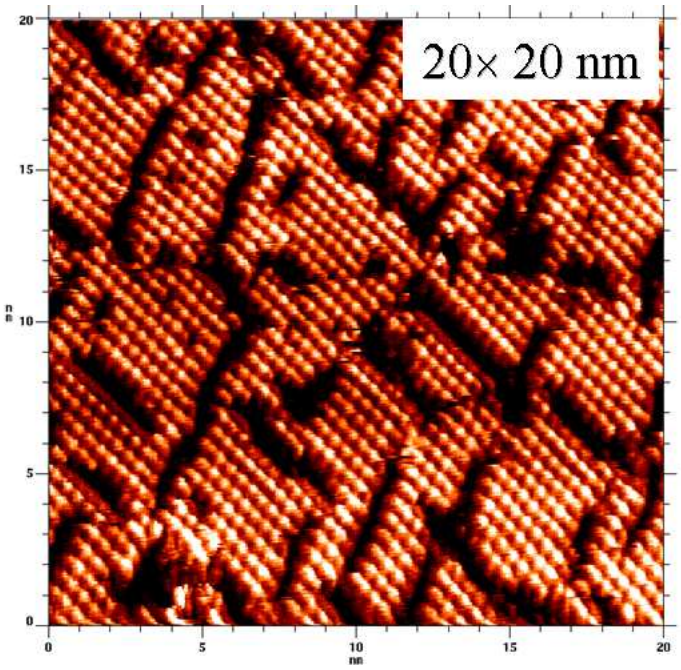

Figure 5.20: Scanning Tunneling Microscopy image of Sr_2RuO_4 at $T = 25K$. Defects preferentially align in the [100] and [010] directions [187].

While the CSRO family is evidently unstable against the rotation distortion, it is more stable versus the tilt instability. While the creation of a surface creates enough of a distortion to freeze the Σ_3 phonon mode on the surface of Sr_2RuO_4, the breaking of symmetry does not induce a tilt even for $Ca_{1.8}Sr_{0.2}RuO_4$ when cleaved at room temperature. While the HTT-LTO phase transition temperatures are not significantly different on the surface compared to bulk values for $x = 0.2$ and $x = 0.3$, there is evidence of the tilt instability as the appearance of the (3,0) and (0,3) beams at temperature $40 - 50K$ above T_c. The weak spots are diffuse above T_c and most likely due to short range correlations developing.

5.7 LEED Analysis Conclusions

Due to the layered structure of the CSRO family the crystals are amenable to cleaving. Cleaving crystals *in situ* allows for the creation of pristine surfaces never complicated by the exposure to atmosphere. However, the layered structure also suggests that the surface structure is likely to be similar to the bulk. Layers of rigid RuO_6 octahedra connected in-plane separated by a rocksalt type layer suggests that the breaking of symmetry should have little consequences on the structure or properties of the surface layer. Bulk properties show quasi 2-dimensional behavior and thus it should be expected that the surface could emphasize the quasi 2-dimensional nature of the material. Indeed the results presented here do show that the surfaces of the CSRO family have remarkable similarities to the bulk structure. The RuO_6 rotation and tilt angles observed are not significantly different than bulk values. In addition, the observed Ru-O bond lengths are not dramatically altered due to the broken symmetry. In fact the most dramatic structural difference between the bulk and surface layers is an inward contraction of the topmost Ca/Sr plane. Other than this outermost distortion, the surface seems bulk-like upon first glance. However, even subtle differences can have a profound impact on properties and phases in correlated electron systems.

The impact of broken symmetry on the surface structure of the CSRO family first appeared as a rigid RuO_6 rotation induced on the surface of Sr_2RuO_4. Bulk data shows the instability of the rotational distortion for the family and the creation of a surface emphasized the instability by freezing the Σ_3 phonon into a static surface reconstruction. However, such is not the case for the tilt instability. While bulk data similarly shows the instability of the system against the tilt distortion, the surface appears more robust against the tilt distortion. For $x < 0.5$, the phase transitions involving the tilt of the RuO_6 are suppressed to lower temperatures. This is true not only for the HTT-LTO phase transition, but for the MIT phase transition as well. While several structural parameters change across the bulk MIT, increasing RuO_6 tilts are one of the typical characteristics of the bulk insulating phase and the surface tilt simply never changes. In addition, a thermal hysteresis is observed across the HTT-LTO phase transition suggesting that the tilt instability is less displacive in character and has more characteristics of a first order phase transition between two distinct ground states.

The MIT is definitely first order in character in the bulk with distinct jumps in structural parameters observed across T_c. Extensive theoretical and experimental studies have shown how the structure is intrinsically linked to bulk transport properties. The increased tilts, and flattened octahedra with shortened Ru-O(2) bond lengths adjusts the bandwidth and orbital occupations to create the Mott insulating state. However, such is not the case on

the surface. While the RuO_6 volume, Ru-O(1) bond lengths and O(1)-O(1) bond lengths take on values characteristic of the bulk insulating phase, the Ru-O(2) bond lengths are characteristic of the metallic bulk and the octahedra tilt is in between the angles achieved in the bulk metallic and insulating phases. What is more remarkable is that the surface structure of $Ca_{1.9}Sr_{0.1}RuO_4$ is static. The numerous sample surfaces all yield the same results as a surface that does not significantly change with temperatures down to 70K below the bulk T_c. While STS and HREELS results observe the MIT on the surface with $T_c \sim 20K$ below the bulk, a dramatic change in surface structure is not observed. While the electron localization mechanism is well established in the bulk, similar behavior is not evident on the surface. Thus one is left looking for new localization mechanisms on the surface as the structural arguments in the bulk simply do not work for the surface.

To understand the true nature of the CSRO surfaces we must observe what does change on the surface and understand why. The most dramatic change on the surface of the family is the topmost Ca/Sr layer. For $0.2 < x \leq 1.0$ the top Ca/Sr layer demonstrates an inward motion of ~ 0.12Å while for $x > 1.0$ the inward motion is negligible. In addition, for $x = 0.1$ it is observed that the inward motion is only 0.6Å, half of the distance observed for all other concentrations with $x < 1.0$ measured at room temperature. The implications are that the inward motion of the top Ca/Sr plane interferers with the tilt of the RuO_6. In the bulk a shrinking cage within which the octahedra is positioned will induce the tilt but the distortions on the surface are highly asymmetric. While the bottom Ca/Sr plane shows very little distortion and the c-axis position of the RuO_6 remains close to its symmetrically defined position using bulk symmetry generators. On the surface of $x = 0.1$, the inward displacement creates an inter-planar distance between the Ru and top Ca/Sr planes similar to those observed in the bulk insulating phases. However, on the surfaces of $0.2 \leq x \leq 1.0$, the inward displacement creates an inter-planar distance much smaller than encountered anywhere in the bulk of the family. Such a large asymmetric distortion most likely interferers with the tilting RuO_6 essentially "pinning" the octahedra in a more upright position making the surface more stable against the tilt distortion across the HTT-LTO phase transition and not allowing the $x = 0.1$ surface to achieve the tilts observed in the bulk insulating phases. Thus the interference lowers the HTT-LTO phase transition temperature for $x < 0.5$ as the additional strain must be overcome before the octahedra can tilt and the interference "locks" the octahedra into the metallic phase orientation not allowing it to achieve the orientation of the bulk insulating phase. While the low temperature data for $x = 0.3$ supports such a claim with the smaller inward displacement than that observed at higher temperatures with no RuO_6 tilt, it is noted that the R_p for the structural refinement is not as satisfactory as the other refinements.

The question arises as to why such a large inward displacement is observed for the Ca rich samples. The reasons are most likely the same reasons that the unit cell volume shrinks as more Ca is added to the bulk system. The smaller Ca cation radii induces a chemical pressure shrinking the unit cell volume. Since the RuO_6 are rigid objects robust against compression, the shrinking cell eventually induces the rotation and tilt distortions allowing the RuO_6 to maintain a fairly constant volume throughout the metallic phases. However, on the surface the rocksalt layer is broken and the restoring forces above the surface plane suddenly vanish. As a result, the top Ca/Sr plane is pulled down into the bulk. The observed displacement as x is varied suggests that the more Sr rich planes have less displacement into the surface. Since the a and b-axis lattice parameters are fixed by the

bulk substrate, the ab-plane does not expand with the inward motion and the Sr rich planes with the larger Sr cations simply have less room to displace inward. As the surface becomes Ca rich, the ab-plane dimensions are still fixed by the bulk substrate but the smaller Ca cations and the removal of the restoring forces above the surface plane allows the Ca/Sr plane to displace further into the surface. Thus for Sr rich samples, no inward displacement is observed within the error of the analysis but the removal of the restoring forces above the surface plane still creates an inward stress. Such an inward stress with the larger Sr cations creates a surface pressure but one which is less asymmetric and more similar to the chemical pressure induced by the uniform Ca substitution in the bulk. It is likely this surface pressure and the subtle strain that it creates is responsible for freezing the unstable Σ_3 mode on the surface of Sr_2RuO_4.

Such an argument suggest a crossover point. A point at which the effective size of the cations in the topmost Ca/Sr plane are small enough to show inward displacements large enough to be observed with the LEED technique. While our data suggests such a crossover point exists somewhere between $1.0 < x < 1.5$, more studies need to be performed to better understand when the surfaces first show significant inward Ca/Sr displacements. However, there is another crossover point which may exist. The bulk studies show the instability of the system against the tilt distortion but our surface results near the quantum critical point show contradictory results. For $x = 0.2$ and $x = 0.3$, the HTT-LTO phase transition is suppressed below the bulk phase transition temperatures by $\sim 20K$ while $x = 0.4$ shows Tc to be at least $70K$ below the bulk T_c. On the contrary, for $x = 0.5$, the surface shows signs of the tilt instability $\sim 80K$ with the $40K$ surface showing the LTO superstructure reflections. Thus a competition appears between the strain energies created by the inward motion of the top Ca/Sr plane and the tilting octahedra. While the $0.5 < x < 1.0$ show significant inward Ca/Sr displacements, the resulting strain energy may be less due to the larger cations effectively making it easier for the tilt instability to be observed. Less strain energy created by the inward Ca/Sr motion makes it easier for the tilting RuO_6 to "push out" the Ca/Sr plane allowing for a lower energy structural ground state with a tilted octahedra. Such an argument would suggest another crossover between those concentrations where the strain from the inward displacement of the Ca/Sr plane wins lowering the observed HTT-LTO T_c and those concentrations where the tilt instability strain energy wins allowing for higher observed T_c. Our data suggests such a crossover point to exist for $x \sim 0.4$.

Bulk studies suggest $x = 0.5$ to be the $T = 0K$ terminus for the HTT-LTO phase transition and a quantum critical point (QCP). Our surface studies suggests the QCP is altered on the surface. While the $x = 0.2, 0.3$ and 0.4 data suggests the HTT-LTO phase boundary is lowered thus moving the QCP to lower x, the observed phase transition on $x = 0.5$ shows that it is not that simple. While the Sr_2RuO_4 surface demonstrates the instability of the system against the rotation distortion by freezing the Σ_3 phonon mode, the surface of $x = 0.5$ demonstrates that there is a point in which the Σ_4 mode is frozen out at higher temperatures by the creation of a surface demonstrating the system instability against the tilt distortion. Thus it is anticipated that the LTO phase transition can be observed on surfaces with $x > 0.5$. As a result the surface QCP is most likely shifted to higher Sr concentrations despite the fact that lower T_cs are encountered for $x < 0.5$. The results of our surface structural studies are summarized in the surface phase diagram for the CSRO family presented in Figure 5.21.

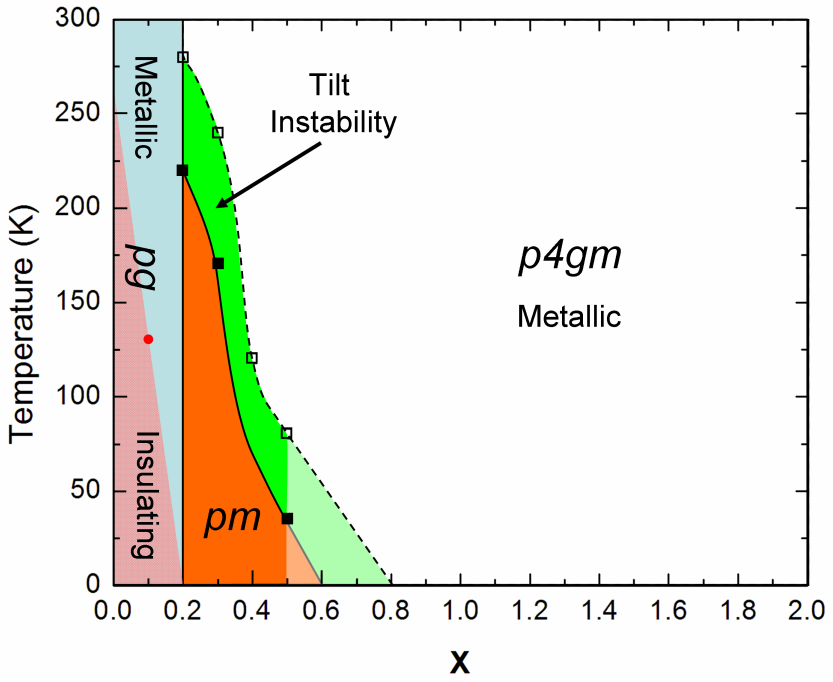

Figure 5.21: Surface phase diagram for $Ca_{2-x}Sr_xRuO_4$. Solid lines denote structural phase transitions, dashed line indicates onset of tilt instability. Light orange and green regions are projections based on current trends. Light red region indicates insulating phase, based on experimental results no structural phase boundary is indicated between metallic and insulating phases for $x < 0.2$.

While it is argued that the the inward motion of the top Ca/Sr plane pins the tilt of the RuO_6 octahedra on the surface of $x = 0.1$, the static surface structure does nothing to explain the observed MIT. Due to the static structure, it would be expected that the surface remains metallic and never enters the insulating phase, but such is not the case as demonstrated by STS and HREELS. For $x < 0.2$ there exists a Jahn Teller (JT) distortion in the bulk. As a result the Ru-O(1) plane is elongated in one direction creating two different Ru-O(1) bond lengths and two different O(1)-O(1) bond lengths in the Ru-O(1) plane. The orbital degrees of freedom are also shown to be active and it is suggested that orbital ordering combined with spin-orbit coupling play key roles in the band filling and magnetic ordering observed in the family. Our surface structural data also suggests the existence of the JT distortion in the surface layer. The refinement R_p's were improved by allowing for different Ru-O(1) bond lengths and all the different $x = 0.1$ surfaces suggested a distinct trend. The only significant structural difference above and below the surface MIT is the atomic positions of the O(1)s. While room temperature data and temperatures below T_c suggest a modest JT distortion, temperatures slightly above T_c show an enhancement of the JT distortion. This enhancement is much larger than any JT distortion existing in the bulk but caution must be advised as the error involved with the in-plane coordinates of the O(1) atoms are among the worst of the analysis. However, all the surfaces analyzed just above T_c have the same trend and the displacement is large enough to show the enhancement exists despite the large associated error. Thus the data suggests active and possibly frustrated orbital degrees of freedom which suddenly change across the surface T_c. The possibility exists for the orbital degrees of freedom to be frustrated due to the structural distortions existing in the surface layer and actively play a role in the MIT at a suppressed T_c due to the frustration.

While our structural studies show the O(1) atomic position to be the only ones with appreciable changes across T_c, our data do observe other changes which could play roles in the observed MIT. For example, the HREELS data show a distinct upshift in the A_{1g} phonon mode energy below T_c however the structural studies show no signs of changes to the Ru-O(2) bond lengths associated with the A_{1g} mode. Such data suggests the possibility of electron-phonon coupling that appreciably changes across T_c. Another example is the large in-plane motions observed for the top Ca/Sr plane. In addition to the large inward motion, the $x = 0.1$ surface also shows large in-plane motions shortening the minimum Ca-O(2) bond distance by ~ 0.1Å from those observed in the bulk. Most would argue that the Ca-O plane plays little role in the transport properties of the Ru-O plane. However, it is noted that the carrier concentration in the Cu-O plane of $La_{2-x}Sr_xCuO_4$ is adjusted by La/Sr substitution on the same Ca/Sr atomic site. Experimental and theoretical studies have also demonstrated how orbital occupations significantly change in the CSRO family as the structure becomes distorted. Thus it is conceivable that severe in-plane and out-of-plane distortions of the top Ca/Sr plane can shift the distribution of charge to maintain neutrality along the Ca-O plane and subsequently effect the Ru-O charge distribution and orbital occupations through the hybridization between the O(2)-p orbitals and the Ru $d_{xz/yz}$ orbitals. A final example involve the observations of the raw data across the phase transition: defects. While the surface structure of $x = 0.1$ does not change across T_c, the raw LEED images shows that the surface itself does change. Defects have been shown to exist on the surfaces of Sr_2RuO_4 and $Sr_3Ru_3O_7$ and both systems show the defects preferentially order along the [100] and [010] directions [187, 188]. Defects created along the [100] and [010] directions with irregular

distances between the defects could easily produce the streaking patterns observed in our LEED data. While it is unfortunate that the nanoscale electronic inhomogenities existing on the doped surfaces of the CSRO family prevent direct observation of defects using the STM, the defects must be real and grow as further cooling or subsequent warming usually results in complete surface degradation and crumbling of the sample. While the surface structure remains in a metallic configuration, defects could interfere with the electronic phase transitions on the surface as they have been observed to interfere with structural transitions on surfaces [169, 172].

The existence of a metal-to-insulator transition not accompanied by a structural phase transition is quite remarkable. While the bulk MIT appears to be well understood, the surface studies casts doubt on how deep our understanding really is. Several possible ideas for the electron localization mechanism on the surface have been presented but it is obvious that the surface MIT is not fully understood. Active research continues as of the writing of the dissertation to further investigate the role of different degrees of freedom in complex oxide systems and their interactions to produce the properties we observe. The surfaces of such systems provides new information and new characteristics never before observed in the bulk. As surface sensitive techniques such as LEED continue to evolve, more complicated systems with more intricate balances between different ground states can be explored. Surfaces can not only be explored for new phases and new properties, but can shed new light on existing bulk phases in correlated electron systems. Hopefully, this dissertation does not serve as an ending to studies on an interesting system, but a new beginning in a new direction to understanding the exotic properties of correlated electron systems and new insights allowing us to harness their potential.

Bibliography

Bibliography

[1] Birgeneau, R. J. & Kastner, M. A. Frontier physics with correlated electrons. *Science* **288**, 437 (2000). 1

[2] Tokura, Y. & Nagaosa, N. Orbital physics in transition-metal oxides. *Science* **288**, 462 (2000). 1

[3] Orenstein, J. & Millis, A. J. Advances in the physics of high-temperature superconductivity. *Science* **288**, 448 (2000). 1

[4] Sachdev, S. Quantum criticality: Competing ground states in low dimensions. *Science* **288**, 475 (2000). 1

[5] Watson, P. R., Van Hove, M. A. & Hermann, K. *NIST Surface Structure Database (SSD) Version 5.0* (National Institute of Standards and Technology, Gaithersburg, MD, 2004). 1

[6] Henrich, V. E. & Cox, P. A. *The Surface Science of Metal Oxides* (Cambridge University Press, New York, NY, 1994). 1

[7] Maekawa, S. *et al. Physics of Transition Metal Oxides* (Springer-Verlag, Berlin, 2004). 1

[8] Bednorz, J. G. & Mller, K. A. Possible high-T_c superconductivity in the Ba-La-Cu-O system. *Z. Phys. B: Condens. Matter* **64**, 189 (1986). 1.1, 5

[9] Cava, R. J., van Dover, R. B., Batlogg, B. & Rietman, E. A. Bulk superconductivity at 36 K in $La_{1.8}Sr_{0.2}CuO_4$. *Phys. Rev. Lett.* **58**, 408 (1987). 1.1

[10] Tarascon, J. M., Greene, L. H., McKinnon, W. R., Hull, G. W. & Geballe, T. H. Superconductivity at 40 K in the oxygen-defect perovskites $La_{2-x}Sr_xCuO_{4-y}$. *Science* **235**, 1373 (1987). 1.1

[11] Cava, R. J. *et al.* Bulk superconductivity at 91 K in single-phase oxygen-deficient perovskite $Ba_2YCu_3O_{9-\delta}$. *Phys. Rev. Lett.* **58**, 1676 (1987). 1.1

[12] Wu, M. K. *et al.* Superconductivity at 93 K in a new mixed-phase Yb-Ba-Cu-O compound system at ambient pressure. *Phys. Rev. Lett.* **58**, 908 (1987). 1.1

[13] Murphy, D. W. *et al.* New superconducting cuprate perovskites. *Phys. Rev. Lett.* **58**, 1888 (1987). 1.1

[14] Mackenzie, A. P. & Maeno, Y. The superconductivity of Sr_2RuO_4 and the physics of spin-triplet pairing. *Rev. Mod. Phys.* **75**, 657 (2003). 1.1, 1.2, 5

[15] Damascelli, A., Hussain, Z. & Shen, Z. X. Angle-resolved photoemission studies of the cuprate superconductors. *Rev. Mod. Phys.* **75**, 473 (2003). 1.1, 1.4

[16] Won, H., Haas, S., Parker, D. & Maki, K. High-T_c cuprate superconductivity in a nutshell. *Phys. Stat. Sol. B* **242**, 363 (2005). 1.1

[17] Maeno, Y. *et al.* Superconductivity in a layered perovskite withot copper. *Nature* **372**, 532 (1994). 1.1, 1.2, 1.2, 1.5, 4.3, 5

[18] Cao, G., Alexander, C. S., McCall, S., Crow, J. E. & Guertin, R. P. From antiferromagnetic insulator to ferromagnetic metal: a brief review of the layered ruthenates. *Matl. Sci. Eng. B* **63**, 76 (1999). 1.1

[19] Ruddlesden, S. N. & Popper, P. New compounds of the K_2NiF_4 type. *Acta Cryst.* **10**, 538 (1957). 1.1

[20] Ruddlesden, S. N. & Popper, P. The compound of $Sr_3Ti_2O_7$ and its structure. *Acta Cryst.* **11**, 54 (1958). 1.1

[21] Randall, J. J. & Ward, R. J. The preparation of some ternary oxides of the platinum metals. *J. Am. Chem. Soc.* **81**, 2629 (1959). 1.1

[22] Imai, T., Hunt, A. W., Thurber, K. R. & C., C. F. O^{17} NMR evidence for orbital dependent ferromagnetic correlations in Sr_2RuO_4. *Phys. Rev. Lett.* **81**, 3006 (1998). 1.1, 1.2

[23] Mukuda, H. *et al.* Novelcharacter of spin fluctuations in spin-triplet superconductor Sr_2RuO_4: O-17-NMR study. *J. Phys. Soc. Jpn.* **67**, 3945 (1998). 1.1, 1.2

[24] Cao, G. *et al.* Itinerant-to-localized electron transition in $CaRu_{1-x}Sr_xO_3$ and $SrRu_{1-x}Pb_xO_3$. *Phys. Rev. B* **54**, 15144 (1996). 1.1

[25] Braden, M., Moudden, A. H., Nishizaki, S., Maeno, Y. & Fujita, T. Structural analysis of Sr_2RuO_4. *Physica C* **273**, 248 (1997). 1.2

[26] Huang, Q. *et al.* Neutron powder diffraction study of the crystal-structures of Sr_2RuO_4 and Sr_2IrO_4 at room-temperature and at 10−K. *J. Solid State Chem.* **112**, 355 (1994). 1.2, 1.2, 3.6

[27] Gardner, J. S., Balakrishnan, G. & Paul, D. M. Neutron powder diffraction study of Sr_2RuO_4 and $SrRuO_3$. *Physica C* **252**, 303 (1995). 1.2

[28] Neumeier, J. J. *et al.* Magnetic, thermal, transport, and structural properties of $Sr_2RuO_{4+\delta}$: Enhanced charge-carrier mass in a nearly metallic oxide. *Phys. Rev. B* **50**, 17910 (1994). 1.2

[29] Walz, L. & Lichtenberg, F. Refinement of the structure of Sr_2RuO_4 with 100K and 295K x-ray data. *Acta Cryst. C* **49**, 1268 (1993). 1.2

[30] Maeno, Y., Maurice, R. & Sigrist, M. The intriguing superconductivity of strontium ruthenate. *Phys. Today* **54**, 42 (2001). 1.2, 1.2, 1.5, 3.6, 4.3, 5

[31] Ohishi, K. & Syono, Y. Dependence of lattice-parameters and T_c on the hole concentration determined by precise measurement of the oxygen-content of $La_{2-x}M_xCuO_{4-y}$ (M = Ba, Sr, Ca). *J. Solid State Chem.* **95**, 136 (1991). 1.2, 3.6

[32] Khan, M. K. R., Mori, Y., Tanaka, I. & Kojima, H. Growth and superconductivity of $La_{2-x}Ca_xCuO_4$. *Physica C* **262**, 202 (1996). 1.2, 3.6

[33] Picone, P. J., Jenssen, H. P. & Gabbe, D. R. Phase-diagram and single-crystal growth of pure and Sr doped La_2CuO_4. *J. Cryst. Growth* **91**, 463 (1988). 1.2

[34] Mackenzie, A. P. *et al.* Extremely strong dependence of superconductivity on disorder in Sr_2RuO_4. *Phys. Rev. Lett.* **80**, 161 (1998). 1.2

[35] Mackenzie, A. P. *et al.* Quantum oscillations in the layered perovskite superconductor Sr_2RuO_4. *Phys. Rev. Lett.* **76**, 3786 (1996). 1.2, 1.2

[36] Bergemann, C., Julian, S. R., Mackenzie, A. P., NishiZaki, S. & Maeno, Y. Detailed topography of the fermi surface of Sr_2RuO_4. *Phys. Rev. Lett.* **84**, 2662 (2000). 1.2, 1.2

[37] Bergemann, C., Mackenzie, A. P., Julian, S. R., Forsythe, D. & Ohmichi, E. Quasi-two-dimensional fermi liquid properties of the unconventional superconductor Sr_2RuO_4. *Adv. Phys.* **52**, 639 (2003). 1.2, 1.2, 1.4

[38] Rice, T. M. & Sigrist, M. Sr_2RuO_4: an electronic analogue of ^{3}He. *J. Phys. Condens. Matter* **7**, L643 (1995). 1.2

[39] Baskaran, G. Why is Sr_2RuO_4 not a high T_c superconductor? electron correlation, hund's coupling and p-wave instability. *Physica B* **223–224**, 490 (1996). 1.2

[40] Ishida, K. *et al.* Spin-triplet superconductivity in Sr_2RuO_4 identified by ^{17}O Knight shift. *Nature* **396**, 658 (1998). 1.2

[41] Luke, G. M. *et al.* Time-reversal symmetry breaking superconductivity in Sr_2RuO_4. *Nature* **394**, 558 (1998). 1.2

[42] Duffy, J. A. *et al.* Polarized-neutron scattering study of the Cooper-pair moment in Sr_2RuO_4. *Phys. Rev. Lett.* **85**, 5412 (2000). 1.2

[43] Tou, H. *et al.* Odd-parity superconductivity with parallel spin pairing in UPt_3: Evidence from ^{195}Pt Knight shift study. *Phys. Rev. Lett.* **77**, 1374 (1996). 1.2

[44] Stassis, C. *et al.* Induced-moment magnetic form factor of the heavy-fermion superconductors UPt_3, UBe_{13}, and $CeCu_2Si_2$. *Phys. Rev. B* **34**, 4382 (1986). 1.2

[45] Luke, G. M. *et al.* Muon spin relaxation in UPt_3. *Phys. Rev. Lett.* **71**, 1466 (1993). 1.2

[46] Heffner, R. H. *et al.* New phase diagram for (U,Th)Be_{13}: A muon-spin-resonance and H_{C1} study. *Phys. Rev. Lett.* **65**, 2816 (1990). 1.2

[47] Mazin, I. I. & Singh, D. J. Ferromagnetic spin fluctuation induced superconductivity in Sr_2RuO_4. *Phys. Rev. Lett.* **79**, 733 (1997). 1.2, 1.4

[48] Damascelli, A. *et al.* Fermi surface, surface states, and surface reconstruction in Sr_2RuO_4. *Phys. Rev. Lett.* **85**, 5194 (2000). 1.2, 1.4, 1.5, 5

[49] Oguchi, T. Electronic band structure of Sr_2RuO_4. *Phys. Rev. B* **51**, 1385 (1995). 1.2, 2.2.6

[50] Singh, D. J. Relationship of Sr_2RuO_4 to the superconducting layered cuprates. *Phys. Rev. B* **52**, 1358 (1995). 1.2, 2.2.6, 5

[51] Adler, P., Goncharov, A. F., Syassen, K. & Schönherr, E. Optical reflectivity and raman spectra of Sr_2FeO_4 under pressure. *Phys. Rev. B* **50**, 11396 (1994). 1.2

[52] Rozenberg, G. K., Milner, A. P., Pasternak, M. P., Hearne, G. R. & Taylor, R. D. Experimental confirmation of a $p-p$ intraband gap in Sr_2FeO_4. *Phys. Rev. B* **58**, 10283 (1998). 1.2

[53] Shen, K. M. *et al.* Surface electronic structure of Sr_2RuO_4. *Phys. Rev. B* **64**, 180502 (2001). 1.2, 1.5, 5

[54] Mukuda, H. *et al.* Spin fluctuations in the ruthenium oxides RuO_2, $SrRuO_3$, $CaRuO_3$, and Sr_2RuO_4 probed by Ru NMR. *Phys. Rev. B* **60**, 12279 (1999). 1.2

[55] Mazin, I. I. & Singh, D. J. Competitions in layered ruthenates: Ferromagnetism versus antiferromagnetism and triplet versus singlet pairing. *Phys. Rev. Lett.* **82**, 4324 (1999). 1.2

[56] Braden, M., Reichardt, W., Nishizaki, S., Mori, Y. & Maeno, Y. Structural stability of Sr_2RuO_4. *Phys. Rev. B* **57**, 1236 (1998). 1.2, 1.2, 1.5, 1.4, 1.4, 1.5, 2.1.2, 3, 4, 5, 5.4

[57] Sidis, Y. *et al.* Evidence for incommensurate spin fluctuations in Sr_2RuO_4. *Phys. Rev. Lett.* **83**, 3320 (1999). 1.2

[58] Servant, F. *et al.* Magnetic excitations in the normal and superconducting states of Sr_2RuO_4. *Phys. Rev. B* **65**, 184511 (2002). 1.2

[59] Ishida, K. *et al.* Normal-state spin dynamics in the spin-triplet superconductor Sr_2RuO_4. *Phys. Rev. B* **64**, 100501 (2001). 1.2

[60] Birgeneau, R. J. *et al.* Soft-phonon behavior and transport in single crystal La_2CuO_4. *Phys. Rev. Lett.* **59**, 1329 (1987). 1.2, 3, 3.4

[61] Cowley, R. A. & Bruce, A. D. Structural phase transitions. *Adv. Phys.* **29**, 1 (1980). 1.2, 3

[62] Shirane, G. Neutron scattering studies of structural phase transitions at Brookhaven. *Rev. Mod. Phys.* **46**, 437 (1974). 1.2, 3

[63] Scott, J. F. Soft-mode spectroscopy: Experimental studies of structural phase transitions. *Rev. Mod. Phys.* **46**, 83 (1974). 1.2

[64] Crawford, M. K. *et al.* Structural and magnetic studies of Sr_2IrO_4. *Phys. Rev. B* **49**, 9198 (1994). 1.2, 3.6

[65] Subramanian, M. A. *et al.* Sr_2RhO_4 and Sr_2IrO_4 - structural and magnetic studies of $4d$ and $5d$ transition-metal analogs of La_2CuO_4. *Physica C* **235**, 743 (1994). 1.2, 3.6

[66] Nakatsuji, S., Ikeda, S. I. & Maeno, Y. Ca_2RuO_4 : new mott insulators of layered ruthenate. *J. Phys. Soc. Jpn.* **66**, 1868 (1997). 1.3, 1.3

[67] Cao, G., McCall, S., Shepard, M., Crow, J. E. & Guertin, R. P. Magnetic and transport properties of single-crystal Ca_2RuO_4: Relationship to superconducting Sr_2RuO_4. *Phys. Rev. B* **56**, R2916 (1997). 1.3

[68] Braden, M., André, G., Nakatsuji, S. & Maeno, Y. Crystal and magnetic structure of Ca_2RuO_4: Magnetoelastic coupling and the metal-insulator transition. *Phys. Rev. B* **58**, 847 (1998). 1.3, 1.3, 1.3, 5

[69] Alexander, C. S. *et al.* Destruction of the mott insulating ground state of Ca_2RuO_4 by a structural transition. *Phys. Rev. B* **60**, R8422 (1999). 1.3, 5.2

[70] Friedt, O. *et al.* Structural and magnetic aspects of the metal-insulator transition in $Ca_{2-x}Sr_xRuO_4$. *Phys. Rev. B* **63**, 174432 (2001). 1.3, 1.3, 1.7, 1.3, 1.4, 1.4, 1.4, 1.12, 2.2.6, 2.2.6.3, 2.2.10.1, 3, 3.3, 3.5, 3.5, 3.6, 4, 5, 5.1, 5.2, 5.2, 5.4, 5.2, 5.3, 5.5

[71] Braden, M. *et al.* Relation between structure and doping in $La_{2-x}Sr_xCuO_{4+\delta}$ a neutron diffraction study on single crystals. *Physica C* **223**, 396 (1994). 1.3, 1.4

[72] Mott, N. F. *Metal-Insulator Transitions* (Taylor and Francis, London, 1990), 2nd edn. 1.3, 4

[73] Bao, W. *et al.* Magnetic correlations and quantum criticality in the insulating antiferromagnetic, insulating spin liquid, renormalized fermi liquid, and metallic antiferromagnetic phases of the mott system V_2O_3. *Phys. Rev. B* **58**, 12727 (1998). 1.3

[74] Nakatsuji, S., Ando, T., Mao, Z. & Maeno, Y. Metal-insulator transition in $Ca_{2-x}Sr_xRuO_4$. *Physica B* **259**, 949 (1999). 1.3, 1.4, 5.2

[75] Nakatsuji, S. & Maeno, Y. Quasi-two-dimensional mott transition system $Ca_{2-x}Sr_xRuO_4$. *Phys. Rev. Lett.* **84**, 2666 (2000). 1.3, 1.3, 1.4, 1.11, 3, 3.3, 3.5, 3.6, 4, 5, 5.2

[76] Nakatsuji, S. & Maeno, Y. Switching of magnetic coupling by a structural symmetry change near the mott transition in $Ca_{2-x}Sr_xRuO_4$. *Phys. Rev. B* **62**, 6458 (2000). 1.3, 1.3, 1.4, 1.4, 3, 3.3, 3.5, 3.6, 5, 5.2

[77] Cao, G. *et al.* Ground-state instability of the mott insulator Ca_2RuO_4: Impact of slight la doping on the metal-insulator transition and magnetic ordering. *Phys. Rev. B* **61**, R5053 (2000). 1.3

[78] Steffens, P. *et al.* High-pressure diffraction studies on Ca_2RuO_4. *Phys. Rev. B* **72**, 094104 (2005). 1.3, 1.3, 5.5

[79] Yamada, K. *et al.* Successive antiferromagnetic phase transitions in single-crystal La_2CoO_4. *Phys. Rev. B* **39**, 2336 (1989). 1.3

[80] Crawford, M. K. *et al.* Structural phase transitions and weak ferromagnetism in $La_{2-x}Nd_xCuO_{4+\delta}$. *Phys. Rev. B* **47**, 11623 (1993). 1.3

[81] Nakajima, K. *et al.* Hole doping effects on 2D spin correlations in $La_2NiO_{4+\delta}$. *J. Phys. Soc. Jpn.* **64**, 716 (1995). 1.3

[82] Fang, Z., Terakura, K. & Nagaosa, N. Orbital physics in ruthenates: First-principles studies. *New J. Phys.* **7**, 1 (2005). 1.3, 1.4, 2.2.6, 2.2.6.1, 3.6, 5

[83] Mizokawa, T. *et al.* Spin-orbit coupling in the mott insulator Ca_2RuO_4. *Phys. Rev. Lett.* **87**, 077202 (2001). 1.3

[84] Anisimov, V. I., Nekrasov, I. A., Kondakov, D. E., Rice, T. M. & Sigrist, M. Orbital-selective Mott-insulator transition in $Ca_{2-x}Sr_xRuO_4$. *Euro. Phys. J. B* **25**, 191 (2002). 1.3, 2.2.6, 4

[85] Jung, J. H. *et al.* Change of electronic structure in Ca_2RuO_4 induced by orbital ordering. *Phys. Rev. Lett.* **91**, 056403 (2003). 1.3, 4.3

[86] Hotta, T. & Dagotto, E. Prediction of orbital ordering in single-layered ruthenates. *Phys. Rev. Lett.* **88**, 017201 (2001). 1.3, 4

[87] Lee, J. S. *et al.* Electron and orbital correlations in $Ca_{2-x}Sr_xRuO_4$ probed by optical spectroscopy. *Phys. Rev. Lett.* **89**, 257402 (2002). 1.3, 2.2.6, 4

[88] Imada, M., Fujimori, A. & Tokura, Y. Metal-insulator transitions. *Rev. Mod. Phys.* **70**, 1039 (1998). 1.3, 4, 5

[89] Edwards, P. P., Ramakrishnan, T. V. & Rao, C. N. R. The metal-insulator transition: A global perspective. *J. Phys. Chem.* **99**, 5228 (1995). 1.3

[90] Pergament, A. Metal-insulator transition: the Mott criterion and coherence length. *J. Phys. Condens. Matter* **15**, 3217 (2003). 1.3, 5

[91] Koga, A., Kawakami, N., Rice, T. M. & Sigrist, M. Orbital-selective mott transitions in the degenerate hubbard model. *Phys. Rev. Lett.* **92**, 216402 (2004). 1.3

[92] Koga, A., Kawakami, N., Rice, T. M. & Sigrist, M. Spin, charge, and orbital fluctuations in a multiorbital Mott insulator. *Phys. Rev. B* **72**, 045128 (2005). 1.3

[93] Liebsch, A. Absence of orbital-dependent Mott transition in $Ca_{2-x}Sr_xRuO_4$. *Europhys. Lett.* **63**, 97 (2003). 1.3, 5.2

[94] Liebsch, A. Mott transitions in multiorbital systems. *Phys. Rev. Lett.* **91**, 226401 (2003). 1.3

[95] Okamoto, S. & Millis, A. J. Electron-lattice coupling, orbital stability, and the phase diagram of $Ca_{2-x}Sr_xRuO_4$. *Phys. Rev. B* **70**, 195120 (2004). 1.3

[96] Friedt, O. *Interplay between electronic, magnetic and structural instabilities in $Ca_{2-x}Sr_xRuO_4$: A neutron scattering study.* Ph.D. thesis, Université Paris XI (2003). 1.4, 3, 3.5, 5.2, 5.3, 5.5

[97] Nakatsuji, S. *et al.* Heavy-mass fermi liquid near a ferromagnetic instability in layered ruthenates. *Phys. Rev. Lett.* **90**, 137202 (2003). 1.4, 1.12, 3.2, 3.6, 5

[98] Shannon, R. D. Revised effective ionic-radii and systematic studies of interatomic distances in halides and chalcogenides. *Acta Cryst. A* **32**, 751 (1976). 1.4, 2.2.6

[99] Wang, S.-C. *et al.* Fermi surface topology of ca[sub 1.5]sr[sub 0.5]ruo[sub 4] determined by angle-resolved photoelectron spectroscopy. *Phys. Rev. Lett.* **93**, 177007 (2004). 1.4, 5

[100] Matzdorf, R. *et al.* Ferromagnetism stabilized by lattice distortion at the surface of the p-wave superconductor Sr_2RuO_4. *Science* **289**, 746 (2000). 1.5, 5

[101] Matzdorf, R., Ismail, Kimura, T., Tokura, Y. & Plummer, E. W. Surface structural analysis of the layered perovskite Sr_2RuO_4 by LEED I(V). *Phys. Rev. B* **65**, 085404 (2002). 1.5, 2.2.10, 4, 5, 5.2, 5.4, 5.5

[102] Ismail *et al.* Surface lattice dynamics of layered transition metal oxides: Sr_2RuO_4 and $La_{0.5}Sr_{1.5}MnO_4$. *Phys. Rev. B* **67**, 035407 (2003). 1.5, 1.13, 3.6, 4, 4.1, 4.2, 4.3

[103] Katsufuji, T., Kasai, M. & Tokura, Y. In-plane and out-of-plane optical spectra of Sr_2RuO_4. *Phys. Rev. Lett.* **76**, 126 (1996). 1.5

[104] Udagawa, M. *et al.* Phonon Raman scattering of Sr_2RuO_4. *Physica B* **220**, 222 (1996). 1.5

[105] Davisson, C. & Germer, L. H. Diffraction of electrons by a crystal of nickel. *Phys. Rev.* **30**, 705 (1927). 2

[106] Davisson, C. & Germer, L. H. The scattering of electrons by a single crystal of nickel. *Nature* **119**, 558 (1927). 2

[107] Desjonquères, M. C. & Spanjaard, D. *Concepts in Surface Physics* (Springer-Verlag, Heidelberg, 1998). 2

[108] Shirane, G., Shapiro, S. M. & Tranquada, J. M. *Neutron Scattering with a Triple-Axis Spectrometer* (Cambridge University Press, Cambridge, UK, 2002). 2, 2.1, 2.1.1, 2.1.2, 2.1.2

[109] Bacon, G. E. (ed.) *Fifty Years of Neutron Diffraction: The Advent of Neutron Scattering* (Adam Hilger, Bristol, 1986). 2

[110] Squires, G. L. *Introduction to the Theory of Thermal Neutron Scattering* (Dover, Mineola, NY, 1978). 2.1

[111] High Flux Isotope Reactor. URL http://neutrons.ornl.gov. 2.1

[112] NIST Center for Neutron Research. URL http://www.ncnr.nist.gov. 2.1

[113] Dolling, G., Smith, H. G., Nicklow, R. M., Vijayaraghavan, P. R. & Wilkinson, M. K. Lattice dynamics of lithium fluoride. *Phys. Rev.* **168**, 970 (1968). 2.1.2

[114] Pendry, J. B. *Low Energy Electron Diffraction* (Academic Press, London, 1974). 2.2, 2.2.2, 2.2.4, 2.2.5, 2.2.5.1, 2.2.5.1, 2.2.7

[115] Van Hove, M. A., Weinberg, W. H. & Chan, C. M. *Low Energy Electron Diffraction* (Springer-Verlag, Berlin, 1986). 2.2, 2.2.2, 2.2.7

[116] Van Hove, M. A. & Tong, S. Y. *Surface Crystallography by LEED* (Springer-Verlag, Berlin, 1979). 2.2, 2.2.7

[117] Barbieri, A. & Van Hove, M. A. private communication. URL http://www.sitp.lbl.gov/index.php?content=/leedpack/. 2.2.2, 2.2.4, 2.2.6.3, 5.1

[118] Park, R. L. & Farnsworth, H. E. The structures of clean nickel crystal surfaces. *Surf. Sci.* **2**, 527 (1964). 2.2.3

[119] Sakurai, J. J. *Modern Quantum Mechanics* (Addison-Wesley, New York, 1985). 2.2.4

[120] Bransden, B. H. & Joachain, C. J. *Quantum Mechanics* (Prentice Hall, New Jersey, 2000). 2.2.4

[121] Mattheiss, L. F. Energy bands for solid argon. *Phys. Rev.* **133**, A1399 (1964). 2.2.4

[122] Loucks, T. *Augmented Plane Wave Method* (Benjamin, New York, 1967). 2.2.4

[123] Slater, J. C. *Insulators Semiconductors and Metals* (McGraww Hill, New York, 1967). 2.2.4

[124] Schwarz, K. Optimization of the statistical exchange parameter α for the free atoms H through Nb. *Phys. Rev. B* **5**, 2466 (1972). 2.2.4

[125] Zangwill, A. *Physics at Surfaces* (Cambridge University Press, Cambridge, 1988). 2.10

[126] Ismail. *The Structure and Dynamics of Magnesium Surfaces.* Ph.D. thesis, The University of Tennessee (1999). 2.2.5.1

[127] Hedin, L. & Lundqvist, B. I. Explicit local exchange-correlation potentials. *J. Phys. C* **4**, 2064 (1971). 2.2.5.2, 2.2.5.2, 2.2.5.2, 2.2.5.2

[128] Watson, R. E., Herbst, J. F., Hodges, L., Lundqvist, B. I. & Wilkins, J. W. Effect of ground-state and excitation potentials on energy levels of Ni metal. *Phys. Rev. B* **13**, 1463 (1976). 2.2.5.2, 2.2.5.2

[129] Rundgren, J. Optimized surface-slab excited-state muffin-tin potential and surface core level shifts. *Phys. Rev. B* **68**, 125405 (2003). 2.2.5.2, 2.2.5.2, 2.2.6.2, 5.1

[130] Neve, J., Rundgren, J. & Westrin, P. A cluster and DVM approach to the generation of LEED potentials: Application to Al(111) and Al(111)p(1x1)O. *J. Phys. C* **15** (1982). 2.2.5.2

[131] Kohn, W. & Sham, L. J. Self-consistent equations including exchange and correlation effects. *Phys. Rev.* **140**, A1133 (1965). 2.2.5.2

[132] Singwi, K. S., Tosi, M. P., Land, R. H. & Sjölander, A. Electron correlations at metallic densities. *Phys. Rev.* **176**, 589 (1968). 2.2.5.2

[133] Shung, K. W. K., Sernelius, B. E. & Mahan, G. D. Self-energy corrections in photoemission of Na. *Phys. Rev. B* **36**, 4499 (1987). 2.2.5.2

[134] Rundgren, J. Electron inelastic mean free path, electron attenuation length, and low-energy electron-diffraction theory. *Phys. Rev. B* **59**, 5106 (1999). 2.2.5.2

[135] Walter, S. *et al.* The rol of an energy-dependent inner potential in quantitative low-energy electron diffraction. *Surf. Sci.* **458**, 155 (2000). 2.2.5.2

[136] Shannon, R. D. & Prewitt, C. T. Effective ionic radii in oxides and flourides. *Acta Cryst. B* **25**, 925 (1969). 2.2.6

[137] Baroni, S. *et al.* URL http://www.pwscf.org. 2.2.6.1, 3.5

[138] Kotliar, G. & Vollhardt, D. Strongly correlated materials: Insights from dynamical mean-field theory. *Phys. Today* **57**, 53 (2004). 2.2.6.1

[139] Lindsay, R. *et al.* Revisiting the surface structure of TiO_2(110): A quantitative low-energy electron diffraction study. *Phys. Rev. Lett.* **94**, 246102 (2005). 2.2.6.1

[140] Beeby, J. L. Diffraction of low-energy electrons by crystals. *J. Phys. C* **1**, 82 (1968). 2.2.7

[141] Pendry, J. B. New perturbation theory for low-energy electron-diffraction intensities. *Phys. Rev. Lett.* **27**, 856 (1971). 2.2.7

[142] Gauthier, Y., Baudoing, R., Lundberg, M. & Rundgren, J. Surface-sandwich segregation and multilayer relaxation on $Pt_{0.5}Ni_{0.5}$(110) measured by low-energy electron diffraction: An observation of face-related segregation reversal. *Phys. Rev. B* **35**, 7867 (1987). 2.2.7

[143] Crampin, S. & Rous, P. J. The validity of the average t-matrix approximation for low-energy electron diffraction from random alloys. *Surf. Sci.* **244**, L137 (1991). 2.2.7

[144] Rous, P. J. *et al.* Tensor LEED: A technique for high-speed surface-structure determination. *Phys. Rev. Lett.* **57**, 2951 (1986). 2.2.8

[145] Rous, P. J. & Pendry, J. B. The theory of tensor LEED. *Surf. Sci.* **219**, 355 (1989). 2.2.8

[146] Rous, P. J. & Pendry, J. B. Applications of tensor LEED. *Surf. Sci.* **219**, 373 (1989). 2.2.8

[147] Rous, P. J. The tensor LEED approximation and surface crystallography by low-energy electron diffraction. *Prog. Surf. Sci.* **39**, 3 (1992). 2.2.8

[148] Pendry, J. B. Reliability factors for LEED calculations. *J. Phys. Chem.* **13**, 937 (1980). 2.2.9, 2.2.9

[149] Corana, A., Marchesi, M., Martini, C. & Ridella, S. Minimizing multimodal functions of continuous variables with the simulated annealing algorithm. *Trans. Math. Soft.* **13**, 262 (1987). 2.2.10.2, 2.2.10.2

[150] Goffe, W. L., Ferrier, G. D. & Rogers, J. Global optimization of statistical functions with simulated annealing. *J. Econ.* **60**, 65 (1994). 2.2.10.2, 2.2.10.2

[151] Kirkpatrick, S., Gelatt, C. D. & Vecchi, M. P. Optimization by simulated annealing. *Science* **220**, 671 (1983). 2.2.10.2

[152] Rous, P. J. A global approach to the search problem in surface crystallography by low-energy electron diffraction. *Surf. Sci.* **296**, 358 (1993). 2.2.10.2

[153] Nascimento, V. B., de Carvalho, V. E., de Castilho, C. M. C., Costa, B. V. & Soares, E. A. The fast simulated annealing algorithm applied to the search problem in LEED. *Surf. Sci.* **487**, 15 (2001). 2.2.10.2

[154] Correia, E. R. *et al.* The generalized simulated annealing algorithm in the low energy electron diffraction search problem. *J. Phys. Condens. Matter* **17**, 1 (2005). 2.2.10.2

[155] H., S. & Hartley, R. Fast simulated annealing. *Phys. Lett. A* **122**, 157 (1987). 2.2.10.2

[156] Tsallis, C. & Stariolo, D. A. Generalized simulated annealing. *Physica A* **233**, 395 (1996). 2.2.10.2

[157] Ibach, H. & Mills, D. L. *Electron Energy Loss Spectroscopy and Surface Vibrations* (Academic Press, New York, NY, 1982). 2.3, 2.3, 2.3.1, 2.3.2, 2.3.2, 4

[158] Ibach, H. *Electron Energy Loss Spectrometers - The Technology of High Performance* (Springer-Verlag, Heidelberg, 1991). 2.3

[159] Persson, B. N. J. Theory of inelastic-scattering of slow-electrons by molecules absorbed on metal surfaces. *Solid State Comm.* **24**, 573 (1977). 2.3.1

[160] Persson, B. N. J. Inelastic-scattering of slow-electrons from adsorbed molecules. *Surf. Sci.* **92**, 265 (1980). 2.3.1

[161] Ho, W., Willis, R. F. & Plummer, E. W. Observation of nondipole electron impact vibrational excitations: H on W (100). *Phys. Rev. Lett.* **40**, 1463 (1978). 2.3.2

[162] Grande, B., Müller-Buschbaum, H. & Schweizer, M. Crystal-structures of rare-earth oxocuprates – La_2CuO_4 and Gd_2CuO_4. *Z. Anorg. Alleg. Chem.* **428**, 120 (1977). 3

[163] Wavelab software package. URL http://www-stat.stanford.edu/~wavelab/. 3.1

[164] Kolaczyk, E. D. Nonparametric estimation of gamma-ray burst intensities using Haar wavelets. *Astrophys. J.* **483**, 340 (1997). 3.1

[165] Charles, C., Leclerc, G., Pireaux, J. J. & Rasson, J. P. Introduction to wavelet applications in surface spectroscopies. *Surf. Interface Anal.* **36**, 49 (2004). 3.1

[166] Charles, C., Leclerc, G., Rasson, J. P. & Pireaux, J. J. HREELS signal processing via wavelets. *Surf. Interface Anal.* **36**, 61 (2004). 3.1

[167] Charles, C., Leclerc, G., Louette, P., Rasson, J. P. & Pireaux, J. J. Noise filtering and deconvolution of XPS data by wavelets and Fourier transform. *Surf. Interface Anal.* **36**, 71 (2004). 3.1

[168] Jin, R. unpublished data. 3.2

[169] Melechko, A. V., Simkin, M. V., Samatova, N. F., Braun, J. & Plummer, E. W. Complex structural phase transition in a defect-populated two-dimensional system. *Phys. Rev. B* **64**, 235424 (2001). 3.5, 5.7

[170] Pérez, R., Ortega, J. & Flores, F. Surface soft phonon and the $\sqrt{3} \times \sqrt{3} \leftrightarrow 3 \times 3$ phase transition in Sn/Ge(111) and Sn/Si(111). *Phys. Rev. Lett.* **86**, 4891 (2001). 3.5

[171] Petersen, L., Ismail & Plummer, E. W. Defect-induced localized lattice distortions in Sn/Ge(111). *Phys. Rev. B* **65**, 020101 (2001). 3.5

[172] Petersen, L., Ismail & Plummer, E. W. Defect-blurred two-dimensional phase transition. *Prog. Surf. Sci.* **71**, 1 (2002). 3.5, 5.7

[173] Proffen, T. & Neder, R. B. DISCUS: A program for diffuse scattering and defect-structure simulation. *J. Appl. Cryst.* **30**, 171 (1997). 3.5

[174] Proffen, T. & Neder, R. B. DISCUS: A program for diffuse scattering and defect-structure simulation–update. *J. Appl. Cryst.* **32**, 838 (1999). 3.5

[175] Kriener, M. *et al.* Structural aspects of metamagnetism in $Ca_{2-x}Sr_xRuO_4$: Evidence for field tuning of orbital occupation. *Phys. Rev. Lett.* **95**, 267403 (2005). 3.6

[176] Baier, J. *et al.* Thermodynamic properties of $Ca_{2-x}Sr_xRuO_4$ in magnetic fields. *Physica B* **378**, 497–498 (2006). 3.6

[177] Grilli, M. & Castellani, C. Electron-phonon interactions in the presence of strong correlations. *Phys. Rev. B* **50**, 16880 (1994). 4

[178] Deppeler, A. & Millis, A. J. Electron-phonon interactions in correlated systems: Adiabatic expansion of the dynamical mean-field theory. *Phys. Rev. B* **65**, 100301 (2002). 4

[179] Plummer, E. W. *et al.* Surfaces: A plaground for physics with broken symmetry in reduced dimensionality. *Surf. Sci.* **500**, 1 (2002). 4

[180] Potthoff, M. Metal-insulstor transitions at surfaces. *Adv. Solid State Phys.* **42**, 121 (2002). 4

[181] Akavoor, P., Phelps, R. B. & Kesmodel, L. L. Charging effects in measurements of high-temperature superconductors with high resolution electron-energy-loss spectroscopy. *J. Vac. Sci. Technol. A* **12**, 587 (1994). 4.1

[182] Rho, H., Cooper, S. L., Nakatsuji, S., Fukazawa, H. & Maeno, Y. Raman scattering studies of spin, charge, and lattice dynamics in $Ca_{2-x}Sr_xRuO_4$ ($0 \leq x \leq 0.2$). *Phys. Rev. B* **68**, 100404 (2003). 4.3

[183] Zhang, J., Ismail, Jin, R., Mandrus, D. G. & Plummer, E. W. unpublished data. 4.3

[184] Hahn, T. (ed.) *International Tables for Crystallography, Volume A: Space Group Symmetry* (Springer, New York, 2005). 5.2

[185] Jin, R. *et al.* Heavy-electron behavior and structural change in $Ca_{1.7}Sr_{0.3}RuO_4$. *cond-mat* 0112405 (2001). 5.6

[186] Zhang, J. D. *et al.* Dopant-induced nanoscale electronic inhomogeneities in $Ca_{2-x}Sr_xRuO_4$. *Phys. Rev. Lett.* (in press). 5.6

[187] Matzdorf, R. unpublished data. 5.20, 5.7

[188] Baddorf, A. P. *et al.* unpublished data. 5.7

Vita

Robert Glenn Moore II was born in Nashville, Tennessee, on November 27, 1970. After graduating from Brentwood High School, Brentwood, Tennessee, he attended Tennessee Technological University in Cookeville where he graduated *magna cum laude* with a Bachelor of Science degree in Mechanical Engineering in 1994. While as an undergraduate he was team captain for the Mini-Baja student design competition finishing laps in front of the competition in both Eastern and Western division races and the Vice President of Alpha Phi Omega National Service Fraternity raising funds and providing service for several local and national organizations. During his undergraduate studies he also enrolled in the Navy's Nuclear Propulsion Officer Candidate program. After graduation he completed six successful strategic deterrent patrols as a submarine officer aboard the USS Alaska (SSBN 732 Gold crew) where he received two Navy and Marine Corps Achievement Medals. In 2000 he returned to the academic world as a student at the University of Washington, Seattle, Washington, receiving a Masters of Science degree in Physics in 2002. For his masters degree, he studied magnetic properties of Co:Pt multilayered thin films utilizing coherent magnetic x-ray scattering. In Fall, 2002, he entered The University of Tennessee, Knoxville, Tennessee as a doctoral student in Physics studying the surfaces of transition-metal oxides. While as a doctoral student he received the Tennessee Advanced Materials Laboratory Fellowship, the UT Neutron Sciences Fellowship from the Joint Institute of Neutron Sciences and was the 2006 recipient of the Fowler-Marion Outstanding Graduate Student Award. He completed his Doctor of Philosophy degree in Physics in 2006.

Rob is married and both he and his wife, Tammy, enjoy hiking, biking, motor cycle riding, traveling and house remodeling. Rob also enjoys reading, playing guitar and playing Go. When asked in kindergarten what he wanted to be when he grew up, Rob responded:"A kitty cat." When asked the same question as a doctoral student, the response was the same.